N°d'ordre NNT : 2022LYSEI060

THESE de DOCTORAT DE L'UNIVERSITE DE LYON
opérée au sein de
L'Institut National des Sciences Appliquées de Lyon

Ecole Doctorale N° ED 34
Matériaux de Lyon

Spécialité de doctorat : Matériaux

Soutenue publiquement le 28/06/2022, par :
Laurabelle Gautier

Critical aspects of Titanium-based Bulk Metallic Glasses for biomedical applications: an investigation on casting defects and corrosion sensitivity

---

Devant le jury composé de :

Jean-Jacques BLANDIN	Professeur	Univ Grenoble	Rapporteur
Jean-Christophe SANGLEBOEUF	Professeur	Univ Rennes	Rapporteur
Anne TANGUY	Professeur	ONERA	Examinatrice
Nathalie BOZZOLO	Professeur	MINES Paris Tech	Examinatrice
Florian SPIECKERMANN	Maitre de conférences	Univ Leoben	Examinateur
Jérôme CHEVALIER	Professeur	INSA de Lyon	Directeur de thèse
Damien FABREGUE	Professeur	INSA de Lyon	Directeur de thèse
Claire GAILLARD	Maitre de conférences	INSA de Lyon	Co-encadrante
Benoît TER-OVANESSIAN	Maitre de conférences	INSA de Lyon	Invité

Département FEDORA – INSA Lyon - Ecoles Doctorales

SIGLE	ECOLE DOCTORALE	NOM ET COORDONNEES DU RESPONSABLE
CHIMIE	**CHIMIE DE LYON** **https://www.edchimie-lyon.fr** Sec. : Renée EL MELHEM Bât. Blaise PASCAL, 3e étage secretariat@edchimie-lyon.fr	**M. Stéphane DANIELE** C2P2-CPE LYON-UMR 5265 Bâtiment F308, BP 2077 43 Boulevard du 11 novembre 1918 69616 Villeurbanne **directeur@edchimie-lyon.fr**
E.E.A.	**ÉLECTRONIQUE, ÉLECTROTECHNIQUE, AUTOMATIQUE** **https://edeea.universite-lyon.fr** Sec. : Stéphanie CAUVIN Bâtiment Direction INSA Lyon Tél : 04.72.43.71.70 secretariat.edeea@insa-lyon.fr	**M. Philippe DELACHARTRE** INSA LYON Laboratoire CREATIS Bâtiment Blaise Pascal, 7 avenue Jean Capelle 69621 Villeurbanne CEDEX Tél : 04.72.43.88.63 **philippe.delachartre@insa-lyon.fr**
E2M2	**ÉVOLUTION, ÉCOSYSTÈME, MICROBIOLOGIE, MODÉLISATION** **http://e2m2.universite-lyon.fr** Sec. : Bénédicte LANZA Bât. Atrium, UCB Lyon 1 Tél : 04.72.44.83.62 secretariat.e2m2@univ-lyon1.fr	**Mme Sandrine CHARLES** Université Claude Bernard Lyon 1 UFR Biosciences Bâtiment Mendel 43, boulevard du 11 Novembre 1918 69622 Villeurbanne CEDEX **sandrine.charles@univ-lyon1.fr**
EDISS	**INTERDISCIPLINAIRE SCIENCES-SANTÉ** **http://ediss.universite-lyon.fr** Sec. : Bénédicte LANZA Bât. Atrium, UCB Lyon 1 Tél : 04.72.44.83.62 secretariat.ediss@univ-lyon1.fr	**Mme Sylvie RICARD-BLUM** Institut de Chimie et Biochimie Moléculaires et Supramoléculaires (ICBMS) - UMR 5246 CNRS - Université Lyon 1 Bâtiment Raulin - 2ème étage Nord 43 Boulevard du 11 novembre 1918 69622 Villeurbanne Cedex Tél : +33(0)4 72 44 82 32 **sylvie.ricard-blum@univ-lyon1.fr**
INFOMATHS	**INFORMATIQUE ET MATHÉMATIQUES** **http://edinfomaths.universite-lyon.fr** Sec. : Renée EL MELHEM Bât. Blaise PASCAL, 3e étage Tél : 04.72.43.80.46 infomaths@univ-lyon1.fr	**M. Hamamache KHEDDOUCI** Université Claude Bernard Lyon 1 Bât. Nautibus 43, Boulevard du 11 novembre 1918 69 622 Villeurbanne Cedex France Tél : 04.72.44.83.69 **hamamache.kheddouci@univ-lyon1.fr**
Matériaux	**MATÉRIAUX DE LYON** **http://ed34.universite-lyon.fr** Sec. : Yann DE ORDENANA Tél : 04.72.18.62.44 yann.de-ordenana@ec-lyon.fr	**M. Stéphane BENAYOUN** Ecole Centrale de Lyon Laboratoire LTDS 36 avenue Guy de Collongue 69134 Ecully CEDEX Tél : 04.72.18.64.37 **stephane.benayoun@ec-lyon.fr**
MEGA	**MÉCANIQUE, ÉNERGÉTIQUE, GÉNIE CIVIL, ACOUSTIQUE** **http://edmega.universite-lyon.fr** Sec. : Stéphanie CAUVIN Tél : 04.72.43.71.70 Bâtiment Direction INSA Lyon mega@insa-lyon.fr	**M. Jocelyn BONJOUR** INSA Lyon Laboratoire CETHIL Bâtiment Sadi-Carnot 9, rue de la Physique 69621 Villeurbanne CEDEX **jocelyn.bonjour@insa-lyon.fr**
ScSo	**ScSo*** **https://edsciencessociales.universite-lyon.fr** Sec. : Mélina FAVETON INSA : J.Y. TOUSSAINT Tél : 04.78.69.77.79 melina.faveton@univ-lyon2.fr	**M. Christian MONTES** Université Lumière Lyon 2 86 Rue Pasteur 69365 Lyon CEDEX 07 **christian.montes@univ-lyon2.fr**

*ScSo : Histoire, Géographie, Aménagement, Urbanisme, Archéologie, Science politique, Sociologie, Anthropologie

Acknowledgements

Voici venue l'heure des remerciements. Après m'être remise de cette journée très particulière que fut celle de ma soutenance, très riche en sciences et en émotions, je vais prendre le temps au fil de ces quelques lignes de remercier les personnes qui ont eu un rôle clé dans la réussite de cette thèse.

Tout d'abord je vais remercier mes rapporteurs, messieurs Jean-Jacques Blandin et Jean-Christophe Sangleboeuf. Merci d'avoir accepté de lire ce manuscrit et de vous y être vraiment intéressés. Vous avez fait un travail remarquable de lecture et vous avez fait remonter certaines questions/remarques/avis vraiment pertinents qui auront une influence sur la suite de la thématique. Je vous ai perçus tous deux, comme d'une profonde bienveillance à mon égard tout en restant dans votre rôle d'examinateur. Je pense que nous aurions pu encore échanger de longues heures sur le sujet des verres métalliques et pour tout ça merci.

Je tiens également à remercier Mme.Nathalie Bozzolo, en qualité de présidente de mon jury. Bien que la thématique ma thèse soit quelque peu éloignée de votre thématique de recherche je vous remercie d'avoir accepté de faire partie de ce jury. En tant que présidente c'est vous la dernière à avoir pris la parole pour faire la restitution concernant ma soutenance. Je tiens ici à vous témoigner ma gratitude pour la justesse des mots que vous avez employé ce jour-là qui m'ont profondément touchée et qui resteront gravés très longtemps.

Je remercie également Mme. Anne Tanguy et M. Florian Spiekermann d'avoir accepté d'évaluer ce travail de thèse. Nos discussions ont été vraiment intéressantes et ce fut un plaisir de vous avoir compté parmi nous. Merci à tous les membres du jury de vous être déplacé jusqu'à Lyon pour que cette soutenance se déroule dans les meilleures conditions. J'espère avoir l'occasion de vous recroiser à l'avenir, peut-être en conférence ou peut-être dans le cadre d'une collaboration.

Mais avant d'arriver à une soutenance il faut déjà avoir un travail à présenter et ce travail a été rendu possible par mes encadrants. D'abord mes deux directeurs de thèse, ce sont de grands scientifiques, Damien.F et Jérôme.C. On pourrait croire que tout les oppose, l'un travail sur métaux l'autre sur les céramiques, l'un est très optimiste, l'autre plus difficile à convaincre. Et pourtant ce duo est particulièrement bien assorti sur les thématiques de verre métalliques. Il est vrai que vous avez tous les deux des emplois du temps bien chargés mais j'ai conscience que vous avez fait beaucoup d'efforts pour ne pas me laisser tomber

même dans les moments difficiles. Vous avez été indulgents et patients avec la petite biologiste catapultée à Mateis sans compétences en matériaux. Merci aussi de ne pas avoir accepté de baisser vos exigences en raison de mon cursus d'origine. Même plus, vous avez toujours été bienveillants et c'est probablement grâce à cette bienveillance de votre part mais aussi à la conviction que vous aviez qu'il y avait de belles choses à faire sur cette thèse que je suis allée au bout. J'ai l'impression de ne jamais vous avoir inquiété, vous m'avez laissé faire mon chemin, encouragé mes idées, vous avez été réjouis ou déçus des résultats avec moi mais avec cette capacité à toujours trouver les mots pour me remobiliser quoi qu'il arrive. Pour tout ça merci, ce que j'ai appris avec vous et vos mots à ma soutenance me laisseront une trace indélébile.

Merci Benoît.TO qui en réalité est bien plus qu'un « invité » dans cette thèse. Toujours de bonne humeur, un mot pour rire, ça a toujours été un plaisir de faire un crochet par Corris pour passer te voir. Merci de m'avoir fait bénéficier de d'avantage de proximité, tu t'es toujours montré très disponible et très intéressé par le sujet BMG. Malgré tout ce temps passé à faire des mesures d'électrochimie tu ne seras pas surpris d'apprendre que ce n'est pas le thème que j'ai préféré dans ma thèse, je suis désolée. Tu en as pourtant passé du temps à m'expliquer les principes généraux en électrochimie mais j'ai toujours eu la sensation que c'était une science un peu trop subtile pour moi.

Claire.G, malheureusement les circonstances de la thèse ont fait que nous n'avons eu que peu d'interactions au cours de ces 3 ans, pas par manque d'envie mais par la réorientation du sujet qui s'annonçait « très bio » au départ et qui s'est avéré « totalement matériau » en définitive. J'espère que tu n'auras pas totalement perdu ton temps et que tu auras peut-être même appris 2-3 trucs au passage.

Des remerciements un peu spéciaux à l'intention de Sophie.C. Tu n'avais rien demandé à personne et pourtant tu as récolté pas mal de travail en plus avec moi. Je ne sais pas ce que tu en penses mais de mon côté c'était un plaisir immense de bosser avec toi. Tu es là, carrée, super réactive, tu expliques super bien, tu es super calée, tu poses des super bonnes questions (pour lesquelles c'est rare que j'ai une réponse) et même quand tu n'en as pas tu prends du temps pour faire les choses bien et jusqu'au bout. Pour moi c'était un « super match professionnel », et même si c'est peu probable, si on avait l'occasion de rebosser ensemble je le ferais sans hésiter. Personnellement j'ai aussi été très impressionnée par ton honnêteté, tu dis les choses les bonnes et les moins bonnes, ça peut faire mal sur le coup mais c'est toujours juste et justifié. Avant la soutenance tu m'as fait un gros coaching, je crois que j'avais un peu besoin qu'on me remette les pendules à l'heure et ce n'était pas inutile puisque c'est notamment grâce à toi que ma présentation s'est si bien passée et que j'ai pu avoir des retours si positifs. MERCI pour tout ! Continue d'être une source d'inspiration pour tout le monde au labo. Et je remercie très chaleureusement la team Anthogyr, tout d'abord Nicolas parce que c'est certain sans toi je n'aurai pas mis un seul pied à Mateis. Merci de m'avoir appris tant de chose à Sallanches, de m'avoir donné quelques armes pour la thèse et de m'avoir fait confiance tout du long. J'aurai adoré te

garder en tant qu'encadrant pour la thèse, tu as été un vrai mentor pour moi au BE. Merci à Anne-Lise et Hervé pour votre gentillesse et votre bienveillance, merci d'être venu m'aider pour de la tomoX et merci de m'avoir usiné de nombreux échantillons. Un grand merci à Laura, tu as réceptionné une remplaçante légèrement angoissée et très inexpérimentée à mon arrivée à Mateis, merci d'avoir aidé à faire mes premiers pas au labo, de m'avoir tant aidé tout du long de la thèse et de m'avoir beaucoup écoutée et rassurée, tu es vraiment formidable, ne change pas.
La thèse se fait avec un thésard et ses encadrants mais aussi et surtout au sein d'un laboratoire. Me concernant j'ai eu beaucoup de chance, après un passage dans l'équipe CERA où je me suis beaucoup plu, j'ai migré dans l'équipe METAL. Et quelle équipe ! Sans vous, je pense que le manuscrit serait actuellement vide. Je pense que je suis tombée sur des permanents et des thésards incroyables. Il y en a eu des misères pendantes ces 3 ans : rupture du ligament croisé au week-end ski doctorants (merci à ceux qui m'ont ramassée sur la piste, ceux qui sont allés chercher un pisteur pour me descendre et ceux qui m'ont tenu compagnie à la clinique de la Rosières), opération du genou, rééducation, COVD-19 et confinement(ssss) et enfin travaux à l'INSA (ce n'est toujours pas fini). Toutes les générations de thésards pensent être dans la pire des configurations mais j'ai bien l'impression que nous n'avons pas démérité.
Les permanents de l'équipe Métal sont une espèce un peu à part : ils sont brillants, disponibles et d'une gentillesse infinie et ils acceptent d'aider les thésards même quand ce ne sont pas les leurs. Quelle ne fut pas ma marge de progression en métallurgie grâce à eux ! Une petite question sur le temps de midi ou au détour d'un couloir, qui se transforme en 1h de théorie sur tableau noir, des teams buildings, des repas de noël et des restos de vacances, c'est aussi ça l'âme de Métal.
Que serait cette équipe sans la présence de son animateur Michel ! Michel tu es bon dans ton rôle animateur d'équipe, en dehors de tes compétences scientifiques qui m'ont beaucoup aidée à de nombreuses reprises. Je retiendrai encore plus je crois tes qualités humaines. Merci de m'avoir écoutée et aiguillée dans la bonne direction. Tu es bien souvent notre bureau des plaintes à nous les thésards c'est vrai, mais tu nous accueilles toujours avec une bienveillance illimitée dont on a tendance à abuser. Je sais que ça te fait toujours quelque chose de voir partir les thésards d'autant plus que les dernières promos étaient vraiment très riches en personnalités brillantes et attachantes. On a souvent un peu de mal à partir de Mateis car on sait qu'on n'aura pas droit à un autre Michel ailleurs. Dans un autre registre, je tiens à te remercier pour l'alpinisme du refuge du fond des fours, tu m'as permis de réaliser un de mes rêves et je n'oublierai jamais ça, merci.
Merci à Frida et Véronique nos gestionnaires adorées. Vous avez fait un travail de titans surtout avec des collègues comme nous, je n'imagine pas à quel point on doit vous taper sur le système parfois. Tout au long de ma thèse vous avez été d'une efficacité monstrueuse, je vous remercie pour tout et je vous tire mon chapeau.
Merci JYB pour toute l'aide que tu m'as apporté. D'abord en tant que directeur de

l'école doctorale (c'était vachement pratique pour nous, on beaucoup perdu au change), de m'avoir conseillée sur les orientations de la thèse et merci pour la science. Je suis toujours très impressionnée par ta capacité à expliquer des choses vraiment complexes de façon si simple même si j'ai plusieurs fois déboulé dans ton bureau avec des questions difficiles sur un matériau qui n'obéit que rarement aux théories des métaux. Je dois bien admettre que tu m'as un peu fait paniquer quelques jours avant ma soutenance mais c'était finalement pour le mieux.
Merci Jérôme et Justine, la dream team de la tomo ! Vous êtes trop forts ! Toujours super agréable de bosser avec vous ! Et merci Justine pour tous les coups de mains que tu as pu me donner tous du long notamment en salle 26 mais pas que.
Merci Xavier.B, déjà pour le four à arc (entre autres), pour tous les autres discussions/questions qu'on a pu avoir. J'étais souvent avec tes thésards alors c'était un peu trop tentant de te demander des choses au passage. Tu es vraiment super dynamique, pointu et souriant c'est un plaisir de bosser avec toi !
Merci Christophe pour la discussion DRX et de m'avoir mis sur la voie de l'identification des phases des sphérulites. Merci aussi d'avoir accepté de récupérer la manip synchrotron de 2023. Je suis sûr que ça donnera quelque chose de sympa.
Merci Florian.M, l'homme de toutes les situations, tu connais tout et tout le monde et en plus tu es rapide. Je ne sais pas si le labo pourrait tourner sans toi ! Heureusement que tu es là et merci ! Dans cette équipe incroyable, je pense avoir eu une chance infinie d'avoir été prise sous les ailes de thésards un peu plus expérimentés que moi, sans eux c'est sûr je ne serai pas docteure aujourd'hui. D'abord les « anciens », merci à Justine, Aléthéa, Gwenaël, Syb, Théo, Alexis, Gabriel, François, Julie qui ont soutenu quelques mois après mon arrivée seulement. Vous avez su inspirer les autres thésards. En tout cas vous avez tous été d'une grande bienveillance et très pédagogues même avec les petits nouveaux.
Ensuite il y a eu une promotion un peu plus spéciale avec Alexandre, Arnaud.J, Marion.C, Lucile et Quentin. Etant arrivée entre deux « promos » vous m'avez très vite adoptée et très vite poussée à vous suivre dans vos folles aventures sportives, Il n'y a pas à dire ça crée des liens ! Pour rentrer un peu plus dans le détail, comment ne pas mentionner le fameux « bureau du Bonheur », je serai surement la dernière à en parler. On était 3 (ou plutôt 4) et on était bien, très bien même ! Lucile, une force immense cachée derrière une grande discrétion. J'avoue ici que ta fin de thèse m'a fait rêver, non pas que ça n'a pas été difficile pour toi, c'est surtout que tu l'as fait tout en maitrise de toi et du sujet. J'ai largement essayé de m'inspirer de toi pour ma propre rédaction/soutenance, je ne pense pas avoir réussi à égaler le maître mais je pense qu'adopter ta technique a eu un bel effet sur moi. En dehors de ça, tu as eu un rôle essentiel car tu sais faire relativiser les autres dans n'importe quelle circonstance et tu as eu l'occasion de t'exercer pas mal avec moi vu ma tendance à dramatiser parfois. Je suis désolée si je t'ai un peu bousculée parfois avec mes questions, avec mes affirmations aussi. Ton départ de Mateis s'est un peu traduit par une rupture d'harmonie au bureau mais ainsi va la vie et tous les thésards finissent par

quitter le nid.
Quentin, que de chemin parcouru ensemble ! Merci d'avoir prolongé ton séjour à Mateis un an de plus pour me laisser le temps de finir ma thèse à mon tour avec toi en support. Je sais que ta propre fin de thèse a été une période de ta vie particulièrement complexe voire douloureuse. Les filles et moi, on a fait au mieux tout du long même si ça n'a pas toujours été à la hauteur de tes attentes. Tu forces mon respect avec tout ce que tu entreprends, tout le monde et très fier de toi, même si tu ne rends pas toujours compte. Si tu pouvais te voir comme les autres te vois je pense que tu serais convaincu. Ton avenir s'annonce billant au CETIM à Cluses, j'espère que tu t'y plairas, pas certaines de pouvoir trouver du travail vers Sallanches pour qu'on soit voisin... En tout cas je te souhaite le meilleur à tous les niveaux.
Marion, d'après les gens de l'équipe il parait qu'on a beaucoup de points communs. J'ai vraiment eu l'impression qu'on se comprenait vraiment sur beaucoup de choses. Ton dynamisme et ta passion pour la recherche sont vraiment très inspirants voire contagieux. Quand je te vois, je vois quelqu'un qui a comme trouvé sa place dans le monde. Je sais qu'actuellement en Belgique tu n'es dans les meilleures conditions mais ne lâche pas, sert toi de cette expérience comme tremplin et va décrocher ta place de MDF tant méritée. PS : je suis désolée de t'avoir tripoté les yeux un certain week-end enneigé.
Tous les trois on ne va plus pouvoir partager notre quotidien et c'est bien dommage, mais on ne se perdra jamais vraiment de vue c'est certain. Impossible d'effacer tous ces moments bons comme les moins bons. Il va falloir qu'on se renouvelle malgré nos changements de vie, on va inventer des traditions comme des réunions annuelles du BDB ou pourquoi pas des vacances communes ?
Il y en d'autres des thésards dans cette équipe et je ne les oublie pas. Manon, on est arrivé exactement le même jour au labo, j'étais en panique mais pas toi j'avais l'impression que tu étais opérationnelle dès le départ. Je crois que ça a tout de suite collé entre nous. Enseigner les TP avec toi c'était top (surtout pour finir la soirée à la Kfet après), ça m'a fichu un sacré coup quand tu as dû partir pour le Japon mais j'étais si heureuse que tu reviennes. Tu as vraiment été une amie et une confidente tout du long de cette aventure. Malheureusement je sais que ton passage à Mateis est loin d'être tout rose mais du fond du cœur j'espère que tout finira par s'arranger et que tu mèneras la vie que tu souhaites une fois que tu te seras débarrassée (ou pas) de ce fardeau qu'on appelle parfois thèse. Garde cette personnalité pétillante, tes convictions bien tranchées et ton franc parlé inimitable que j'apprécie tant. Merci de m'avoir aidée pour pleins de choses et surtout pour les coups durs. Merci de m'avoir accompagnée à l'hôpital pour mon genou et de ne pas m'avoir laissé seule le matin de ma soutenance.
Marion.B et Justine.T, à l'heure où j'écris ces lignes vous êtes sur la dernière ligne droite ! Courage, vous êtes clairement sur les bons rails pour terminer. C'est sur il y aura de la peur et du stress mais je serai là en soutien si vous avez besoin ! Merci Justine pour ton calme et ta bonne humeur constante. Tu es toujours prête à aider les autres et à les écouter même si

toi-même tu as un sujet de thèse assez capricieux il me semble. Merci pour les sorties skis, vélo, Miribel etc... C'était trop bien ! Merci Marion d'avoir rejoint notre bureau, tu n'es peut-être pas tombée au meilleur moment, Quentin et moi on a dû être vraiment chiants chacun à notre façon sur la fin, désolée. En tout cas toi, tu es inébranlable, pourtant tu es largement dans la catégorie circonstances défavorables, mais tout du long tu as su rester assez stoïque et équilibrée (je pense que Baptiste a contribué). Même si je ne comprends pas toujours tout ce que tu fais (la simu c'est un univers trop complexe pour mon petit cerveau) tu te démènes avec beaucoup d'énergie et de rigueur. Je crois que tu as hâte de terminer et à raison. La thèse n'a jamais été une fin en soi pour toi, tu as toujours pensé à « la suite » et même si ça n'est pas encore fixé je ne m'inquiète pas vraiment pour toi, pleine de ressources et pleine de caractère je pense que tu feras des étincelles où que tu ailles.

Merci au trio de choc Arnaud.A, Maxime et Théophile, vous êtes rafraichissants, toujours une vanne en stock et surtout une capacité à relativiser et ne pas s'inquiéter que j'aimerais avoir. Toujours un plaisir de vous croiser dans les couloirs et de passer du temps avec vous en soirée.

Les « un peu plus jeune » de l'équipe Louis.H, Florian.S, Yohan et Quentin.G , on a forcément passé un peu moins de temps ensemble au labo mais suffisamment pour constater que certains sont vraiment des graines de chercheurs en puissance. Je n'ai pas la moindre inquiétude à votre sujet, vos thèses seront géniales à n'en point douter et j'espère que certains tenterons de passer MDC plus tard dans leur parcours.

Les « derniers arrivées », vous êtes (très) nombreux, j'ai l'impression que Métal a hérité d'une fine équipe très cohésive, l'ambiance de l'équipe n'en sera que meilleure. Je pense que vous êtes super solidaires entre vous, essayez de le rester même si certains vont passer pas mal de temps à l'étranger. Vous allez avoir encore quelques galères avec le déménagement mais tenez bon c'est peut-être bientôt fini. Je vous souhaite en tout cas de très belles thèses.

Le laboratoire Mateis est grand et en plus de l'équipe Métal il y a plein d'autre équipes. Côté CERA j'ai surtout envie de remercier Laurent.G et Helen.R. Côté SNMS je voudrais chaleureusement remercier Thierry.D qui m'a largement aidé à dompter le MEB Supra. Côté Corris, je voudrais remercier aussi Sabrina, Hugo, Kevin et Liliana qui m'ont souvent aidés.

Enfin je vais remercier ma famille et mes amis. Sarah, Chloé et Maxime merci d'avoir toujours été des soutiens et ce depuis longtemps. J'espère que l'avenir nous permettra de nous voir un peu plus souvent !

Merci à mes parents qui n'étaient pas forcément très partants pour la thèse au départ et à qui j'ai donné bien du souci. Ils ont dû se sentir impuissants bien des fois dans mes moments de doutes. Vous me suivez bien sur depuis toujours et vous m'avez vu grandir et évoluer avec chaque nouvelle difficulté. Je pense que le jour de ma soutenance vous avez pu voir que « la petite dernière » qui avait un peu de mal à l'école autrefois à force de

persévérance et d'effort à fini par faire son petit bonhomme de chemin jusqu'au doctorat. J'espère que vous êtes fiers et que vous le resterez parce que si j'ai pu faire tout ça c'est surtout grâce à vous.
Marine, ma sœur, c'est vrai qu'on a des caractères bien différents et qu'on ne s'entend pas toujours sur tout. Mais ça ne nous empêche pas d'être solidaire et de savoir qu'on peut compter l'une sur l'autre en cas de besoin. Tu y as toujours cru à cette thèse, peut-être même plus que moi. J'espère que toi aussi tu as éprouvé de la fierté ce jour-là. J'espère que de ton côté tu trouveras le job de tes rêves et que tu pourras pérenniser ton installation dans un endroit qui te plait.
Alexandre, mon amour, on s'est rencontrés quand ma thèse a démarré, je pense que tu ne savais pas dans quelle galère tu allais t'embarquer. En 2020, tu changes de travail, je me fracasse un genou et tu emménages à Lyon, je me fais opérer et on se fait confiner tous les deux dans mon petit appartement, c'est ce qu'on appelle un démarrage sur les chapeaux de roues. S'en suit une période avec beaucoup de rééducation, de travail et de restrictions. Même quand j'étais épuisée par tout ça tu as toujours été compréhensif, rassurant et encourageant. Merci de m'aimer comme je suis de m'aider à m'assumer et de me soutenir au quotidien. Tu sais que je m'en fais beaucoup pour l'avenir mais quand je me dis que je vais le construire avec toi je suis rassurée. J'espère qu'on se soutiendra toujours aussi fort pour toutes les nouvelles aventures de notre vie.

French summary

Les implants dentaires font partie des dispositifs médicaux implantables les plus vendus aujourd'hui dans le monde. Le secteur bénéficie d'une forte croissance constante directement liée à un nombre de patients toujours plus important. Les implants dentaires sont des dispositifs médicaux très fiables mais les échecs existent encore. Le milieu est fortement concurrentiel et la recherche fait l'objet d'investissements conséquents pour aboutir à des innovations concrètes. Les principales voies d'amélioration des implants dentaire reposent principalement sur trois idées :

- La miniaturisation des implants ;
- L'amelioration de l'ostéointégration via l'état de surface ;
- La composition chimique des alliages (éviter les éléments potentiellement nocifs).

Pour répondre à ces attentes, le travail décrit dans ce manuscrit s'est concentré sur l'étude de la nuance de verre métallique massif (BMG) $Ti_{40}Cu_{36}Zr_{10}Pd_{14}$. Cette nuance dévoilée en 2007 est décrite depuis comme très prometteuse en tant que biomatériau et fait l'objet de nombreux travaux publiés. La plupart de ces travaux décrivent ce matériau comme particulièrement bien adapté à la fabrication d'implant dentaire. Malgré tous ces travaux, la nuance de BMG $Ti_{40}Cu_{36}Zr_{10}Pd_{14}$ n'est toujours pas commercialisée. Deux thèses (dont celle -ci) successivement réalisées au sein du laboratoire MATEIS ont permis d'apporter des éléments nouveaux soulignant les verrous techniques et scientifiques qui empêchent son utilisation à l'échelle industrielle dans le secteur médical. Le Dr.Aléthea Liens dans son manuscrit a mis en évidence deux points bloquants principaux concernant la nuance $Ti_{40}Cu_{36}Zr_{10}Pd_{14}$:

- La présence de défauts cristallins appelés sphérulites, qui sont probablement impliqués dans la rupture prématurée des échantillons notamment en traction et en fatigue.
- La tenue en corrosion limitée de l'alliage comparée à la plupart des verres métalliques (potentielle implication des sphérulites).

Les résultats décrits dans les chapitres de ce manuscrit font directement suite au travail du Dr.Aléthea Liens. Pour déterminer la nature de ces sphérulites jusqu'alors non rapportées dans la littérature pour cette nuance de verre métallique, il a fallu dans un premier

temps les observer et les décrire. Pour se faire, un travail de mise au point du protocole de polissage a été mis en place permettant de particulièrement bien mettre en évidence leur microstructure en microscopie. La microstructure des sphérulites est paticulièrement complexe, on peut y voir des aiguilles au centre avec différentes phases et une coquille à l'interface avec la matière amorphe. Pour faire le lien entre les propriétés mécaniques du BMG et les sphérulites en plus de leur microstructure, il manque des informations essentielles : leur diamètre et leur position dans les barreaux. Etant donné l'absence de de contraste chimique entre les sphérulites et la matrice amorphe, la tomographie à rayons X du laboratoire ne nous a pas permis de voir en 3D les sphérulites et d'avoir une distribution directe et réelle de taille des sphérulites. L'obtention de ses données a dû se faire par de nombreuses observations 2D de coupes polies auxquelles il a fallu ajouter une analyse statistique complexe (Méthode de Saltykov) pour estimer les diamètres réels. Les résultats présentés dans le chapitre 1, ont permis de montrer que les sphérulites peuvent avoir de grands diamètres (plusieur centaines de μm) et que leur position est aléatoire dans les pièces. Le lien avec les résultats des essais mécaniques nous a permis de dire que les sphérulites sont d'avantages un point faible en traction et en fatigue qu'en compression (moins sensible à la présence de défauts). Cependant nous avons pu démontrer que les sphérulites étaient capables de se déformer plastiquement en compression mais que leur taille est supérieure à la taille de la zone plastique estimée expliquant ainsi le comportement purement fragile en traction. Nous avons alors supposé que sans les sphérulites, les propriétés mécaniques en traction et fatigue pourraient être encore meilleures avec une approche de matériau composite (matrice amorphe + sphérulites). En effet, une maîtrise de leur taille et de leur répartition lors de la fabrication des barreaux pourrait permettre d'obtenir une déformation plastique plus importante avant rupture.
L'implication des sphérulites dans le processus de corrosion a également été étudiée dans le chapitre 1. L'hypothèse principale était qu'un couplage galvanique entre la matrice amorphe et les sphérulites pouvait avoir lieu, ce qui aurait pu expliquer le phénomène de piqûration préalablement observé. Des essais de corrosion locaux ont été réalisés à l'aide d'une microcellule. Les résultats ont permis de rejeter l'hypothèse du couplage galvanique (la matrice amorphe et les sphérulites ont des potentiels de corrosion trop proche). Cependant la coquille autour des sphérulites semble se dissoudre préférentiellement en solution saline sans pour autant être le point de départ de la piqûration.

A ce stade, l'organisation détaillée et la nature des phases des sphérulites n'étaient pas identifiées, et nous n'avions a fortiori pas non plus de scénario de croissance. Dans un système quaternaire tel que TiCuZrPd, peu étudié notamment en termes de cristallographie de par sa nouveauté, il est difficile d'identifier des phases. Le chapitre 2 du manuscrit décrit comment avec différent outils tel que la DRX et l'EBSD et en faisant le choix de se baser sur le diagramme binaire du CuTi, certaines phases semblaient bien correspondre (CuTi B2, Cu_3Ti_2 , $CuTi_3$ ...). Ce sont des analyses qui ont justifié la nécessité des lames minces

au FIB pour vérifier ces tendances. Les analyses TEM ont relevé un comportement instable du matériau sous le faisceau d'électrons (voir annexe C du manucrit) rendant les observations particulièrement complexes. Cependant, d'avantage de détails de la microstructure ont pu être observés au MET qui se sont révélées être des mises en ordre supplémentaires. Les phases précédemment identifiées en EBSD ont donc été confirmées par le MET. C'est l'élaboration de nos premier barreaux avec un diamètre réduit à 3 mm qui a permis de voir des sphérulites à différents stade de leur croissance (précoce, intermédiaire et mature). Les observations ont permis de proposer un scénario de croissance détaillé et robuste des sphérulites dans le BMG $Ti_{40}Cu_{36}Zr_{10}Pd_{14}$, jamais décrit auparavant dans la littérature. Ce chapitre met en avant le fait que c'est la phase Cu_3Ti_2 qui germe en premier dans l'amorphe et que c'est probablement le nombre de germes et la vitesse de refroidissement qui conditionnent la morphologie finale de la sphérulite. Malheureusement cette étude ne nous a pas permis de déterminer le mécanisme à l'origine de l'apparition de la phase Cu_3Ti_2 .

Dans le chapitre 3, des essais sur plusieurs paramètres de coulée par succion au four à arc ont été étudiés ainsi que leur influence sur le rapport $\frac{cristallin}{amorphe}$, dont :

- La vitesse de refroidissement : en changeant le diamètre du moule.
- L'étape de chauffe : soit en faisant varier l'intensité de l'arc soit changeant le nombre d'homogénéisation de l'alliage mère.
- L'influence de l'hydrogène.
- l'influence des traitements thermiques.

La vitesse de refroidissement a une influence directe et significative sur le rapport $\frac{cristallin}{amorphe}$. Plus la vitesse de refroidissement est importante, plus les sphérulites sont rares et petites, mais même en utilisant un moule en cuivre de ⌀3mm, de petites sphérulites sont encore visibles malgré un diamètre critique de 6-7mm pour $Ti_{40}Cu_{36}Zr_{10}Pd_{14}$ dans la littérature. Pour l'étape de chauffe, l'intensité de l'arc n'a pas été démontrée comme étant un facteur changeant la distribution des sphérulites en nombre (pas plus de germination) et en taille (pas plus de croissance). Les barreaux fusionnés/retournés 6 et 14 fois avant coulée ont été testés en flexion quatre points, les résultats sont très peu reproductibles et n'ont pas permis de déterminer le lien clair entre la microstructure et les propriétés mécaniques. Cependant il semblerait que ce soit la position et la taille des sphérulites qui conditionnent la contrainte à la rupture des éprouvettes. En effet, il est probable que plus une sphérulite :

- A un gros diamètre ;
- Est proche de la surface ;
- Se situe sous un rouleau ;

- Ou soit sur la face en traction (proche de la zone de sollicitation maximale) : plus l'éprouvette cassera tôt.

De plus, une analyse chimique de surface a révélé un contraste avec l'hydrogène (plus d'hydrogène au centre des sphérulites et dans l'amorphe). L'hydrogène pourrait donc être l'origine de la germination de la phase Cu_3Ti_2 et donc responsable de l'apparition des sphérulites. Des barreaux ont donc été fabriqués sous atmosphère enrichie en hydrogène, dans ces barreaux il semblerait que le volume occupé par des sphérulites soit plus important que sans hydrogène. Les barreaux ont été testés en compression. Les résultats ont été très peu reproductibles (du fragile au ductile). Au final, on suppose donc que l'hydrogène facilite l'apparition des sphérulites et qu'il est donc préférable de l'éviter.

Les sphérulites ne sont pas considérées comme des structures métastables étant donné leurs conditions d'apparition. Pour savoir quel serait leur comportement au cours de traitements thermiques isothermes en bain de sels ont été réalisés. Après les essais, les sphérulites étaient toujours présentes et leurs tailles n'avaient pas changé. Cependant, la matrice autour des sphérulites s'est dans un premier temps relaxée puis cristallisée. La question en suspens est la suivante : les phases dont sont composées les sphérulites sont-elles des phases d'équilibre que l'on pourrait retrouver dans l'alliage mère ?

Dans le chapite 4, des observations microstructurales de l'alliage mère de la nuance $Ti_{40}Cu_{36}Zr_{10}Pd_{14}$ ont permis de vérifier que les phases d'équilibre ne sont pas celles observées dans les sphérulites. Mais que l'alliage mère a une microstructure très complexe avec au moins cinq phases différentes qui coexistent. Pour comparer les comportements en corrosion de l'amorphe et du cristallin, l'alliage mère a été testé dans les mêmes conditions que le verre métallique dans une solution saline. Au cours de ces essais, il a été remarqué que les phases cristallines les plus riches en Pd et en Cu de l'alliage mère avaient tendance à se dissoudre plus facilement que celles riches en Ti et en Zr qui ont la capacité de se passiver naturellement. Malgré toutes les tentatives liées au processus de fabrication pour éliminer les sphérulites ou contrôler leur taille, aucune n'a fonctionné. Les problèmes initiaux de corrosion et les sphérulites sont donc toujours présents dans cette nuance de verre métallique.

L'utilisation de ce matériau pour la fabrication d'implant dentaire semble être de plus en plus compromise, mais l'ajustement de la composition de l'alliage pourrait suffire à éviter l'apparition des sphérulites. On sait qu'il est possible d'éliminer les sphérulites en ajoutant des éléments d'additions mais ceux-ci ont tendance à diminuer les propriétés mécaniques globales de l'alliage sans améliorer la résistance à la corrosion. Basés sur les compositions chimiques des phases de l'alliage mère, des essais de casting ont été réalisés sur trois "nouvelles" compositions chimiques. Malheureusement, aucunes d'elles ne s'est avérée amorphe dans les conditions de fabrication testées mais l'une d'entre elle a tout

de même montrée une dureté exceptionnelle laissant entrevoir des propriétés mécaniques intéressantes même sous forme cristalline mais une résistance en corrosion limitée étant donné sa haute teneur en Cu et Pd.

En conclusion, beaucoup d'efforts et de ressources ont été consacrés à l'identification et à la description précise des défauts de coulée du verre métallique $Ti_{40}Cu_{36}Zr_{10}Pd_{14}$. Nous sommes maintenant certains de leur influence délétère sur les propriétés mécaniques de l'alliage. Malgré plusieurs approches différentes, aucune d'entre elles n'a permis de produire des verres métalliques sans sphérulites. De plus, la résistance à la corrosion du verre métallique reste également un problème au vu de l'application visée, et le contenu de ce manuscrit diminue fortement le potentiel du BMG $Ti_{40}Cu_{36}Zr_{10}Pd_{14}$ comme biomatériau. La maîtrise du processus de fabrication de ces matériaux est et reste une source d'incertitude quant à la qualité des pièces produites. La communauté des verres métalliques mentionne rarement ces inconvénients, qui devraient être étudiés plus en profondeur afin de mieux répondre à ces problèmes.

Contents

General introduction/context/state of the art

Today, teeth loss represents an increasingly important public health issue, particularly in relation to the ageing of the population. Indeed, even if there is an obvious lack of data on teeth loss and oral health treatments quality on a worldwide scale, it seems that the need for dental care is globally growing. The work of Elani et al. in 2018 [ELA 18], clearly states that tooth loss affects an individual's ability of chewing, the quality of life and aesthetics representation of oneself. The importance of the burden is obviously related to the number of teeth missing in an individual[GER 10]. Elani et al. also state that over the period 1999 to 2016, both teeth loss and number of missing teeth declined over time in the USA despite an ageing population but suggest that there are racial/ethnic disparities, partially explained by socio-economic status [WU 14]. However, the prevalence of dental implants has continued to increase, particularly among the elderly. This increase is clearly less important for people who do not have supplementary health insurance (specific to the USA since the American public health system does not cover the costs of dental restoration) or people who have a relatively low level of education (high school degree or below). They did a projection for the dental implant prevalence in future, it is getting from 5.7% in 2016 to 17% in 2026 inside the edentulous population. It is very likely that the results of this study can be extrapolated to other geographical areas of the world especially in rich countries. This currently leads to a strong market growth for dental implants that is estimated to be 8.8% per year. As an illustration the Straumann group (world leader dental implant manufacturer) announces 27 million implants placed annually for the company (2020 annual report – Straumann Group).

There are many reasons to believe that the dental implant market has a 'bright future' that justifies the investment made in research and development in this field [CHA 17]. Whether there is a global decrease in incidence of dental caries and periodontal conditions in developed countries, there is an increase in incidence of complete and partial edentulism, for elderly population, which is highly prone to teeth loss. The demand for teeth restora-

tive technologies, and focus on quality dental care are expected to boost the market growth.

What is a dental implant?

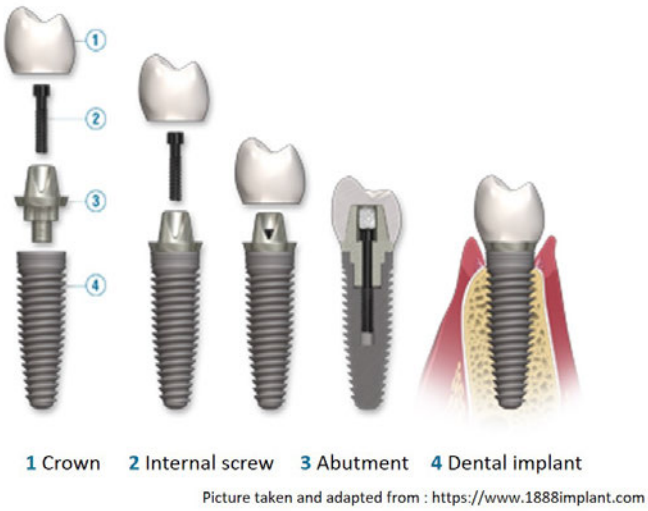

FIGURE 1 – Illustration of an implant/abutment/crown assembly, these are the four parts of a dental restoration.

A dental implant is a small threaded piece (like a screw) on average 8 mm long and between 3 and 5 mm in diameter. This screw will be directly implanted into the jawbone (mandible or maxilla) where the root of the missing tooth used to be. The dental implant is therefore in direct contact with the bone tissue and, depending on the design of the implant, it may also be in partial contact with the soft tissue: the gingiva. In most cases, the implant is supplemented by three additional parts to complete the restoration: an abutment, an internal screw and a prosthesis (illustrated in Fig. 1). The abutment will ensure the junction between the implant and the prosthesis (or crown), the abutment is screwed on the implant via the internal small screw. Finally, a custom-made prosthesis is the only aesthetic part visible from the outside and is generally glued to the abutment.

- **What are the main causes of implant failure?**

Today, the mean success rate and mean survival rate of implants are 89.7 % and 94.6 %, respectively, after more than 10 years[BAZ 20]. There are five mains origins of dental implant failure and there are represented in Fig. 2.

1. Local bacterial infection/inflammation which, if not treated early, can develop into peri-implantitis which inevitably leads to implant removal [SCH 18]. The responsible bacteria can be introduced during the implant placement but, in most cases it is a lack of hygiene on the patient side or patient risk factor such as diabetes or smoking for example [SCH 18]. Indeed, during the implantation, the gingiva is incised and does not play its role of hermetic barrier against micro-organisms anymore. The bacteria can then enter in contact with the surface of the implant and get inside

the internal hollow portion of the implant because of gaps at the implant-abutment connection [QUI 93]. This is the most common complication with dental implants.

2. Another source of failure, rare but nevertheless mentioned in the literature, is the brutal fracture of the implant, which is the consequence of poor fatigue strength or toughness or the presence of a manufacturing defect (not detected during the quality controls of the manufacturer), of a bad dimensioning of the implant or sometimes a bad choice in implant type according to the clinical situation and orientation in the bone by the dentist [SCH 00].

3. Low resistance to wear and corrosion can result in the release of particles which are then released into the body and accumulate in various tissues, leading to serious symptoms in the patient (hypersensitivity, allergies, etc.).

4. The mismatch between elastic modulus between implant and surrounded bone may give a rise to stress shielding phenomenon, but it concerns more orthopedic implants than dental implants, this point will be discussed further, later in this introduction.

5. Finally, it can happen that during the surgery, the drilling of the bone releases too much heat [MIS 14], especially during the installation of a large diameter implant, which kills the cells present locally and prevents osseointegration for a considerable time (months), the implant will be surrounded by a fibrous encapsulation which will leads to its removal due to lack of stability and pain in the patient's jaw.

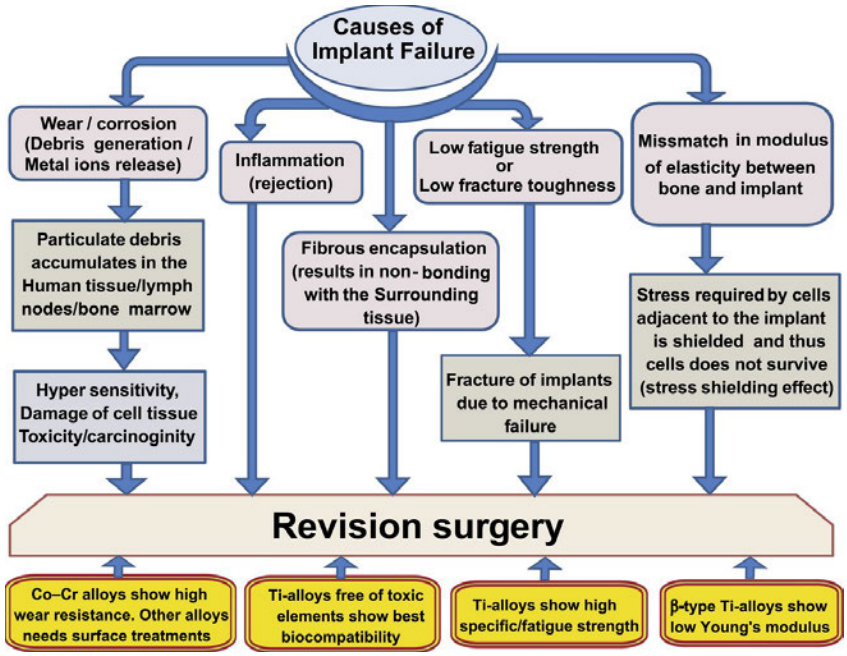

FIGURE 2 – Schematic representation of the main causes of implant failure. Reproduced from [GEP 13].

What are the essential features of a dental implant today?

Mechanical requirements

The first criterion refers to the necessary mechanical properties adapted to the application. Obviously, it is not difficult to imagine that a tooth is repeatedly stressed throughout an individual's life. The maximum vertical biting forces are estimated to be around 89-150 N at the incisors (anterior region), 133-334 N at the canines, 220-445 N at the premolars (intermediary region) and 400-600 N at the molars (posterior region)[CRU 11]. Moreover, it appear in literature that the stress level is different between natural tooth and a tooth rehabilitation. Indeed it seems that loading of a dental implant increase stress and strain in the alveolar bone compared to those on a natural tooth which have a periodontal ligament (absorbing some stress)[ROB 19]. The resulting stresses vary according to the tooth configuration and can be in various directions. However in most of the cases, it is not a simple compression case, see for example Fig. 3 [BRU 88]. Estimating the stresses in a human jaw is not trivial and there are specific dental implant standards detailing test protocols for testing the mechanical properties of materials chosen for the manufacturing of dental implants (such as ISO 14801). The acceptance criteria are very severe and are mainly based on static and fatigue tests of the implant manufactured in the considered material. The objective of these standards is obviously to avoid any occurrence of premature implant failure due to insufficient initial mechanical properties or anomalies in the manufacturing process.

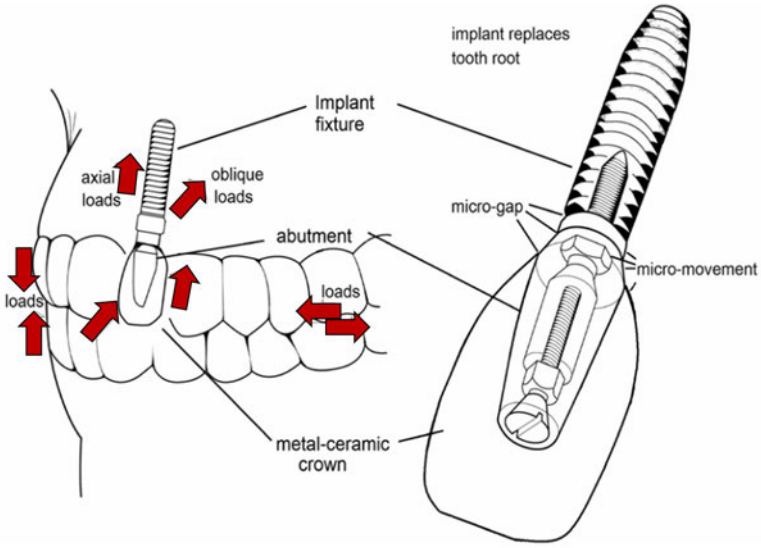

FIGURE 3 – Illustration of the loads (red arrows) experienced by a dental implant in a human jaw. Reproduced from : [CRU 11].

As already referred, the orientation of the occlusal force stresses (represented in Fig 3)

are very important: axial loads propagate the stress through the dental implant system to the bone tissue (1st interface), while oblique loads can originate overload on implant structural materials and bone tissue [PAP 96]. Plus, there are stress concentration zones [ABU 10] on the screw which is placed to fix the abutment (2nd interface), and a last interface between the prosthesis and the abutment, the materials of the different parts are generally different and under fatigue load mastication solicitation some failure can occur [MAN 09]. In recent years, the trend in dental implants has been towards miniaturization of the implants and has been coordinated with improvements in the performance of the materials already used [HAS 14]. Now it seems that these usual materials (Ti alloys and technical ceramics) have reached a plateau in terms of performance, which is driving the research for new materials for this application [DUR 15].

The main mechanical properties of the most common materials currently and previously used for dental implant/orthopedics implants manufacturing are summarized in Tab. 1. The materials can be separated into several groups: commercially pure titanium's and its alloys and some ceramics which are the two main groups currently used and 'Roxolid' which was specifically developed for dental implant requirements [ION 20]. In the past, stainless steel and Cr-Co alloys were also used.

TABLE 1 – Main properties of materials currently used for dental implants. The gathered characteristics are: material density (g/cm^3), Vickers hardness (HV), Young's modulus (E) in GPa, Yield strength (MPa), the ultimate tensile strength, the strain to failure (%) and the toughness (MPa$\sqrt{m}$).

Material name	Density (cm^3)	Hardness (HV)	E (GPa)	Yield strengh (MPa)	UTS (MPa)	Elongation (%)	Strain to failure (MPa$\sqrt{m}$)	References
UTS Cp-Ti grade I	4.51	122	102	170	240	24	/	[NII 98]
UTS Cp-Ti grade II	4,51	145	102	275	345	20	58 - 66	[NII 98]
UTS Cp-Ti grade III	4,51	220	102	380	450	18	68	[NII 98]
UTS Cp-Ti grade IV	4,54	280	104	485	550	15	99 - 135	[NII 98]
TA6V	4.43	349	110-114	825- 869	895 - 930	6 - 10	65 - 90	[NII 98]
TA6V ELI	4.43	310	101 - 110	795 - 875	860 - 965	10- 15	92	[NII 98]
Roxolid® (Ti15Zr)	4,75	/	54,5	750 - 818	950 - 1020	5 - 7	/	[MED 16]
Y-TZP	6	1200	220	900-1200	900-1200	0	4 - 10	[DUR 15]
Co-Cr (Vitallium)	8,3	395	200	680	960	10	/	[JAB 14]
Stainless steel (316L)	8	240	180	220-245	585-565	40	112-270	[SON 11]

The large difference in elastic modulus (E) between these materials and the one of the cortical bone (jaw or mandibular) which is between 10 - 18 GPa [ZYS 99] can raise the question of stress shielding. It is often mentioned when dealing with orthopedic implants and prostheses [HUI 93][KAN 20] and may lead to bone resorption around a large implant

(e.g. hip or knee prosthesis). The phenomenon can lead to fractures and the inevitable removal of the implant/prosthesis (see Fib. 4). This phenomenon is explained by the fact that the implant will support the body's load instead of the bone itself, which will eventually resorb itself after intermediate/long term. The main idea here, is that the bone cells (osteocyte) are "stress sensor" and regulate the bone metabolism equilibrium between bone synthesis and resorption. If the cells sense stress, they will promote bone synthesis to enable the skeleton to withstand the stresses of movement (e.g. walking). If the bone is not under sufficient stimulation, osteocytes will promote bone resorption. Bone resorption is observed on patient who have been bedridden for a long time or astronauts in long time mission (absence of gravity so they did not have to support their own weight).

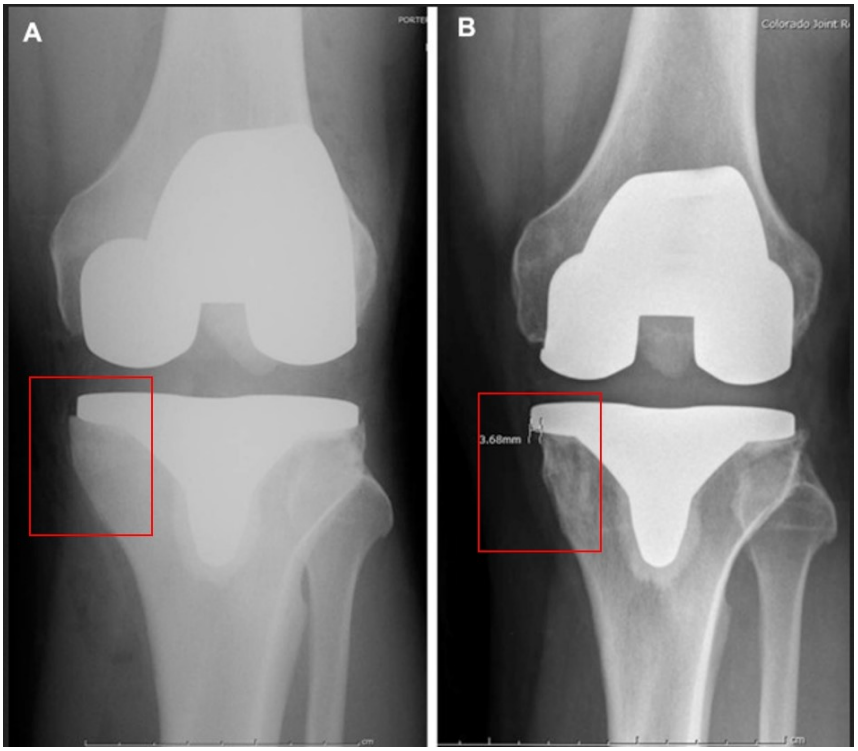

FIGURE 4 – X-rays of a knee on which a total knee prosthesis has been placed. Radiography A was taken immediately after the prosthesis was placed. Radiography B was taken 2 years after the prosthesis was placed and shows significant bone loss, especially in the tibial area, due to stress shielding effect. Taken from [MAR 17].

In the case of dental implants, there is no real stress shielding phenomenon recognized, since the concerned bone is not long and others natural teeth around the implant continue to play their role and therefore regulate the synthesis/resorption balance of the nearby bone. However in literature, there are cases of a decrease in the vertical level of crestal bone (cortical bone just under the gingiva) [ALB 17]. This phenomenon can have several origins including bacterial infections, traumatic surgical protocol or pathological bone metabolism. But, one of the main reasons for this surface bone loss is probably mechanical:

it may be a mismatch of stiffness between the implant and the bone but this is sometimes an implant design issue [BAG 08][Vel 06]. If the load is not well distributed over the entire height of the implant (to stimulate all the bone length), there may be over- and under-loading, which in the long term leads to a decrease in the crestal bone level (see Fig. 4). We also know that the bone density is more or less important (with a variation between individuals) and depends on the position in the jaw. In addition, the angle at which the implant is placed by the dentist has a strong influence on the stress distribution. The phenomenon of bone crestal resorption underlines the importance of the choice of material and design of the implant in order to obtain a satisfactory implant stability and aesthetic results.

Biocompatibility

When dealing with implantable medical devices, a second essential criterion is obviously biocompatibility. It should also be mentioned that in the case of orthopedic and dental implants, friction/wear/ageing phenomena should not be ignored and may be accompanied by ionic and/or particles release (see for example in [Bag 97] with mercury release of dental amalgams). In this context, it can be estimated that the ideal implant would consist only of atomic species recognized as being perfectly harmless for the organism. Even in the long term, the material should have excellent resistance to wear (limited ions released under stress).

In order to obtain the CE or FDA authorization, which allows a new implantable medical device to be released on the market, manufacturers are required to carry out all experiments described in the standard ISO 10993 (or equivalent), which is a mandatory. These are very time-consuming and costly steps that are necessary but greatly slows down the launching of innovative products. As it can be seen in Fig. 5, many experiments in vitro and in vivo with significant results have to be done to fulfill all the requirements.

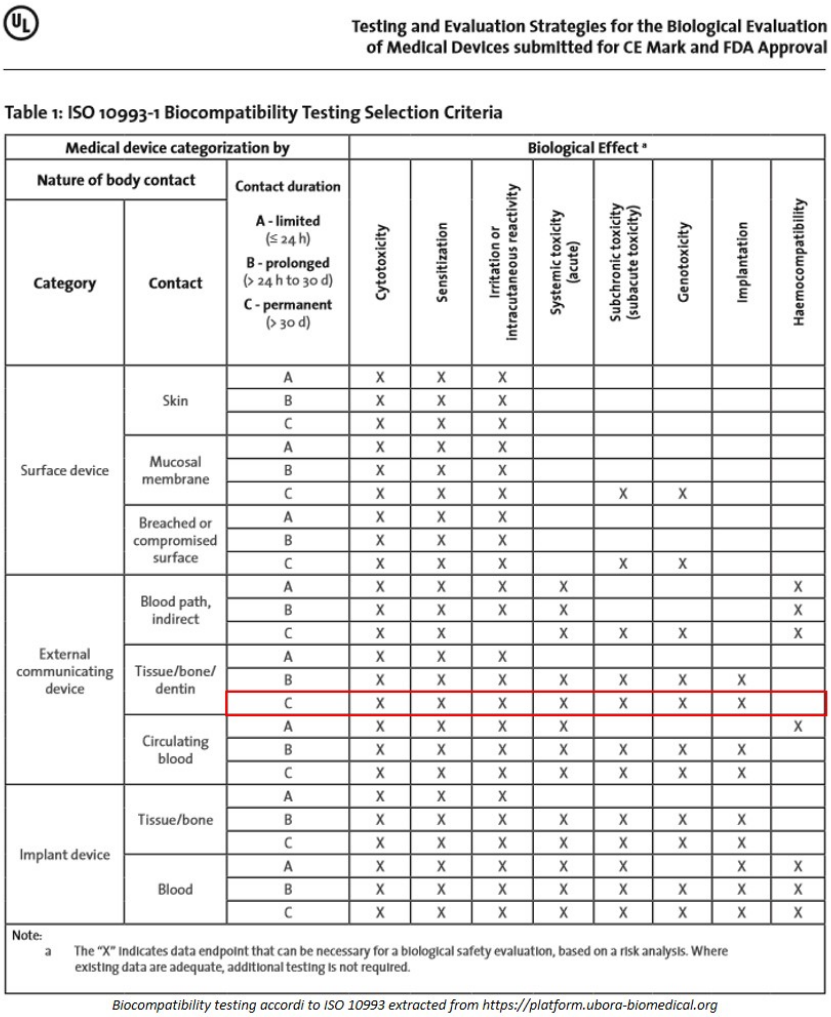

Testing and Evaluation Strategies for the Biological Evaluation of Medical Devices submitted for CE Mark and FDA Approval

Table 1: ISO 10993-1 Biocompatibility Testing Selection Criteria

Medical device categorization by			Biological Effect [a]							
Nature of body contact		Contact duration								
Category	Contact	A - limited (≤ 24 h) B - prolonged (> 24 h to 30 d) C - permanent (> 30 d)	Cytotoxicity	Sensitization	Irritation or intracutaneous reactivity	Systemic toxicity (acute)	Subchronic toxicity (subacute toxicity)	Genotoxicity	Implantation	Haemocompatibility
Surface device	Skin	A	X	X	X					
		B	X	X	X					
		C	X	X	X					
	Mucosal membrane	A	X	X	X					
		B	X	X	X					
		C	X	X	X		X	X		
	Breached or compromised surface	A	X	X	X					
		B	X	X	X					
		C	X	X	X		X	X		
External communicating device	Blood path, indirect	A	X	X	X	X				X
		B	X	X	X	X				X
		C	X	X		X	X	X		X
	Tissue/bone/ dentin	A	X	X	X					
		B	X	X	X	X	X	X	X	
		C	X	X	X	X	X	X	X	
	Circulating blood	A	X	X	X	X				X
		B	X	X	X	X	X	X	X	
		C	X	X	X	X	X	X	X	
Implant device	Tissue/bone	A	X	X	X					
		B	X	X	X	X	X	X	X	
		C	X	X	X	X	X	X	X	
	Blood	A	X	X	X	X	X		X	X
		B	X	X	X	X	X	X	X	X
		C	X	X	X	X	X	X	X	X

Note:
a The "X" indicates data endpoint that can be necessary for a biological safety evaluation, based on a risk analysis. Where existing data are adequate, additional testing is not required.

Biocompatibility testing accordi to ISO 10993 extracted from https://platform.ubora-biomedical.org

FIGURE 5 – This table was extracted from the standard ISO 10993- Biological evaluation of medical devices, which is the main standard to obtain a CE mark to allow the commercialization of a dental implant today. For ease of reading, the line focused on dental implants has been circled in red. Boxes filled with a cross indicate the need for the manufacturer to conduct the study to exclude the associated risk.

Osseointegration

The next property that follows directly all the required elements of ISO 10993, but goes even further is the osseointegration of the implant. Even though this property has not always been considered essential in the past [ALB 05], it is now universally accepted that the placement of an implant is mainly successful when it is osseointegrated. Osseointegration refers to the fact that there is creation of a direct contact between the bone and the implant, i.e. that bone tissue is able to form on the implant's surface. The osseointegration was first described by Branemark [BRA 86]. Branemak is a pioneer in the evolution of success criteria for dental restorations, and his work led to the shift from

fibrous encapsulation to osseointegration.

- **How is an implant placed and osseointegrated?**

In this paragraph, a brief description of the implant placement is given. It can be described in several successive steps:

1. The dentist will first cut away the gingiva tissue and spread it to have access to the bone underneath.
2. Then, in most cases, the dentist will drill into the patient's bone to a depth that corresponds to the height of the future implant. He will successively use several drills, first of small diameter and then larger until he has created a hole slightly narrower than the outer diameter of the implant.
3. Then, he will insert/screw the implant (generally self-tapping) directly into the patient's bone with a torque given by the manufacturer specification according to the clinical situation. It is the thread of the implant that will ensure the primary stability. During insertion, the implant is in direct contact with blood and debris of packed bone tissue.

As illustrated in Fig. 6, the presence of blood within the implantation's site is the sign of the presence of certain cell types such as: platelets, red blood cells (erythrocytes) and immune system cells. These cells will initiate the process of neovascularization (creation of new vessels) between the bone and the implant surface within the first 4 days of implantation. In parallel and for several weeks, numerous macrophages will clean the space between the surface of the implant and the still intact bone by eliminating bone and vessel debris. They will also stimulate the activation of nearby osteoblasts. Osteoblasts are the cells able to synthetize new bone material (not mineralized at first, which leads to a temporary decrease in the stability of the implant). They will attach more or less well to the surface of the implant and over time (4 to 8 months) cells will create "mineralized bone bridges" (also thanks to the good vascularization, which is essential for the survival of bone cells) between the bone present at the beginning and the implant's surface. The direct contact between the bone and the implant constitutes the secondary stability or osseointegration which is mandatory for the long- term success of the implant stability. The quality of osseointegration of an implant is assessed by direct quantitative measurements using bone-implant contact via microscopy (BIC) [GUG 19] and mechanically by pull-out and removal torque tests [CHA 10]..

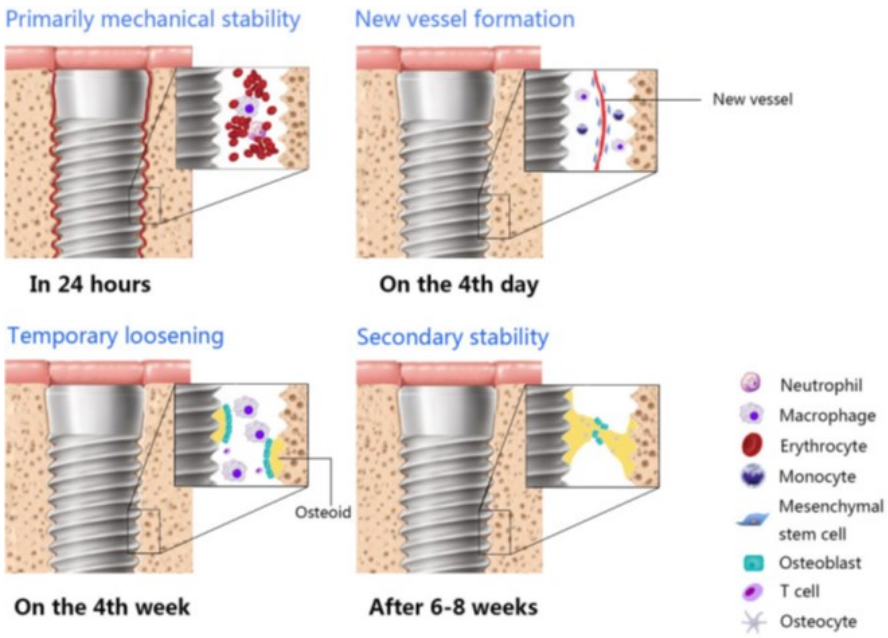

FIGURE 6 – Schematic illustration of successive steps from implantation to a fully osseointegration of a dental implant. It describes four main steps and it underlines which cellular population is involved at each step. First the primary stability is mainly provided by the implant's design. During the surgery, the implant is in direct contact with blood tissue (erythrocytes, macrophages and neutrophils). After 4 days, new blood vessels are forming which is essential for the supply of cells of the future bone. After 4 weeks, there is temporary instability/loosening of the implant since the physical contact between the bone and the implant is being synthesized (osteoblast) but has not yet taken place. Finally, after 6-8 weeks, the physical contact between the bone and implant is effective, this is the secondary stability, the implant has been osseointegrated (osteoblasts and osteocytes). Illustration extracted from [WAN 15].

- **From osseconduction towards osseoinduction**

The term osseointegration can be used to describe several level of biomaterial behaviors [35]. In the majority of cases, the biomaterials are 'at best' osseoconductive, i.e. they act as a passive support where the cells and molecules of the environment of the implantation site will be able to attach, spread and migrate. Then various biological processes will result in the production of new bone tissue in contact with the implant. However, the future of implantable medical devices for orthopedic and dental purposes tends to be oriented towards osseoinduction: the material is no longer a simple support but has an active role and stimulates bone reconstruction. There are different strategies to achieve osseoinduction. Most of the time it is a matter of functionalizing the surface of the support material with specific biomolecules that aim to stimulate the differentiation of specific cell types. Another approach to achieve osseoinduction is to modify the surface features of the implant. It is known that surface topography can have a significant influence on the behavior and differentiation of various cell types. Many research teams are currently working on these topics but the understanding of all the mechanisms involved and the

differences in response depending on the cell type make the consensus difficult. However, this aspect will be further discussed later in the manuscript.

Corrosion performance

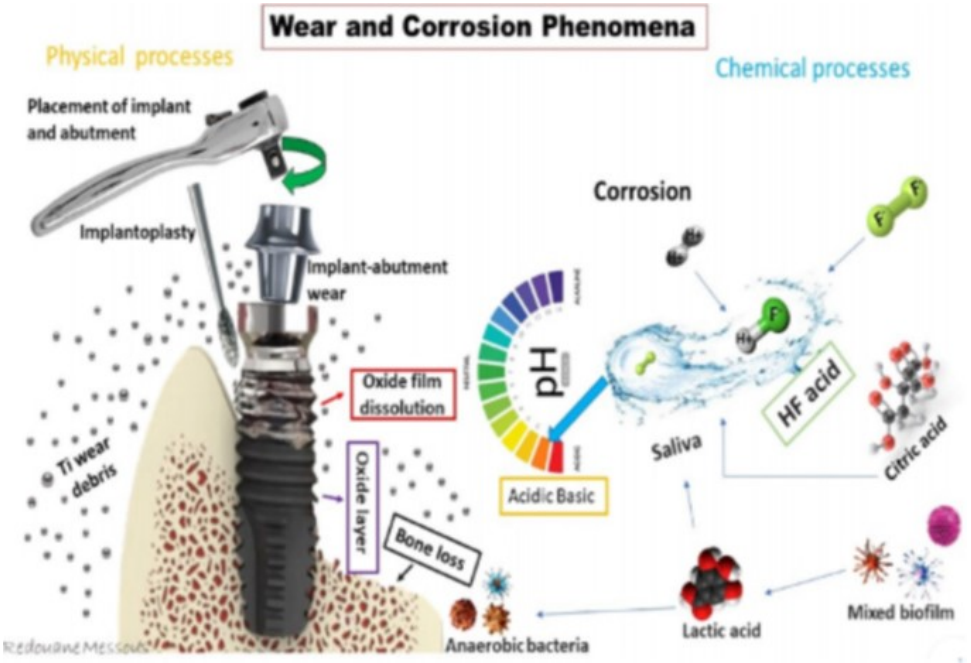

FIGURE 7 – Illustration of the physical and chemical degradation pathways of a dental implant linked to wear and corrosion phenomena. Some wear can be present in during the implantation resulting in the release of Ti- based particles. Another way of dental implant degradation is the decrease of bone level which will let the bone and implant exposed to bacteria colonization. The present bacteria will locally decrease the pH, which will lead to dissolution of the passive film at implant's surface and release of metallic particles. The illustration was taken from [MES 21].

One specific attention of the dental sector is the corrosion resistance of the used materials. The ionic release of an implanted material into the body should be minimized as much as possible. This characteristic is all the more important in the dental sector as the implant may be in contact with an aqueous solution with change in pH over the long term (the saliva). Saliva is globally different from one individual to another in terms of composition and pH (the extremes would be 3.5 to 8.3 temporary values depending on diet according to [LOK 16]), its composition changing in short periods for the same individual, which makes its study particularly complex. Another member of the oral environment are biofilms (colonies of bacteria that synthesize their own extra-cellular matrix). Under normal circumstances (without an implant) the gingiva acts as a protective and hermetic barrier that prevents bacteria from colonizing and degrading the underlying tissue. In the case of a dental restoration, the implant/abutment junction may not be completely sealed (depending on the design and load applied) or with an imperfect gingival junction. Bacte-

ria present in the environment can enter and proliferate in the gingiva/abutment gap and even move down to the implant/bone level [Vel 06] as described in Fig. 7. Once in place, bacteria will acidify the local environment, which can lead to corrosion and associated release of particles and can result in various consequences, including some implant removal due to peri-implantitis, systemic disorders, neurological syndromes and pain [CRU 11] [MES 21].

Aesthetics

Finally, even if the primary role of an implant is to restore the chewing function, the aesthetic aspect is primordial for the patient. Ideally, the full dental renovation is invisible and the gingiva rises well around the prosthesis which must have a color and a translucency identical to the other teeth. Teeth and the smile are of great importance for an individual's self-image especially in our western society. The importance of how others see you on the perception of oneself [HOM 15]. In Western societies, having a full smile with very aligned and white teeth is part of the standard of beauty imposed by almost all telecommunication media. Having an unsightly smile can lead to the development of a complex which can have psychological consequences for patients.
As a conclusion, the requirements of a "good" dental implant can be summarized by the main following requirements: it must be biocompatible, have sufficient Yield and ultimate strengths and fatigue endurance. It should be corrosion resistant, able to be osseointegrated and must not be noticed from natural teeth.

Dental implants currently on the market

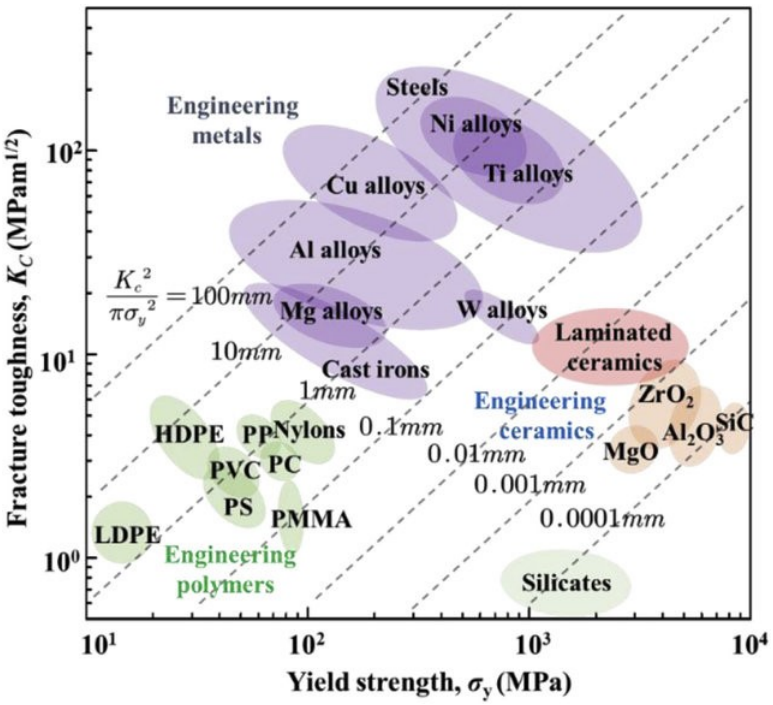

FIGURE 8 – Ashby plot showing Fracture toughness K_{IC} (MPa$\sqrt{m}$) vs σ_y the Yield strength (MPa) of the most common materials used today in technical applications. Diagonal lines show the plastic-zone sizes $\frac{K_{IC}^2}{\pi\sigma_y^2}$. The materials which have the best couple of toughness and Yield strength are the steels, Ni alloys and Ti alloys for the metals. The other material types with a good combination of toughness and Yield are the engineering ceramics. Extract form [DEM 11].

Fig. 8 is an Ashby plot showing various categories of materials according to their Yield strength and toughness. It can be seen that ceramics have the highest Yield strength (but a limited toughness) whereas the metals have the best toughness (but a limited Yield strength). These two families of materials together account for the vast majority of dental implants manufactured today. Not all metals and ceramics are suitable for the manufacture of dental implants. The following sections will focus more in details on Titanium and its alloys as well as ceramics and more specifically Yttria-stabilized tetragonal zirconia polycrystal (Y-TZP).

Commercially pure Titanium and its alloys

Key features and benefits

Among the biomaterials, the most common materials for the manufacture of dental implants are metallic implants and are almost exclusively represented by titanium and its alloys [LEV 51]. In this category, we find the so-called commercially pure titanium, graded from grade I to grade IV. Grade I correspond to the purest grade, whereas grade

IV corresponds to the grade containing the most interstitial elements (O, C, Fe, etc.). The amount of interstitial elements affects the mechanical properties of Ti. Cp Ti IV has a Yield strength (170-485 MPa) and an UTS (240-550 MPa) about twice as high as Cp Ti I. There is also the Ti-6Al-4V (also referred as TA6V or Ti64) alloy and its ELI (Extra Low Interstitial) version which show much higher mechanical properties than CpTi as it can be seen in Tab. 1.
The main difference between Cp Ti and TA6V lies in the crystallographic organization: Cp Ti is single-phase with an α HCP phase whereas TA6V shows both α HCP and β BCC phases. Optimization of TA6V alloys are conducted by thermomechanical treatments, which allows grain size control and thus increases the mechanical strength and fatigue resistance. Ti and its alloys have impressive toughness and high fatigue endurance [MAR 16].
In addition, Titanium and its alloys have the ability to passivate, i.e. to form spontaneously a particularly stable protective layer of dense surface oxides [DAV 00]. This ability makes those materials particularly resistant to corrosion with a low ionic leaching even after many years of implantation. Titanium and TA6V are biocompatible and well osseointegrated materials. Titanium and TA6V were for a long considered as inert materials for the human body, but like for every foreign metallic element in the case of a large ions release (tribo-corrosion phenomenon, for example) some drawbacks could happened [WAN 09]. However, in most of the case, no fibrous encapsulation are reported for titanium implant unlike Cr-Co or steel which is a great advantage to prevent implant loosening. The explanation of such a good properties rely mainly on Titanium chemistry [KAU 19]. After the implantation, Titanium is exposed to biological environment which can contain hydrogen peroxide. The reaction between Titanium surface oxide and hydrogen peroxide enable carbonated hydroxyapatite layer (similar to the mineral phase of the bone) to form directly on the implant surface. Finally the collagen fibers (main constituent of the organic phase of the bone) is attracted to this carbonated hydroxyapatite layer which will ensure the strong bond between the implant and the bone tissue [HAN 03].
Titanium and its alloys also have an impressive corrosion resistance especially in physiological condition, it rely on a thick, dense and stable oxide layer which spontaneously form on the implant. This layer is really well bonded to its substrate and if it is deteriorate damaged ions are continuously released in the environment but the Titanium repassivation time is really short [HAN 03] even compared to stainless steel that is one of the main reason why Titanium alloys are the gold standard choice for dental implant manufacturing.

Limitations of Titanium and its alloys

Titanium and its alloys also have few limitations. There is a quite large difference in Young's modulus between bone and titanium, which can lead to a decrease in vertical crestal bone level. The TA6V alloy is also the subject of some controversy due to its

chemical composition. Vanadium and Aluminum have been recognized as having potentially deleterious effects on the body, some advocates of the precautionary principle wish to minimize its use.

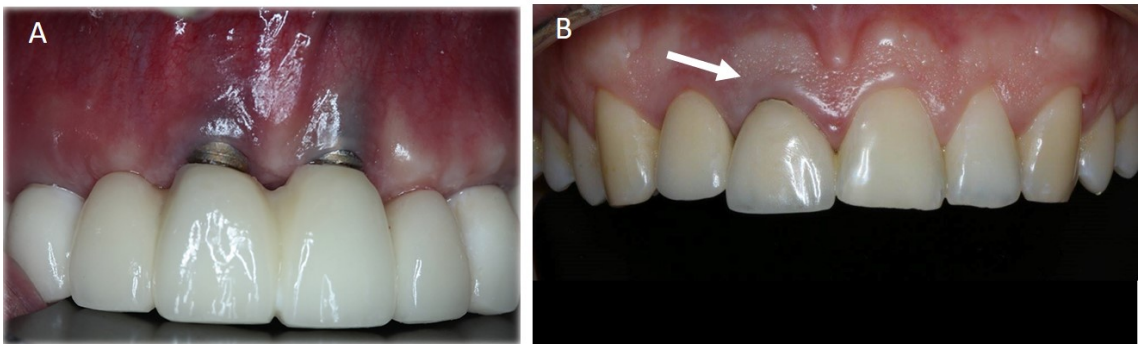

FIGURE 9 – Pictures of two dentitions, which illustrate the aesthetic problems that can occur with the use of Titanium implants. In A, there has been a lowering of the crestal bone and the implant is directly visible and exposed to the outside environment. In B, the implant is not directly visible but it can be guessed through the transparent gingiva due to the presence of an unsightly grey area. Illustrations taken from [BEH 20].

Finally, as illustrated in Fig. 9, there are aesthetic issues for some patients. The color of the implant can be seen through the gingiva, which is considered particularly unsightly. This may be due to a lowering of the vertical crestal bone level, a sagging of the gingiva or a particularly transparent type of gingiva [BEH 20].

Ceramic implant

Key features and benefits

The Yttria-stabilized tetragonal zirconia polycrystal (Y-TZP) is mainly used for the manufacture of dental implants. This material has many advantages such as a very good corrosion resistance. It is widely accepted that it is biocompatible and has very good osseointegration properties.
This ceramic (Y-TZP) has a particularly interesting property called "phase transformation toughening ability". This phenomenon is described in details in [GAR 75],[WAN 89]. Pure zirconia ($Zr0_2$) is at room temperature organized according to a monoclinic lattice, at higher temperature, it changes into a tetragonal lattice. In the case of Yttrium addition (doping element), Y helps to maintain the zirconia in its tetragonal lattice even at room temperature. If cracks appear on the surface of the Y-TZP, a transformation from tetragonal to monoclinic phase will take place locally in the cracked area. This transformation is accompanied by an increase in the volume of the crystal lattice (tetragonal $\rightarrow$ monoclinic), which induces compressive stress around the crack and thus hinders its propagation to a certain extent. This process increases the toughness of zirconia (ceramics are often criticized for having a too low toughness). Ceramics with this capability have

therefore become the materials of choice for biomedical applications;

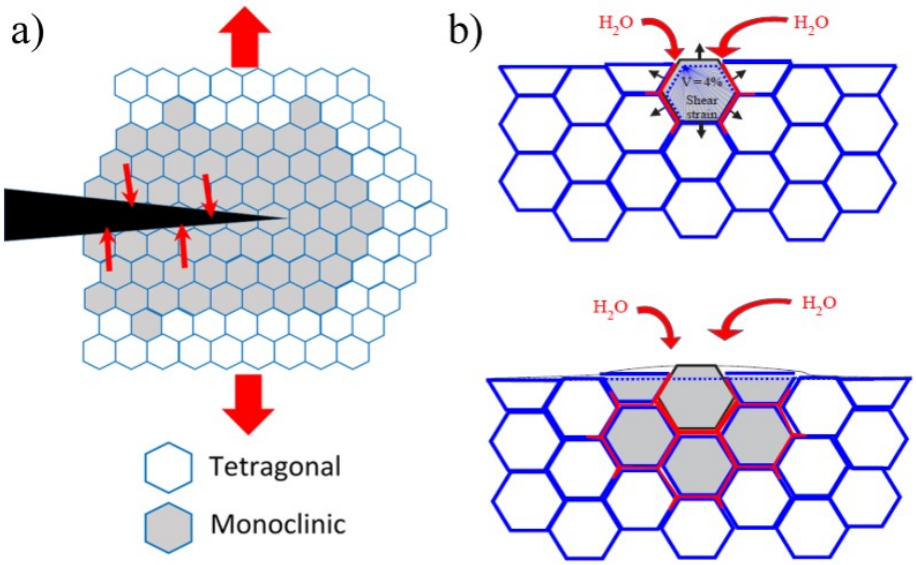

FIGURE 10 – Schematic illustration of (a) phase transformation toughening, which lead to compression around the crack and hinders crack extension and (b) ageing [HAS 14]. In (b): Nucleation on a particular grain at the surface, leading to micro-cracking and stresses to the neighbors (top); growth of the transformed zone, leading to extensive micro-cracking and surface roughening (bottom). Red path represents the penetration of water due to micro-cracking around the transformed grains. Extract and reproduce from [PAL 14].

Moreover, Y-TZP implants have the particularity of having a dense white color close to that of the teeth and bone, which makes them the implants of choice in terms of aesthetic considerations. Their surface is considered as allowing the cells of the soft (gingiva) and hard (bone) tissues to adhere and proliferate more efficiently than on titanium [OSM 15].

Limitation of the ceramics

As mentioned above, the toughness of Y-TZP remains modest compared to metals and this material is thus sensitive to the presence of defects, which can lead to premature and sudden failure of some implants. Similarly, the fatigue strength of Y-TZP implants remains lower than that of a TA6V.

There is a lack of long-term experience of the failures of Y-TZR implants due to the lack of clinical data over long periods. In addition, Y-TZP is subject to ageing (low temperature degradation), which is a tetragonal to monoclinic transformation that occurs spontaneously at room temperature in the presence of water. This phenomenon can gradually create micro-cracks that allow water to penetrate deeper and deeper into the material, which can lead to catastrophic premature failure [CHE 07]. For more details, a comprehensive and robust study of the difference in properties between ceramic and titanium dental implants has been conducted in [OSM 15].

Ultimately, dental implants are among the best-selling implantable medical devices in the world, with a very high implantation success rate, with decades of setbacks in the long-term fate of metal implants. So, is there really room for improvement in this application?

The improvement trends for dental implants

Miniaturization of implant

Classification by size		
Implant type	Diameter	Height
wide	4.5mm-6.0mm	13.0mm - 15.0mm
Standard	3.5mm – 4.5mm	12.0mm – 15.0mm
Mini implants	3.0mm – 3.5mm	8.0mm – 12.0mm
Narrow	1.7mm – 3.0mm	5.0mm – 9mm
		http://www.dentaledu.tv

FIGURE 11 – Classification table of the different types of dental implants according to dimensions (diameter and height).

In order to minimize the size of the area impacted by an implant placement or in complex clinical situations, it would be enviable to use smaller implants than those currently available. Unfortunately, it appears that a performance plateau for Titanium alloys and Y-TZP ceramics has been reached in terms of mechanical properties. Those properties are considered as insufficient to reduce the size of the implants. Moreover, for some patients, the bone density is insufficient for the placement of a "classic" implant. To deal with this problem, a majority of manufacturer have developed implants with the previous described materials, either wide with a large diameter or, conversely, long and narrow implants as presented in Fig. 11. Finally, to avoid the problem of stress shielding or problem of stress distribution, the ideal solution would actually be to miniaturize (in all dimensions) the implants with a material having a really high mechanical and fatigue resistance and Young's modulus closer to the bone.

Improvement of surface feature: not only osseoconduction but osseoinduction

It is widely recognized in the scientific community that the properties of the substrate on which bone tissue cells adhere can influence their behavior [ANS 10][FEL 15][KEL 03] [SME 16][WIR 08]. There are three main surface-related features that can influence the integration into a biological tissue: the stiffness of the substrate, its wettability and its surface topography (at different scales).
Within the surface topography category, there are many techniques to modify the surface characteristics of dental implants which are usually machined for metallic implants and

sintered for ceramic implants. Implants are rarely used with a "as machined/sintered" surface state. There are post-manufacturing surface treatments widely used, such as: chemical etching and/or sandblasting (which are subtractive techniques). There are also other types of treatments such as coating techniques: anodizing and plasma spray (additive techniques). And finally, there are also other less common techniques such as laser texturing or Micro-Arc Oxidation (MAO). SEM pictures of typical dental implant surface state can be see on Fig. 12.

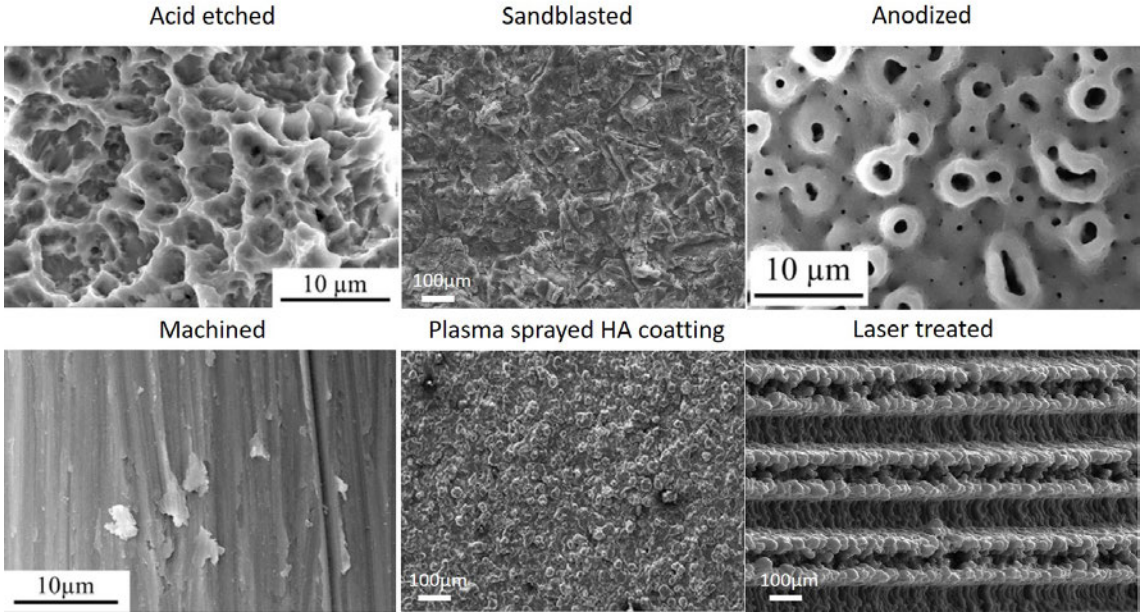

FIGURE 12 – SEM photographs of several dental implant surfaces that have been treated with different surface modification processes such as: machined, acid etching, sandblasting, anodization, plasma spaying and laser treatment. The treatments corresponding to the surface state is directly mentioned above the relevant pictures. The pictures were taken from [JAR 08] and [LEG 07].

Many articles are interested in the influence of the surface state on the cellular behavior in vitro or on the osseointegration of implants in vivo (in animal and clinical models) [ANS 10] [FEL 15] [WIR 08][SCH 99]. Even if the understanding of the mechanisms involved in bone remodeling is rather well known today [Flo 15], the light has not yet been perfectly shed on the interactions between cells and materials. There is no absolute consensus in the scientific community on this topic, and even sometimes results are contradictory. It is nevertheless possible to identify some major principles on the surface states of implants that have demonstrated an acceleration or a greater bone/implant contact surface compared to a machined surface state.

The implants currently on the market are predominantly rough and therefore generally hydrophilic (low contact angle) [SCH 99], [HOT 16]. The roughness (more or less important according to the manufacturers) is desirable for several reasons. First, it allows the implant to be completely covered with blood very quickly when the implant is placed,

accompanied by a specific adsorption of proteins and circulating cells, the presence of which seems to greatly accelerate the bone healing process [KOP 15]. Furthermore, the roughness allows, with a larger specific area, to increase the bone/implant contact surface compared to a smooth surface, which will ultimately result in an improved mechanical strength of the implant after osseointegration. Finally, roughness is important for the primary stability of the implant.

The surface chemistry also has a great influence on the efficiency of the osseointegration process. Titanium oxides and calcium phosphates are found on the surface of most implants. Bone tissue cells have a high overall affinity for those chemical compounds. Sandblasting or plasma spay with calcium phosphate particles or derivatives are effective ways to improve bone tissue response.

The surface topographies look different under microscopy but also from the point of view of studying their surface parameters. Some surface features can be studied by interferometry or confocal microscopy [BIG 11]. Cells on the surface of implants are able to organize themself, spreading out, moving and adapt their shape to a surface. The study of cell/textured surface relationships is a recent topic for which there are still many questions. Nevertheless, it is accepted for example that the concave or convex character of a surface can induce variable stress on the nucleus of the cell, which can induce cascades of metabolic signals that can lead to various outcomes, such as multiplication, displacement or entry into the differentiation process [ANS 18]. The understanding of cell/roughness interactions and especially their control is undoubtedly one of the main levers to reduce the healing time of tomorrow's dental implants.

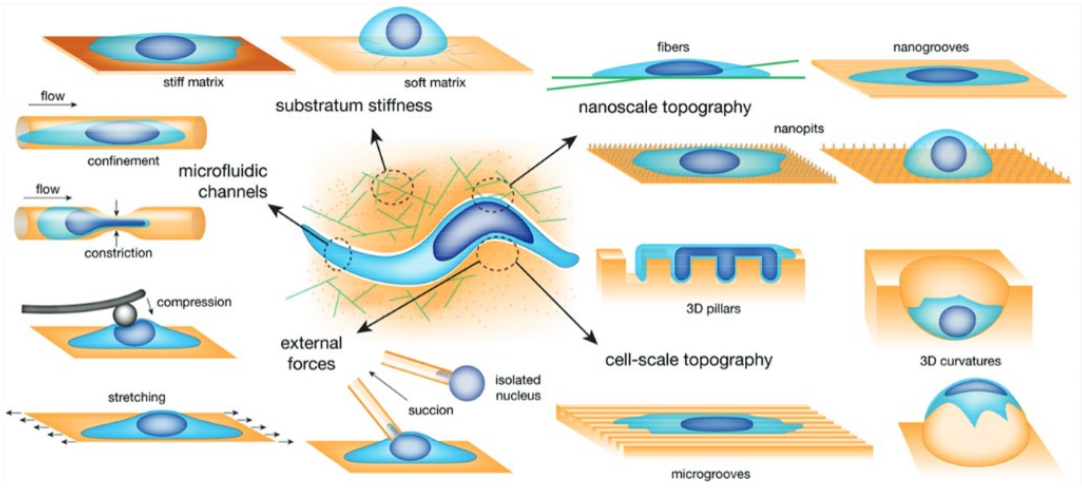

FIGURE 13 – Diagram illustrating the different properties of a substrate that can influence the behavior of cells brought into contact with it. The main properties shown here are: the substratum stiffness, the cell scale and nanoscale topography. External forces and microfluidic channels can also be used to influence cell's behavior. Illustration extracted from : [ANS 18].

Chemical composition of the material

Another area for improvement is the chemical composition of the alloys, as some of the doping element are currently being debated due to their potential harmfulness to the body. Tab. 2 below is a summary of elements that are currently controversial or already considered harmful in alloys for biomedical applications. Ideally, an alloy should not contain any of these elements, in particular Cobalt, Chromium, Aluminum, Vanadium. TA6V also contains significant amounts of Aluminium and Vanadium.
Copper may be considered harmful, but it has also an antibacterial effect [LI 19] at specific concentration and some really deleterious effect on the body's cells has been already demonstrated in the case of intra-uterine device (IUD) [COR 04] in short term after implantation which is far from dental implant situation.

TABLE 2 – Summary table of the recognized biocompatible elements and recognized harmful elements. This information were extracted from the work of [CAL 13].

Biocompatible elements	Harmfull elements (adverse body reactions)
Ti, Nb, Ta, Zr, Si, Mo, Sn, Pd, In, Sr, B, Ca, Mg	Be, Al, V, Cr, Mn, Fe, Co, Ni, Cu, Zn, Ag

Only few materials can claim to meet such severe chemical specifications such as: cp-Ti and ceramics. However, a new category of material discovered only a few decades ago, called Metallic Glasses (MG) or amorphous metallic alloys could well meet all these requirements. This new type of materials is presented in the next section.

Introduction to metallic glasses

Amorphous structure

Metallic glasses are materials made up of several different metallic atomic species in significant proportion. What differentiates them from most metals we use, is the organization of the atoms inside the material as illustrated in Fig. 14. Most of the metallic materials are under crystalline structure in their equilibrium state, with short and long-range order (mono or poly-crystalline and mono or multi-phased). On the contrary, amorphous solids like metallic glasses do not have organization or eventually very-small range order (some inter-atomic distances).

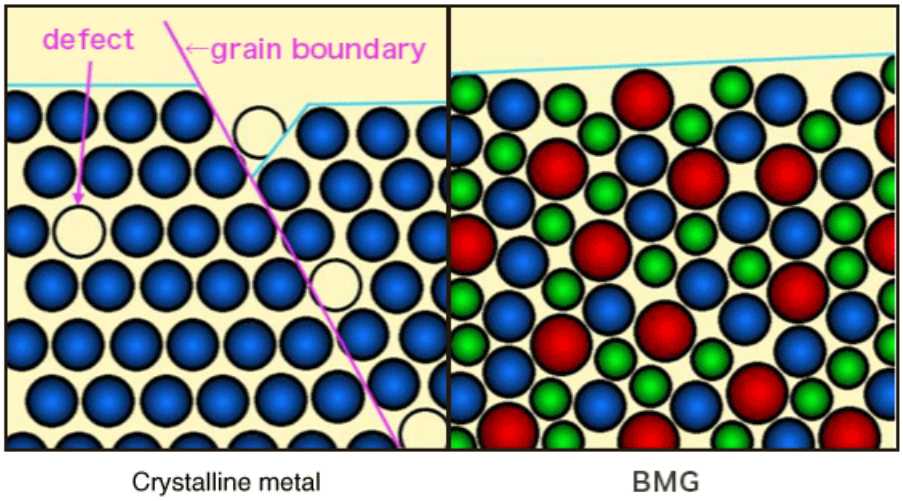

FIGURE 14 – On the left, schematic illustration of a typical metal structure: short and long range order of the atoms. Crystalline metals have generally grain boundaries and defects(lacunae, interstitial element and dislocations). On the right, amorphous metallic structure with at least 3 atomic species with neither long nor short range ordering.

Manufacturing metallic glasses

Metals are known for their ease of crystallization. Metallic atoms have the ability to rearrange themselves at very high speeds [DAV 75], so the whole challenge of metallic glasses lies in the cooling rates that can be experimentally achieved with current means and therefore directly limits the size of the parts that can be obtained. Indeed, the greater the thickness of the part, the more difficult it will be to manufacture it as an amorphous solid, with a risk that the core of the piece will be crystalline.
A schematic TTT (time/transformation/temperature) diagram is represented in Fig. 15. On the left graph (A), the situation for a conventional metallic alloy (crystallized) is represented. In order to remain in the supercooled liquid domain at room temperature (light blue area), it is necessary to either: cool fast enough to avoid the crystallization

nose (B) or change the chemical composition of the alloy to shift the crystallization nose to the right (C).

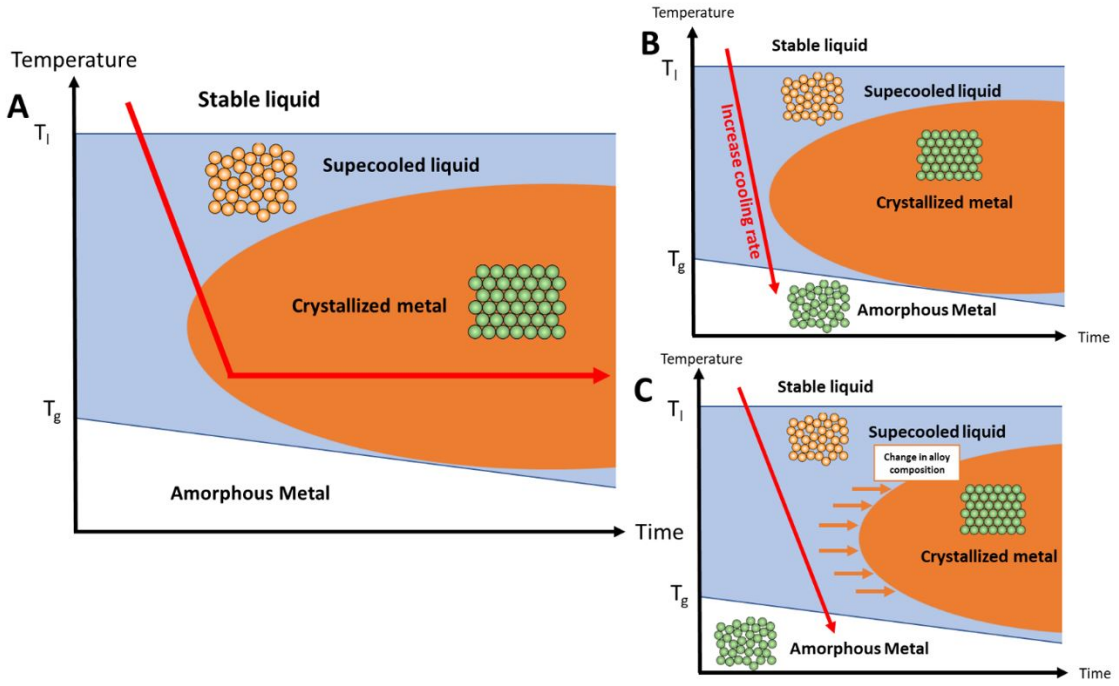

FIGURE 15 – Schematic illustrations of TTT diagrams (time-temperature-transformation) of two different strategies to obtain an amorphous metal compared to a crystalline metal. In A, TTT diagram of a conventional crystallized metal with short- and long-range atomic organization. In B, TTT diagram of an amorphous metal, which is cooled fast enough to avoid atomic organization in short and long range. In C, TTT diagram of an amorphous metal of which the composition has been changed to shift the crystallization nose to the right (it takes much more time for atoms to organize into a crystal lattice) to cool down fast enough to avoid atomic organization.

Glass formation can therefore only occur if the system is cooled quickly enough (not sufficient time for crystal nucleation and growth). The cooling rate during manufacture will determine the amount of free volume between the atoms. The higher the cooling rate, the more free volume there is. The amount of free volume has a direct influence on the mechanical properties of the alloy. The glass transition temperature depends on the amount of free volume trapped in the glass, the faster the glass is cooled, the higher the free volume and finally the higher the glass transition temperature. For each BMG, there is not only one T_g but several according to cooling rates, then it is better to talk about a fictive temperature (T_{fic}) which more accurately describes the kinetic aspect of the glass transition temperature. As can be seen in Fig. 16, at higher cooling rates, the fictive temperature is shifted to higher temperatures: Glass 1 is cooled faster, it has a higher T_{fic} and its volume is slightly larger than those of glass 2. Glass 2 is cooled at a slower rate, has a slightly lower fictive temperature and its volume is smaller. The difference of

volume between metallic glasses (that would have been cooled down at different rates) may then have an influence on mechanical and other properties.

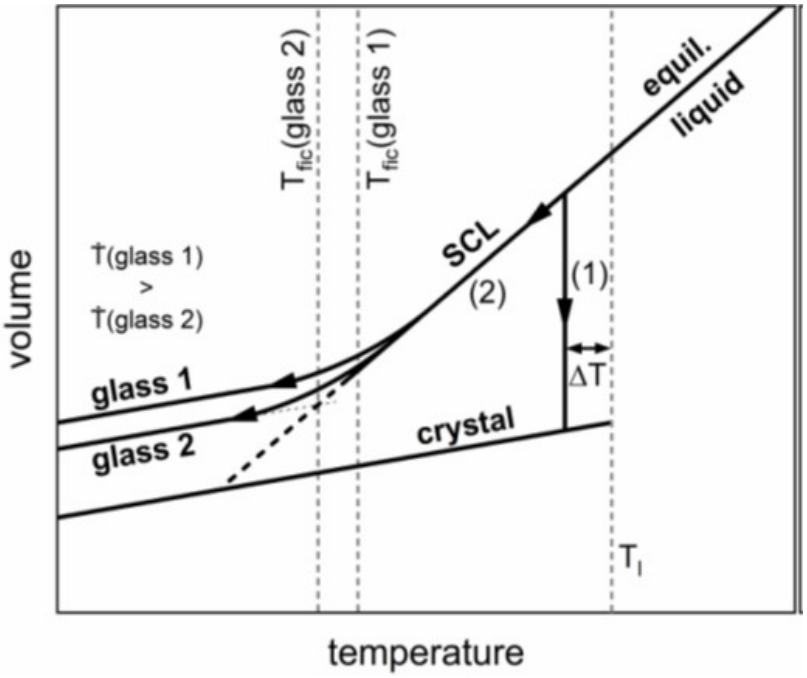

FIGURE 16 – Graph of volume versus temperature during crystal and glass formation. Above the liquidus, temperature the metal is completely liquid. In the case of a conventional alloy (1) the atoms rearrange into crystal(s) which drastically reduces the volume in the material. In the case of a metallic glass cooled down quickly enough, it remains in the supercooled liquid (SCL) zone (2) and there is a much smaller decrease in volume than in the crystal. It is possible to obtain two metallic glasses of the same composition with different cooling speeds, both will be amorphous. But if the cooling is faster (glass 1) the material will have a slightly larger volume than in an amorphous that has been cooled a little more slowly (glass 2). The difference of volume between the two metallic glasses can have influence on mechanical and other properties. Image taken from [BOC 19].

Influence of alloy composition

- **Inoue's Laws**

The ability of an alloy to be obtained in an amorphous state is very much conditioned by its chemical composition. Inoue and his team were pioneers in the elaboration of bulk metallic glasses [INO 01][INO 95][INO 08][INO 00]. They defined three empirical laws to produce an amorphous solid. These three rules are summarized below [INO 00]:

- three or more different atomic species (the more, the better),
- large atomic radius mismatch between species (at least 12%),
- mixing enthalpies between species as negative as possible.

Up to date, many BMGs have been developed by these three empirical rules method. In the case of eutectic or near eutectic compositions, it is known that the metallic elements

of the alloy will have difficulty in mixing with each other. Those specific compositions have a specific characteristic during solidification (slow cooling), the material is passing from liquid directly into two crystallized phases solid at a quite low temperature (compared to other composition of the same system). The resulting BMG's compositions were most often a near deep eutectic composition [BUS 07].

The concept of GFA (Glass Forming Ability) is strongly associated to Inoue's laws and is the main indicator of the possibility of an alloy to be manufactured as a bulk metallic glass. The evolution of GFA estimation over time is described in details in [JIN 09]. Initially it was mainly the temperature range of the supercooled liquid region (i.e. the difference between the crystallization and glass transition temperatures, $\Delta T = T_x - T_g$) [INO 93]. The larger the difference, the larger the diameter of the amorphous metal parts can be. As new compositions appeared, the community realized that the experimental data did not match the previous simple calculation very well. New criteria appeared, such as Gamma ($\gamma = \frac{T_x}{(T_l+T_g)}$) in [LU 02] and Delta ($\delta = \frac{T_x}{(T_l-T_g)}$) in [CHE 06], which depend also on T_g, T_x and T_l (liquidus temperature).

- **Theory of free volume**

There is an important concept to take into account when dealing with BMGs: the concept of free volume for metallic glasses, which is the free and available space between the disorganized atoms in the amorphous solid. This thermodynamically unstable state of supercooled solid contains a significant quantity of free space inside its own structure but it tends to decrease with time, because the material tries to reach an equilibrium state. If the free volume of the material slowly decreases, it will therefore increase the atomic density of the material with time. The available free volume has a direct influence on the possible atomic moves and it directly influences the properties of the material (mechanical and chemical properties)[LIM 10]. Some teams are currently working on the refinement of BMG relaxation state by heat treatment to optimize the amount of free volume, in order to improve the mechanical properties. The concept of free volume and BMG deformation mechanisms will be developed further in the BMGs mechanical properties section below.

After the presentation of those theoretical principles on BMG manufacturing, the different processes used to produce metallic glass under different shapes will be described in the section below.

Cooling faster: metallic glass manufacturing

Because metallic atoms have natural facility to organize themselves into crystals lattice, it is difficult to produce them under amorphous state. In practice, there are different ways to produce metallic glasses (thin films, ribbons and bulks), all the processes described below are based on obtaining the fastest cooling rate as possible.

Physical Vapor Deposition (PVD)

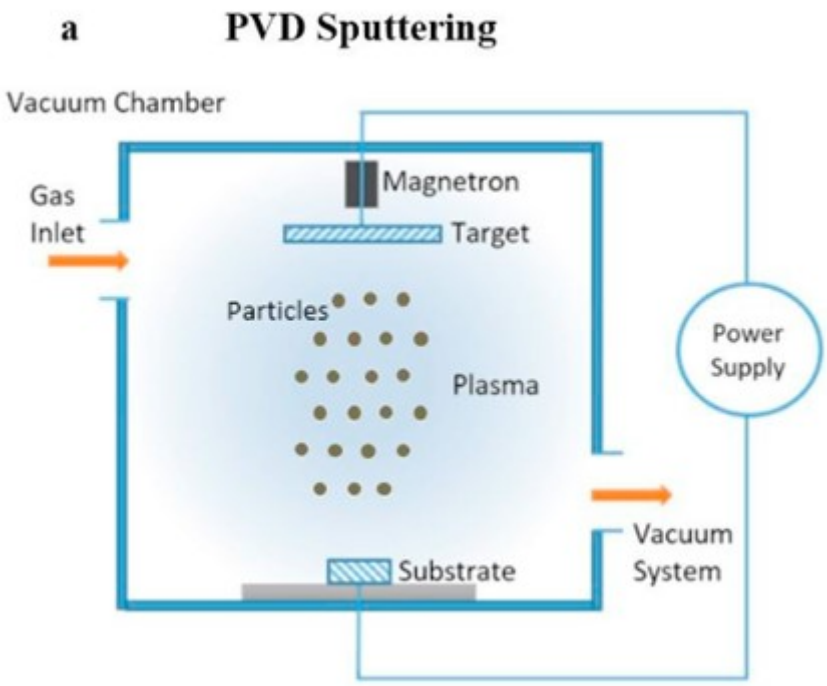

FIGURE 17 – Schematic illustration of Physical Vapor Deposition (PVD) principle. In a controlled atmosphere chamber, a plasma extracts atoms from one or more targets, which will then deposit on a substrate. This technique allows to produce very thin coatings (hundreds of nanometers) with well-controlled target compositions. The cooling rate of this method is very high, which makes it possible to have thin amorphous coatings but neither bulks nor ribbons. Illustration taken from [BAP 18].

The PVD (physical vapor deposition) sputtering is commonly used to make thin film metallic glasses. It is a succession of several atomic layer sputtered from pure or alloyed metallic elements targets (principle illustrated in Fig. 17). This manufacturing process is mostly a strategy for manufacturing coatings to protect or confer new properties to massive parts made of other materials. For example, [ETI 17] used thin metallic glasses (MG) film for antibacterial activity and [TSA 12] for sharpness improvement of surgical blades. This method is also used to screen potential BMG grades without the need to use a large amount of sometimes precious metals and without the problem of repeatability/mastery of bulk shape manufacturing like in [LOU 17] for mechanical and biocompatibility tests. This approach is mainly targeting corrosion or wear resistance objectives. PVD allows much higher cooling rates than the next following methods.

Melt spinning

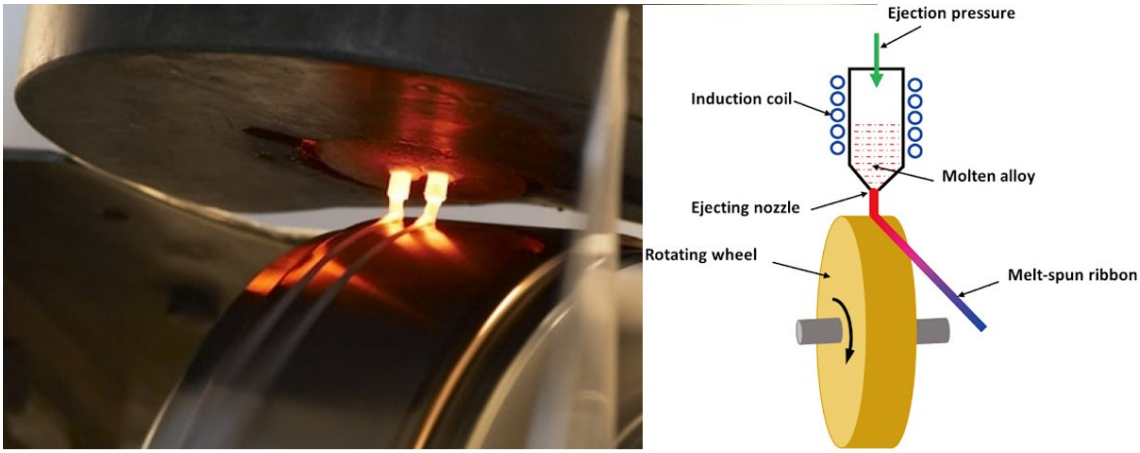

FIGURE 18 – Picture and scheme illustrating the melt spinning process to obtain amorphous ribbons. The alloy is heated to its liquid state, then a valve is opened to let the liquid flow at a low rate (ribbon width control) over a water-cooled copper wheel. The wheel rotates throughout the process at a controlled speed (which will depend on the viscosity and the desired ribbon thickness). This process has important cooling rates but only allows to produce ribbons, not bulk samples .Illustration taken from: https/:hittech.com (left image) and [RON 18] (right image).

The melt spinning is a technique used to manufacture metallic glass in ribbons shape with controlled width (milimetres to centimetres) and thickness (10µm to 800µm). It is presented in Fig. 18. In a typical melt spinning process, there is a rotating a water-cooled copper wheel (high thermal conductive materials) under a closed heated crucible which contain the master alloy. When the liquidus temperature is reached, a thin stream of liquid metal is dropped onto the surface of the rotating wheel. The heat of the molten liquid is absorbed into the roller rapidly. The cooling rate reached is on the order of 10^4–10^7 °C/s, which is fast enough to prevent nucleation and growth of stable phases for a wide range of MG compositions.

The cooling rate of the melt-spinning process depends on the several factors below [RON 18]:

- the thickness of the future ribbons is normally controlled by changing the spinning speed of the copper wheel;
- the width of the ribbons is controlled by the opening diameter of the ejecting nozzle and pressure;
- the cooling rate depends on the heat transfer from the melted alloy to the copper wheel surface, which depends on interface energy between the melt and the roller surface, heat conductivity of the roller material, heat transfer between the roller and cooling water, etc.

Melt spinning is mainly used as a preliminary step to the manufacture of bulk MGs (if the tested composition is not amorphous in ribbons, there no chance that it will be

amorphous in bulk form). The cooling rate in melt spinning is intermediate, slower than the one achieved in PVD but much higher than that of copper mold suction casting (presented in the next paragraph). There are direct applications of these ribbons, notably in the field of magnetism and electrical conduction [INO 08].

Arc- melter furnace - Copper mold suction casting

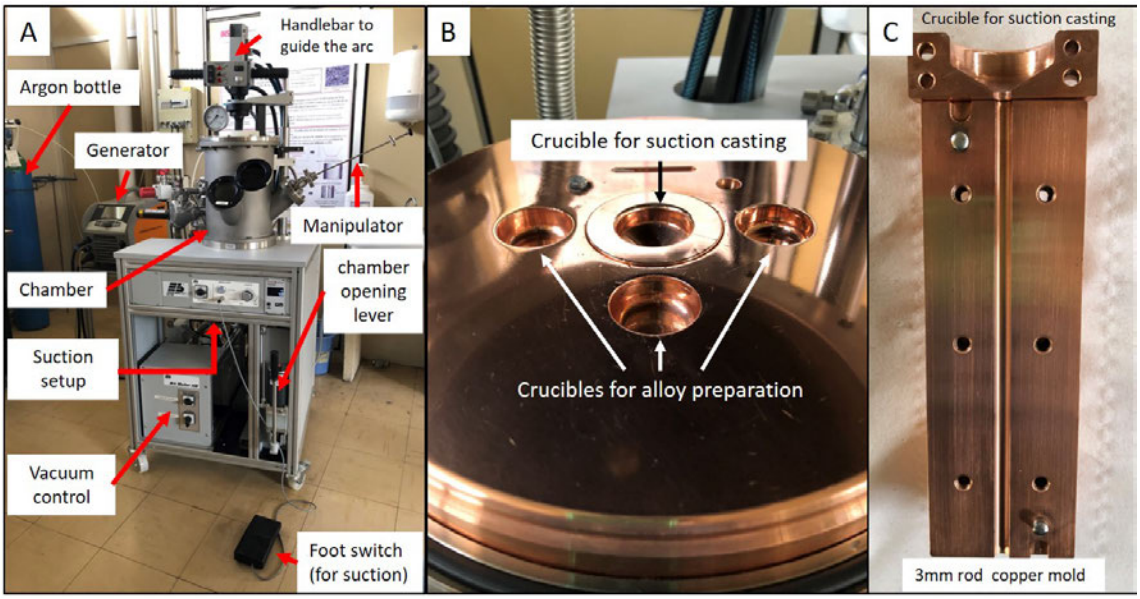

FIGURE 19 – Three pictures of the arc melter with suction casting device used in this thesis at Mateis laboratory. A, is a general view or the arc melter installation. On the picture several elements can be seen such as: the generator to create the electric arc, the handlebar to guide the arc into the chamber, the manipulator to flip the master alloy and the foot switch to open the valve for suction. B, is a picture taken inside the chamber, which is a massive copper plate with cooling channels. There are three crucibles to handle the master alloy preparation and one perforated crucible in the middle for the suction casting. C, is a picture of 3mm rod copper mold.

In this thesis, the focus is on arc melting furnace and suction casting illustrated in Fig. 19, essentially because the target application is dental implant manufacturing and it requires bulk parts. The principle is simple and starts with the preparation of the master alloy, i.e. the alloy with the targeted chemical composition in the form of an ingot and in crystalline state,(master alloy). To obtain this, the pure metals are precisely weighed and meticulously cleaned before being melted together in the arc furnace chamber using an intense electric arc in a neutral atmosphere (Argon). The master alloy can be melted/flipped several times by using the manipulator, in order to be homogenized in a crucible before it is considered ready to be cast.
The arc melter suction casting is used to make bulk samples generally in rod shape but not exclusively. One of the crucial parameters in copper mold casting is the diameter of the mold used (as illustrated in Fig. 19C). Indeed, the dimensions of the mold directly

condition the cooling speed of the alloy. The larger the diameter of the mold, the lower the cooling rate of the alloy and the more time the alloy atoms have to reorganize and form crystals [KOZ 15].
For the suction casting step of sample preparation, presented in Fig. 20, the master alloy will then be placed in the central crucible (as illustrated in Fig. 19B and C) drilled above the rod copper mold. Once the metal is considered perfectly liquid under the electric arc, the valve between the furnace chamber (under neutral gas) and the casting part of the furnace (secondary vacuum reservoir) is opened. The pressure differential sucks the liquid metal into the copper mold, which allows the alloy to cool down quickly.

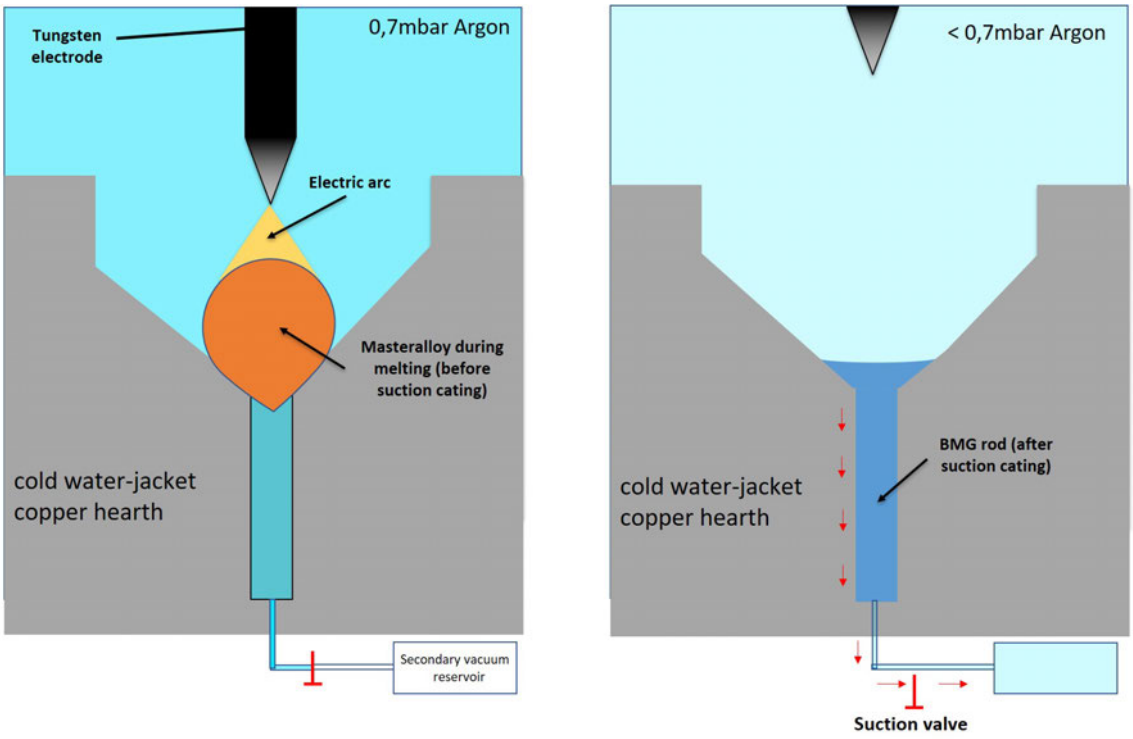

FIGURE 20 – Schematic illustration of the suction casting process. On the left, the molten alloy is in the central crucible just before suction, the suction valve is closed and there is Argon everywhere but in the secondary vacuum reservoir. On the right, the operator did used the foot switch (and switch off the electric arc) to open the suction valve, the pressure difference will push the liquid metal into the rod copper mold which will quickly cool down the alloy.

The composition of the alloy is the key parameter to consider whether a bulk sample can be amorphous, partially or fully crystallized[TUR 69] [INO 00]. This feasibility is reflected in the GFA and critical diameter already described above (calculations formulae are detailed in the 'Materials and Methods' chapter). In practice, researchers generally carry out casting tests with molds of increasing diameter. Then, they characterize the resulting rods through XRD to check the macroscopic presence or absence of diffraction peaks (which reflects the presence or absence of a crystalline organization), which is the

most common experimental method for obtaining the critical diameter. For GFA calculations, researchers rely mainly on DSC (differential scanning calorimetry), a technique based on recording the difference of heat flow between an empty crucible and a crucible containing a piece of metallic glass subjected to one or more controlled thermal cycles in order to determine T_g , T_x and T_l [BAD 07].

Others methods (tilt casting, sintering and additive manufacturing)

In addition to the most conventional methods described above, there are other techniques for the manufacturing of bulk metallic glasses. The following list is not exhaustive but aims to provide an overview of other methods that exist:

- Tilt casting is another method of making solid parts. Like suction casting, it involves the use of an arc melter furnace. The main difference is that the crucible containing the liquid metal alloy can be tilted to quickly fill a copper mold [SOI 11]. The cooling rates are of the same order of magnitude as those obtained in suction casting.
- SPS (spark plasma sintering) can be used to make bulk samples. This requires an amorphous powder of the desired composition which can be obtained by atomization (as for additive manufacturing processes). Then it is possible to choose the pressure, temperature and holding time of the SPS device to sinter and compact the amorphous powder grains. Thus it is possible to obtain fully dense parts at a temperature well below T_g to avoid any crystallization [HAR 09].
- Additive manufacturing is a method that has been gaining interest for just over two decades. These techniques are based on selective laser melting (SLM) or electron beam melting (EBM) technologies which consist of the melting of amorphous powder grains layer by layer. The laser allows very high heating and cooling rates to be achieved in each layer. With this process it is possible to overcome the notion of critical diameter to obtain large parts with complex geometries [MAH 18]. However, this manufacturing process needs to be further studied, understood and improved as the printing parameters must be optimized for each grade of metallic glass to avoid crystallization. Indeed, there is a heated affected zone (HAZ) which corresponds to the equivalent of a short annealing of the layer below the printed one and results in partial crystallization of the metallic glass [WU 12]. There are also problems with residual stresses occurring during the printing process which may lead to cracking of the parts [WIL 17].

Specific properties of metallic glasses

Mechanical properties at low temperature

In this section, some properties shared by the majority of metallic glasses will be presented. This section aims to give the reader an overview of the potential of metallic glasses. The specific properties of $Ti_{40}Cu_{36}Zr_{10}Pd_{14}$, specifically studied during this thesis, will be detailed later in this section.

- **Deformation behavior**

The mechanisms of fracture and deformation are different from those of crystalline metals. Given the absence of long-range organization, the notion of defects (dislocations, gaps, etc.) cannot be considered when understanding the mechanical behavior of BMGs. After a review of the literature, it seems that metallic glasses can be separated into two categories, on one hand, the ones that show macroscopic brittle behavior and on the other hand, those that show some plasticity.
The deformation of metallic glasses takes place in the same way for all grades at low temperature, there is a heterogeneous local deformation which results in the appearance of shear bands on the maximum shear stress plane. A shear band is a very local (nanoscale) plastic deformation associated with local thermal activation. The formation of bands has been theorized by many authors, most notably Argon [ARG 79] and Spaepen [SPA 77].
For Argon, it is rather a question of shear motion of clusters of a hundred atoms moving to accommodate the shear stress. In order to move, the atoms involved need to change their energy level. This change in energy level results in the formation of STZs (shear transformation zones), which are not considered as defects. Indeed, it is theoretically impossible to anticipate the formation of a shear band in metallic glass since there is no structural defect/noticeable point related to their occurrence. However, it is known that failures generally occur along the maximum shear plane.
For Spaepen, it is rather a matter of discrete atomic jumps in series. This theory is directly linked to the one of free volume, since atomic jumps would be facilitated in the presence of a large free volume in the metallic glass. The amount of free volume frozen in the glass during casting will have a very important influence on the deformation of the grade considered. As with crystalline metals, it is the thermal history that determines the behavior of the material during mechanical testing. Both shear band mechanisms are illustrated in Fig. 21.

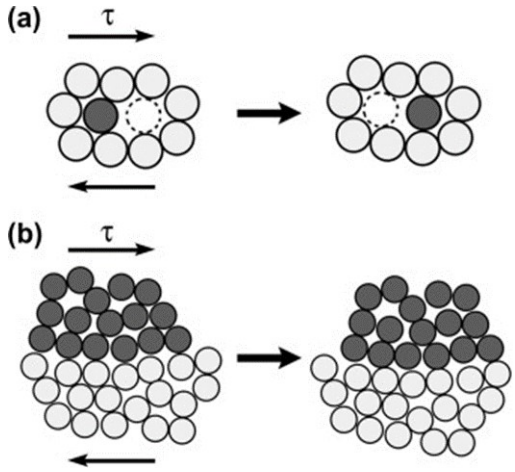

FIGURE 21 – Schematic illustration of shear band formation according to Spaepen's model (a) and to Argon's model (b). Both modes are based on the presence of free volume inside the glass. (a) For Spaepen it is more isolated atomic moves. (b) For Argon it is entire atomic clusters moves. Reproduced from [TAK 11].

Several criteria have been developed to correlate the intrinsic properties of the material and its macroscopic mechanical behavior (ductile or brittle). Here we describe the work of [LEW 05] and [KUM 13]. [LEW 05] highlighted the use of the μ/B ratio (μ is the shear modulus and B is the bulk modulus) to estimate the mechanical behavior of each grade at low temperatures. They show that the lower the μ/B ratio, the greater the chance the material to show plasticity. The higher the μ/B ratio, the more likely the material will exhibit brittle behavior. The μ/B indicator is also used to estimate whether an annealing treatment is likely to lead to embrittlement. Generally, annealing results in structural relaxation, i.e. a decrease in free volume in the material. According to the Spaepen model, if the free volume is reduced, there will be less space available for atomic jumps to take place, which will lead to immediate brittle fracture and hence embrittlement after annealing. In Lewandoski's article, they state that if μ/B is between 0.41-0.43 or equivalently a Poisson's ratio μ is less than 0.31, the BMG will have a brittle behavior. It is interesting to note that the Poisson's ratio of BMGs is about 2/3 of their crystalline counterparts, yet BMG are more brittle than their crystalline counterparts. However, this model seems to have some limitations, as highlighted in [MAD 12]. A more recent approach by [KUM 13], further extended by [KET 18], claims the existence of a fictive temperature T_{fic} specific to each metallic glass composition which depends also of its thermal history, which is an overall indicator of the structural disorder inside a glass. There is also a critical T_{fic} which is the temperature for which structural relaxation is the fastest (relaxation nose). Further information on the determination of the fictive temperature is available in the article of Tong et al. [TON 15]. The main idea is to perform some isothermal thermal treatments at different temperatures and different durations and then followed by mechanical tests to determine the positions of the relaxation and crystallization noses. What we learn from

Kumar et Al. work is that each BMG has a crystallization nose and a structural relaxation nose. It is the position of the relaxation nose in relation to the crystallization nose in the TTT diagram that will determine the mechanical behavior of the alloy at room temperature and its susceptibility to become brittle following relaxation as presented in Fig. 21. For all BMGs, the cooling rate of the alloy is considered sufficient to pass the crystallization nose (R_c). There are then two configurations. For the first, the relaxation nose is shorter than the crystallization nose, which corresponds to type I BMGs, then an amorphous but relaxed and therefore brittle BMG at room temperature is obtained. For the second, type II BMG, the relaxation nose is longer than the crystallization nose. The cast BMG obtained will have a sufficient amount of free volume to allow plastic deformation at room temperature. From a practical point of view, the authors suggest to calculate the difference $T_f - T_{fic}$.

- If $T_f - T_{fic} < 0$ then the BMG is a type I, it will be brittle and susceptible to anneal unless even faster cooling (increasing T_f) can prevent crystallization and relaxation, the BMG can therefore become ductile.
- If $T_f - T_{fic} > 0$ then the BMG is a type II, it will be ductile in its as cast form and not very sensitive to structural relaxation.

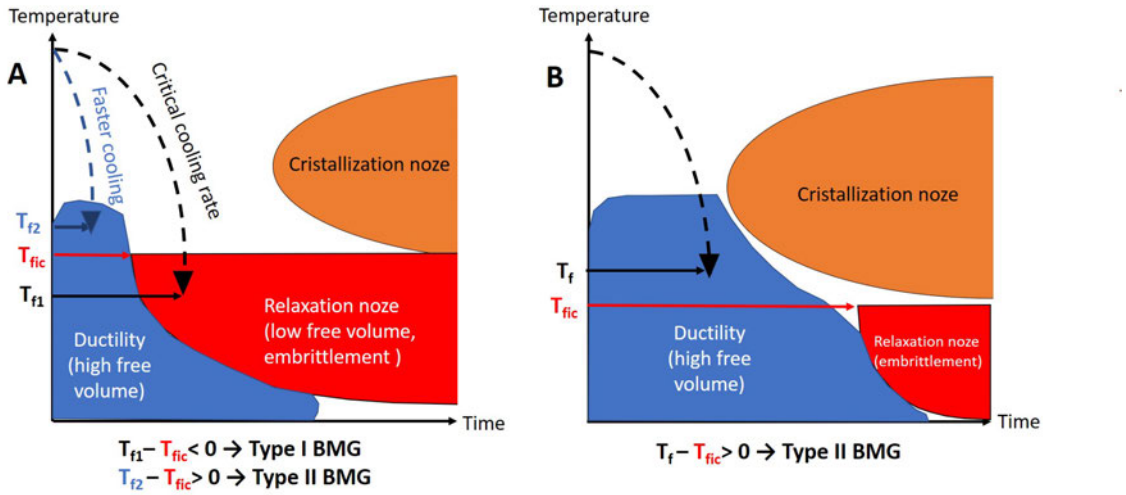

FIGURE 22 – A and B are TTT diagrams of the two type BMG according to Kumar et Al. A, illustrates the TTT diagram of a type I BMG. For this type of BMG, relaxation nose is shorter than the crystallization nose then an amorphous but relaxed and therefore brittle BMG at room temperature is obtained. In this case the fictive temperature ($T_{fic\ 1}$) is lower than the critical fictive temperature. Sometimes, it is possible to increase the cooling rate and increase the fictive temperature ($T_{fic\ 2}$) to change a type I BMG to a type II. B, illustrates the TTT diagram of a type II BMG. For this type of BMG, relaxation nose is longer than the crystallization nose then an amorphous and not relaxed therefore ductile BMG at room temperature is obtained. Adaptation of [KUM 13].

- **Hardness, Yield Strength and Young Modulus**

One of the most remarkable properties of metallic glasses is their extremely high Yield strength. In fact, most compositions have a Yield strength and mechanical strength between 1 and 5 GPa (close to the theoretical limit)[ECK 07][SCH 07c]. The explanation for such Yield strength lies mainly on the abscence of disclocations, lacunae or intersitial elements. For the cristalline materials those defects allow plastic deformation under lower shear stress than the theoretical stress expected. Indeed, in the case of BMG at room temperature, the atoms have a very limited mobility but the distances between the atoms being globally higher (density slightly lower than the crystalline equivalent) allows a considerable stress in the elastic regime.The free volume gives some space to the atoms inside the material to move more easily and which reduces the interaction forces between atoms. The hardness of BMGs is globally high up to 1100 HV [SCH 10], making them very appropriate for wear application.
Morover, the absence of defects and dislocation slow down the strain of the material because there is no starting point. If we remain in the elastic regime, the material will return to its initial state when the stress is removed, but the stress is stored as elastic energy and must be released. Metallic glasses therefore have a higher mechanical strength than steels and ceramics as illustrated in Fig. 23, such a combination of properties makes them more than attractive as structural materials [ASH 06]. On the other hand, metallic glasses have a relatively low Young's modulus, generally between 80 and 100 GPa as represented in Ashby plot of Fig. 23. These values are lower than those obtained on their crystalline equivalents. This property is mainly due to the presence of free volume.

- **Toughness and fatigue endurance**

There is currently no general trend in the literature to describe metallic glasses. Amorphous metals therefore exhibit toughness values that vary from as low as the values characteristic of brittle ceramics to as high as the engineering metals [ASH 06][DEM 10] [NAR 15]. This can be compared to high performance steels and technical ceramics where the toughness is respectively superior to 100 MPa.$sqrtm$ and between 5 to 8 MPa.$\sqrt{m}$ as illustrated in the Ashby plot Fig. 24. It appears again that the toughness depend on the amount of free volume. The lower the free volume, the lower the toughness is [KRU 11]. On the contrary, the fatigue endurance limit increases when the free volume is reduced (probably because it limits the fatigue crack initiation)[LAU 08].

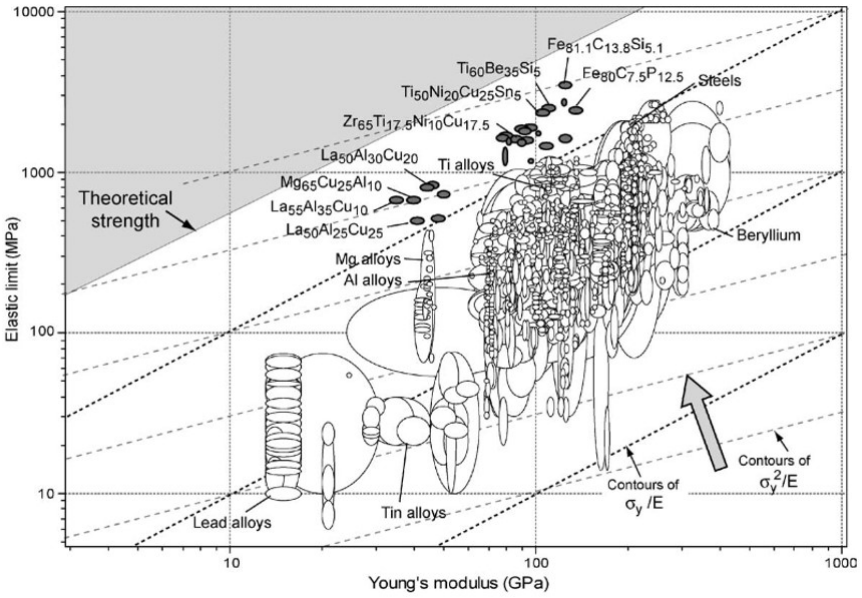

FIGURE 23 – Ashby plot of elastic limit σ_y plotted against Young modulus E for 1507 metals, alloys, metal matrix composites and metallic glasses (dark dots). The contours show the Yield strain σ_y/E and the resilience $\frac{\sigma_y^2}{E}$. The alloys in black are BMGs. Illustration and caption reproduced from [ASH 06].

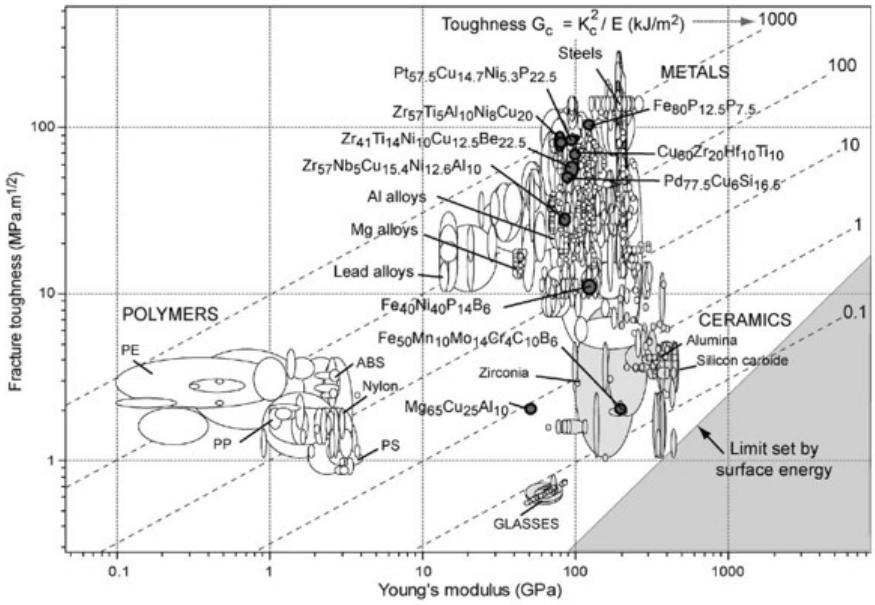

FIGURE 24 – Ashby plot of the fracture toughness and modulus for metals, alloys, ceramic, glasses, polymers and metallic glasses (black dots). The contours show the toughness G_c in kJ.m^2. The plot is reproduced from [ASH 06].

The determination of the fatigue life of materials is not easy and depends on many factors such as: fatigue-loading mode, sample geometry, material quality, fabrication pro-

cedure, and microstructure. Those factors could influence the fatigue behavior[GON 16]. In the case of Zr-based BMGs, [WAN 14] under compression–compression loading and tension-tension loading, they sometimes demonstrate excellent fatigue resistance. The fatigue-endurance limits of Zr-based BMGs vary from 150 to 1050 MPa. The fatigue limits of BMGs are comparable with the conventional crystalline materials, such as ultrahigh-strength steel, IN 718 superalloy, TA6V and Zirconium alloys, depending upon the composition of BMG alloy tested and the test methods as illustrated in Fig. 25. according to [LAU 08], controlling free volume and residual stresses appears to be a viable way to tailor the fracture and fatigue properties of bulk metallic glasses.

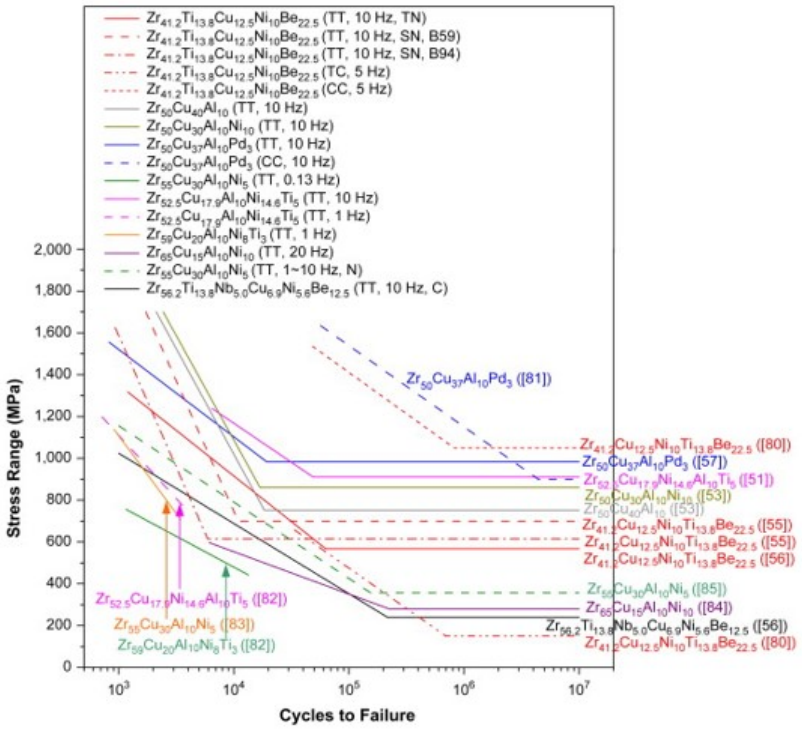

FIGURE 25 – Stress-lifetime curves for uniaxial fatigue of Zr-based BMGs in air (TT: tension–tension, TN: tapered notch, SN: sharp notch, TC: tension–compression, CC: compression–compression, N: nanocrystalline, C: composite). Illustration and caption reproduced from [WAN 14].

- **Bulk metallic glass composites**

There is another approach to obtain a solid metallic glass with ductile behavior without having to sacrifice its Yield strength. Many teams are currently working on the development of metallic glass "composites" [ECK 07][CHE 21][HOF 13][HOF 08]. In most cases, seeking to have an amorphous matrix with the advantageous properties of typical BMGs (low Young's modulus, very high Yield strength, etc.) with reinforcements consisting either of another material or by a partial crystallization of the considered BMG (crystalline reinforcement embedded in amorphous matrix of the same composition) during its man-

ufacturing process. The presence of reinforcements in the material is intended to improve the plasticity of the material at room temperature once the Yield strength is exceeded. To date, several BMG systems have proven to be good candidates for the manufacture of metallic glass "in situ" composites, i.e. a crystalline phase usually forms in the amorphous part during the manufacturing process. Since the appearance of the crystalline phase is conditioned by the chemical composition of the alloy and the cooling rate, the challenge in the production of these composite materials is to optimize the amorphous /crystalline volume ratio. Zr-Cu [ESC 19] and Ti-Cu-Ni [GAR 13] based alloys are the main systems studied in this direction. In these alloys, during manufacturing, a B2 type phase appears. This metastable phase has the capacity to undergo a martensitic type transformation under stress or during a heat treatment associated with an increase in the volume of the lattice (B2-> B19')[LIU 12b] [PAU 09]. Some teams have demonstrated the ability of specific BMGs to significantly increase their toughness or fatigue strength thanks to their ability to slow down crack propagation (blocking effect).

Corrosion Behavior

Corrosion resistance, which as mentioned earlier in the introduction is an essential property for use in the medical sector, is also an advantage of most metallic glasses. Amorphous metal alloys have generally better corrosion resistance than their crystalline counterparts [RAM 15] [SCU 07][WAN 13b].
This trend can be explained by several factors. First, due to the lack of grain boundaries, which are often the starting point of the corrosion process via pitting or crevice corrosion. In addition, BMGs have a very homogeneous chemical composition, unlike crystalline metals which may contain several phases with different chemical compositions. Changes in composition can cause local changes in potential which can result in galvanic coupling.
Nevertheless, like most of the properties mentioned in this section of the manuscript, the chemical composition of the considered grade has a major influence on its corrosion resistance [BHA 98][PAR 02]. It can be noted that Zr-based and Ti-based alloys benefit from the phenomenon of passivation (spontaneous creation of a very adherent oxide layer) which generally provides them a high corrosion resistance also in amorphous state [WAN 13b].

Thermoplastic forming

As the final application targeted in this manuscript is dental implant, we have been focusing so far in the mechanical properties of metallic glasses close to room temperature (37°C for a dental implant). But the phenomena mentioned above are no longer applicable when approaching the glass transition temperature. According to the graph in Fig. 26, if the deformation mechanism is non-homogeneous at room temperature and for very high mechanical stresses, there is the appearance of shear bands (purple zone), and thus the material behaves differently depending on the applied load, temperature and loading speed

[SCH 07c].

- At low stress and temperatures below 0.8 T_g , the material remains in the elastic range (white zone).
- At low stress and temperatures above 0.8 T_g , the material switches to a homogeneous deformation regime in the Newtonian regime (yellow zone).
- At higher stresses and above 0.8 T_g , the material switches to a homogeneous deformation regime in the non-Newtonian regime (orange zone).

The ability of amorphous metals to deform near T_g is equivalent to that of thermoformable plastics. Metallic glasses therefore have the ability to be shaped by the same processes as those used for polymers. As described above, near T_g it is possible to deform the material without crystallizing it (see Fig. 27). In the case of a dental implant, this characteristic represents a great advantage compared to crystalline materials. Metallic glasses therefore offer the possibility of obtaining parts with complex surface features [BER 17] [SAR 17][SCH 07b]. In the case of dental implants, this property offers the possibility of surface texturing with precise and customized patterns to improve the integration of the implant in its biological environment.

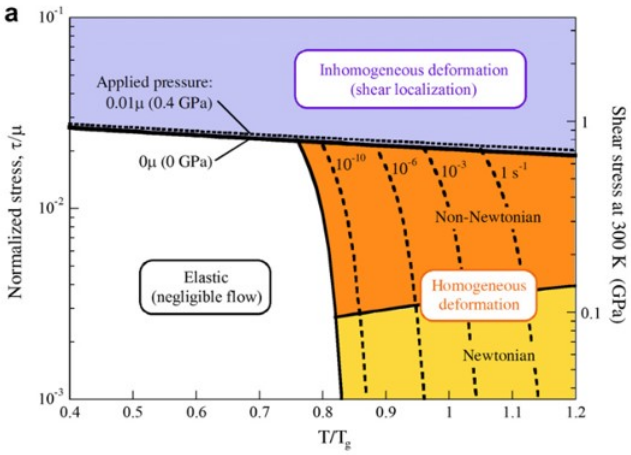

FIGURE 26 – Schematic deformation map of BMGs. The dominant deformation mechanism is shown on a temperature scale normalized to T_g and depending on the shear stress normalized to the shear modulus. Illustration and caption reproduced from [SCH 07c].

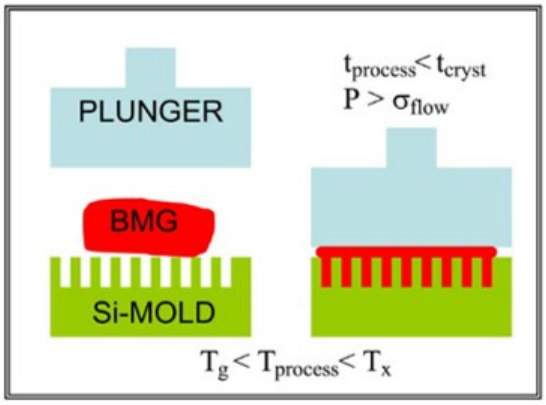

FIGURE 27 – Schematic illustration of the thermoplastic-forming (TPF) of BMG. (a) Amorphous BMG is positioned on the mold. (b) Heating the setup to a temperature between T_g and T_x for a time shorter than t where a pressure is applied that exceeds the flow stress of the BMG at the processing temperature results in the filling of the mold cavity. Illustration and caption taken from [SCH 07b].

BMG applications

FIGURE 28 – Picture of the current main applications od BMGs. Reproduced form: [HOF 13].

Metallic glasses are difficult to produce and often contain very expensive chemical elements (Platinum, Palladium, Gold, etc.), which limits their use in industry (depending on the final piece use). However, their aesthetic properties (very shiny and not easily scratched), make them a material of choice for watchmaking and jewelry. In addition, their amazing ability to store elastic energy and then release it, has led to the development of high-performance technical sports equipment such as golf clubs and tennis rackets that have no equivalent (see Fig. 28). If metallic glasses are for the moment distributed rather in

the sectors of the sporting equipment and the luxury, other applications in microelectronics and magnetic applications exist [INO 08].

BMG grades for biomedical applications

General overview of BMG biomedical grades

In the Tab. 3, a non-exhaustive presentation of promising grades of solid metallic glasses developed for biomedical applications is given. Not all of biocompatible BMGs grades have been listed because there are too numerous, but these are the most promising ones and their main characteristics have already been determined. The selection was based on the main requirement for dental implants, namely critical diameter, UTS, ductile behavior, Young's modulus, biosafety and corrosion resistance. The majority of the grades are Ti and Zr based and generally do not contain harmful elements. However, some of them do contain Ni/Al/Ag, which are controversial [CAL 13]. Nevertheless, these grades largely meet the current standards of in vitro tests, especially because these materials release very few elements into their environment. Given the vast number of candidate grades for biomedical applications, each with more attractive properties than the previous, one can wonder why there are currently no commercial medical devices on the market ?

TABLE 3 – Comparison table of the most promising BMG compositions for biomedical application in the literature. The BMGs principal characteristics such as: critical diameter, ultimate tensile stress (UTS), plasticity, Young Modulus, biosafety and corrosion resistance are gathered.

Alloy composition	Critical diameter (mm)	UTS (MPa)	Plasticity Y/N	E(GPa)	Biosafety Y/N	Corrosion resistance	Ref
$Zr_{70}Ni_{16}Cu_6Al_8$	3-5	1500	Y	70	Y	Good	[IDA 18]
$Zr_{50}Cu_{35}Al_7Nb_5Pd_3$	3	1800	Y	88	Y	Good	[HUA 12]
$Ti_{47}Zr_7Cu_{38}Fe_{2.5}Sn_2Si_1Ag_2$	3	2028	Y	100	/	Good	[LIU 20]
$Ti_{47}Cu_{38}Zr_{7.5}Fe_{2.5}Sn_2Si_1Ag_2$	7	2080	Y (compression)	100	Y	Good	[PAN 15]
$Ti_{40}Cu_{36}Zr_{10}Pd_{14}$	6	2010	Y	100	Y	Medium	[LIE 19]
$Ti_{40}Cu_{34}Zr_{10}Pd_{14}Sn_2$	4	1970	Y (compression)	114±20	Y	Medium	[LIE 19]
$Ti_{40}Cu_{33}Zr_{10}Pd_{14}Sn_2Si_1$	10	1645	Y (compression)	108±22	Y	Good	[LIE 19]

The paradox of metallic glasses: a lot of research and articles but very few commercialized products

A large number of articles (see Fig. 29) have been published on bulk metallic glasses, which are often described as very promising for many applications. However, the number of real industrial outlets is actually limited to niche applications. The expected democratization of metallic glasses has not yet taken place. In this paragraph, possible explanations for BMG's absence from the medical market are discussed.

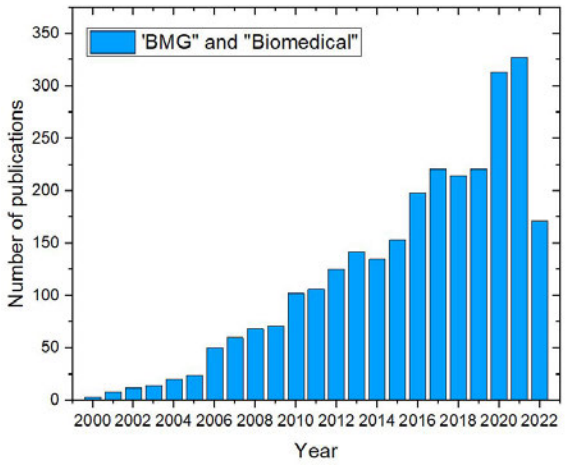

FIGURE 29 – Number of publications related to both "BMG" and "biomedical" from 2000 to 2022 on Science Direct website request.

The gap between research and industry (different objectives, means of characterization, quality approach, etc.)

The specific case of metallic glasses illustrates particularly well the differences in priorities between the academic and industrial field. While the researchers are seeking novelty and proof of possible industrial application, others (industrials) see it as a technical achievement that is only accessible at laboratory scale (academic) and cannot be transferred to the mass production. In many publications, researchers will often highlight the most attractive properties, while not reporting possible defects in the parts, which are probably related in the case of BMG to the complex manufacturing process. In a large number of publications, X-ray diffraction is the only method used to assess the fully amorphous state of the piece, not as a strategy but rather because of the unsuspected nature of some defects. We will see in chapter 1 that this technique may not be sufficiently sensitive in some cases to detect heterogeneities of crystalline nature. Another feature of many papers on the mechanical characterization of metallic glasses is the almost systematic and exclusive use of compressive tests. It is true that compressive tests are particularly easy to set up, the used specimen are small and easy to prepare, resluts are generally reproducible and show a high compressive strength, a relatively low Young's modulus and plasticity before fracture. But on the same alloy, one can have radically different results in tensile test[ZHA 03a] [ZHA 03b], with a lack of reproducibility, premature failure and above all a brittle macroscopic behavior making metallic glasses much less attractive to industry. There is no enough comparable data on fatigue endurance and toughness evaluation [NAR 15] [GON 16].

'Unpredictable' results with copper mold suction casting

On the other hand, the manufacturing process of metallic glasses by arc melting turns out

to be relatively unpredictable with many parameters that can have an influence on the final state of the obtained rods (continuity, surface aspect, length, porosities, unmelted zone...). The manufacturing process is not enough discussed in the literature despite a panel of "specific laboratory" protocols that team keeps to themselves. The adaptation of the suction casting process to mass production is relatively complex and above all very sensitive according to the targeted application and depends also on the alloy's composition. Moreover, the quality control associated with the production of these parts, particularly in the medical and aeronautical fields where manufacturing defects are not tolerated, can be very costly and therefore prohibitive.

Limiting medical innovation through regulation

It should also be kept in mind that there is an increasing amount of regulatory work to be done for a new medical device to obtain CE or FDA approval for the launch on the market. The whole process of bringing a new medical device to market is very expensive which will strongly prevent small companies from making such an investment. In future, it is probable that only large companies will be able to finance the innovative implants of tomorrow. In order to encourage manufacturers to invest in the use of metallic glasses at industrial scale, it will be necessary to demonstrate the superiority and show repeatable results of BMGs over more conventional solutions which have already proved their efficiency in the case of dental implants. In addition to the manufacturers of the implants, it is also necessary to convince the health professionals who are ultimately choosing the implant reference they will use for their patients.

The $Ti_{40}Cu_{36}Zr_{10}Pd_{14}$ grade

Why picking up $Ti_{40}Cu_{36}Zr_{10}Pd_{14}$ among others alloys composition ? There are several arguments in favor of choosing this grade for the manufacture of dental implants:

- First, this grade does not contain any controversial elements such as Nickel or Aluminum and has been shown to be biocompatible [LIE 18], [ZHU 07a].
- In addition, this grade has a critical diameter of 6 - 7 mm announced by [ZHU 07a], [ZHU 07b], which is a sufficient diameter for the machining of conventional size implants (diameter less than 4.5 mm) or narrower and therefore a possible miniaturization of implants.
- This grade has much better mechanical strength in compression and tension (2000 MPa) compared to TA6V (930 MPa) combined with a Young's modulus approximately 12% lower than for TA6V (115 MPa).
- The fatigue life and toughness of this specific composition alloy have not been published so far but Alethea Liens [LIE 19] did some experiments during her PhD to determine them. She estimated the fatigue endurance by rotative bending test and following the ISO 14801 standard. The toughness was evaluated with Single-Edge

Notched "V" Beam (SENVB) in four-point bending test. The results were satisfactory given the intended application (results presented partly in chapter 1). The study of [YAM 14] showed interesting fatigue endurance limit of $Ti_{40}Cu_{34}Zr_{10}Pd_{14}Sn_2$ alloy of 762 MPa but with a lack of repeatability incriminating casting micro-defects.

- The corrosion resistance of this grade is not as good as that of TA6V but it has been considered so far to be more than sufficient for dental use [129], [130].
- • The possibility of thermoplastic forming on the $Ti_{40}Cu_{34}Zr_{10}Pd_{14}$-$M_2$ (M=Sn or Ga) system has already been investigated by [115], [116] and according to the results on these very close to $Ti_{40}Cu_{36}Zr_{10}Pd_{14}$ grades (same atomic system and close GFA) there are good reasons to believe that it will have good surface texturing ability.
- The brightness and aesthetic aspect of this metallic glass with innovative surface texturing may be a marketing asset to dentists [SCH 07a].

Problematic and Challenges

This thesis project aims to critically and objectively evaluate the $Ti_{40}Cu_{36}Zr_{10}Pd_{14}$ grade as a biomaterial for a dental implant final application. While manufacturers in the sector seek innovation to improve the performance of their implants, to our knowledge no new material has been brought to the medical device market in the last decade. The state of the art on $Ti_{40}Cu_{36}Zr_{10}Pd_{14}$ BMG alloy unanimously portrays the grade as being particularly well suited to the requirements of the dental sector, especially because it has been already shown to be biocompatible. This grade has impressive (compressive) mechanical properties that could allow implant's miniaturization and has the potential to provide innovative surface texturing at low cost. However, the work of Dr.Aléthea Liens during her PhD [LIE 19] has first highlighted the lack of reliability of this grade. Indeed, she noted a global scattering, particularly during mechanical characterization under tensile and fatigue loading. Apart from a no more than correct corrosion resistance and a relatively low toughness, she also noted the presence of spherical defects (which will be called spherulites hereafter) on fracture surfaces. The spherulites have been observed particularly in tensile and rotating bending tests (fatigue tests). This thesis follows the investigations of Aléthea Liens on the BMG grade $Ti_{40}Cu_{36}Zr_{10}Pd_{14}$ and aims to answer many of the following questions that we have attempted to answer in each of the chapters during this PhD work.

- What is the number spherulites in cast rods and their distribution in terms of size ?
- How can their presence be systematically detected ?
- Do they influence the mechanical and electrochemical properties of the BMG ?

Chapter 1 is a published work [132], where we highlighted the presence of those spherical crystal defects and estimated their size and distribution in the rods made by copper mold suction casting. The spherulites are not easy to detect, which explains to a large extent why very little work has been done on the detection of such defects. In this context, we also need to understand what is the impact of spherulites on the mechanical properties and on the corrosion resistance of this BMG. The discussion will highlight the importance of detection of the spherulite's presence, which in our case have a significant deleterious effect on the mechanical properties of the alloy mainly due to their too large diameter leading to premature failure. This chapter will discuss the need to identify the nature of the spherulites in order to help to control their size and distribution to maintain the high potential of this grade for the manufacturing of dental implants.

- What is the microstructure and crystalline organization of a spherulite ?
- Are there several phases ?
- What are these phases ?
- How do spherulites appear ?

In addition to understanding the influence of spherulites on the properties of the grade, there is a need to understand what spherulites are made of in terms of microstructure and to identify the present phases. Chapter 2 (article under submission) will focus on an in-depth study of the microstructure and crystallography of spherulites. It is mainly based on electron microscopy observations. The discussion of this chapter will focus on a scenario for the appearance and growth of these spherulites in $Ti_{40}Cu_{36}Zr_{10}Pd_{14}$ metallic glass. It will also give some clues on the possibilities of eliminating/reducing the size of spherulites inside the rods.

- Can the spherulites be eliminated/reduced in diameter by changing the casting parameters ?
- Do these changes in the casting process have an influence on the mechanical properties of the BMG ?
- Can heat treatments change the size and crystallography of spherulites ?

Chapter 3 will present the study of the influence of the casting process parameters on the mechanical properties and investigates the "thermal stability" of spherulites. This chapter's discussion will highlight the difficulty in obtaining this alloy in a fully amorphous bulk and the difficulty in controlling suction casting process by arc melter. Despite attempts to customize the structure of this BMG as a composite (amorphous matrix + crystalline spherulite), the chapter will end with a questioning of the choice of alloy composition and the possibility to try others composition in the same atomic system for dental implant manufacturing.

- What is the structure of the alloy in its equilibrium state (fully crystalized alloy) ?
- What phases are present ?
- Are they the same as those of spherulites ?
- What is the corrosion behavior of the equilibrium alloy ?
- Can the chemistry of the equilibrium alloy's phases help us to suggest promising amorphous grades ?

Finally, Chapter 4 will deal with the characterization of the alloy in its equilibrium form, i.e. fully crystallized (master alloy). It will be discussed that behind a complex microstructure different from spherulite, the alloy is polycrystalline and its phases have very different chemical compositions and corrosion resistances. Through the study of the master alloy, we found as an opportunity to do a screening of potential new grades discriminated by electrochemistry. Among the master alloy's phases, some seem promising and will be the subject of a casting test to evaluate their potential to be produced in bulk amorphous form. Finally, a general conclusion will summarize the main results of all the chapters and will attempt to provide a clear and unbiased analysis of the future of the $Ti_{40}Cu_{36}Zr_{10}Pd_{14}$ BMG grade for the manufacture of dental implants. In order to distance

ourselves from the results accumulated during this thesis, perspectives on the future of metallic glasses as a biomaterial will then be proposed.

Materials and Methods

Sample preparation by copper mold suction casting in arc melter

The arc furnace and its operation have already been presented in the introduction of the manuscript (Figures 19 and 20 in Introduction). The illustration of the main steps of sample preparation can be seen in Fig. 30 and describe in details in the next paragraphs [FOR 11].

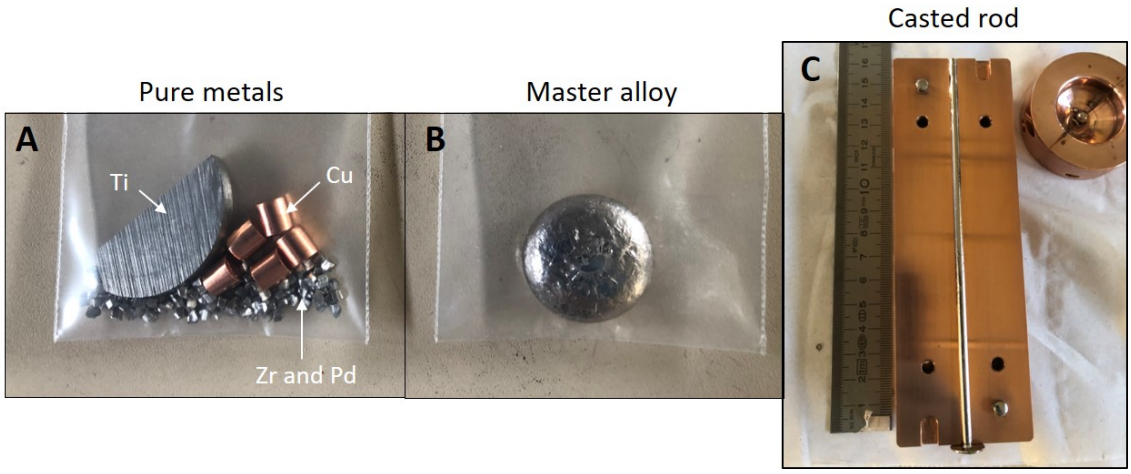

FIGURE 30 – Pictures of the main rod's preparation steps. A) Weighing and cleaning of pure metals. B) Melting and flipping of pure metals to obtain the master alloy. C) Rod's casting by suction.

Conventional protocol of amorphous rods (chapter 1 and 2)

Ingots with a targeted composition of $Ti_{40}Cu_{36}Zr_{10}Pd_{14}$ (at.%) were prepared by arc melting furnace from previously carefully washed pure elements (see Fig. 30A). Rods with 3 mm and 5mm diameter were prepared using a suction copper mold-casting apparatus (Arc melter AM 200, Edmund Bühler GmbH, Bodelshausen, Germany), with a primary vacuum below $5x10^{-2}$ bar and a secondary vacuum below $5x10^{-5}$ bar. Before switching on the electric arc, the chamber was filled with 0.7 bar of high purity Argon atmosphere (Air Liquide). The current intensity was 200A, raw materials were melted and flipped 4 times for 30 seconds each time to obtain the master alloy (see Fig. 30B). The master alloy was melted and flipped again 2 times before suction casting (see Fig. 30C).

Effect of liquid temperature and hydrogen pollution on rods (Chapter 3)

The electric arc intensity effect on the alloy were investigated by using 200A, 300A and 400A (associated with 6 melts and flips). The number of melts/flips were investigated too with comparison of a classic 6 melts/flips and 14 melts/flips before suction.
The role of hydrogen in spherulite apparition was investigated by replacing the classic filling of the chamber with 0.7 bar of high purity Argon atmosphere by 0.7 bar of Argon + 3% of H_2 during the master alloy preparation and casting.

Study of the $Ti_{40}Cu_{36}Zr_{10}Pd_{14}$ master alloy and new BMG compositions (Chapter 4)

Ingots with a targeted composition of $Ti_{40}Cu_{36}Zr_{10}Pd_{14}$ (at.%) were prepared by arc melting from previously carefully cleaned pure elements. $Ti_{40}Cu_{36}Zr_{10}Pd_{14}$ master alloy was prepared using an arc melter (AM 200, Edmund Bühler GmbH, Bodelshausen, Germany), with a primary vacuum below $5x10^{-2}$ mbar and a secondary vacuum below $5x10^{-5}$ mbar. Before switching on the electric arc, the chamber was filled with 0.7 bar of high purity Argon atmosphere. The current intensity was 200A, raw materials were melted and flipped 4 times for 30 seconds each time to obtain the master alloy.
Ingots with three targeted compositions of $Ti_{65}Cu_{21}Zr_4Pd_{10}$, $Ti_{26}Cu_{43}Zr_{15}Pd_{16}$ (at.%) were prepared by arc melting from previously carefully washed pure elements. Rods were prepared using a suction copper mold-casting, with a primary vacuum below $5x10^{-2}$ mbar and a secondary vacuum below $5x10^{-5}$ mbar. Before switching on the electric arc, the chamber was filled with 0.7 bar of high purity Argon atmosphere. The current intensity was 200A, raw materials were melted and flipped 4 times for 30 seconds each time to obtain the master alloy. The master alloys were melted and flipped again 2 times before suction casting in copper mold with various diameter from 1 to 6mm in diameter (see Figure 4.11 in chapter 4).

Elements used and purity

The elements Zirconium and Palladium were purchased from the supplier HMW Hauner. The Zirconium was under granular shape < 3mm and a purity of 99.95%. The Palladium was under granular shape < 3mm and a purity of 99.95%. The copper and Titanium were purchased from Goodfellow. The copper was supplied as small cylinders with a diameter of 5mm and length of 5 mm. The purity of the used copper was 99.995% The Titanium was taken from a bar of 5cm in diameter and cut into slices. The purity of the Titanium was 99.6%.

Material characterization

X-Rays Diffraction (XRD)

After the production of the BMG rods, X-Ray Diffraction (XRD) with a Bruker AXS D8 (Billerica, Massachusetts, USA) device equipped with a copper tube were performed on the samples. The X-Ray tube was set at 4 keV voltage and 4 0mA current with a Cu Kα of 1.54 Å irradiation wavelength. The detector used was a Lynxeye, which was used over a range 2θ from 10 to 90° with an 0.0167° increment, with a slit of 0.4 mm and a scan speed of 1s/step during spinning at 20 rpm. The post-acquisition processing of the diffractograms was conducted on the Eva software (Bruker). The Rietveld method was performed on Topas software (Bruker).

Thermal stability

Differential Scanning Calorimetry (DSC)

A commercial device Setaram Labsys EVO, under argon atmosphere (flow rate of 20 mL/min) has been used for the isothermal measurement of the $Ti_{40}Cu_{36}Zr_{10}Pd_{14}$ BMG systems. The two following cycles from with a first heating step from 40 to 1000°C with heating rates set to 10°C/min to prevent an eventual overshoot from occurring. Then temperature has been maintained during 10 minutes à 1000°C . And finally, the last cooling step from 1000°C to 40°C at 10°C/min. The weighed mass of the unique sample tested was 653 mg.
Before measuring with a BMG sample, a vacuum cycle was systematically performed to establish the baseline which was directly subtracted from the raw curves obtained. T_g, T_x and T_l were determined on the obtained curves as represented in Fig. 31.

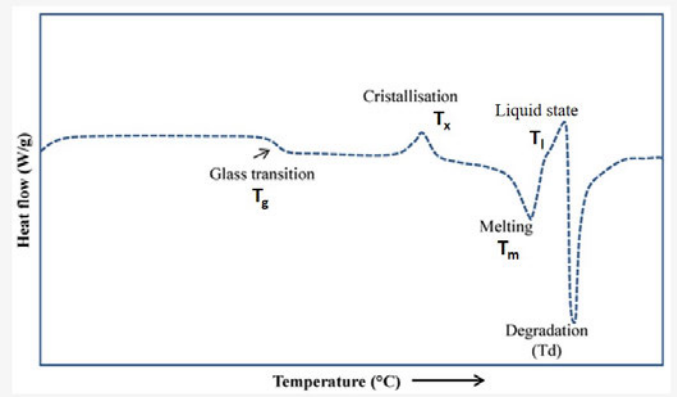

FIGURE 31 – Schematic view of a representative DSC curve where, the specific temperatures position are placed on the curve. Reproduced from [Ley 20]

For the measurement made on the basic composition, presented in Figure 3.11 in chapter 3. The sample was placed in a Alumina crucible(AlO_2) itself placed in another crucible

made of Platinum as recommended by Setaram. Unfortunately, an interaction occurred between the alumina crucible and the metal in the liquid state, making impossible to remove the sample out of the crucibles after the measurement(see Fig. 32A). This did not allow the crucibles to be reused. Ti and Zr rich metals have a very strong affinity with the oxygen in general and there is some oxygen contained in alumina. We believe that the BMG has interacted with the oxygen from the alumina crucible causing a covering of the entire interior of the inner crucible and welding the crucibles and their covers (see Fig. 32B). In order to prevent this phenomenon from occurring again, which can induce artifacts on the curves obtained, it seemed preferable to use the method suggested by Dr.Benedikt Bochtler in his manuscript [BOC 19], i.e. graphite crucibles coated with Yttrium and heat-treated in a vacuum at 1200°C for 1 hour before use. This method should be tested in the future. Albeit the interaction between the sample and the crucibles, the data obtained are thought to give correct values of the key temperature (see results in **Chapter 3**).

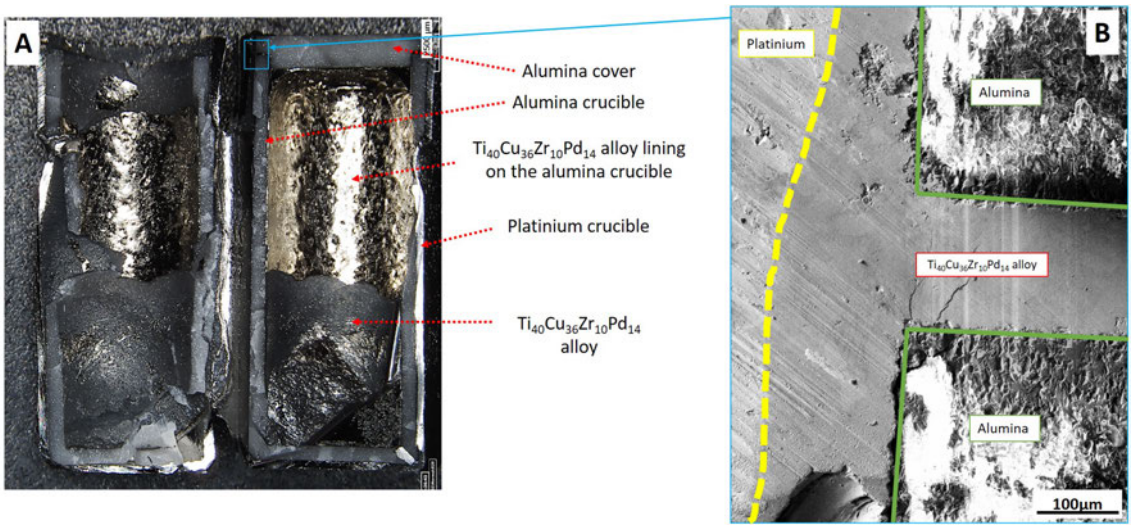

FIGURE 32 – A, picture of the crucibles (Alumina + Platinum) used during DSC analysis of **Chapter 3** open in two parts. B, SEM picture of the of Platinum and Alumina crucible with $Ti_{40}Cu_{36}Zr_{10}Pd_{14}$ alloy after DSC measurements. The $Ti_{40}Cu_{36}Zr_{10}Pd_{14}$ alloy passed between the crucible and the alumina cover and welded to the platinum crucible during cooling.

Salt bath heat treatments

The heat treatments were all carried out on pieces of 3mm diameter as cast rods of the $Ti_{40}Cu_{36}Zr_{10}Pd_{14}$ grade (manufactured in standard condition). The pieces were immersed in a salt bath previously set at the chosen temperature: 450°C, 500°C, 550°C and 600°C for 1 hour.

Microscopy

Optical Microscopy (OM)

Optical microscopy observations were conducted after different polishing steps on a Buehler semi-automatic polishing machine Ecomet 250 (Esslingen, Germany), first with SiC papers successively with grains of # 600, # 800, # 1200 and # 2500. The final mechano-chemical polishing step was performed on a Buehler ChemoMet synthetic polishing pad with a solution made of 75% of colloidal silica suspension (OP-S,Struers) and 25% H_2O_2(ChimiePlus). Observations were realized using an Hirox RH-2000 digital microscope (River Edge, NJ, USA).

Scanning Electron Microscopy (SEM)

The observations of polished surfaces were carried out by Scanning Electron Microscopy (Zeiss Supra 55, Oberkochen, Germany), in backscattered electron imaging (BSE) using an acceleration voltage ranging from 10 to 30 keV, after polishing using silica suspension and 25% H_2O_2 (as described before in OM).

Energy-Dispersive X-ray Spectroscopy (EDXS)

To ensure that the composition of each sample was consistent with the desired one and that no vaporization of elements had occurred during the master alloy's processing, the composition of all the cast rods were controlled by Energy Dispersive X-Ray Spectrometry (EDXS) using a 50mm^2 Silicon Drift Detector (Oxford Instruments, High Wycombe, UK) in the SEM at an acceleration voltage of 20 keV. Moreover, EDXS was used to quantify the chemical composition of the different phases that were present.

Electron Back Scattered Diffraction (EBSD)

EBSD analyses were made with an Oxford Instruments EBSD Symmetry camera (Abingdon-on-Thames, UK) with an accelerating voltage of 10 or 20 keV, depending on the step size required. The EBSD data were post-processed using ATEX [BEA 17]. Phase identification in the case of a non-equilibrium state with four different components is a difficult task. This study was focused on a detailed description of the microstructure of the spherulites in order to better understand their nucleation and growth mechanism, using usual electron microscopy observations techniques. In order to determine non-referenced phases, dedicated methodology and instrument are required, which were not available in the case of those observations. Therefore, in order to find possible candidates for the different phases that were observed, as in [YAN 11] the strong hypothesis was made, which is that the minor elements (Zr and Pd) would be in substitution for the major elements (Cu and Ti). This rather strong assumption was necessary to identify possible candidates, from the Cu-Ti system, among all possible structures from the literature. It is worth

noting that this assumption is quite classical and can be found in literature on alloys with a composition close to the one studied here [YAN 11][FOR 11][MAR 87] .
Phase identification was performed using the phases presented in Tab. 4.

TABLE 4 – Candidate phases (phase name, spacegroup, a, c, references) used during this study.

Phase name	Spacegroup	a(Å)	c(Å)	References
Cu_3Ti_2	I4 m m m	3.14	13.962	[ERE 66]
tetragonal CuTi	P4/m m m	3.14	2.856	[KAR 51]
$CuTi_3$	P4/m m m	4.158	3.594	[KAR 51]
CuTi-B2	Pm-3m	3.14	3.14	[Zha 94] from CuZr adjusted

Transmission Electronic Microscopy (TEM)

The FIB thin foils were prepared on a FEI Strata DB 235 at IMEN laboratory (Lille, France), using a Ga FIB source. Transmission Electron Microscopy observations were realized on a JEOL 2010F TEM operating at 200 kV, equipped with a 60mm^2 Oxford Instrument EDXS detector. The results are presented in **chapter 2**.

ASTAR

At the TEM scale, orientation maps were acquired with the ASTAR system from NanoMEGAS SPRL (Brussels). With this TEM attachment, the electron beam is scanned over the area of interest and the successive diffraction patterns are recorded with an optical camera and memorized. Phase and/or orientation maps are reconstructed by indexing the patterns with a dedicated template matching algorithm [RAU 14]. ASTAR acquisitions were performed on a field-emission transmission electron microscope at 200 kV at SIMAP Lab(JEOL 2100F). The results are presented in **chapter 2**

Chemical Analysis: Time of Flight - Secondary Ion Mass Spectrometry (Tof- SIMS)

The Tof-SIMS experiments were done by SCIENCE ET SURFACE company (www.science-et-surface.fr). A piece of polished $Ti_{40}Cu_{36}Zr_{10}Pd_{14}$ BMG with spherulites on the surface was provided to the company. Tof-SIMS is a technique in which an ion beam (primary ion) is irradiated on a solid sample and mass separation of the ions emitted from the surface (secondary ions) is performed using the difference in time-of-flight treated by mass spectroscopy. Prior the analysis, an in-situ ionic cleaning was carried out to remove organic contamination from the surface. The determination of the nature of the chemical compounds present on the surface of the samples of a whole spherulite in positive and negative polarity were done. The results are presented in **chapter 3**.

Hydrocarbon, oxidized species, nitrogen, phosphorus, sulphurs and halogens are preferentially detected in negative polarity, metals and alkalis in positive polarity.

Mechanical properties

Vicker's Hardness

The hardness measurements were performed on a Buehler Micromet 5140 machine (Esslingen, Germany). The samples were first mirror polished and the measurements were conducted with a load of 0.5kgF for **chapter 1 and 3**. They were repeated fifteen times on the spherulites and on the amorphous matrix. For the **chapter 4**, loads of 0,3kgF and 1kgF were used and 10 measurements per condition were done.

Compressive tests

The compression tests were conducted on 6 cylindrical samples of 3mm diameter and 5mm height for **chapter 1 and 3**. The tests were performed on an INSTRON 5967 machine (Nordwood, USA) with an optical extensometer and a 30kN load cell. The displacement rate was fixed at 0.5mm/min.

Tensile tests

Tensile tests were performed on the same machine used for the compressive tests (INSTRON 5967). To avoid premature specimen's failure in conventional jaws, a self-aligning fixture (with an additional degrees of freedom) was used and the edges of the specimens were threaded for this test (see Fig. 33). The test specimens were machined in a dog-bone shape, with a working part of 5mm long (for a total length of 20 mm) and a diameter of 2.46 mm. The test speed was set to 0.058 mm/s.

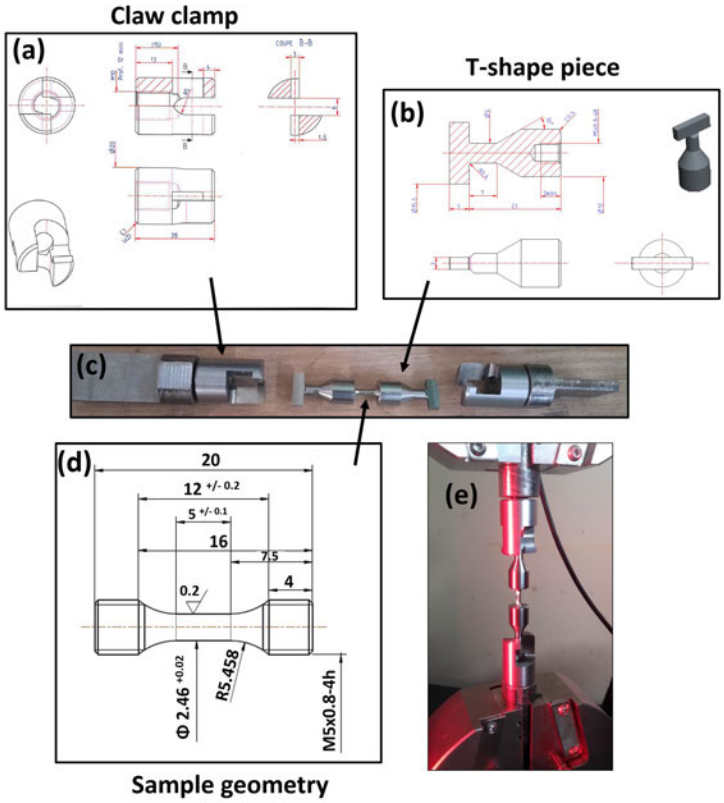

FIGURE 33 – Reproduced from [LIE 19]. Geometries of (a) the claw clamp piece, (b) the T-shaped piece and (d) a tested sample used during tensile tests. Image of the all general set up before (c) and during testing (e).

ISO 14801: Load to failure and fatigue tests on dental implant representative sample

Mechanical characterization and evaluation of the load to failure of reference implant representative samples (call hereafter REPSAMPLES) were evaluated on a BOSE ELF3300 testing machine (New Castle, PA, USA) following the geometrical specifications of ISO 14801 (displacement rate of 5 mm/min)[DAM 96]. The geometry of the samples consisted in an outer diameter: ⌀2.8 mm and ⌀2.3 mm in the deeper thread. They were embedded in a resin having a Young's modulus of 7 GPa after polymerization (Rencast© Resin, HUNTSMAN) and with 3 mm of non-impregnated threads simulating bone resorption. Hemispherical caps were sealed onto the top of the sample in order to ensure a constant lever arm of 11 mm on each assembly for mechanical testing. Which is achieved through a force applied at 30° to the longitudinal axis of the implant (picture of the assembly visible in Figure 1.10 in chapter 1).
Fatigue tests were performed using the same machine and geometry described in the previous paragraph. REPSAMPLES were tested in air at room temperature with a frequency

of 15 Hz. A sinusoidal load between 0.1 and 1 times the maximum applied load was used. The fatigue limit was set to 5x10^6 cycles in this case, if no failure occurred at 5x10^6 cycles, then the maximum load was increased by 10 N. The test was following the IACS UR M53 Appendix IV standard. The fatigue fracture surfaces were observed by SEM in order to identify the fracture initiation and behavior.

Toughness evaluation: Single Edge V Notched Bending (SENVB)

To determine the toughness of the material, a method known and considered to be accurate and reliable for materials with brittle behavior was used, namely the Single-Edge V-Notched in Bending (SEVNB) method [DAM 96]. For this purpose, 3 samples with a rectangular cross-section were notched with a femtosecond laser to a known depth with 16 passes of 50 μJ infrared ultra-short laser pulse. The use of the laser leads to much finer and sharper notches than can be obtained with a more traditional method such as razor notching [Tur 14]. The dimensions of the specimens were as follows: length 25 mm, width 2 mm and thickness 4mm. The notch length was comprised between 210 and 250 μm with a very sharp notch tip radius (around 5 μm). The specimens were tested at 0.5 mm/min on a four-points bending test until failure. From the load to failure values, it is possible to calculate the critical stress intensity factor K_{IC} by knowing the notch length:

$$K_{IC} = \frac{3 \cdot F \cdot (L - l)}{2 \cdot b \cdot W^2} \cdot Y \cdot a \tag{1}$$

Where L and l are the outer and inner spans (21 and 10mm, respectively), b is the thickness of the samples (4mm), W is the width (2mm). F is the load to failure in N and a is the notch length in mm (measured precisely for each sample). Y is a constant defined by the following formula:

$$Y = \left(\frac{1.1215\sqrt{\pi}}{\beta^{\frac{3}{2}}}\right) \cdot \left[\frac{5}{8} - \frac{5}{12}\alpha + \frac{1}{8}\alpha^2\beta^6 + \frac{3}{8}e^{-6.1342\frac{\alpha}{\beta}}\right]$$

With

$$\alpha = \frac{a}{W}$$

and

$$\beta = 1 - \alpha$$

Four-point bending tests (4PB)

Four-point bending tests were performed on machine (INSTRON 8562). The test specimens were machined (3mm as cast rods) to 2,8mm in diameter (for a total length of 35 mm). The test speed was set to 0.5 mm/s. The spacing between the lower rollers of the assembly was 21mm and 10mm between the upper rollers. The following Fig. 34 is a scheme

of the used assemble with a representation of the upper face solicited in compression and the lower face under tension.

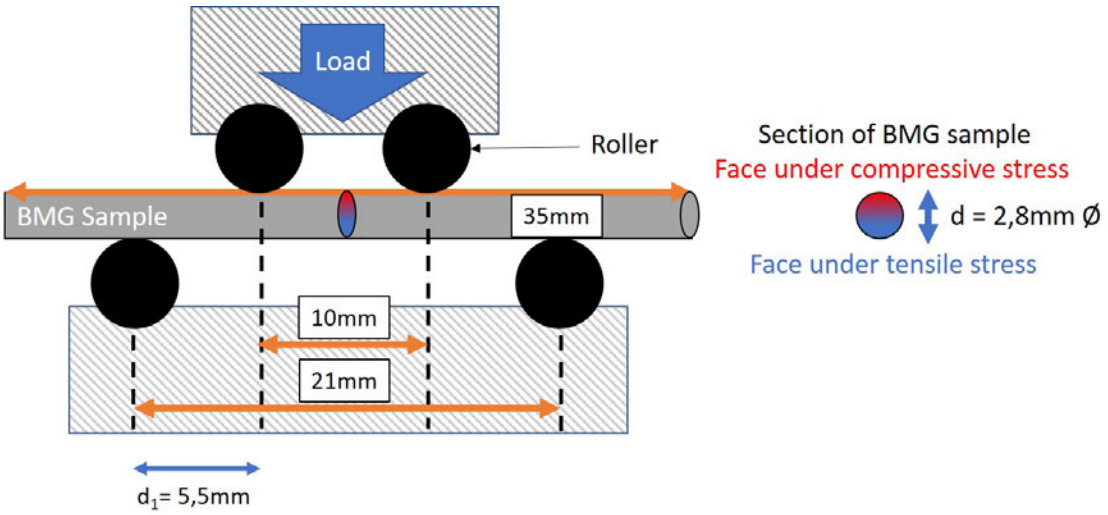

FIGURE 34 – Schematic illustration of the four points bending test assembly used in **Chapter 3**. All dimensions of the assembly and samples are shown in the image. The dimensions d and d_1 are mandatory to access the stress applied during the test, d = 2.8mm is the cylindrical specimen diameter and d_1 is the space between the upper and lower rollers.

Where d and d_1 are respectively the diameter of the samples (2.8mm) and the difference of spacing between the upper and lower rollers (5.5mm). F_m is the load to failure in N. The calculation of the stress for four-point bending test(σ_{4PB}, MPa) is given by the following relation (ISO 3327):

$$\sigma_{4PB} = \frac{16 F_m d_1}{\pi d^3} \tag{2}$$

X-rays tomography

Prior to mechanical four-point bending test to avoid premature failure due to large porosities or heterogeneities in the specimens, the casted rods were characterized by X-rays Tomography. Fast acquisitions, were done using a VtomeX (GE Phoenix-Xray GmbH, Boston, MA, USA) with a voxel resolution of $3\mu m^3$. The specimens were cut in defect-free areas after observations. The relevance of X-ray tomography for studying metallic glasses is presented and further discussed in Appendix A.

Electrochemical characterizations

Macroscopic corrosion behavior (polarization curves)

The assembly of the classic a three electrodes electrochemical assembly for voltammetric analysis, using a Gamry instrument 600+ potentiostat (Philadelphia, Pennsylvania, USA) with graphite rod as counter electrode and an Ag/AgCl ($E_{Ag/AgCl}$= 224 mV vs Standard Hydrogen Electrode at 25°C) as reference electrode (as illustrated in Fig. 35(a)). Prior to electrochemical measurements, both BMG and reference samples (TA6V) rods of 5mm in diameter were polished using abrasive papers down to #2500 in order to obtain a smooth surface before the test. In order to expose only a known surface of the rod (rod 's section around 19.63mm^2), the rod is embedded in a non conductive transparent resin (ClaroCit, Struers) and linked to the installation by a copper wire (see Fig. 35(b)). An aerated and neutral saline solution composed by 0.9% of NaCl (pH= 7.4) at 37°C was used as the electrolyte. This solution was chosen as it is recommended in the ISO 10271 standard, dedicated to the corrosion test methods for metallic materials used in dentistry. As the susceptibility of passive material to localized corrosion is directly affected by the presence of chloride ions, saline solution is an adequate electrolyte to measure such a property. Before starting the test, the sample edges were covered with varnish to prevent electrolyte from leaking between the resin and the edge of the sample. and taken in picture in optical microscopy to determine precisely the sample's surface. Before plotting the polarization curves, open circuit potential (OCP) measurements were performed during 6 hours to achieve the steady-state in the NaCl solution. Then, a linear polarization with a scan rate of 0.17 mV/s, from -0.5 V vs Ag/AgCl to +1 V vs Ag/AgCl. The corrosion potential (E_{corr}), the pitting potential (E_{pit})and the passive current density were estimated from the polarization curves. After the tests, the surfaces were observed with SEM, to characterized the corroded surface morphology. The curves corresponding to this test are already published in [LIE 18]. The results are presented in **chapter 1 and 4**.

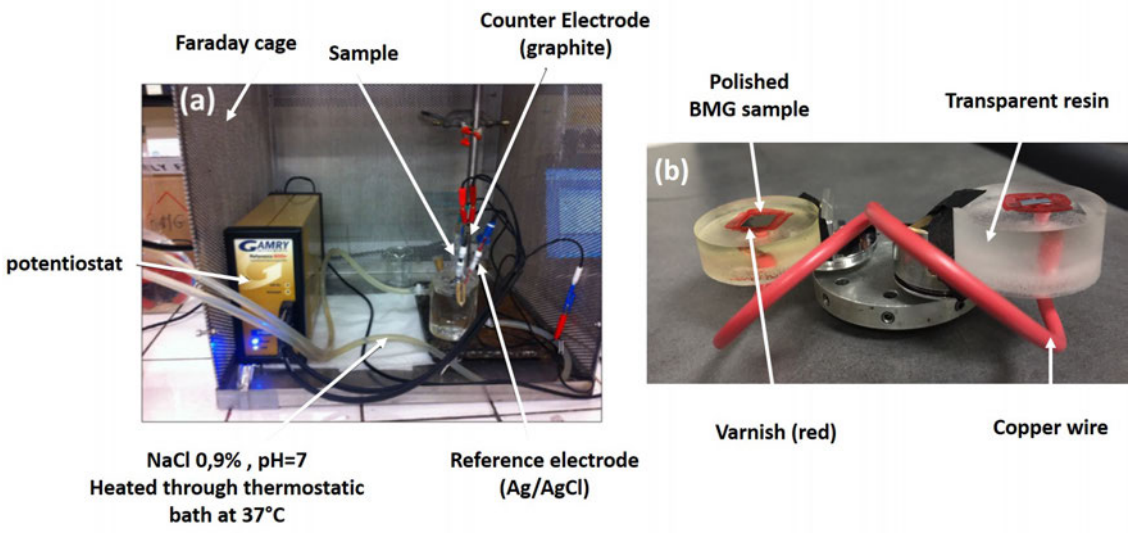

FIGURE 35 – (a) Picture of the three electrodes assembly used during the PhD to study corrosion resistance following the standard ISO 10271. (b) Zoom on two sample's aspect (embedded in transparent resin) and electrically linked to the assembly by a copper wire.

Local electrochemical behavior (Microcell)

The local measurements are based on the same principle as described in the previous paragraph (Macroscopic corrosion behavior), the main difference is the reduction in size of the measuring area (working electrode). This technique makes possible the electrochemical analysis of selected small areas (about 50 μm in diameter maximum) such as a single heterogeneity size. It is possible to study these very small areas via the preparation of tight stretched glass capillaries (with silicone gasket at the end of the capillary in this study). To do so, capillaries of 1mm diameter in borosilicate were hot stretched with a capillary stretching machine [AND 16]. Then, the ends of the capillaries were hand-polished (with a sheet of wet SiC #1000 to have a surface at 90° to the long axis of the capillary) to have a disc shape for the opening of the capillary. The diameter of the capillary opening corresponds to the metallic glass area exposed to the electrolyte which can have a diameter from 20 to 50μm (controlled by optical microscopy). To ensure a good contact between the sample and the capillary and ensure the water tightness, silicone gasket is obtained by repeating back and forth with the end of the capillary at 90° of a silicone layers, between each back and forth, ethanol and water are injected successively with a syringe into the capillary to ensure its opening. The capillary is considered ready for measurement when the silicone seal is about 30μm on each side of the capillary. Then, the capillary is put in place and filled by the electrolyte, as well as the electrochemical cell containing the working electrode and the counter-electrode (here Platinum). The reference electrode (Ag/AgCl) is outside the cell, but connected to the assembly by a pipe filled with electrolyte opening into the cell. The experiment assembly is presented in Fig. 36.

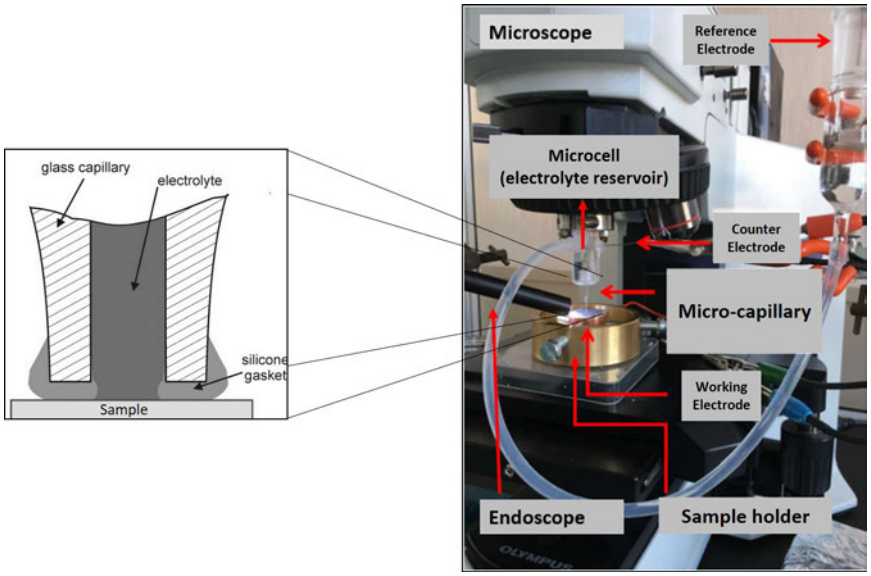

FIGURE 36 – On the left, scheme reproduced from [AND 16] illustrating the contact between sample's surface (here BMG) and the stretched end of the glass capillary containing the electrolyte (here NaCl 0.9%), the water tightness between sample and electrolyte is guaranteed by a silicone gasket. On the right, picture of the entire microcell assembly used during this PhD.

The local electrochemical equipment was connected to a Gamry Instrument Reference 600+ potentiostat (Philadelphia, Pennsylvania, USA). Prior to electrochemical measurements, BMG samples were ground using abrasive papers, followed by colloidal silica suspension as previously described in order to see clearly the spherulites on the 5 mm in diameters BMG rods. The NaCl 0,9% solution was also used for this test. Before potentiodynamic polarization measurements, OCP measurements were performed during 30 min to stabilize the samples in the saline solution. Finally, linear polarization was performed, with a scan rate of 0.17 mV/s from anodic -0,4 V vs Ag/AgCl to 0,8 V vs Ag/AgCl. The corrosion potential (E_{corr}), the pitting potential (E_{pit}) and the passive current density were estimated from anodic polarization curves. After the tests, the surfaces were observed with optical microscopy to check the change of the surface state. Six measurements on the amorphous matrix and 6 measurements on the spherulites (measurement considered in relation to the OCP values were realized). The results are presented in **chapter 1**.

Interrupted tests (cyclic polarization)

Complementary tests was performed on a sample with another surface preparation to highlight the nucleation of the pitting phenomena. The samples were polished using abrasive papers down to #2500 and by a final step with OP-S 75% and H_2O_2 as in Microscopy section above in this chapter. Then, the corrosion potential was measured during 30 min to stabilize the sample's potential in the saline solution. Finally, cyclic

polarization was performed, with a scan rate of 0.17 mV/s from anodic -0,2 V vs Ag/AgCl to 0,5 V vs Ag/AgCl with a maximum of current density (threshold value) set to $0.5 A/cm^2$ in chapter 1 and to $1 mA/cm^2$ in chapter 4: just start the pitting phenomenon and then the potential was reversed with the decrease of the current density. This method was used for **chapter 1 and 4**. .

Statistical methods

Saltykov's method

In this study, the mean diameter of the spherulites could not be defined through 3D measurements and only 2D images of the samples were available. X-Ray Tomography was indeed tested, but there was no density contrast between the spherulites and the amorphous phase. Saltykov's method [SAL 58] was performed on these 2D observations, with statistical coefficients to correct the measurement's bias and obtain an average diameter closer to reality. The results are presented in **chapter 1**.

F-Test to Compare Two Population Variances

An F-test (Snedecor and Cochran, 1989 [SNE 89]) is used to test if the variances of two populations are statistically equal or different. The two-tailed version tests against the alternative that the variances are not equal. Below are described the formulas used to calculate the mean and the variance on the observations made in **chapter 3**. The assumption of the normal distribution of the variables was made. The tested hypothesis are:

$$H_0 : V_x = V_y$$

$$H_1 : V_x \neq V_y$$

V_x and V_y are the variances of the population X and Y.
First step to make an Equality of Two Variances test is to calculate the mean ($\bar{x}$) of the variable studied by following the next formula:

$$\bar{x} = \frac{1}{n}\sum_{i=1}^{n} x_i$$

Then, the Variance formula is as follow:

$$V_x = \frac{1}{n}\sum_{i=1}^{n}(x_i - \bar{x})^2 \tag{3}$$

V_x is the sample variance of population X . Then the test statistic corresponds to:

$$F_{obs} = \frac{V_x}{V_y}$$

X and Y populations have F-distributions with n_x-1 (population X) and n_y-1 (population Y) degrees of freedom if the null hypothesis of equality of variances is true. Otherwise it follows an F-distribution scaled by the ratio of true variances. The null hypothesis is rejected if F is either too large or too small based on the desired α level (i.e., statistical significance) so:

$$If F_{obs} \notin \left[f_{\frac{\alpha}{2}}(n_x - 1; n_y - 1); f_{1-\frac{\alpha}{2}}(n_x - 1; n_y - 1) \right] \quad (4)$$

We reject H_0 at the risk threshold α, otherwise we are not in a position to reject H_0 so the variances are not considered to be different. For all the tests in **chapter 3**, the risk threshold $\alpha = 0.05$.

The following table contains the upper critical values of the F distribution. This table is used for one-sided F tests at the $\alpha = 0.05$ level.

TABLE 5 – This table is used for one-sided F tests at the $\alpha = 0.05$ level.

n_x/n_y ↓	**11**	**12**	**13**	**14**	**15**	**16**	**17**	**18**	**19**	**20**
1	242,983	243,906	244,69	245,364	245,95	246,464	246,918	247,323	247,686	248,013
2	19,405	19,413	19,419	19,424	19,429	19,433	19,437	19,44	19,443	19,446
3	8,763	8,745	8,729	8,715	8,703	8,692	8,683	8,675	8,667	8,66
4	5,936	5,912	5,891	5,873	5,858	5,844	5,832	5,821	5,811	5,803
5	4,704	4,678	4,655	4,636	4,619	4,604	4,59	4,579	4,568	4,558
6	4,027	4	3,976	3,956	3,938	3,922	3,908	3,896	3,884	3,874
7	3,603	3,575	3,55	3,529	3,511	3,494	3,48	3,467	3,455	3,445
8	3,313	3,284	3,259	3,237	3,218	3,202	3,187	3,173	3,161	3,15
9	3,102	3,073	3,048	3,025	3,006	2,989	2,974	2,96	2,948	2,936
10	2,943	2,913	2,887	2,865	2,845	2,828	2,812	2,798	2,785	2,774
11	2,818	2,788	2,761	2,739	2,719	2,701	2,685	2,671	2,658	2,646
12	2,717	2,687	2,66	2,637	2,617	2,599	2,583	2,568	2,555	2,544
13	2,635	2,604	2,577	2,554	2,533	2,515	2,499	2,484	2,471	2,459
14	2,565	2,534	2,507	2,484	2,463	2,445	2,428	2,413	2,4	2,388
15	2,507	2,475	2,448	2,424	2,403	2,385	2,368	2,353	2,34	2,328
16	2,456	2,425	2,397	2,373	2,352	2,333	2,317	2,302	2,288	2,276
17	2,413	2,381	2,353	2,329	2,308	2,289	2,272	2,257	2,243	2,23
18	2,374	2,342	2,314	2,29	2,269	2,25	2,233	2,217	2,203	2,191
19	2,34	2,308	2,28	2,256	2,234	2,215	2,198	2,182	2,168	2,155
20	2,31	2,278	2,25	2,225	2,203	2,184	2,167	2,151	2,137	2,124

Chapter 1

Impact of spherulite-type crystalline defects on the mechanical and electrochemical properties of $Ti_{40}Cu_{36}Zr_{10}Pd_{14}$ metallic glasses

One of the limitations to the use of certain bulk metallic glasses is related to the formation of crystalline zones or defects, often called “spherulites ”, during the casting process. In the case of $Ti_{40}Cu_{36}Zr_{10}Pd_{14}$ (at.%) metallic glass, which is a candidate for biomedical applications, spherulites of diameter up to few hundreds of microns were previously reported, but their crystallographic features and their role in the mechanical behavior and the corrosion resistance remains to be determined. In this work, a detailed description of the microstructure of spherulites is provided. Tensile, compression and fatigue tests were carried out. In addition, corrosion behavior was studied by global and local electrochemical measurements. The spherulites have a deleterious effect on the tensile and fatigue strength of the alloy, even if it still retains strength properties that are far superior to conventional crystalline materials. The electrochemical studies do not show any difference in potential between the spherulite and the amorphous matrix, which indicates that the presence of spherulites is probably not the direct cause of the pitting phenomenon observed, which is unfortunately a clear drawback of this alloy when considering biomedical implants.

1.1 Introduction

There are only few articles in the literature dealing with spherulite crystalline defects in amorphous metals. This might be in part due to the use of X-Ray Diffraction, generally used to check if cast rods are amorphous or crystalline. In most cases, samples having diffractograms that show broad halo without any distinct peaks originating from the crystalline phase are considered as 'amorphous' [YAM 14] [LIE 18]. This macroscopic characterization may not be precise enough to assess the presence of spherulites in small overall content. Another possible origin to the low number of publications concerning spherulites is the difficulty of observing them before and after mechanical testing. In most studies on Bulk Metallic Glasses (BMG), the authors focus on compression tests. However, it was shown in [LIE 18] that casting defects in the $Ti_{40}Cu_{36}Zr_{10}Pd_{14}$ grade were not visible on the fracture surface of parts tested in compression, whereas they were clearly visible on samples tested in tension [LIE 18][ZHA 03a]. These defects can be large in size, randomly distributed and can therefore negatively affect the mechanical properties of the material [LIE 18][YOK 15][HIN 19], in particular by causing premature failure in tension and/or cyclic fatigue. The presence of spherulites may have a negative effect on fracture toughness, as it was shown in three points bending test on pre- cracked samples of an ZrCuAlNi BMG [HIN 19][BER 20]. On the other side, some authors consider the presence of a crystalline phase surrounded by an amorphous matrix as an opportunity to improve the mechanical resistance of BMGs. It has been reported in the literature [PAU 09] [LIU 12b][KIM 18] mainly on CuZr(Ti or Al) ternary alloys, that there is a spontaneous formation of a B2 phase during the casting of rods, if the crystalline particles are controlled in size and homogeneously distributed in the parts, can bring ductility and thus improve the usual usual brittle behavior of this grade. If few papers are dealing with

a deep characterization of spherulites in some BMG and others tend to show that they may have an effect on mechanical properties, there is not so far, a comprehensive characterization in $Ti_{40}Cu_{36}Zr_{10}Pd_{14}$ alloys, while they are often cited as promising candidates for biomedical applications [LIE 18][ZHU 07a]. This publication therefore aims at highlighting the presence (by a morphological and chemical characterization) of spherulite-type crystalline defects in the widely studied $Ti_{40}Cu_{36}Zr_{10}Pd_{14}$ (at.%) grade and their influence on the overall material's mechanical properties and corrosion resistance.

1.2 Results

1.2.1 Microstructural observations

1.2.1.1 Optical microscopy

With the polishing protocol set up for this study, the 'spherulites' are easily visible under light microscopy as shown in Fig. 1.1. Most of them exhibit a spherical shape, with a clear interface with the amorphous matrix. Their diameter is relatively large, reaching several hundreds of μms. At high magnification, some details of the microstructure can be seen: in the center of the spherulites, very fine needles can be seen, looking like dendrite or martensitic phases. This could be due to a preferential growth direction of theses structures from the core to the periphery of the spherulites. Closer to the interface with the matrix, the microstructure of the spherulite becomes less clear. These observations show that the spherulites are likely crystalized. Moreover, two different gray levels in the spherulite on the right picture can be distinguished, which could correspond to different crystalline phases or crystallographic orientations contrasts.

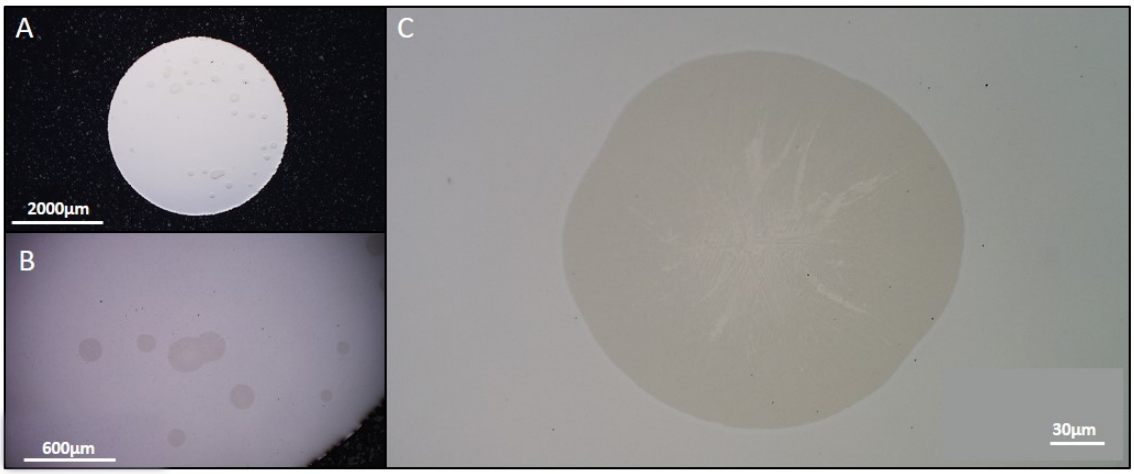

FIGURE 1.1 – Optical microscopy observations of the TiCuZrPd Bulk Metallic Glass after mechano-chemical polishing with colloidal Silica, showing several spherulites. (A) Global sample appearance. (B) Zoom on the lower part of the rod. (C) High magnification picture of a spherulite.

1.2.1.2 Statistical analysis of mean spherulite diameter

In this study, the mean diameter of the spherulites could not be defined through 3D measurements and only 2D images of the samples were available. X-Ray Tomography was indeed tested, but there was no density contrast between the spherulites and the amorphous phase. Saltykov's method [SAL 58] was performed on these 2D observations, with statistical coefficients to correct the measurement's bias and obtain an average diameter closer to reality. The results shown in Fig. 1.2 suggest a mean diameter around 150 μm,

some spherulites being of several hundreds of microns in size. Moreover, the observations did not show any preferential location of the spherulites in the sample (no difference between the core and the periphery of the rods).

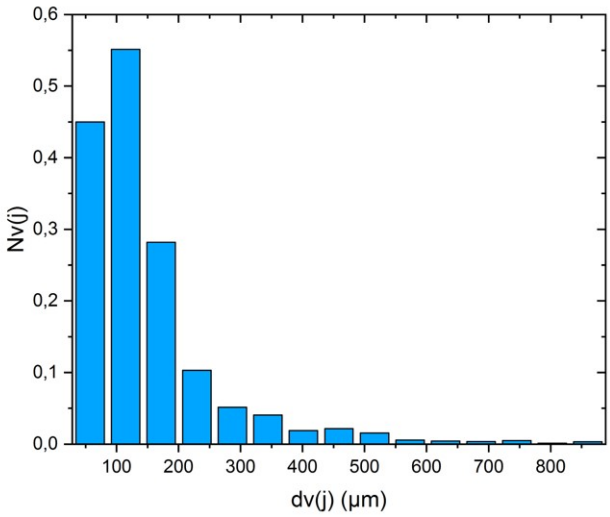

FIGURE 1.2 – Histogram of spherulites dimensions, analysed by the Schwartz-Saltykov method [SAL 58].

1.2.1.3 XRD analysis

In most studies involving metallic glass [CAL 03][ZHU 12][HUA 20], XRD is used as a mean to check the amorphous state of the parts before conducting further experiments. This conventional method was used on a rod of the TiCuZrPd grade, which after polishing exhibited a lot of spherulites in optical microscopy (around 40 spherulites on a surface of around 19.6 mm^2, which is around 2 spherulites by mm^2 , see Fig. 1.1). The diffractogram shown in Fig. 1.3 presents only broad halos with the absence of well-defined peaks. Thus, it could be considered as characteristic of an amorphous metal alloy, even though the presence of numerous spherical defects was noticed on the sample's surface. The surface percentage occupied by spherulites on this sample has been calculated and it is equal to 1.2%, which represents a low fraction of global surface thus too small to be detected by XRD. This sheds a light on the limit of standard XRD to detect spherulites in such BMG systems.

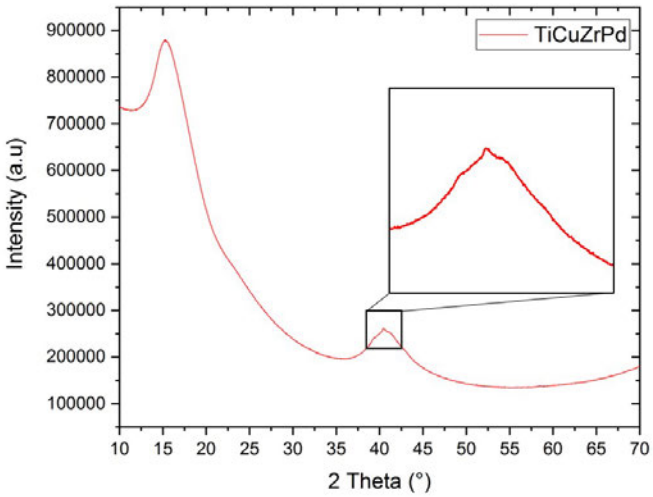

FIGURE 1.3 – XRD pattern of the $Ti_{40}Cu_{36}Zr_{10}Pd_{14}$ BMG between $10° < 2\,\theta < 70°$. The presence of spherulites is hardly visible, except if a careful analysis of the 41° broad halo is conducted, which may suggest a small crystalline fraction.

1.2.1.4 Scanning electronic microscopy (SEM)

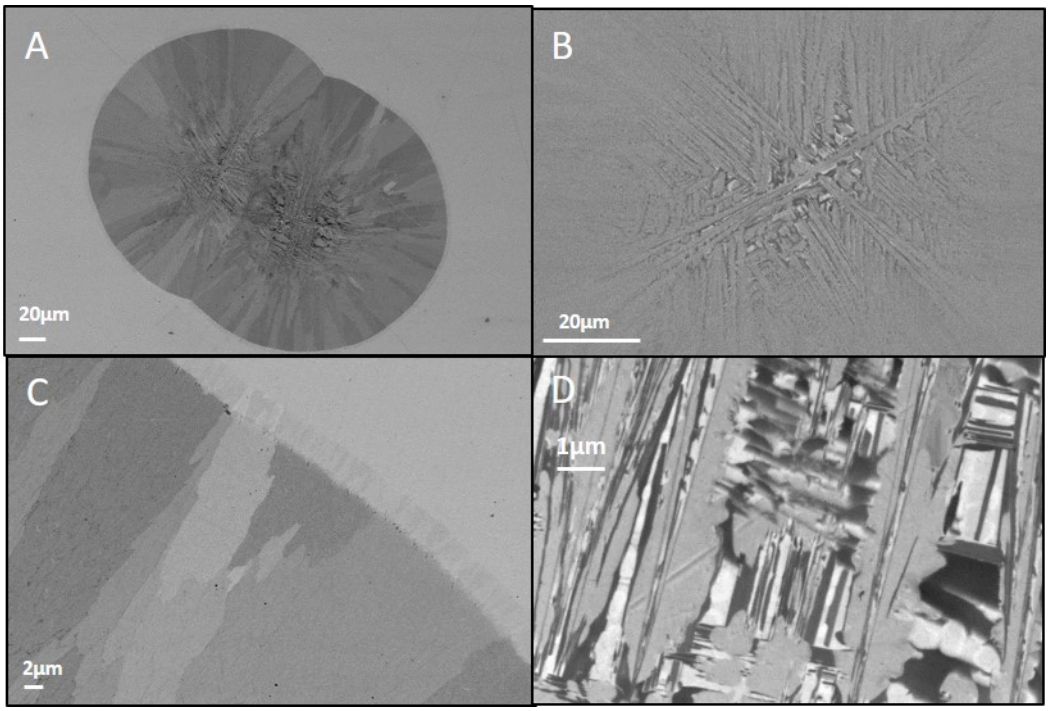

FIGURE 1.4 – SEM-BSE (Back Scattered Electron mode) images of spherulites. (A) Global view of two adjacent spherulites. (B) Higher magnification of the needles in the center part of a spherulite. (C) Higher magnification of spherulite/matrix interface, which shows a 'shell' around the spherulite. (D) Close look at the center of the spherulite, showing different types of needle-shape crystals.

Fig. 1.4 gathers several SEM pictures of spherulites at different magnification. The observations of SEM pictures suggest three successive distinguishable zones of the spherulite's microstructure. From the center to the periphery:

1. Well delimited needles/slats that go in all directions of the space, which were already observed by optical microscopy (Fig. 1.1), the three gray contrasts being either due to differences of composition or to different orientations ('channelling' of the electrons);
2. Then the microstructure refines as a transition phase with very small grains then large and elongated grains with different gray contrasts (different orientations or compositions);
3. Finally, the presence of a thin shell with an average thickness of 3.7 μm ($\pm$ 1.2 μm). consisting of columnar nano-grains.

1.2.1.5 Electron backscatter diffraction (EBSD)

Due to the complex composition of the alloy and of the out-of-equilibrium processing method, the exact phase(s) present are not known. However, it was possible to index the major portion of the spherulite grains by declaring a simple cubic crystalline phase with parameters corresponding to a B2 CuPd phase, with a Face-Centered Cubic (FCC) lattice type and a space group Fm-3m (225). The dimensions of the lattice are a = b = c = 3.766 Å, $\alpha = \beta = \gamma = 90°$ and the unit cell volume is 53.41 $Å^3$. EBSD is not a phase identification tool and here it is only possible to conclude that de main crystalline phase of the spherulite is probably FCC with a lattice parameter close to 3.766 Å. The map shown in Fig. 1.5, positioned on a spherulite's quarter, indicates that the grains are well indexed and mostly oriented towards the [0 0 1] planes. The map of local disorientation indicates values between 0.5 and 2° of disorientation (with a maximum occurrence at 0.6°). Moreover, it can be seen that the shell has not been indexed either probably because the size of the crystals is too small or it is constituted by another crystalline phase.

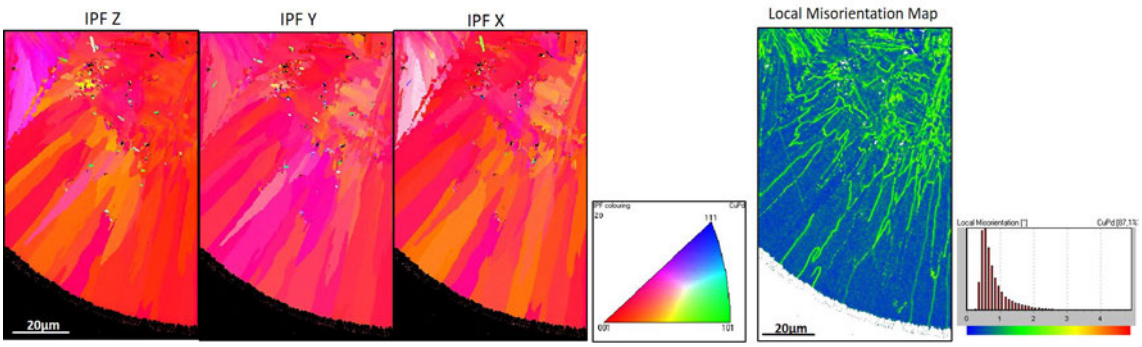

FIGURE 1.5 – (Left) IPF representations of EBSD map of a part of spherulite. The only visible indexed phase is CuPd. (Right) Corresponding local misorientation map.

1.2.1.6 Energy dispersive X-ray spectroscopy (EDXS)

Fig. 1.6 shows the atomic surface distributions superimposed with SEM images of the microstructure of the spherulites. A spatial atomic segregation of the constituent elements of the alloy can be seen on the "needle "part at the center of the spherulite. Three phases may be distinguished from this map (top left): Palladium rich lamellae, an intermetallic (interdendritic) Zirconium rich phase (light gray) and finally another intermetallic CuTi rich phase (dark gray). On the other maps, this segregation is only slightly or not visible at all. It leads to the conclusion that segregation is occurring mainly at the center of the spherulite whereas the outer part is more homogeneous in chemical composition. At the interface with the amorphous part, no segregation can be seen.

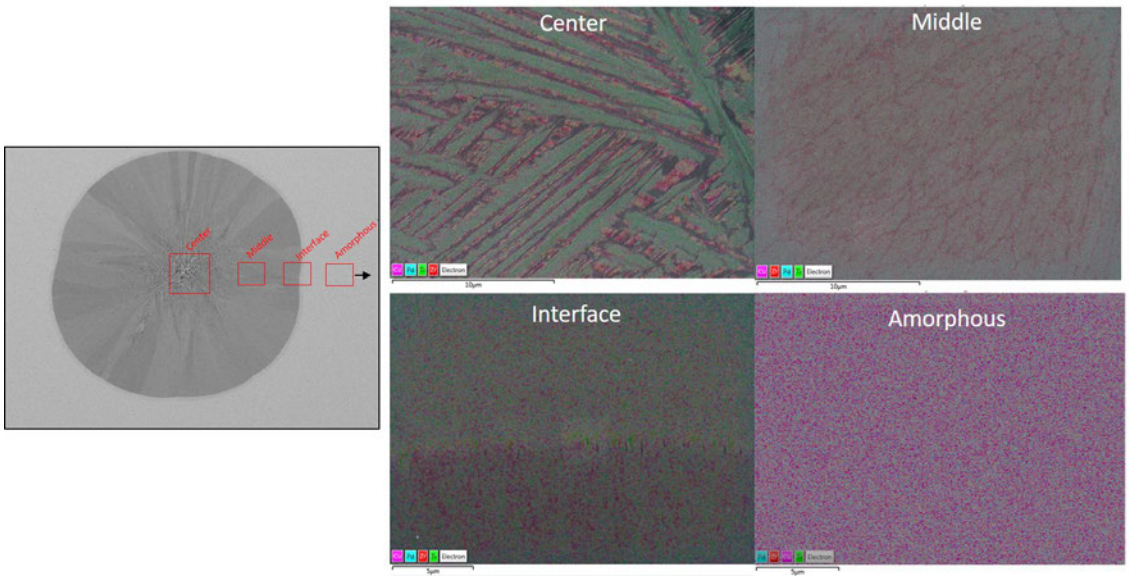

FIGURE 1.6 – (Left) SEM picture of the spherulite with locations of the different map's spots analyzed by EDXS. (Right) EDXS maps of Ti, Cu, Zr and Pd elements superimposed with SEM pictures at different places of the spherulite.

1.2.2 Mechanical characterization

1.2.2.1 Hardness Vickers measurements

Tab. 1.1 shows average values of hardness in the spherulites and in the amorphous matrix. The amorphous matrix has a much higher average hardness (556 HV) than the spherulites (307 HV). Fig. 1.7 illustrates the difference in indent size between amorphous matrix and spherulites, which is in line with the values measured. Moreover, in some cases in the spherulites, some lines can be seen that look like crystalline- plasticity slip bands, which can be found in common crystalline metallic materials. These features are not noticed in the amorphous matrix.

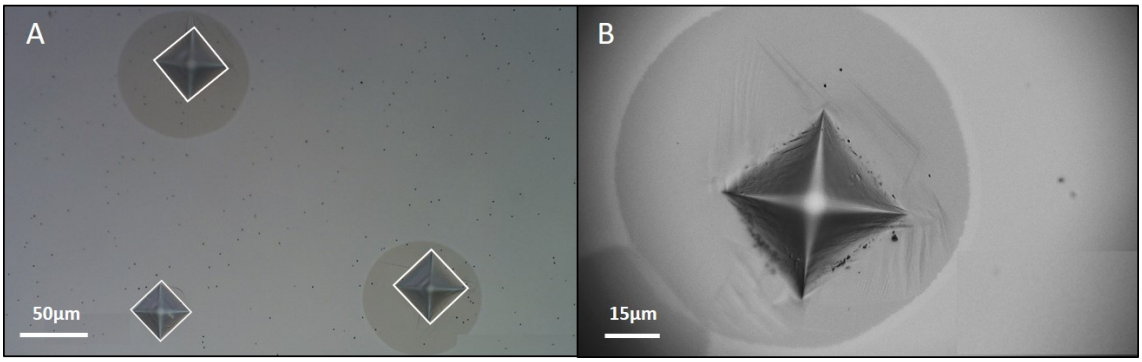

FIGURE 1.7 – Observation of Vickers indentations, (A) showing a different Hardness of the amorphous matrix and the spherulites and (B) crystalline plasticity in the spherulite.

TABLE 1.1 – Hardness Vickers measurements on amorphous matrix and spherulites.

	Hardness (HV)
Spherulites	307 (± 3,5 HV)
Amorphous matrix	556 (± 4,5 HV)

1.2.2.2 Compression and tensile tests

Mechanical properties (Young's modulus, compressive strength, elastic and plastic strains, load to failure and fatigue limit) obtained from the overall set of mechanical tests are summarized in Tab. 1.2. Several compression stress-strain curves can be seen in Fig. 1.8 . The curves are superimposed on the elastic part (with an elastic deformation of about 2%), with a small dispersion on strength but with variations in plastic strains at failure from one specimen to another (between 0.2 and 0.7%).
The compressive strength value calculated from these curves is on average equal to 2 GPa and Young's modulus is about 105 GPa. The picture of the compression fracture surface in Fig. 1.8B has a very matte appearance which corresponds to a propagation of the crack in mode II, in line with a surface fracture angle of around 45° observed here for every sample. The origin of the fracture is not apparent and no spherulite is visible. Tensile stress-strain curves of the BMG for four specimens are also given in Fig. 1.8C. The first conclusion to be extracted from these curves is that all specimens except one show brittle fracture before plasticity. The mechanical strength is ranging between 1075 and 1820 MPa, a very large dispersion. It is interesting at this point, to see that the sample 4 revealing a very short plateau, thus likely (limited) plasticity, broke at the highest stress (1820 MPa), which is not far from the compressive yield strength. Fracture surfaces of all the tensile specimens exhibit spherulites. The picture of the tensile fracture surface is very different from the compressive fracture surface. The starting point of the crack appears to be two large, adjacent spherulites. The crack then propagated in mode I in the rest of the specimen.

TABLE 1.2 – Young's modulus (E), compressive strength ($sigma_{max}$), elastic strain (ε_e), plastic strain (ε_p), load to failure and fatigue limit for TiCuZrPd estimated from the compressive, tensile, load to failure and fatigue curves.

Alloy	Test	E(GPa)	σ_{max}(MPa)	ε_e(%)	ε_p(%)	Load to failure (N)	Fatigue limit (N)
TiZrCuPd	Compression	105±1	2010±15	2±0,05	0,3 - 0,7	/	/
	Tension	97,5±1,8	1075 - 1820	1,6±0,3	0,05 – 0,19	/	/
	ISO 14801	/	/	/	/	600±136	300

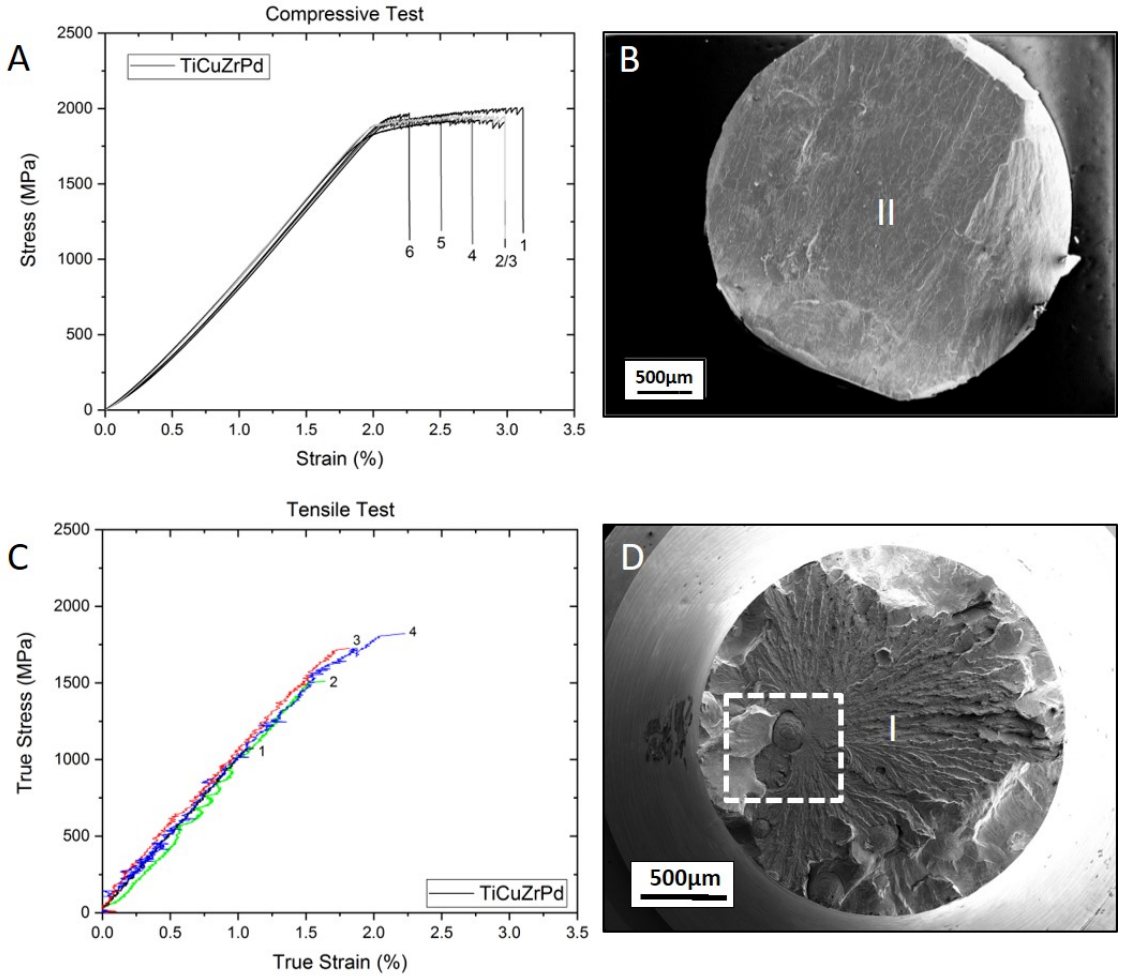

FIGURE 1.8 – (A) compressive stress-strain curves obtained on 6 samples of TiCuZrPd BMG with (B) SEM picture of a representative fracture surface extract from [LIE 18]. (C) tensile true stress-strain curves obtained on 4 samples of $Ti_{40}Cu_{36}Zr_{10}Pd_{14}$ with (D) SEM picture of a representative fracture surface which illustrates the presence of casting defects.

Fig. 1.9 illustrates the ability of spherulites to deform in compression. Fig. 1.9A shows an area of the sample (not on the fracture surface but on one polished side of the specimen) before and after the compression test. It can be clearly seen that the spherulite

has deformed plastically under the compressive stress through crystalline- plasticity slip bands (white arrows). Shear bands (red arrows) can be seen around the spherulite in the amorphous matrix, oriented perpendicular to the compression axis. On the high magnification picture, these multiple small shear bands tend to gather into a single shear band when moving away from the spherulite. These observations lead us to believe that the spherulites deformed first, which led to the premature formation of shear bands in the amorphous matrix around them. These observations will be addressed again in the discussion of the article.

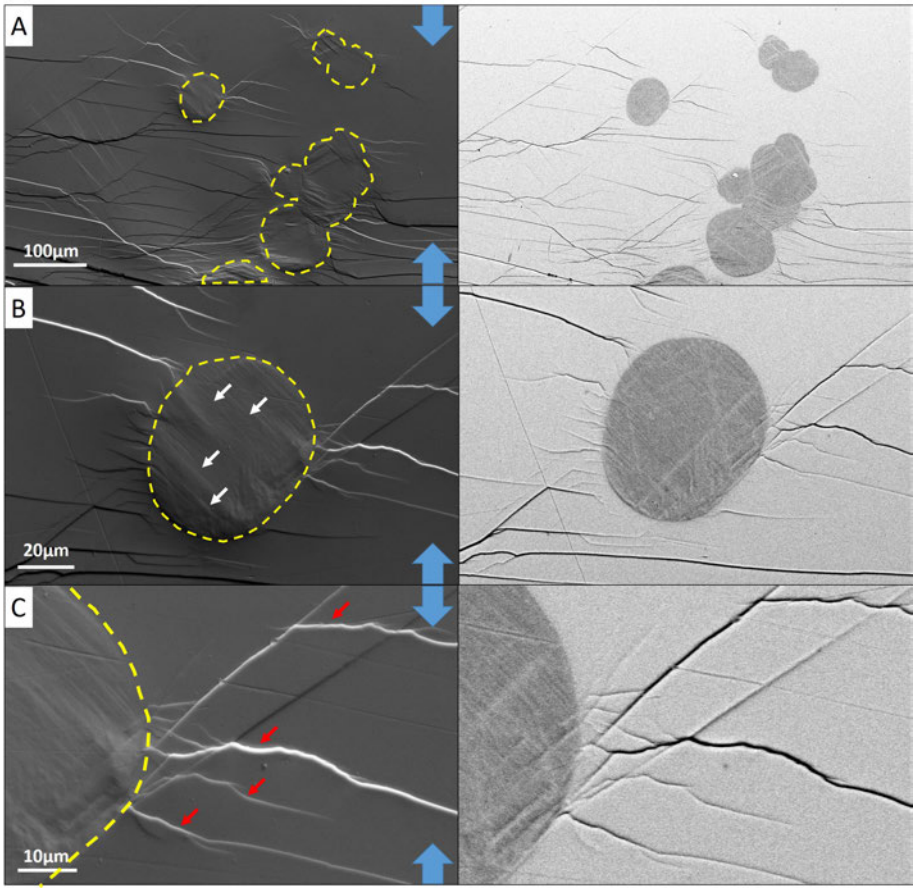

FIGURE 1.9 – (A) SEM picture at the surface a compression specimen after testing (failure at 1.8 GPa) in SE (left) and BSE (right) mode. (B) Higher magnification of one spherulite after the compression. (C) Higher magnification at the interface between the spherulite and the amorphous matrix. The blue arrows symbolize the direction of the compression test. Red arrows represent the shear bands in the amorphous matrix and the white arrows represent the plastic deformation through dislocation movement inside the spherulites.

1.2.2.3 Load to failure: standard ISO14801

Fig. 1.10 shows the stress-strain-displacement curves up to rupture of 6 REPSAMPLES, tested according to ISO 14801. The loading configuration of the ISO 14801 leads to a

bending mode of the implants (the tensile and compressive side of the specimen is given on the fracture surface shown in Fig. 1.10. It can be seen that there is a high variability of maximal load to failure between all these specimens, ranging from 366 to 744 N. However, all of them except one broke in the elastic range and therefore did not show any plasticity (the curvature in the load-displacement being related to the deformation of the acrylate resin). On the fracture surface shown in Fig. 1.10 , the starting point of the crack is clearly visible as a large spherulite on the tensile surface of the specimen. This is probably one of the worst situations that can be encountered in this test (a large spherulite on the tensile side). The rest of the surface of the specimen has a very matt appearance which corresponds to a fast fracture zone (stage II on the picture) with a last fracture of the compressive ligament (denoted III). The crack does not pass through the spherulites but around them, which shows a decohesion between the matrix and the spherulites at the interface. Overall, fracture occurs in mode I, i.e. with a crack propagation perpendicular to the maximal tensile stress.

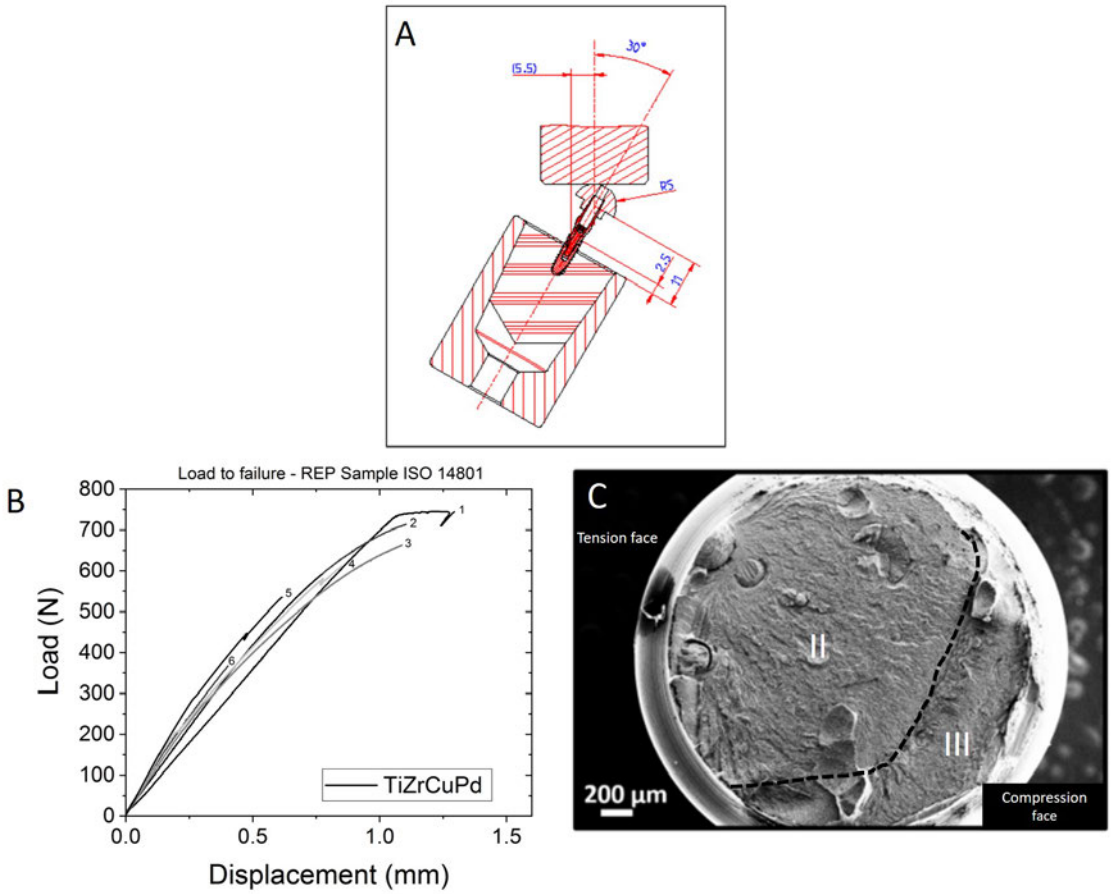

FIGURE 1.10 – (A) scheme of the ISO 14801 standard mechanical test on dental implants. (B) load displacement curves on 6 dental implant prototypes (REPSAMPLES). (C) representative fracture surface.

1.2.2.4 Fatigue test: standard ISO14801

Fig. 1.11 shows the S-N curve for the REPSAMPLES. The fatigue limit of this BMG is estimated to be 300 N, which is high for a biomedical metal alloy considering the small dimension of the samples tested here [MAR 14] [MAR 16] . There is some dispersion in the results, again related to the presence of the spherulites inside the pieces. Fig. 1.11B shows a typical fracture surface: the starting point of the crack propagation on the tensile side is associated to a spherulite of around 500μm in diameter near the surface. The crack propagated in fatigue mode I (stage I in the picture) for some time and then a fast fracture mode appears (stage II) with a surface feature similar to the one observed during the load to failure tests. As for the static tests, a decohesion between matrix and spherulites can be seen. From this overall set of experiments, it is clear that spherulites can act as critical defects in tension and as nucleation sites in fatigue.

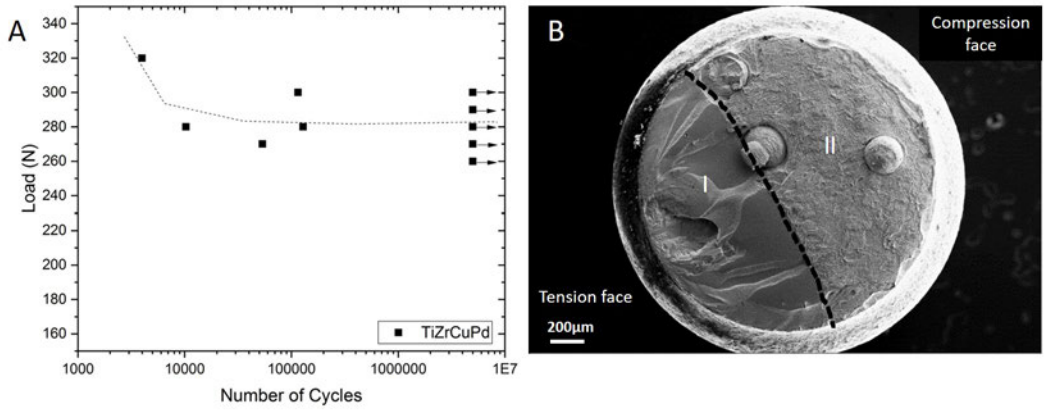

FIGURE 1.11 – (A) typical fatigue Wöhler curve (cycles to failure versus maximum applied load) deduced from a staircase method test on 5 dental implant prototypes. (B) Typical SEM picture of a sample fracture surface.

1.2.2.5 Four-point bending test–SEVNB

The results of the four-point bending test on notched samples are summarized in Fig. 1.3 . With the data obtained thanks to Eq. (1) (Materials and Methods), we were able to calculate a K_{IC} ranging between 32 and 42 MPa$\sqrt{m}$.

TABLE 1.3 – Summary of the four-point bending tests on SEVNB samples. a: notch dimension, σ_{max}: maximum stress recorded, K_{IC}: calculated critical stress intensity factor.

Material	Test	a(mm)	σ_{max}(MPa)	K_{IC}(MPa.$\sqrt{m}$
$Ti_{40}Cu_{36}Zr_{10}Pd_{14}$	4PB SEN(V)B	213 - 261	612 - 1005	32 - 42

1.2.3 Corrosion resistance characterization

1.2.3.1 Macroscopic corrosion behavior

The polarization curve of the BMG from -0.5 to 1 V vs Ag/AgCl in a 0.9% NaCl solution obtained after 6 h of immersion is available in [LIE 20] where the BMG is compared to a TA6V benchmark. The cathodic branch exhibits the same shape for the two materials and it is linked with the oxygen reduction occurring on both surfaces. Nevertheless, the TA6V has a lower current density on the cathodic part. The value of the corrosion potential E_{corr} of TA6V is lower than that of TiCuZrPd suggesting a difference in reactivity between both materials. In the anodic branch, the current density then increases with the potential for both alloys to achieve a passivation plateau. Both materials behave as a passive material and the 6 h of immersion seems sufficient to grow a stable passive film. Conversely to TA6V, the polarization curve of the TiCuZrPd BMG exhibits an abrupt increase in current density at a potential of around 360 mV vs Ag/AgCl which corresponds to pitting potential (E pit). Fig. 1.12A and B shows SEM pictures of the surface of the samples tested in electrochemistry. The entire surface of the TiCuZrPd sample is damaged by the test and covered with corrosion products. Numerous pits and crevices are observed on the overall tested surface. However, it seems that the pitting corrosion sites are not totally random and a specific pattern may be observed suggesting that there are preferential nucleation sites. These nucleation sites might correspond quite well to the position, size and morphology of the spherulites. To demonstrate this finding, a less severe test was performed.

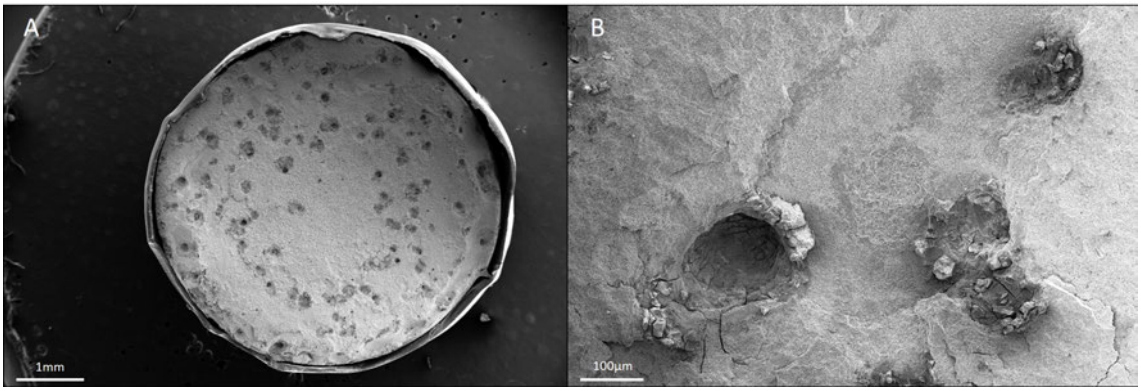

FIGURE 1.12 – (A) SEM picture of one TiCuZrPd sample after polarization from -0.5 to 1 V vs Ag/AgCl in a 0.9% NaCl solution obtained after 6h of immersion. (B) higher magnification of the sample's surface state after the test.

1.2.3.2 Local electrochemical measurements

Fig. 1.13B shows the OCP curves of the entire sample (blue curve), and some corresponding to local measurements on spherulites (red curves) and matrix (black curves).

The first information is that all the curves reach a stable potential value between 0 V and 0.2 V vs Ag/AgCl of potential after immersion of 30 min. Independently of the location of the measurement, the value of OCP after 30 min is almost the same for all the measurements. For the potentiodynamic curves (Fig. 1.13A), only three curves have been shown (for ease of reading) but many measurements have been made on the amorphous matrix and on the spherulites. The cathodic parts of the curves are close from one measurement to another regardless of the targeted area. The values of E_{corr} for the global TiCuZrPd is around 0 V vs Ag/AgCl and those corresponding to local spherulites measurements are in average close to 0 V vs Ag/AgCl or slightly lower. For the matrix's ones, there is a little more dispersion, but the average value is also around 0 V vs Ag/AgCl. Then the anodic branches are increasing following a passivation plateau shape more or less long before a sudden increase, corresponding to pitting phenomenon. Interestingly, the electrochemical behavior is similar whatever the location of the measurement.

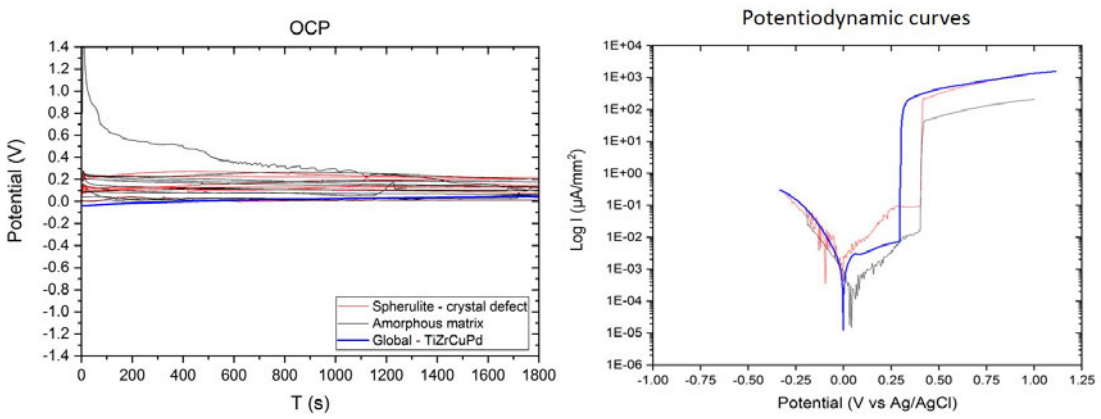

FIGURE 1.13 – (A) potentiodynamic curves of local measurements on spherulite (red curves) or amorphous matrix (black curves). (B) Open Circuit Potential (OCP) local measurements on spherulite (red curves) or amorphous matrix (black curves). The blue curves are reported for comparison purpose from [LIE 20].

Two examples of optical microscopy observation after the local measurements on spherulite and amorphous matrix are displayed in Fig. 1.14. There are in accordance with the previous curves. Indeed, on both pictures, a dark ring around the capillary position consisting of corrosion products deposition is observed. The appearance of the sample's surface reaction after measurements seems to be identical on both areas. Fig. 1.15 shows two SEM pictures of the sample surface after a cyclic polarization test with a low threshold (low enough to identify the starting point of the pitting). Spherulites are not preferential starting points for pitting. It seems rather that the starting point is on areas that appear random from the amorphous and spread. Furthermore, the spherulite shell seems also to preferentially dissolve, creating a void around the spherulite, which can lead to a release of the spherulite into the saline solution.

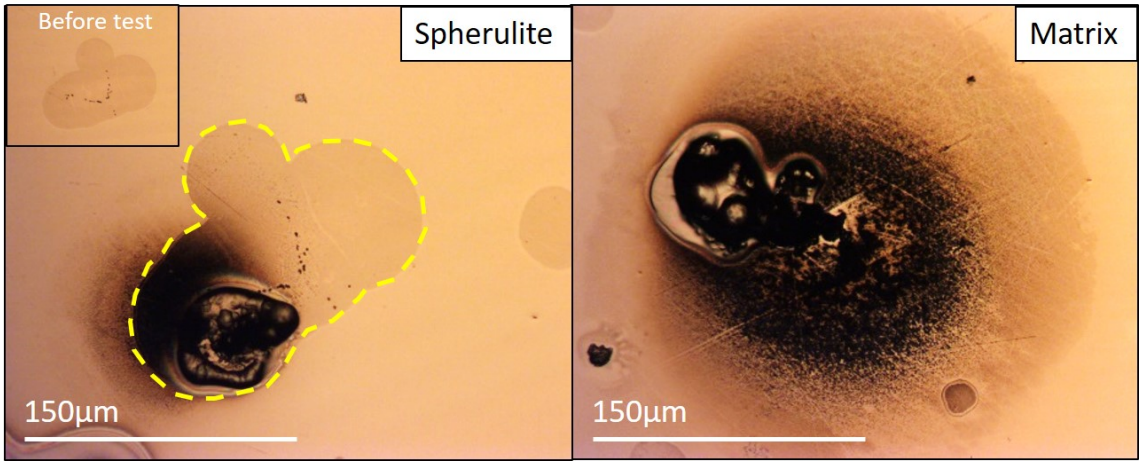

FIGURE 1.14 – Optical observations of the surface of one sample after local corrosion measurements. Left: Spherulite (the insert shows the spherulite before the local corrosion test). Right: Amorphous matrix.

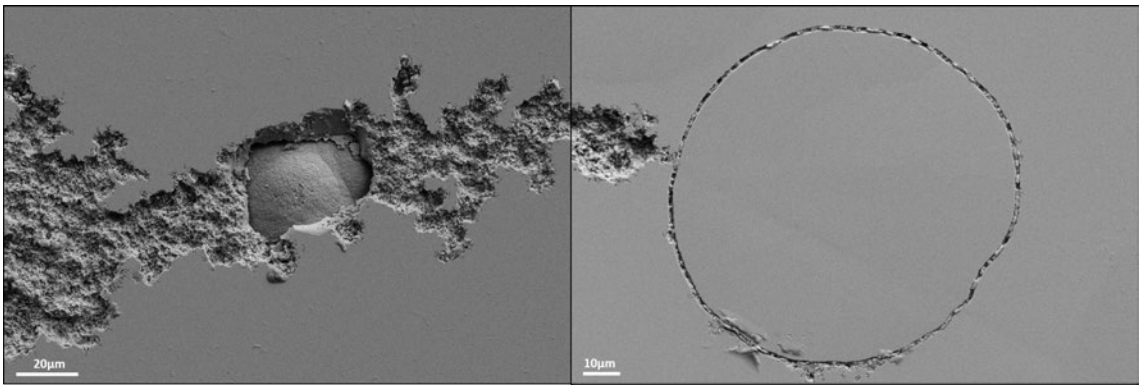

FIGURE 1.15 – SEM pictures of one TiCuZrPd sample after a cyclic polarization in NaCl 0.9%. The shell at the interface between amorphous matrix and spherulite seems to dissolve preferentially.

1.3 Discussion

Bulk metallic glasses are metallic materials with unique properties that are particularly interesting for the biomedical field. In this context, it has already been shown in the literature that the TiCuZrPd grade is very promising for dental implants manufacturing [ZHU 07a][HUA 20]. However, casting defects such as spherulites were not studied in detail so far, while they could alter its properties, particularly mechanical and electrochemical, and therefore may limit its industrialization. This study gives new insights on the characterization of these spherulites and their influence on the properties of use for dental application.

1.3.1 Spherulite: a complex microstructure

Microstructural observations of spherulites have revealed that they have a fine microstructural core, with lamellae oriented in all directions, which suggests that spherulite growth starts from the center to the periphery, this hypothesis is shared with a previous article [SUN 13] . However,the clear interfaces between the spherulite, the surrounding shell and the amorphous matrix are the result of crystallization mechanisms. There is a difference in microstructure between the center of the spherulite and its periphery, the grains are increasingly larger which could be the result of solidification of the same phase with a temperature gradient. Even if the mechanisms of appearance of these spherulites are not clearly elucidated in this article, their observations have allowed us to describe a very particular microstructure which has many points in common with the B2 phase in ZrCu alloys [KIM 18] [ESC 19]. Another scientific team has already observed the same type of defects in a Zr base BMG [SUN 13] but with a laser deposition process. According to their work, the thermal treatment kinetics are involved in the spherulite apparition in the laser heat-affected zone. In many studies on BMGs, the reference technique to check the amorphous state is X-ray diffraction. Indeed, in most papers, diffractograms show broad halos characteristic of amorphous materials. It is demonstrated here that this technique is ineffective to affirm that a piece is really fully amorphous. A sample with a large number of crystalline spherulites on its surface presented a 'typically amorphous' diffractogram even with a very long acquisition time. This result can be explained by the fact that the surface percentage occupied by the spherulites is too small to obtain a signal, even if they are numerous and large. This result therefore challenges the use of DRX as a method to verify amorphous state and suggests a more in-depth study of the casted samples to assess the absence of crystalline defects whose presence may play a role on many properties of the material. Spherulites have a hardness 45% less important than the amorphous matrix, in line with literature [SYP 14] . Moreover, their distribution appears clearly random. Concerning the hardness difference between spherulites and matrix, it can be easily explained by the fact that the amorphous phase has no crystalline lattice planes on which dislocations can slide and no grain boundaries. Plastic deformation in the amorphous phase results in the formation of very small shear bands (the phenomenon is more visible with higher loadings) [XIE 08] . In spherulites, there are defects related to the crystalline organization, including grain boundaries and dislocations (not studied here), which result in easier local plastic formation than in amorphous matrix. This leads to a higher hardness of the amorphous matrix than the crystalline spherulites, as shown in previous article [WU 10]. In addition, EDXS allowed us to illustrate atomic segregation on the central dendritic part of the spherulites. Spherulites consist mainly of a FCC phase (Fig. 1.5), which seems to have lattice parameters close to B2 CuPd phase. On the other side, other phases are present and would deserve further exploration. Some TEM observations were performed on the spherulites and the amorphous matrix. They are not presented here because it would have led to a very long paper and they will be the scope of

a specific future publication. The results confirm the above-mentioned results, the amorphous matrix presenting no atom arrangement and corresponding diffraction FFT was diffuse, which indicates that it is amorphous at the atomic scale. On the spherulite we gathered several FFT patterns showing several crystalline phases. A robust identification of these phases could improve our understanding of their presence and maybe even help to identify the critical parameters responsible for the presence of these defects and thus to avoid their formation. It is important to notice that there is really small variation in the atomic composition of the alloy between the amorphous matrix and the spherulites during our EDXS measurements, which is coherent with the results found by Sun and Flores [SUN 13] and thus hinders somehow their detection. For example, X-Ray tomography in contrast mode was not successful. Spherulites having a large size, a lower hardness and a crystalline nature different from the amorphous matrix, they inevitably have an impact on the mechanical properties of the alloy by inducing a mismatch of their elastic limit.

1.3.2 TiCuZrPd BMG's mechanical properties

The mechanical characterization of BMG TiCuZrPd rods enabled us to determine the main mechanical properties of the material. As already mentioned in previous literature, this BMG does not present a high Young's modulus but a very high mechanical strength [GON 16] . A modest value of Young's modulus for a metal might be interesting for implant applications, since it may limit stress-shielding phenomena [KAN 20] . Although showing a certain ductility in compression, this BMG exhibits a brittle fracture behavior in tension as already mentioned by Liens et al.[LIE 18]. In a large number of papers on BMGs, the compression test is chosen because of its simplicity and the potential of making experiments with a low amount of material on small samples. On the other hand, the fracture surfaces observed for compression lead us to believe that this test is not completely suitable for evaluating the mechanical properties of a metallic glass, especially if they are to be used with other loading configurations in practice (as it is the case for dental implants for example). The presence of spherulites cannot be observed on the fracture surface of samples tested in compression, while they are clearly visible in tension. It is thought that the visibility of spherulites on the surface of the tensile specimens can be explained by the different modes of failure between compression and tension. In tension, mode I is predominant and this will enhance the influence of the defects on the properties by favoring the nucleation of cracks at the interface by stress concentrations at the spherulite/amorphous phase interface [HIN 19]. The larger a spherulite and the closer it is from the sample surface, the more premature the rupture (see surface fracture of Fig. 1.8). On the other hand, in compression, mode II will be promoted and it is less sensitive to presence of defects. In tensile samples, the spherulites come visible at the fracture surface since cracks can initiate from the spherulites and propagate at the interface with the amorphous region. In compression, the spherulite first plastically deform and create the premature formation of shear bands (see Fig. 9). The spherulites

deformation may be the reason why some plasticity can be seen on the compressive stress-strain curves and why they are not visible on the fracture surface [BER 20]. In any case, with spherulites of several hundred of micrometers diameter, the spherulites seem to be deleterious for the mechanical properties in both solicitation mode.

1.3.3 Estimation of the critical size defect

Taking the strengths obtained in tension and the size of the largest spherulite present on the fracture surfaces of each tensile specimen can allow estimating the toughness, for the hypothesis is that they are the critical defect at the origin of the failure. Using the standard equation of the K_{IC} calculation for simple configurations considering the stress at failure, σ_r , and the defect size a [ASH 93] gives:

$$K_{IC} = \sigma_r \times \sqrt{\pi \times a} \tag{1.1}$$

The spherulite's radii measured on the surfaces are between 110 and 255 μm and the stresses at failure are between 1073 and 1820 MPa. Thus, the toughness K_I can be estimated with Eq. 1.1 between 30 and 36 MPa$\sqrt{m}$, which is in line with the K_{IC} measured by SEVNB (Tab. 1.3). This confirms that the spherulites acts as stress-concentrators and defects and are thus to a certain extent detrimental to the strength. The lack of reproducibility of the fatigue results on REPSAMPLES does not allow us to really conclude on the fatigue limit of this alloy, even if among the curves there is a high load at breakage (more than 600 N) and a fatigue limit around 300 N. These properties are still promising for a biomedical alloy, although their dispersion is a concern. Fracture surfaces showed spherulites close to the surface in tension, which visibly leads to spherulite matrix decohesion and thus probably to a critical and premature crack initiation. There is a wide dispersion in the results which could be related to the size of the spherulite and/or their distance from the surface in tension. The mean value of the toughness measured by the SENVB test was of K_{IC} = 36.2 ($\pm$ 4.2 MPa $\sqrt{\text{m}}$). As far as we know, the toughness value of this alloy has not yet been published so it is impossible to compare our results with those of the literature but this is in line with what we approximate in tension. From this value(s) of K_{IC} and the yield stress of the material measured in compression, it is possible to evaluate the dimension of the plastic (process) zone, given by Ashby and Cebon [ASH 93] :

$$d_y = \frac{K_{IC}^2}{\pi \sigma_e^2} \tag{1.2}$$

Where d_y is the size of the plastic zone in m, K_{IC} the toughness in MPa$\sqrt{\text{m}}$ and the yield stress in compression in MPa. The corresponding plastic zone size before failure should be comprised between 100 and 180 μm. It is accepted that if the critical defect size in a material is larger than the size of the plastic zone, then there is fracture before

plasticity [ASH 93] . According to Fig. 2 , spherulites with a diameter greater than 200 μm are present in the material, i.e. larger than the plastic zone diameter. These large spherulites may be few in number, but their presence can easily explain the early brittle fractures that have been observed in tension and on the ISO14801 standard assembly. In this case, spherulites have been shown to have a negative influence on the mechanical properties of the alloy [BER 20] . However, a control of the size of these spherulites and therefore their reduction to below the size of the plastic zone can be a perspective for the optimization of this alloy. For example, by varying the heating temperature, the diameter of the rods during casting and/or the cooling rate, one may control (limit) the size of the spherulites, so that the largest would be below 100 μm, which would certainly insure plasticity before fracture, even in tension and would limit the risk of fatigue crack growth under cyclic loading.

1.3.4 TiCuZrPd BMG: corrosion behavior

Since EDXS has shown that spherulites are of the same average chemical composition or almost the same as the amorphous matrix, it was important to know whether their presence has an influence on the corrosion resistance of the alloy. In the dental domain, the corrosion issues in the oral environment are of prime concern and thus the electrochemical properties of the materials of the future implant must be fully un- derstood. After an overall electrochemical study of TiCuZrPd, it appears that this is a passivable material. This ability to form a protective oxide layer on the surface is requested in the dental environment because it protects the implant from the external environment and thus ensures a certain longevity. However, in the case of TiCuZrPd, pitting corrosion is observed at a relatively low potential [HUA 20]. The pictures of the sample's surface after the test are in favor of the involvement of spherulites in the pitting mechanism, hence highlighting the interest of carrying out local electrochemical study. Several possibilities exist to explain the role of casting defect on the phenomenon of pitting of TiCuZrPd BMGs. The first one is that the spherulites by their crystallographic organization can modify the spherulite's potential compared to the amorphous matrix. In that case, it is possible that a local galvanic coupling will be created between the matrix and the spherulite, because all the specific conditions will be gathered (immersed in solution, one part nobler than the other and a direct electric transfer between both parts). It is important to note that the curves from local measurements are in fact numerous and sometimes not very reproducible, this measurement technique is difficult to implement and really very sensitive to the slightest change, it is nevertheless possible to draw trends. However, local electrochemical measurements indicate that in the tested saline conditions, the OCP measured after 30 min is similar for amorphous matrix and spherulite. Furthermore, the electrochemical behavior of both lo- cations is also very similar. Consequently, these findings seem to invalidate the galvanic coupling theory. Another hypothesis for the role of the spherulite which was evidenced Fig. 15 . Indeed, the interface area between the amorphous matrix

and the spherulite, (the small shell ob- served by SEM) seems to be more sensitive to dissolution than the matrix and the spherulites themselves. Consequently, as proposed in [LIE 20], the saline solution attacks preferentially the shell structure maybe because of a small difference in chemical composition. The propagation of the corrosion damage may allow the penetration of the chloride ions under the spherulite and then provoke local crevice corrosion. However, it is important to mention that deviation of corrosion behavior was noticed during the local electrochemical test on amorphous matrix and that for short pitting test, corrosion attacks were mainly observed in the matrix. Both findings indicate that the chemical composition of the BMG is probably not homogenous on the overall surface. Consequently, the pit nucleation phenomenon is not strictly stochastic but depends of the local chemical composition of the matrix.

1.3.5 Spherulite as reinforcement in the BMG?

The work presented in this article does not allow to conclude on the origin and exact nature of spherulites. However, there is some literature on so-called 'composite' metallic glasses with an amorphous BMG matrix and a crystalline reinforcing phase, which should in principle provide ductility to BMGs. There are many different grades, but the one that has attracted our particular attention are the CuZr based grades with the addition of Ti or Al as a doping element to increase the GFA. In 2009, Pauly and co-workers [PAU 09] reported the presence of a B2 phase (CuZr) which forms spontaneously when the rod is cooled. The proportion of this phase is highly dependent on the diameter of the part and therefore on the cooling rates. The B2 phase is represented by crystalline spheres not randomly distributed in the rods (which aggregate in the center part of the rods). They also specify that the B2 phase can be transformed into the so-called martensitic B19 phase (with highly visible needles) under the effect of stresses, composition or cooling speed. This transformation from phase B2 to B19 is known and has been shown to bring plasticity [ESC 19] . The overall challenge of BMG is to have a small proportion of B2 distributed in a totally random way in the rods and which induces plasticity without reducing mechanical resistance. An- other team demonstrated that crystalline spheres act as strong barriers for the rapid propagation of shear bands [HIN 19][BER 20]. Using a finite element model, they specify that if the spherulites are monodisperse and randomly distributed, then the strain field are more uniform and shear bands can interact and multiplied, which should be beneficial for plasticity. Kim et al. [KIM 18] give some clues on the origin and growth of this B2 phase, and mention polymorphism crystallization induced by "reduced interface kinetics of solid/liquid interface ". They could also see a shell around the spherulites (about 1 μm width), as we observed in the present work. The growth of the spherulites seems to continue until the glass around it solidifies. These elements could link the appearance of spherulites with the presence of oxygen or other pollution elements during casting or perhaps a too low purity of the raw material. Pollution by third-party elements, even at very low contents, could act as a starting point for nucleation. Another

explanation could be the spontaneous formation of phase B2 CuTi due to an insufficient cooling rate to freeze the entire bar in an amorphous state [SON 16] . The crystal defects observed in the TiCuZrPd grade are of large diameter and exhibit a complex microstructure. Nevertheless, even if such defects are present, the grade shows very good mechanical properties. Therefore, modifying (decreasing) the size of these spherulites while maintaining their random distribution to improve the mechanical/corrosion resistance properties and provide ductility, as is the case with BMG's ZrCu, can be a strong option in the future, to end-up with more reliable, strong and ductile biomedical grade BMG's.

1.4 Conclusion

This study demonstrates the presence of heterogeneities in the TiZrCuPd grade, which were not precisely described so far for this composition. These heterogeneities exhibit the shape of large crystalline spheres, up to several hundreds of μms, which nevertheless remain undetected by X-rays. These spherulites do not occupy a large volume fraction, but their large size and much lower hardness than that of the amorphous material are the cause of premature failure of the parts, in particular under tensile loading, where failure occurs before plasticity. The exact nucleation origin of these spherulites during the process would deserve further work and observations of the microstructure of these spherulites is complex, with martensitic needles in the center and a phase identified as CuTi B2 very present, probably with Zr/Ti and Cu/Pd substitutions. Another objective of the paper was to find out whether the presence of these defects was the cause of the modest corrosion resistance of this alloy. It was shown here that the corrosion and pitting potentials were similar for the spherulites and the amorphous matrix. Therefore, assuming that some corrosion dissolutions initiate on the amorphous matrix, the spherulites, themselves, are probably not the most deleterious to the corrosion resistance. However, the shell at the spherulite/amorphous interface, exhibiting probably a different chemistry, seems to dissolve preferentially in saline solution and have to be controlled. At the end of this study, it is relevant to ask whether it is more strategic to try to preserve these 'defects' while controlling (decreasing) their size and distribution rather than trying to prevent their appearance, as a controlled crystallization of small particles in a glassy matrix seems to provide ductility and improve toughness in other BMG systems.

Chapter 2

Spherulitic growth process in Ti-based metallic glass: microstructure, phase identification and growth mechanism

$Ti_{40}Cu_{36}Zr_{10}Pd_{14}$ metallic glass is often considered a promising candidate for biomedical applications, in particular for the manufacturing of small size dental implants. Nevertheless, its processing and limited glass forming ability leads to the appearance of crystalline spheres called "spherulites". These spherulites play a major role in the deformation behaviour of this alloy. It is therefore a critical issue for its future industrial use to identify their nature and better understand their growth process, to enable control of their size distribution and localization. This article presents a fine detailed description of the microstructure of theose crystalline defects, from the sub millimetre to nanometric scales, using TEM transmission electron microscopy (TEM), energy-dispersive X-ray spectroscopy (EDXS)/electron backscatter diffraction (EBSD) coupled with scanning electron microscopy (SEM) and X-ray diffraction (XRD) characteriszation. Several phases are identified thanks to the combination of EDXS/EBSD and TEM information, in particular a TiCu B2 phase, analogous to the ZrCu B2 phase usually presents in other composite metallic glasses. The presence of other phases such as Ti_2Cu_3 phase and the $CuTi_3$ phases is also detected. The spherulites being are studied at different times of during their growing growth process, and a growth scenario is proposed based on the characterisation observations. The nucleation step of the spherulites remains however unclear despite in-depth investigation. Thus, different hypotheses are discussed.

2.1 Introduction

Metallic glasses are widely recognised as having a far superior elastic limit compared with their crystalline counterparts, making them particularly attractive for biomedical, luxury, high-performance sports and wear-part applications [CHE 11]. Most bulk metallic glass (BMG) grades offer good corrosion resistance [SCU 07] and the ability to deform without crystallising near their glass-transition temperature (T_g) [DUA 07]. The alloy $Ti_{40}Cu_{36}Zr_{10}Pd_{14}$ exhibits good biocompatibility together with a very high elastic limit (approximately 2 GPa, mostly measured in compression) and a low Young's modulus (approximately 100 GPa) [LIE 18]. It is therefore an interesting candidate for the manufacture of dental implants of reduced size, i.e., with less impact on the implantation site. This composition was discovered by Inoue and collaborators [ZHU 07a] to offer an alternative to the current crystalline alloys, which contain non-biocompatible atomic species such as Aluminium, Vanadium, Nickel, Cobalt, and Chrome [CAL 13].
Although many BMG grades have been shown to be fully amorphous, even for specimen presenting quite large diameters (several millimetres), certain other grades are only partially amorphous, such as Cu-Zr and Cu-Ti based BMGs [HOF 13]. In the alloy $Ti_{40}Cu_{36}Zr_{10}Pd_{14}$ alloy, large spherical crystalline defects (later called spherulites) which can be several hundreds of micrometres in diameter, are unfortunately often present (even in quite small samples) and are randomly dispersed in the as-cast rods [GAU 22]. They are cannot be observed using standard X-ray diffraction(XRD) techniques, or after compression testing, nevertheless they clearly affect the tensile strength and fatigue properties [GAU 22]. Preliminary observations have revealed that spherulites are most likely composed of a cubic phase (CFC structure, 3.14 Å lattice parameter). Inside the spherulites, a fine sub-micrometric microstructure has been observed but not yet detailed, revealing that several phases may coexist. To date, the exact nature of the spherulites and their formation mechanism remains undescribed. According to Sypien et al [SYP 14], the differential scanning calorimetry(DSC) curves for this alloy (initial amorphous state) revealed several

crystallisation peaks, indicating the presence of different phases. The phases identified in [CZE 16] were all from the CuTi binary phase diagram, under the assumption that Zr atoms substitute at Ti sites and Pd atoms substitute at Cu sites. This strong assumption allowed Sypien et al to reveal the presence of the $(Ti,Zr)_3(Cu,Pd)$ phase, $Ti_2(Cu,Pd,*)$, and $(Ti,Zr)_2(Cu,Pd)$ phases from scanning electron microscopy (SEM)-energy dispersive X-ray spectroscopy (EDXS) measurements. The reason for the proposed phases is the large solubility of Pd and Cu [OKA 13] and of Ti and Zr [HAR 94]. However, no crystallographic evidence for the presence of those phases has been provided.
Premature failure can be observed in the $Ti_{40}Cu_{36}Zr_{10}Pd_{14}$ alloy, with severe consequences for the biomedical applications targeted [LIE 18]. As the spherulites deform plastically [HON 18], if their size is controlled and limited, they could allow global plasticity of the specimen before failure. This would require the optimisation of the spherulite size and volume fraction during the specimen elaboration. The aim of this study was to provide a multi-scale microstructural characterization of the spherulite from the sub millimetre to nanometric scale. The microstructure of the spherulite formed in a $Ti_{40}Cu_{36}Zr_{10}Pd_{14}$ alloy was observed using optical and electron microscopies. Two different types of crystalline defects were observed: large-scale spherulites (almost millimetric, already well developped) and spherulite precursor dendrites (50μm in length). Focused ion beam (FIB) thin foils, extracted at the center and surface of the spherulites, were used to identify the phases present. The information gathered were used to propose and discuss a scenario for the growth of spherulites as well as hypotheses for their nucleation.

2.2 Results

Many spherulites with diameters ranging from several tens to several hundreds of micrometres and randomly distributed were present in the rods. SEM–EDXS analysis confirmed that the chemical composition of the amorphous phase (light grey region in Fig. 2.1A) corresponds to the nominal composition of the alloy, i.e. $Ti_{40}Cu_{36}Zr_{10}Pd_{14}$. However, the spherulites (darker grey region in Fig. 2.1A) show a slight enrichment in Pd and a slight depletion in Cu, with a measured global composition of $Ti_{40}Cu_{36}Zr_{10}Pd_{14}$ and thus, a very small change in chemical composition. Fig. 2.1B presents the diffractogram acquired in the area indicated in Fig. 2.1A, which is an agglomeration of spherulites over a total area of several mm^2. The diffractogram contains six main peaks of high intensity. Phase identification was performed using the Rietveld method. The CuTi B2(cubic) phase with a lattice parameter adjusted 3.14 Å (theoretically 3.077 Å , green peaks in Fig. 2.1B) matches well with the diffractogram and the density of the [0 0 2] plane is larger than expected, indicating a possible preferred crystallographic orientation. No other phase could be identified from this diffractogram. EBSD analysis confirmed the XRD results as most of the surface of the spherulites was indexed as the cubic CuTi B2 phase (Fig. 2.1C). Note that the needle in the central part was indexed as the Cu_3Ti_2 phase.

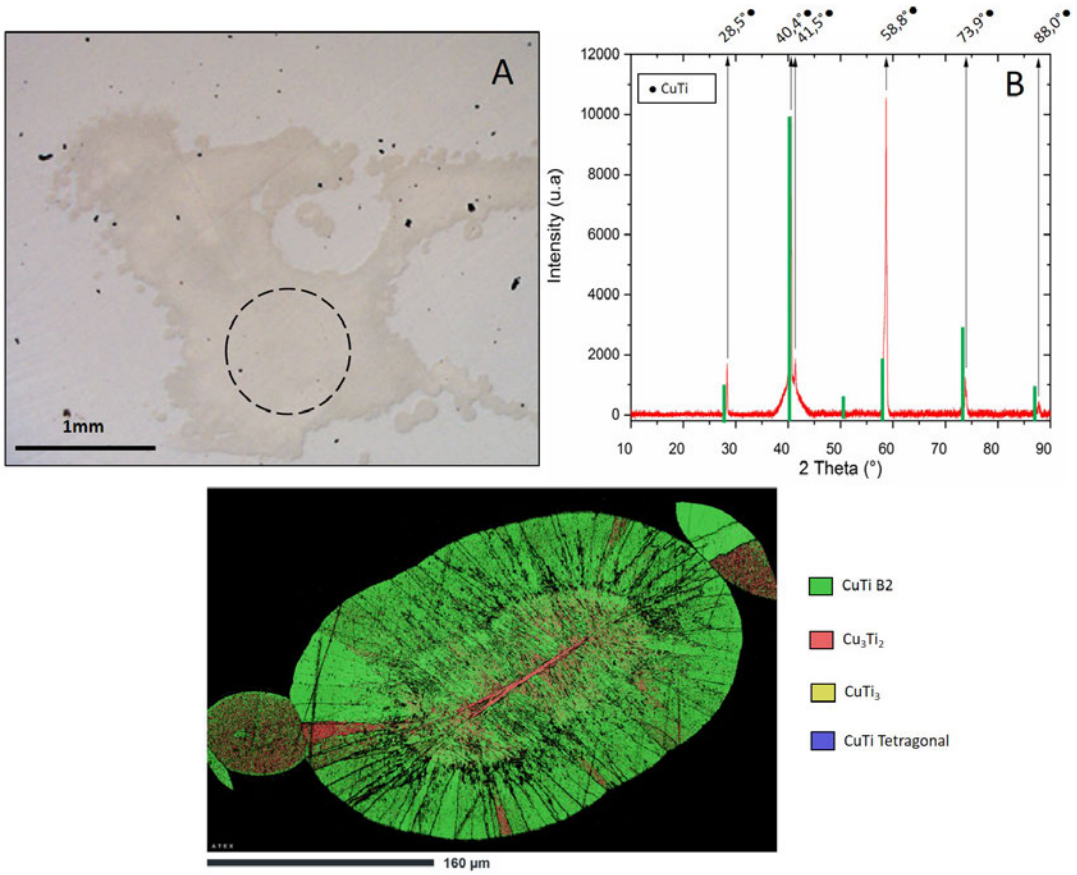

FIGURE 2.1 – A) Illustration of spherulite region analysed using XRD. B) XRD pattern of large millimetric spherulite aggregate, confirming the presence of CuTi B2 phase as a major constituent, with a peak extinction at 51.4° of the plan [1 1 1]. The used CuTi B2 phase has *Pm-3m* space group and a theoretical lattice parameter of 3.077 Å (adjusted here to 3.14 Å by the Rietveld method). C) EBSD phase map of entire spherulite.

Three typical spherulite morphologies observed in the rods in SEM-BSE mode are presented in Fig. 2.2. In Fig. 2.2A, the spherical large spherulite of approximately 140μm diameter, consist of a much finer microstructure in the core than in the periphery. These spherulites are composed of long needles (length of approximately 50μm and thicknesses of a few micrometers) that split in all directions, which appear bright. These needles will be referred to as 'primary needles'. Finer dark needles of a few micrometres long and few tens of nanometres thick neighbour the bright needle and will be referred to as 'secondary needles'. Finally, these two phases are encircled by a grey phase which grow with a spherical shape.
Similar contrasts and phase distributions were observed in the two other spherulites types,

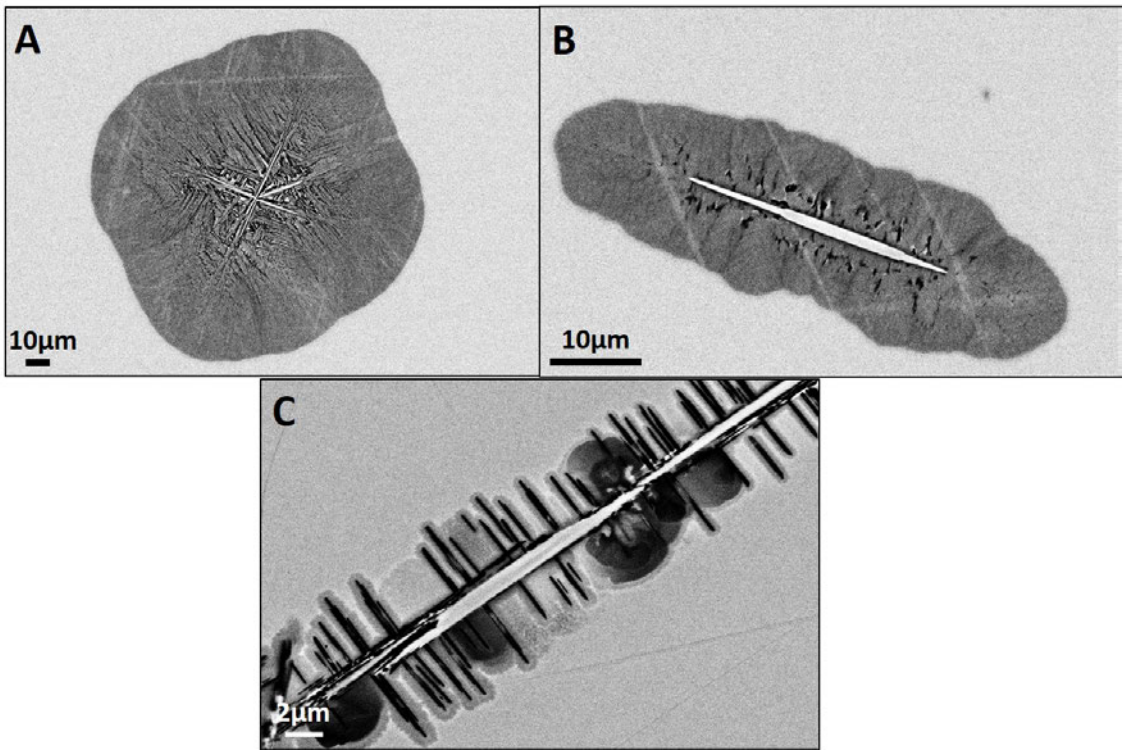

FIGURE 2.2 – Example of spherulites observed in the $Ti_{40}Cu_{36}Zr_{10}Pd_{14}$ alloy, observed in SEM-BSE mode: A) large spherulite of more than 100 μm in size in the core of the as-cast rod, B) smaller spherulite of fews μms in the periphery of the rod, and C) small needle shape defect, which corresponds to an earlier stage of crystals growth. In all cases, the core of the defect consists of white long needles, together with a darker phase, from which a grey phase seems to be growing.

Fig. 2.2B and C, with smaller sizes, and fewer needles. One bright long needle was also present, together with thinner dark needles (oriented perpendicularly to the bright needles), both surrounded by a grey phase. The arrangement and morphology of the phases are therefore very similar to that observed at the center of the spherical spherulites in Fig. 2.2A. Higher magnifications observation were performed to better understand the microstructure of these defects.

2.2.1 Phase identification at the core of the spherulites at the micrometres scale

Fig. 2.3A and B present SEM-BSE micrographs of one large spherulite at two magnifications. In Fig. 2.3B, at higher magnification, three grey shades are observed, indicating the presence of at least three different phases: white needles of width of approximately 2μm (point 1), black needles of size of approximately 1μm (point 4 and 5), and a more diffuse thinner grey phase (points 2 and 3). EDXS measurements were performed at 20keV, which corresponds to an interaction volume diameter of approximatey 1.2μm x

1.2μm. Considering the size of the microstructure, the measured chemical composition might sometimes overlap with that of the neighbouring phase. Additionally, EBSD maps were acquired over the same area; the band contrast (BC) and phase maps are presented in Fig. 2.3C and Fig. 2.3D respectively. The EDXS and EBSD results are summarised in Tab. 2.1.

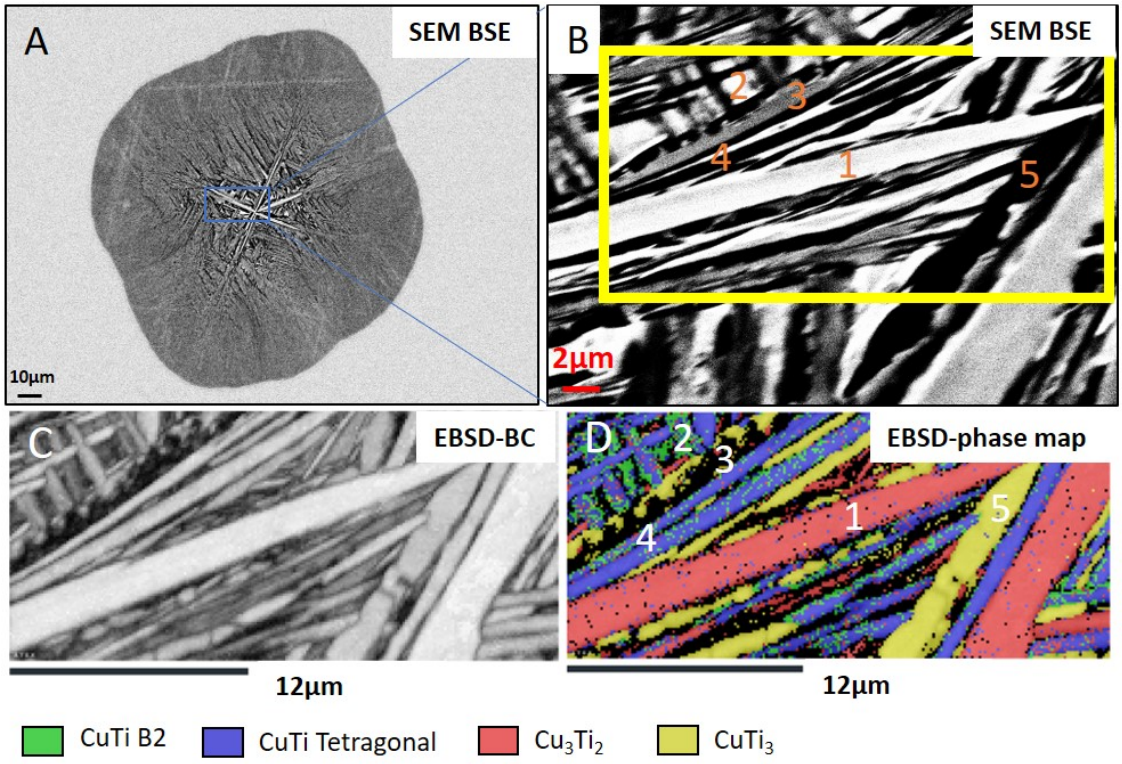

FIGURE 2.3 – A) and B) SEM-BSE micrographs of core of a large spherulite at different magnifications. B shows the areas targeted for the EDXS measurements (orange numbers). C) and D) Band contrast map and EBSD map of phase repartition of image B).

TABLE 2.1 – Summary of SEM-EDXS point analysis of central part of the spherulites.

Point	Composition (at.%)	Ratio (Cu+Pd)/(Ti+Zr)	Candidate Phase (EDXS)	Indexed phase (EBSD)
1	Ti_{30} Cu_{44} Zr_6 Pd_{20}	1.8	Cu_3Ti_2 or Cu_2Ti	Cu_3Ti_2
2	Ti_{45} Cu_{33} Zr_{10} Pd_{12}	0.8	CuTi	CuTi B2
3	Ti_{24} Cu_{40} Zr_{18} Pd_{18}	1.4	Cu_3Ti_2	Non indexed
4	Ti_{43} Cu_{28} Zr_{11} Pd_{18}	0.8	CuTi	CuTi tetragonal
5	Ti_{60} Cu_{19} Zr_8 Pd_{13}	0.5	$CuTi_2$	$CuTi_3$

Five phases with distinct chemical compositions were identified:

1. The large white primary needles, with composition $Ti_{30}Cu_{44}Zr_6Pd_{20}$, are particularly rich in Cu and Pd. This phase was indexed as the Cu_3Ti_2 tetragonal phase. Its (Cu+Pd)/(Ti+Zr) ratio is 1.8, which is close to that expected for the Cu_3Ti_2 phase.
2. The homogeneous grey phase, with composition $Ti_{45}Cu_{33}Zr_{10}Pd_{12}$, exibits a chemical composition close to the nominal one. It was indexed from EBSD as a cubic CuTi B2 phase, and its (Cu+Pd)/(Ti+Zr) ratio is close to 1.
3. The white phase close to the primary needle, with composition $Ti_{40}Cu_{36}Zr_{10}Pd_{14}$, is particularly rich in Zr and poor in Ti. It could not be indexed by EBSD, as no diffraction signal was collected from this area, most likely due to the small size of this phase structure.
4. The secondary black needles (oriented at 90° to the primary needle), with a measured composition of $Ti_{43}Cu_{28}Zr_{11}Pd_{18}$, exhibit a chemical composition very close to that of the homogeneous grey phase (point 2) with a slight increase in Pd. This phase was indexed as tetragonal CuTi, and its (Cu+Pd)/(Ti+Zr) ratio is close to 1.
5. The darker globular phase, with chemical composition $Ti_{60}Cu_{19}Zr_8Pd_{13}$, was surprisingly rich in Ti at the expense of copper. It was indexed as $CuTi_3$ although its (Cu+Pd)/(Ti+Zr) ratio is close to 0.5.

Similar observations were performed on the other spherulite morphologies, see Fig. 2.4. In this case, the microstructure was much simpler: only four phases were present in the spherulite's core. The 'primary needle' is indexed as the Cu_3Ti_2 phase, and the secondary needles as CuTi tetragonal phase. At the periphery of the CuTi secondary needles, some areas may exhibit some chemical ordering, as they were indexed as the CuTi-B2 phase with the same orientation as the originating CuTi secondary needle. Note that when using EBSD, it is difficult to assess whether the phase is ordered or not, with the indexation observed for the core and the needles periphery being sometimes CuTi, sometimes CuTi-B2. Indeed, the diffraction patterns for both phases are very similar, and a dedicated indexation algorithm should be used to discriminate between the two phases. Finally, the fourth phase indexed as $CuTi_3$ was located close to the primary needle with a globular shape and a diameter of a few hundreds of nanometers.

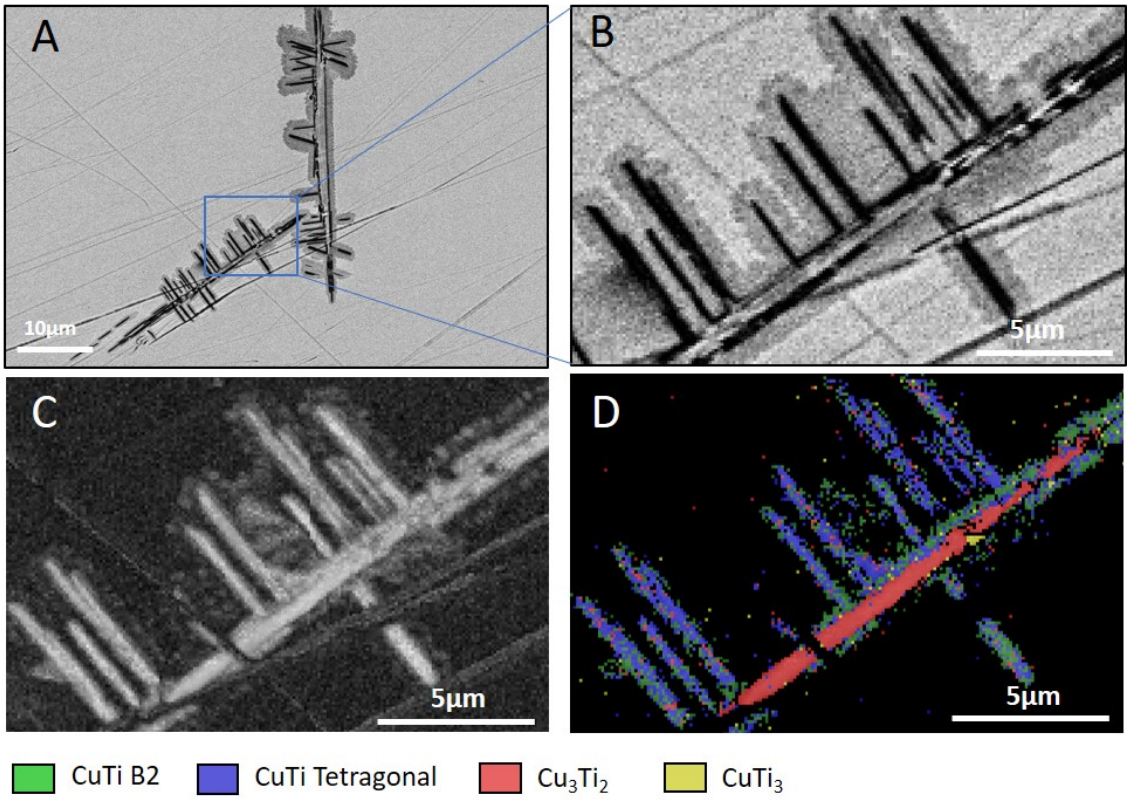

FIGURE 2.4 – A) SEM-BSE micrograph of a needle-shaped defect at the periphery of the as cast rod at different magnifications. B) Higher magnification image of region in A. C) Corresponding band-contrast map D) Corresponding EBSD map of phase repartition of image B.

2.2.2 Orientation relationship between the different phases

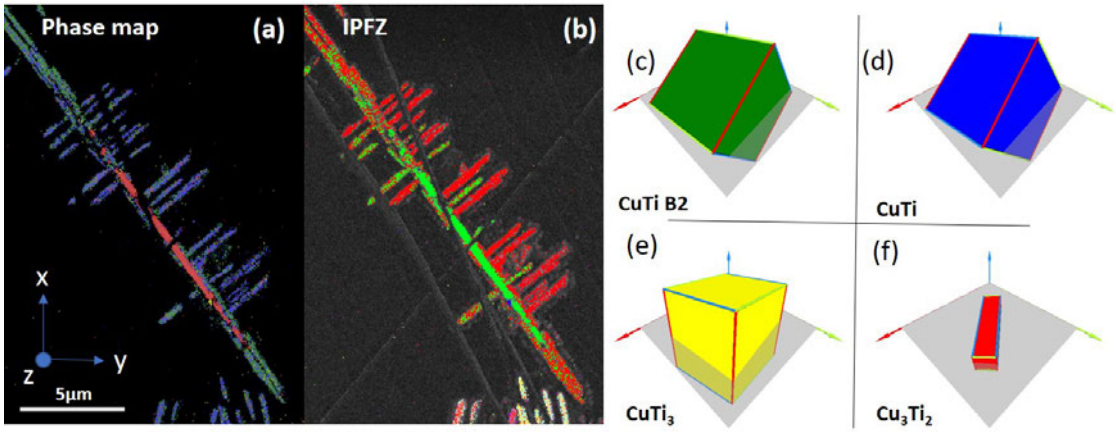

FIGURE 2.5 – Orientation relationship between the four major phases, illustrated for the needle shaped spherulites (a) Phase map (b) IPFZ orientation map, and orientation of (c) CuTi-B2,(d) CuTi tetragonal, (e) $CuTi_3$ and (f) Cu_3Ti_2 phases.

The same orientation relationship was observed between the major phases for all the spherulite morphologies (Fig. 2.5):

$$\mathbf{<001>Cu_3Ti_2//<001>CuTi//<001>CuTi_3}$$
$$\mathbf{<010>\ Cu_3Ti_2//<010>CuTi//<\text{-}110>CuTi_3}$$

This finding confirms that the smaller spherulites did grow via the same mechanism as the large globular ones in Fig. 2.2), and that the four phases identified are the main ones involved in their nucleation-growth mechanism.
To better describe and understand the microstructure of the large globular spherulites, additional TEM measurements were performed on a FIB foil extracted from the core of the spherulite.

2.2.3 Fine microstructure of the larger spherulites at the nanometric scale

A detailed characterisation of the microstructure of the largest spherulites at the nanometric scale revealed that their microstructure is even more complex and finer than that described from SEM. Indeed, Fig. 2.6A presents a general view of the thin foil extracted at the center of the spherulite, revealing a much finer microstructure than that described from SEM observation. In Fig. 2.6B, several wide needles, corresponding to the primary or secondary one observed from SEM, are visible and encircled by a yellow dashed line (noted as 1 in Fig. 2.6B). One can notice that the needles are all perpendicular to each other, such as for the 'small' spherulites observed previously by SEM. Bright thin laths of a few nanometres thick are present in the middle of those primary laths (1'). The CTEM contrast on those large laths indicate that some of them are distorted (1"), and internal stress might have appeared during the simultaneous growth of the different needles. The primary laths interface is tortuous and decorated with secondary phases. For instance, a dark phase of a few nanometre thick is visible (3) as well as white phases in between the laths (2).

The major grey phase (1 in Fig. 2.6B) was identified using SAED, Fig. 2.7(a) and (b) as the CuTi-tetragonal phase, which is in good agreement with previous XRD and SEM-EBSD characterisation. The 1' phase, which appears as long white stripes in Fig. 2.7(a) has a periodicity of 6Å (Fig. 2.7(c)). This phase presents the same electron pattern as the CuTi laths, with additional spots, typical for the chemical ordering in Fig. 2.7(e). This additional ordering is that presented in [MAR 87], with an intermediate long period structure (a = 3.13Å and c = 5.919Å). Thus, the CuTi-tetragonal phase undergoes chemical ordering after formation.

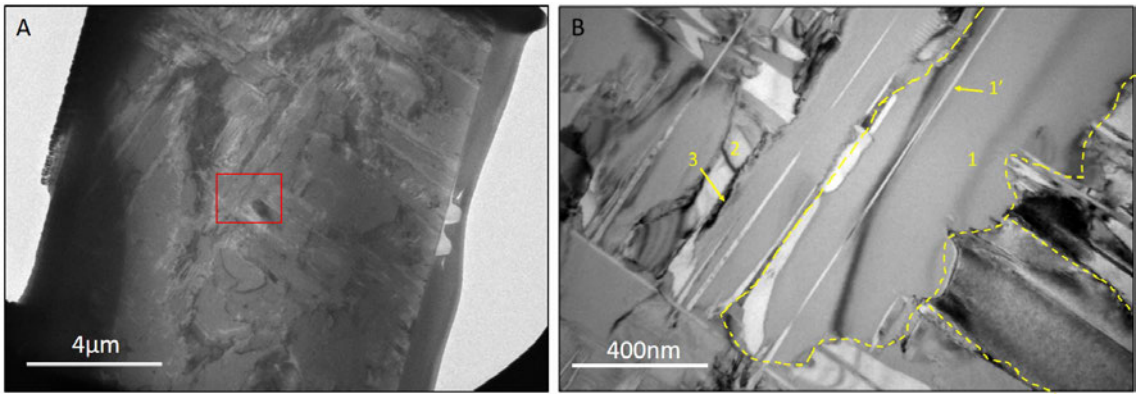

FIGURE 2.6 – A, low magnification TEM images of FIB foil extracted from the core of a large spherulite. Image B, zoom-in of the area indicated in red in image A.

.

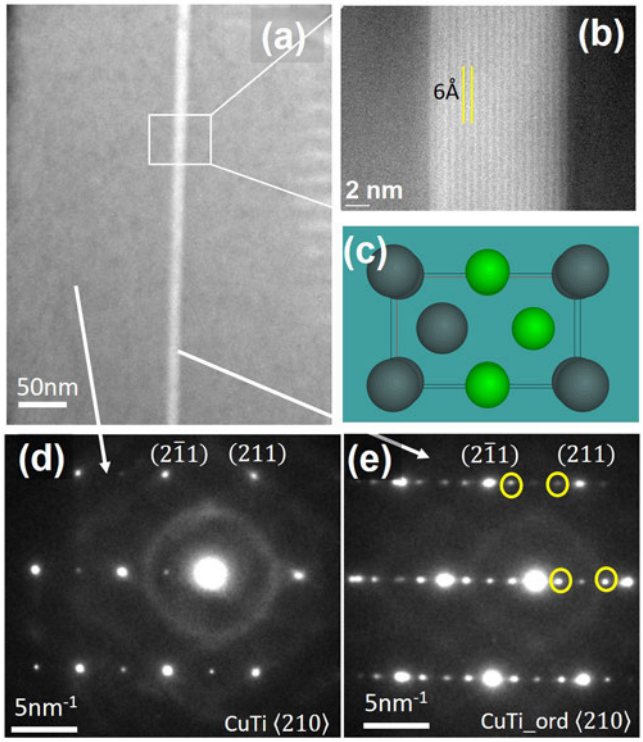

FIGURE 2.7 – (a) CTEM micrograph of CuTi laths and (b) corresponding SAED pattern, indicating a <210> orientation of the CuTi tetragonal phase. (c) An additional phase, of few nanometre in thickness, for which a 6Å periodicity is visible in that orientation, was identified as a CuTi-ordered phase from the pattern in (d), already described in [MAR 87]. (e) corresponding SAED pattern, the ordering leads to the presence of additional spots, which were successfully indexed as the CuTi-ordered phase with zone axis <210>.

.

Additionally, a typical eutectoid-like structure was observed within the CuTi laths, with a few nanometres-thick lamellas, see Fig. 2.8(a). Orientation mapping performed using TEM with the ACOM/ASTAR tool enable the product of the eutectoid reaction to be identified as CuTi and $CuTi_3$ (see red squared area in Fig. 2.8(b)). The orientation map indicates that the CuTi phase present in the eutectoid aggregate does not have the same orientation as the initial CuTi lath (Fig. 2.8(c)). The reaction appears to start at the interface and to propagate within the lath. Additionally, a few nodules of the Cu_3Ti_2 phase were observed close to the decomposed area.

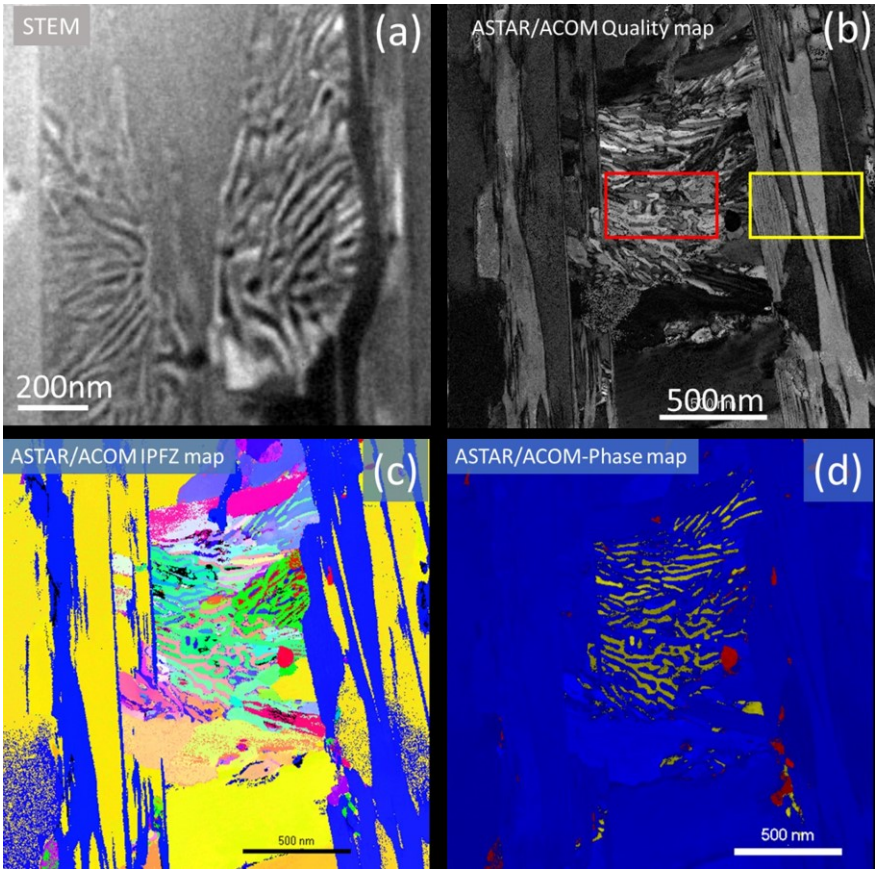

FIGURE 2.8 – Evidence of phase decomposition occurring in the CuTi phase, observed using (a) STEM, with Z contrast, and (b-d) ASTAR/ACOM orientation mapping on another area. (b) Quality map of analyzed area. (c) Corresponding orientation IPFZ map and (d) corresponding phase map with three identified phases (CuTi-tetra in blue, Cu_3Ti_2 in red and $CuTi_3$ in yellow).

.

2.2.4 Microstructure of interface between large spherulites and amorphous matrix

SEM–BSE micrographs of the interface between the spherulite and amorphous matrix are presented in Fig. 2.9. At the crystalline/amorphous interface, an intermediate phase

of approximately 3 and 4μm in thickness is visible with light-grey contrast. This contrast might arise from chemical contrast and/or crystallographic contrast. This shell is present around all spherulites and likely consists of columnar grains. Black nanometric precipitates with elongated shape and dark contrast are also present at the interface between the spherulite and shell. Most of these precipitates are oriented 45° relative to the interface. To better analyze the chemical composition and crystallographic nature of this region, a thin foil was extracted using FIB at a localization similar to the one indicated by the orange line in Fig. 2.9B.

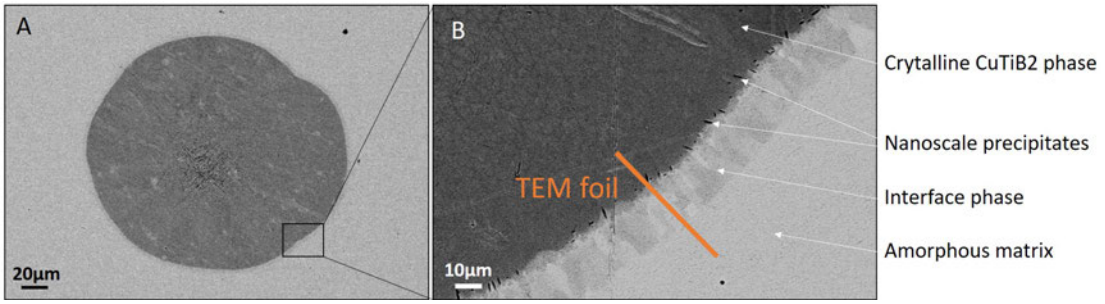

FIGURE 2.9 – SEM-BSE observation of a spherulite/matrix interface: A) low magnification of the spherulite and B) detailed view of the black rectangular zone presented in A), showing the presence of nanoscale dark precipitates, as well as an interface shell, of around 3-4 µm thick.

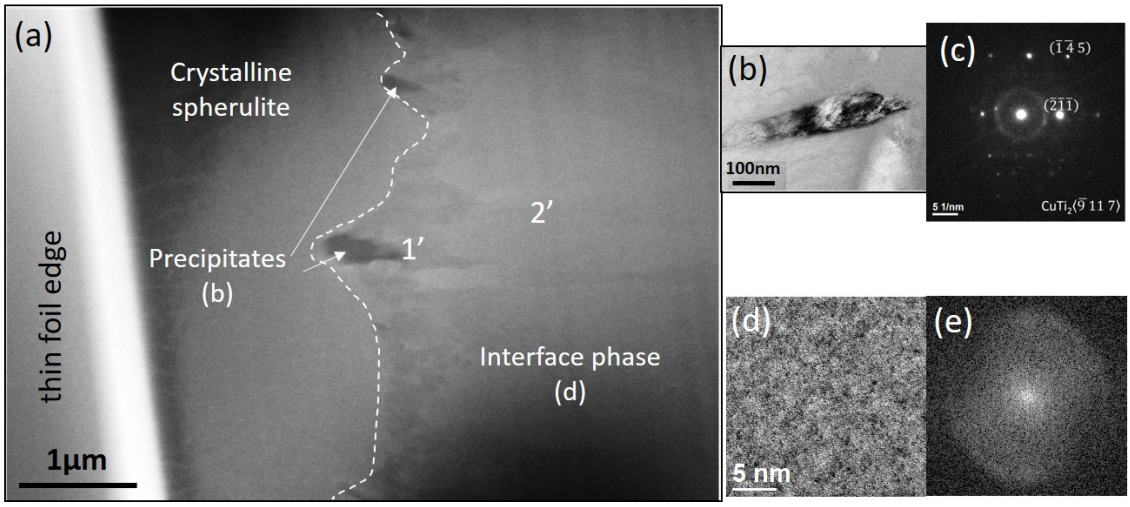

FIGURE 2.10 – A) SEM observation of the FIB lamella extracted at the interface of the spherulite. Two distinct areas are visible: the crystalline spherulite on the left, composed mainly of CuTi phase, from previous observations, and the interfacial region on the right. B) and C), TEM CTEM micrograph of one precipitate and corresponding FFT. D) and E) higher magnification TEM micrograph of the interfacial area and corresponding FFT. The noted numbers 1' and 2' are the position where the EDXS measurements were done and reported in Tab. 2.2.

.

Fig. 2.10 presents the localization of the chemical analysis realized at the interface.

The corresponding measurements are presented in Tab. 2.2.

TABLE 2.2 – Chemical measurements performed using SEM on the thin foil extracted at the interface.

Point	Composition (at.%)	(Cu+Pd) /(Ti+Zr) ratio	Phase candidate	SAED Diffraction
1'	$Ti_{47}Cu_{20}Zr_{12}Pd_{21}$	0.7	Cu_3Ti_2	$CuTi_3$
2'	$Ti_{37}Cu_{25}Zr_{14}Pd_{23}$	1	CuTi	Amorphous

The chemical composition of the precipitates corresponds to $Ti_{47}Cu_{20}Zr_{12}Pd_{21}$. The precipitates are rich in Ti and Pd. From TEM SAED, one precipitate was indexed as the $CuTi_3$ phase. The chemical composition of the shell is $Ti_{37}Cu_{25}Zr_{14}Pd_{23}$ indicating a local enrichment in Zr and Pd compared with the nominal composition of the alloy. The Cu+Zr/Ti+Pd ratio is close to 1. A higher-magnification micrograph of the interfacial region is presented in Fig. 2.10(d). Surprisingly, this area that shows a contrast typical for columnar grains, presents no atom arrangement. Its corresponding FFT pattern is diffuse, indicating that the area is amorphous.

2.3 Discussion

Numerous spherical crystalline defects of several hundred micrometres and randomly dispersed were observed in suction casting parts of the $Ti_{40}Cu_{36}Zr_{10}Pd_{14}$ alloy. The presence of such spherulites is not often reported in the literature. Multi-scale electron microscopy observations revealed that their microstructure is complex.

Thanks to the composition measurements of the indexed phases and the EBSD measurements, reliable quantification of the different phases was performed. Only phases containing the two major elements of the grade, i.e. Cu and Ti, were considered as possible solutions. This rather simple assumption is first based on previous literature results [YAN 11] [FOR 11], and second coherent with the fact that Zr and Pd have electronic structures and atomic radii that allow them to substitute for Ti and Cu,respectively [HAR 94]. All the results (XRD patterns, EBSD maps, EDS, SAED-TEM and ASTAR TEM analysis) were consistent with this hypothesis, and it was observed that the major phases present have similar structures as: Cu_3Ti_2 , CuTi (tetragonal and B2 cubic) and $CuTi_3$.

All the spherulites morphologies presented the same phase arrangement: a primary needle with a similar structure as the Cu_3Ti_2 phase surrounded by perpendicular secondary needles of the CuTi-tetragonal phase. A third phase, with a macroscopic globular shape, indexed as the $CuTi_3$ phase is also present between the needles. All these phases are surrounded by large globular grains of the CuTi B2 phase. Note that for all the morphologies and spherulite sizes, the dimensions of the primary and secondary needles (between 20 and 40μm long and 1 and 2μm wide), as well as their orientation relationships (see Fig. 2.5) remained unchanged. Therefore, these phases are considered as the precursor.

Some areas were nevertheless not indexed using EBSD mapping, which is due to their nanometric size. At an even finer scale, using TEM ASTAR ACOM orientation mapping, structures typical for an eutectoïd reaction were observed (Fig. 2.8). The product phases were identified as CuTi and $CuTi_3$. For a CuTiZrNi amorphous alloy, Yang et al.[YAN 11], reported that the CuTi phase is unstable and undergoes a eutectoid reaction that also forms $CuTi_3$ among other phases. A similar type of reaction is expected for the present alloy, and the presence of this eutectoid aggregate indicates that the initial CuTi-tetragonal phase is not stable.

Additionally, a chemical ordering was observed in some of the CuTi-tetragonal needles, resulting in the appearance of nanometric large domains presenting long-range chemical ordering (Fig. 2.7). This phenomenon was already reported by Marschall [MAR 87] in an amorphous CuTi binary alloy. As this type of structure was only observed in the core of the large spherulites and not in the early structures, this decomposition occurs after the formation of the spherulite (in the solid state).

A growth scenario was deduced from these observations, and is illustrated in Fig. 2.11.

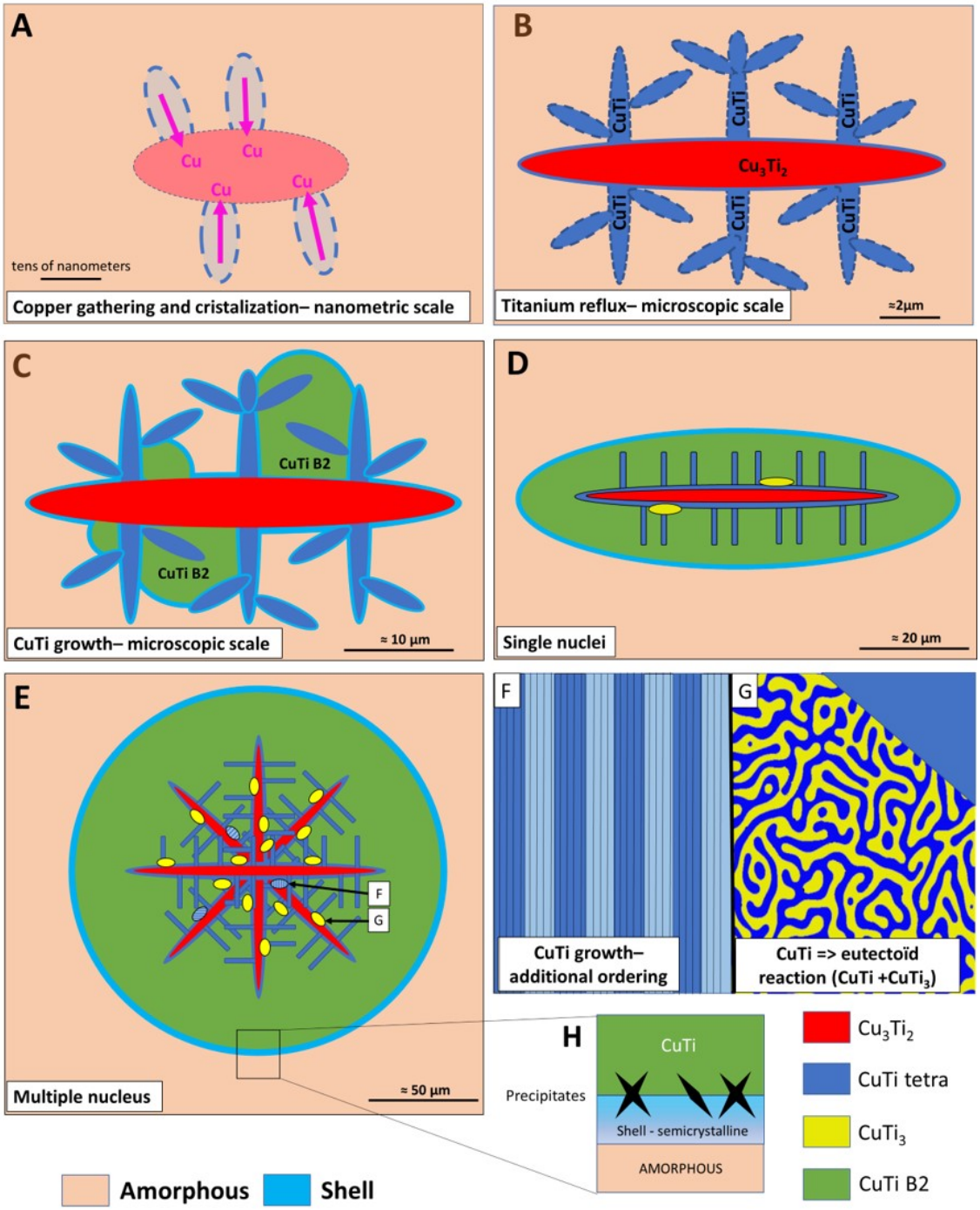

FIGURE 2.11 – Schematic representation of the growth mechanism proposed for the spherulites. B, rejection of Ti away from the Cu_3Ti_2 primary needles (red) and subsequent formation of CuTi secondary needles (dark blue). C, apparition of ordered CuTi B2 (green) around the secondary needles. D, resulting microstructure observed for small spherulites composed of a single nuclei of Cu_3Ti_2 . E, microstructure of larger spherulites, revealing showing the presence of several Cu_3Ti_2 primary needles. Additional phases are observed within these large spherulites with nano-scaled ordering of the CuTi phase (F) and the formation of the $CuTi_3$ phase through a eutectic reaction (G). H, is the shell of the large spherulites is composed of nano-scaled precipitates, and of a semi-crystalline layer

.

As described in Fig. 2.11, after nucleation, the Cu_3Ti_2 primary needle acts as a nucleation site for the other phases. These primary needles are enriched in Cu and poorer in Ti compared with the matrix (Fig. 2.11A). Thus, there is a diffusion flux of Ti from the needle towards the interface, while the Cu diffuses from the matrix towards the needle Therefore, a depletion of Cu around the needle is observed, which leads to the appearance of the secondary CuTi tetragonal needles (Fig. 2.11B), which are poorer in Cu compared with the matrix (composition $Ti_{45}Cu_{28}Zr_{11}Pd_{18}$). These needles do grow perpendicularly to the primary ones, and the orientation relationship between the two phases is the following <001> Cu_3Ti_2 //<001>CuTi and (001)Cu_3Ti_2 //(001)CuTi. Finally, a third phase appears, with a composition really close to that of the amorphous matrix and a globular shape, and with a similar phase structure as CuTi-B2 Fig. 2.11C. This phase might crystallize from the interface of the primary and secondary needles towards the amorphous matrix. For spherulites located in the core of the rods, CuTi globular grains encapsulate several needles in a spherical shape (Fig. 2.11E), whereas for the ones located closer to the external surface, the globular grains were smaller than the secondary needles (see Fig. 2.2 A and B and Fig. 2.11D). This finding indicates that the cooling rate may affect the growth kinetics of the spherulites. At a slower cooling rate, the CuTi globular grains have more time to grow and encapsulate the needles. Finally, as CuTi-tetragonal is not stable, a eutectoid reaction can occur, leading to the appearance of CuTi and $CuTi_3$ laths, see Fig. 2.11G. Some CuTi laths also undergo an additional chemical ordering, with the appearance of nanometre-thick ordered laths see Fig. 2.11H. This particular organization may enable the material to have a more thermodynamically stable interface.

The exact reason for the nucleation of the Cu_3Ti_2 primary needle remains unknown. This could occur before solidification, in the liquid phase or within the solid amorphous phase. No evolution was observed in the microscopic analyses during heat treatment at 500°C (just below T_g) of the sample, indicating that the amorphous phase is rather stable. Moreover, larger spherulites were mainly observed in larger rods or in the core of rod, indicating that the cooling rate has a direct effect on the growth rate of the spherulites. Therefore, we assume that the germs are most likely present in the liquid phase, during casting. Small longitudinal spherulite precursors, as illustrated in Fig. 2.11D contain only one primary needle of Cu_3Ti_2 , whereas the large spherulites (Fig. 2.11E) contain many Cu_3Ti_2 needles. This indicates that the nucleation of the primary needle, with one or more needles, directly affects the final shape and size of the spherulites. It is possible to formulate several hypotheses about the effect of the manufacturing process on the appearance of the spherulites. First, there may be not enough melting steps before the casting of the rod, which could result in non-melted areas or non-chemically homogeneous areas, therefore still organised areas at a very small scale. It is known that germination sites can be very small (a few nanometres) [HU 09]. Second, it is also possible that the cooling rate applied is not high enough to avoid the crystallization nose of the Cu_3Ti_2 ; the enthalpy of formation may be too low [INO 00]. Finally, there may also be some impurities in the

pure materials or oxygen/hydrogen contamination during the casting that act as preferential nucleation sites for Cu_3Ti_2 . Several studies suggest that spherulites may affect the mechanical properties. According to [HIN 19][LIU 12b], if the spherulites have a diameter below 100μm, plasticity before failure can be observed. This has been verified in this system in [GAU 22]. The presence of small, ductile spherulites in the amorphous matrix may generate a composite material behavior but may induce a brittle behaviour for larger sizes. Composite metallic glasses are mainly known for ZrCu and TiNi grades [CHE 21], the aim being to control the volume fraction of the crystalline phase to maintain a high mechanical strength while having a plastic deformation before failure in compression. The amorphous fraction is free of grains and of grain boundaries with no residual dislocations/stresses, giving it very high mechanical strength and a very high elastic energy storage. The crystalline fraction identified as the B2 ZrCu phase has, via a martensitic type transformation (under stress), the ability to transform into the B19' phase which macroscopically provides a lot of ductility. There is a blocking effect already documented in the literature that slows down crack propagation (increase in cell volume frome B2 to B19')[ZHO 20]. Although several studies have suggesedt that the same phenomena occur for TiCu grades [CHE 21], these are much less studied, and there is no published data in this sense for the grade studied here. As illustrated in Fig. 2.8, decomposition and ordering structures are indicators of a potential phase transformation.

To better control the mechanical properties of the material, the size of the spherulites must be controlled. Which can be realised using different methods. The first one consists of targeting the best glass forming ability (GFA) alloy composition, as illustrated in the work of Sypien et al [SYP 17] who studied this type of alloy with 10, 14 and 20 at.% Pd (replacing by Cu). A simple calculation of $GFA = \frac{T_x}{T_g + T_l}$ suggests that the alloy with Pd 14 at.% has the smallest GFA. It is probable that a small change in composition could decrease the enthalpy of crystallization and then reduce the volume fraction of crystals in the rods, however, to our knowledge this analysis has never been performed. The second and most important parameter for the size distribution control is the casting process. Arc melter suction casting does not allow precise control of the temperature, raises some questions about the master alloy chemical homogeneity (and the number of melts steps required [HU 09]) and the intensity of the arc used should be investigated in future studies.

2.4 Conclusion

This paper focused on a detailed description of the fine microstructure of crystalline spherulites embedded in an amorphous matrix of the $Ti_{40}Cu_{36}Zr_{10}Pd_{14}$ BMG alloy. This study reveals a complex microstructure very fine in the core (with two types of needles) and less and less complex until reaching the interface with the amorphous matrix. This interface contains precipitates of $CuTi_3$ and a not fully organized shell. Thanks to EDXS chemical composition analyses and the use of the CuTi binary diagram, candidate phases were proposed and tested in EBSD and on diffraction images from TEM analysis. The following phases structures were formally identified : Cu_3Ti_2 , $CuTi_3$, CuTi B2 and CuTi tetragonal. These phases are always observed at the same place in the spherulites and with the same orientation relationship to each other.
Spherulite structures at different stages of growth (from primary to mature) were observed allowing us propose a growth process consisting of the following main steps:

1. Formation of large needles of the Cu_3Ti_2 phase (primary needles)
2. This phase is surrounded by a second phase with finer needles oriented at 90° of a phase close to CuTi tetragonal (secondary needles). During solidification, a eutectoid reaction occurs which leads to the appearance of a small amount of $CuTi_3$.
3. The entire structure is surrounded by a semi-crystalline shell, which ensures the transition between order and disorder.
4. The CuTi B2 phase is present in majority in mature spherulites (the other phases are only present in the central part). It grows between the CuTi tetragonal phase and the shell in all directions until the temperature is too low to allow atomic movements giving the spherical shape to the spherulites.

Chapter 3

Impact of casting parameters and relaxation treatments on the microstructure and mechanical properties of $Ti_{40}Cu_{36}Zr_{10}Pd_{14}$ BMG

3.1 Introduction

Metallic glasses are materials with exceptional compressive yield strength and (at least theoretical) very good corrosion resistance due to the absence of dislocations and grain boundaries respectively, which leads them to be potential candidates as biomaterials for implants [ZHU 07a][ZHU 07b] [LIE 18]. However, following the recent discovery of crystalline spherulites in the biomedical BMG $Ti_{40}Cu_{36}Zr_{10}Pd_{14}$ (see chapter 1 and 2), the use of this grade for dental implant manufacturing has been questioned. BMG systems such as CuZr and CuTi appear to have a significant amount of crystalline fraction in the final piece. Indeed, they have ease to form B2 phases during the copper mold suction casting process [HON 18] [JIA 18b][CHE 21]. As a result of these findings, more and more researchers are adapting their strategy to counteract the brittle behaviour of BMGs by using the presence of this crystalline phase that arises during casting to improve the plasticity without sacrificing the mechanical strength or elastic properties of the BMG. The challenge for the "metallic glass composites" community is thus to control the size/distribution of the crystalline phase in the amorphous matrix[LIM 10][BER 20][PAU 09], the main guideline being to present spherulites sufficiently small after the process (i.e. all smaller than 100 μm) to avoid them to be considered as critical defects (see chapter 1 and 2).
The suction casting is one of the most common process used to manufacture BMG; however, it seems that each laboratory has its own know-how and protocols, sometimes with customized machines. These elements may explain, at least partly, the lack of reproducible results in literature, particularly in the evaluation of the toughness and endurance in fatigue for one grade [ZHA 03a], [YAM 14]. In the case of the $Ti_{40}Cu_{36}Zr_{10}Pd_{14}$ grade, the spherulites exhibit an important size (several hundred of microns) and are randomly distributed according to our previous work. They have so far been assimilated to defects

involved in premature mode I failures [BER 20], [HIN 19]. They could also be involved in the early appearance of shear bands leading to mode II failure. Their specific role in the material's response to corrosion has not been fully explained, although it would appear that the interface area between spherulite and amorphous matrix is particularly sensitive to dissolution but not really the spherulite itself. There is still no consensus on the influence of the presence of crystalline fraction on corrosion resistance. Its seems to vary from one composition to another, sometime crystalline phase increases the corrosion resistance and sometimes it decreases it. This depend mainly on the chemical composition of both. If the crystalline phases is enriched in highly corrosion resistant elements it will not dissolve preferentially at the expense of the amorphous matrix which will dissolve preferentially as explained in [DEB 12], [DEB 14]. In the case of $Ti_{40}Cu_{36}Zr_{10}Pd_{14}$, the difference in chemical composition between spherulite and amorphous matrix is very small indeed, so the moderate corrosion resistance of the BMG will probably not significantly be improved even without spherulite. The microstructure and constitutive phases of spherulites in the $Ti_{40}Cu_{36}Zr_{10}Pd_{14}$ BMG have been studied by electron microscopy (SEM and TEM) in the previous chapter. It would seem that the nucleation of the Cu_3Ti_2 phase is the first step in the appearance of spherulites. We still do not know the exact origin of the first nucleation of this phase but it is likely that the manufacturing process by suction casting has a pivotal role in the appearance of spherulites. First aspect studied here is the influence of cooling rate on the spherulite (number and size). To do so, two rods, one of ⌀5mm and one of ⌀3mm have been casted in the same conditions. The microstructures are compared by repeated optical microscopy observations. By increasing the cooling rate, it is expected to limit spherulite growth or maybe even avoid nucleation.

Strong assumption about spherulite nucleation adopted in this study, is that maybe there is unmelt areas (chemical heterogeneities are preferential nucleation sites) during the master alloy and rods preparation which can lead to spherulite apparition. In order to investigate this hypothesis, two distinct experiments are carried out in this study based on the melting step. As the temperature of the alloy during melting and casting is directly dependent on the arc intensity [RAD 92], it is likely that an increase in intensity will allow the melt of any previously unmelt areas. So, the first one relies on casting tests using different electric arc intensities (200, 300 and 400A). By increasing the are intensity it is likely that there are fewer spherulites in the rods because there will be theoretically less unmelt areas. The second approach, is based on the article [HU 09] which claims that the number of melts/flips has an significant impact on macroscopic mechanical properties of the alloy $Zr_{55}Al_{10}Ni_5Cu_{30}$. Increasing melts/flips number can improve chemical homogeneity and therefore limit nucleation mechanisms. To do, some rods were prepared with 6 and 14 melts/flips before casting, those rods were mechanically test in four-point bending test. Four-point bending test is chosen because compressive test seems to be less sensitive to the presence of casting defect ([GAU 22], [ZHA 03a]) and the tensile test would have required the machining of specimens (difficult in 3mm diameter rods) which would have result in

useful part of the same order of magnitude as a large spherulite. Four-point bending allows to stress at least one side of the sample under tensile stress and the other under compressive stress (see Material and Methods chapter for more details).
Another potential source of nucleation is pollution by light elements such as oxygen, carbon and hydrogen. Some previous studies suggest that the raw materials and vacuum quality can have a significant influence on the microstructure and amorphous state of as-cast rods. For example in [LIU 02] and [KER 06], the authors investigated the influence of oxygen level during casting. Both studies conclude that the oxygen presence has a deleterious influence on Zr-based BMG mechanical properties associated with embrittlement mainly due to crystallization under micrometric needles crystals shape. Others elements can be trigged inside the BMG structure such as hydrogen. In literature hydrogen is mainly considered as a microalloying element able to increase GFA of some alloys and therefore increased the free volume amount and alloys ductility ([GRA 15][SU 12][DON 12]). A TOF-SIMS (Time Of Flight - Secondary Ion Mass Spectrometry) acquisition is performed here to access the presence of light elements inside the spherulites. Additional casting tests are performed with enriched H_2 atmosphere to evaluate the influence of hydrogen on amorphous/crystalline ratio and on mechanical properties (compressive tests).
In BMG community, one of the common ways of customizing mechanical properties is to perform thermal treatment on the as cast rods to perform structural relaxation. The relaxation generally reduces the free volume of the BMG and increases it hardness but decreases its yield strength and its ability to deform plastically [XIA 10]. On the contrary, another approach rejuvenation which consist in different treatments (cold rolling, shot peening cryogenic cycle...) to increase free volume in the alloy and therefore improve its capacity to deform plastically [KRU 16]. Here, we choose to investigate the influence of thermal treatment on size and structure of spherulite using salt bath, XRD and microscopy. The temperatures chosen for heat treatments are previously based on DSC analysis (also used to perform GFA and critical diameter calculation in the Discussion).
Statistical analysis of the two population distributions (Snedecor method [SNE 89] described in Materials and Methods) of spherulites number and size are conducted to ensure the significance of studied parameters on spherulite numbers and size. The links between the studied parameters, the microstructure and mechanical properties will be addressed in the discussion of this chapter.

Organization of results:

1. Influence of the cooling rate
2. Influence of the melting parameters
3. Influence of light elements (hydrogen)
4. Influence of post-casting heat treatments

3.2 Results

3.2.1 Influence of the cooling rate

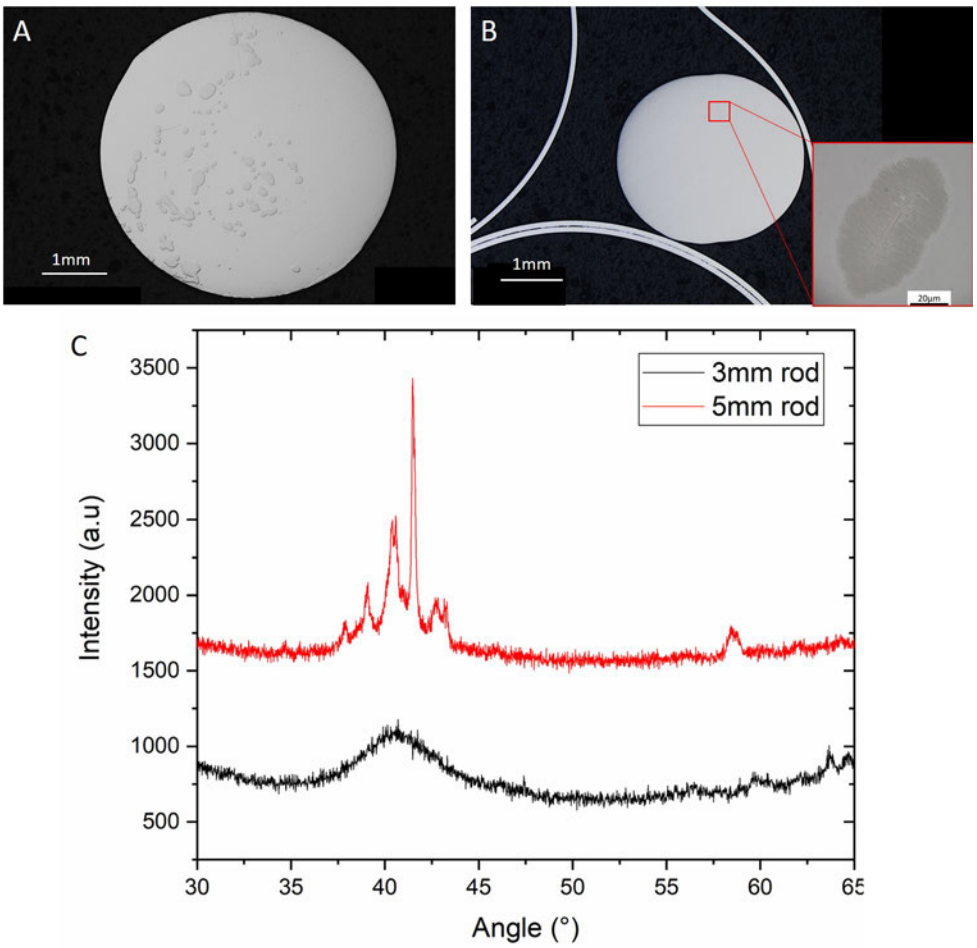

FIGURE 3.1 – A and B are optical pictures of polished $Ti_{40}Cu_{36}Zr_{10}Pd_{14}$ rod's cut. A, is a 5mm diameter as cast rod, and B is a 3mm diameter as cast rod. In picture A, we see a large number of spherulites randomly distributed throughout the rod and are visible. In B, there is no visible spherulites but an inset view of a small spherulite is visible. C, XRD diffractograms corresponding to each of the samples in A and B.

The study starts with the investigation of the importance of the cooling rate by the casting in different copper mold diameter. Two molds, one of 5mm and one of 3mm are used in the exact same conditions. The samples are polished to study their microstructure and analysed in XRD. Fig. 3.1 illustrates the difference of microstructure for the same alloy composition ($Ti_{40}Cu_{36}Zr_{10}Pd_{14}$) made in a 5mm diameter mold (A) and in a 3mm diameter mold (B). For the 5mm as cast rod, numerous and randomly distributed large spherulites can be observed. Observations at higher magnification also revealed preferential crystallization at the interface with the mold in some areas. In comparison, for

the 3mm as cast rod, no or very few spherulites (of small size) are visible on the picture, and as for the 5mm diameter rod, observations made at higher magnification also showed preferential crystallization at the interface with the mold in some areas but the thickness of the crystallized interface is less important. The diffractogram associated with each of these samples is presented in Fig. 3.1C, it agrees with the observations made previously. Indeed, well defined diffraction peaks are obtained for the 5mm as cast rod which betray the presence of numerous spherulites while no peak is observed for the 3mm as cast rod (none or few spherulites). To quantitatively reflect the difference in size and number of spherulites in the rods, microstructural observations by optical microscopy were made. The results are shown in Tab. 3.1.

TABLE 3.1 – Summary table of number of spherulite observed, number of spherulite/mm^2 and ⌀5mm rods and ⌀3mm rods.

Condition	⌀5mm (200A)	⌀3mm (200A)
Total number of slices observed	11	15
Total number of spherulite observed for each condition	69	4
Mean number of spherulite/mm^2	0,3	0,04
Mean diameter for on spherulite (μm)	172	76
Maximum diameter observed (μm)	740	118
Minimum diameter observed (μm)	37	32

For the 5mm diameter there are about 0.3 spherulites/mm^2. For the ⌀3mm diameter rods, there are about 0.04 spherulites/mm^2. The observations confirm that there are far fewer spherulites in the ⌀3mm diameter rods: about 10 times less. Furthermore, the size of the spherulites decreases with increasing cooling rate, on average 172μm for ⌀5mm rods and 76μm for ⌀3mm rods.

3.2.2 Influence of melting parameters

3.2.2.1 Arc intensity

Even in the 3mm as cast rods there are few small spherulites. It was anticipated that either the cooling was fast enough to avoid nucleation in the 3mm rods or limit spherulite growth. One major hypothesis, as mentioned in introduction, relies on the possible non-melted regions during the casting, the arc intensity can play a key role in this matter. We would have liked to investigate different arc intensities with 5mm diameter rods where an evolution of the quantity of spherulites is more likely to be observed. Unfortunately, the casting of 5mm diameter rods is experimentally difficult to achieve due to the viscosity of the alloy at such temperatures. Indeed, the alloy flows spontaneously into the mold without the operator having time to start the suction process. The samples are manufactured with a 3mm diameter mold. Two rods per conditions have been casted. The investigated arc

intensities are: 200A, 300A and 400A. The sample are then cut in few slices and mirror-polished to do some a F-Test to compare two variances at the level of significance p=0.05.

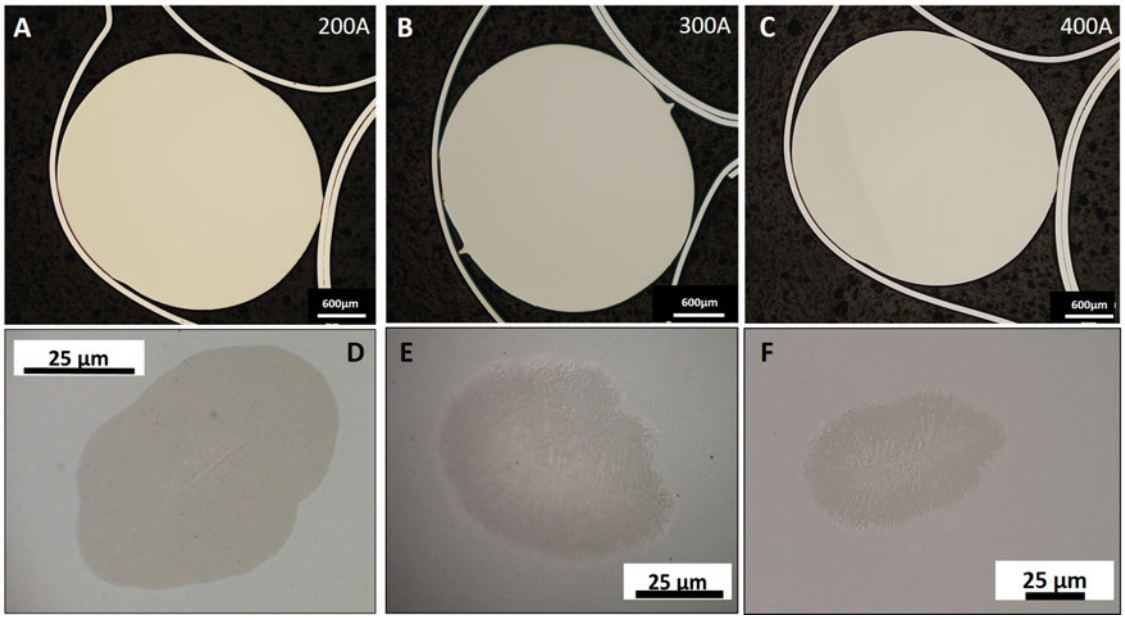

FIGURE 3.2 – Pictures A, B and C were taken using optical microscopy and illustrate the aspect of the microstructure of 3mm casted rods with different electric arc intensities and D,E and F are higher magnification pictures of the spherulite inside the rods. A and D- 200A. B and E- 300A. C and F- 400A.

Fig. 3.2 shows representative views of the microstructure observed in casted rods using various arc intensities (200, 300 and 400A). There is no visible significant difference between the three conditions in pictures A, B and C. The bar plots shown in Fig. 3.3A and B illustrate respectively the distribution of spherulite number and mean size of spherulite surface. On those plots, the result of the F-test is specified, this analysis test is done with the values gathered in Tab. 3.2. It can be seen that there is no statistical significance of the influence between the electrical intensity (of the arc during casting) on the number and spherulite's size inside the rods except for the number of spherulite between 200A et 400A (significantly more for 400A than for 200A).

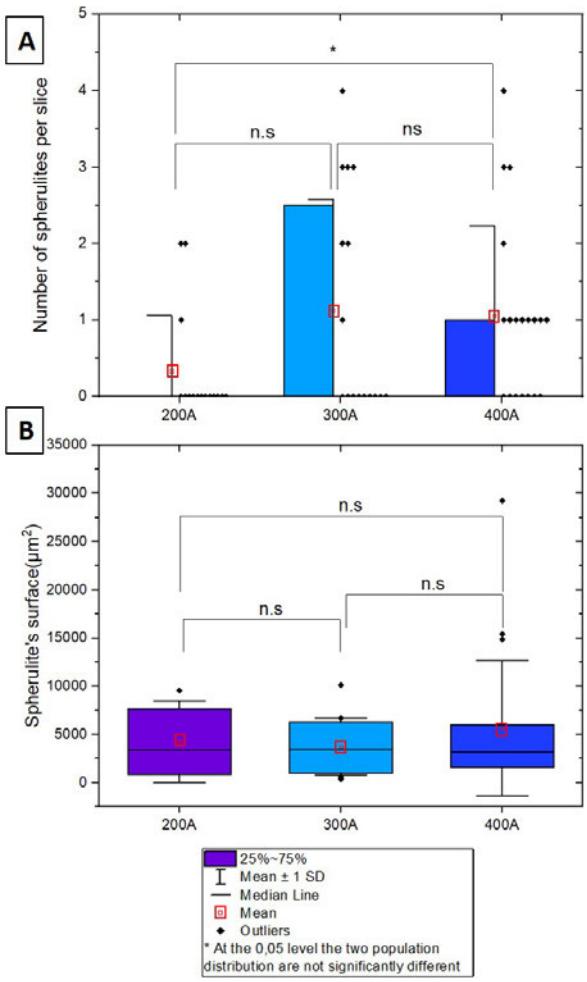

FIGURE 3.3 – Bar plots representing respectively the number of spherulites/slice(A) and the mean surface for one spherulite (B) as a function of the arc intensity used during rods casting. The statistical comparison of the distributions by a F-test (comparison of variance) is carried out at power p=0.05.

TABLE 3.2 – Summary table of mean, standard deviation (SD) and Variance of the number of spherulite/slice and spherulite's mean surface for each arc intensity (200,300 and 400A) used in Fig. 3.3.

	Condition	200A	300A	400A
Fig. 3.3A	Total number of slices observed	15	16	19
	Mean number of spherulite/slice	0,3	1,1	1,1
	SD	0,7	1,5	1,2
	Variance	0, 52	2,12	1,39
Fig. 3.3B	Total number of spherulite observed for each condition	4	18	20
	Mean area for one spherulite (µm2)	4250	3730	5670
	SD	4230	2920	7000
	Variance	$1.78x10^7$	$8.52x10^6$	$4.90x10^7$

Table 3.3 – Summary table of average Vickers hardness on amorphous matrix with standard deviation measured at 0.5kgF for the following three conditions 200, 300 and 400A (10 measurements per condition) as the arc intensity value used to manufacture the 3mm rods.

	200A	300A	400A
Hardness (HV 0,5kgF)	543 ± 8	543 ± 6	540 ± 10

The Tab. 3.3 reports the Hardness of the previous casted rods using an arc intensities of 200, 300 and 400A. The mean hardness in the amorphous matrix values are respectively 543 HV, 543 HV and 540 HV, those values agree with previous measurements (chapter 1). It seems that the electric intensity of the arc during casting have no important influence on sample's hardness. This result is consistent with the previous one, i.e. there is no significant change in microstructure so there is no significant change in hardness according to arc intensity with samples of 3mm diameter.

3.2.2.2 Remelted number

It is considered that the temperature reached through the electric arc is not homogenous over the entire thickness of the alloy during each melt, it is therefore legitimate to ask whether the number of melts is sufficient (6 in general) to have a chemically homogeneous alloy without a non-molten zone. As previously mentioned, those could be at the origin of the appearance of spherulites. Two rods are casted, coming from the same master alloy and the same number of melts. For 14 melts/flips the denomination is sample 1 and 2 and for 6 melts/flips it is sample 3 and 4. The rods from which the specimens are taken from, are previously scanned by X-ray tomography to avoid the presence of porosities before being tested in four-point bending tests. But prior to mechanical test, to quantify the crystalline matter amount evolution, a F-test at the 0.05 level was done as previously and presented in Fig. 3.4. The analysis was carried out on the data extracted from the observations of 15 polished sections per rod (four samples in total), the data are gathered in Tab. 3.4.

Table 3.4 – Summary table of the data plotted in Fig. 3.4. It gathers the average surface area of crystallized samples in % (15 measurements per rod), standard deviations and variances for each of the four rods tested in four-point bending.

Sample	14 melts - sample 1	14 melts - sample 2	6 melts - sample 3	6 melts - sample 4
Mean of cumulative crystalline matter/slice(%)	3.6	0.3	0.8	3.6
SD(%)	2.5	0.4	0.7	3.3
Variance	6.0	0.2	0.4	10.9

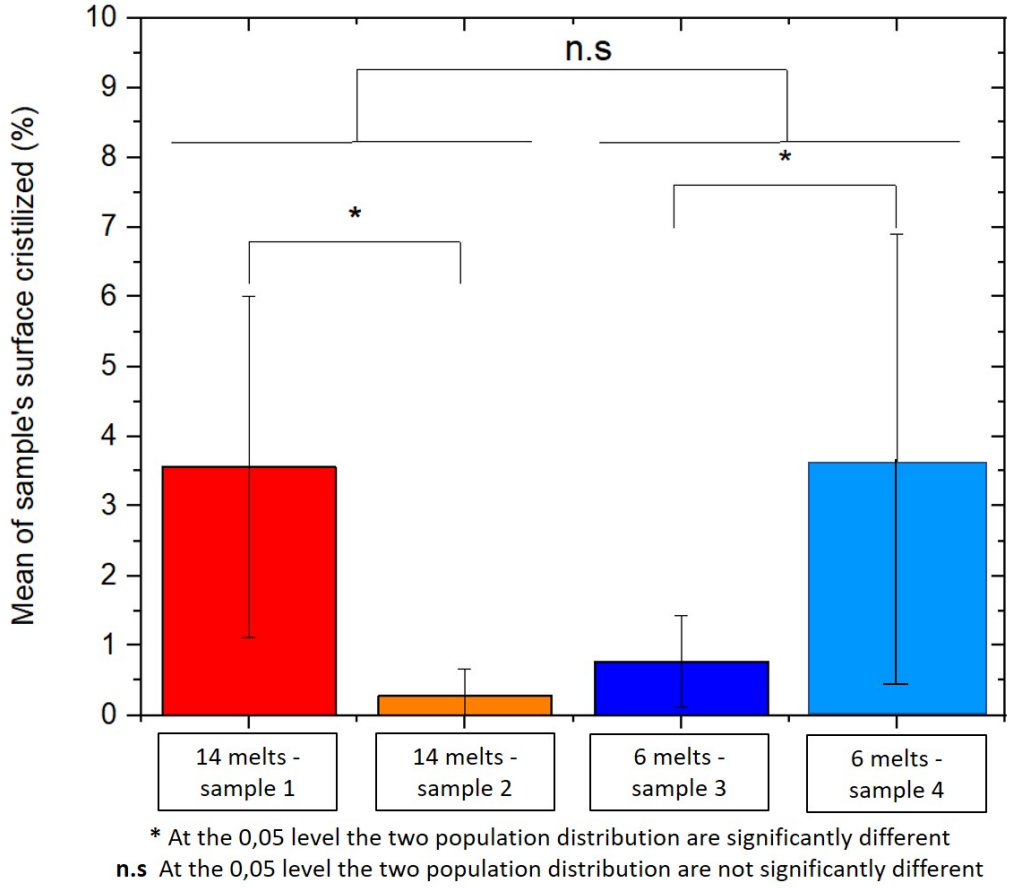

FIGURE 3.4 – Bar plot showing the means and standard deviation of % area crystallized per polished section for each rod tested in four-point bending. A F-test at a 0.05 level was performed to check the significant difference in distribution between the rods.

This analysis indicates that there are significant differences in distribution of the % of crystallized surface between 2 rods that are prepared under the same conditions (for 14 and for 6 melts). For the sample 1, there is an average of 3.56% of crystallized surfaces whereas for the sample 2, only an average 0.28% of the surfaces which are crystallized. For sample 3, on average 0.77% of the observed surfaces are crystallized, whereas for sample 4, a mean of 3.60% of the surfaces are crystallized. The data are pooled into two categories (14 and 6 melts with and N=30 observations/categories), and there is no significant change in distribution between the pooled 14 and 6 melts. The link between the number of melts and the volume of crystallized material has not been demonstrated here.
To investigate the influence of the number of melts on mechanical properties, four-point bending tests is carried out on 3mm as cast rods (machined to 2.8mm) which master alloy is either melted/flipped 6 times before casting or 14 times before casting. Four-point bending is chosen to avoid pure mode II loading (compression), which has already been

shown to be less sensitive to casting defects (Chapter 1) and easier to perform than tensile tests (larger useful part of specimens tested in bending). The four-point bending allows one side of the specimen to be tested in tension and one side in compression (See Figure 34 in Material and Methods). The use of four-point rather than three-point bending also allowed us to limit shear on the useful part of the specimen and to present a large surface of the material in tension.

Fig. 3.5A shows the stress-displacement curves for four-point bending tests conducted on cylindrical BMG specimens with two numbers of melts (14 or 6) compared to specimens from 5mm as cast rods (with diameter rectification before test). The stress σ_{4PB} is estimated by the Eq.(2)(Material and Methods). There is a wide spread of results in this test with mechanical strengths ranging from 590 to 3700 MPa. The B, C, D and E pictures show a comparison of the appearance of the fracture surface of the worst and best specimens. For the specimen that broke at low load (pictures B and C) it can be seen that the fracture occurs at about 90° on tensile side with a very flat aspect. Seen from above (B), it seems that the initial fracture appears in the left corner close to the maximum tensile stress point. For the specimen that showed surprisingly high mechanical strength (D and E), it exhibits rough fracture surface with both shiny and matt areas corresponding to more ductile fracture, (e.g. after the test, the specimens are no longer able to roll perfectly on a flat surface). It is likely that the starting point appears in the lower right corner of image D. Zooming in on this area in particular, nothing special is observed, no spherulite is visible. Furthermore, it appears that the specimens from sample 2 and sample 3 (orange and dark blue curves) broke at lower displacement than the other specimens (with less crystalline matter). It can also be seen that the specimens from a 5mm as cast rod showed more than satisfactory mechanical strength. It appears that the specimens that broke at the highest stresses plasticized before breaking, which is not the case for the specimens that broke rapidly in a brittle manner.

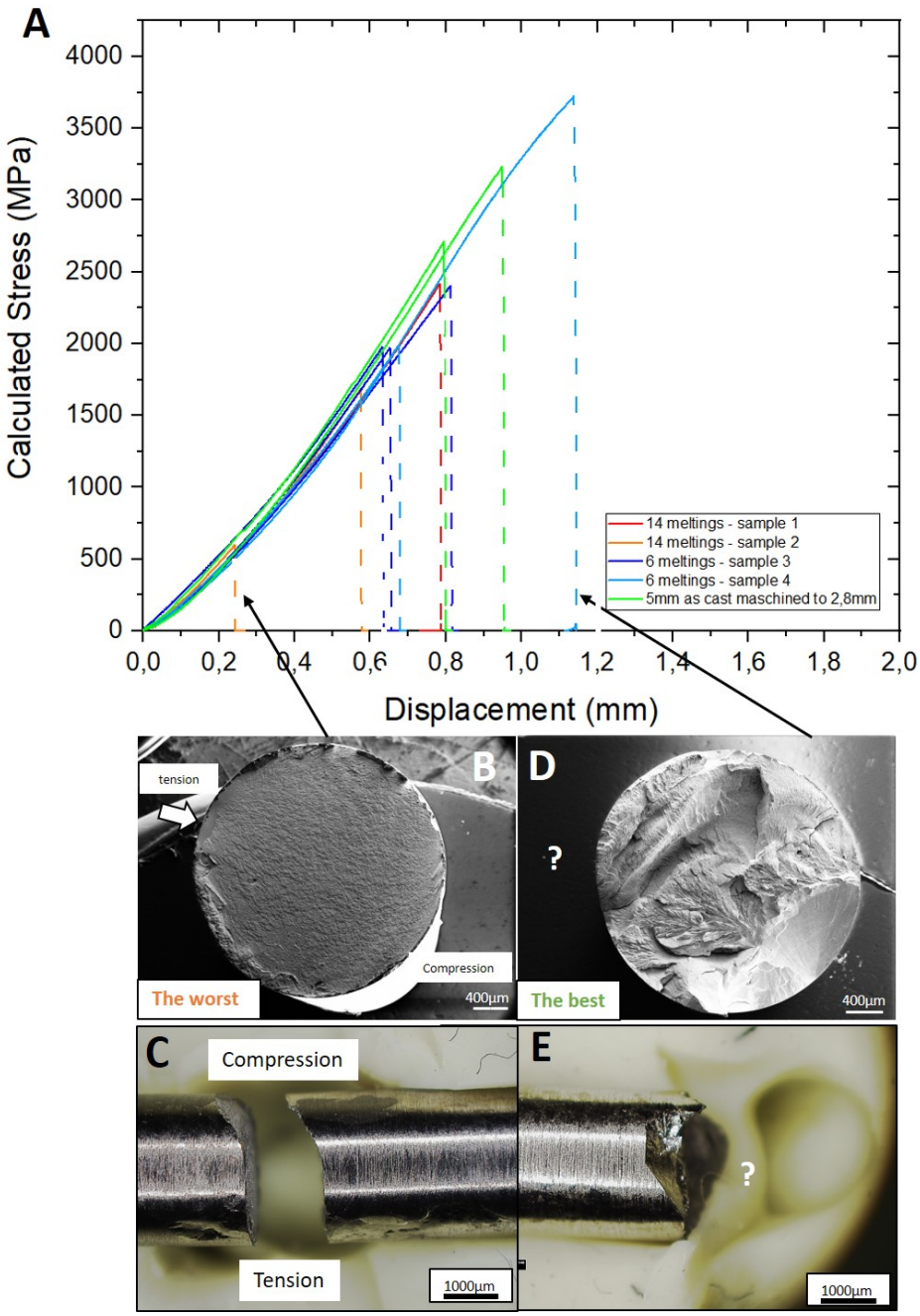

FIGURE 3.5 – A) Stress (MPa) vs. displacement (mm) curves for two samples populations. The red and orange curves represent the rods for which the master alloy had been melted and flipped 14 times before the casting. The dark and light blue curves represent the rods for which the master alloy had been melts/flips 6 times before the casting. B and D are respectively SEM pictures of the "worst" and "best" sample's fracture surface according to Yield strength after test. C and E are pictures of the "worst" and "best" samples profile.

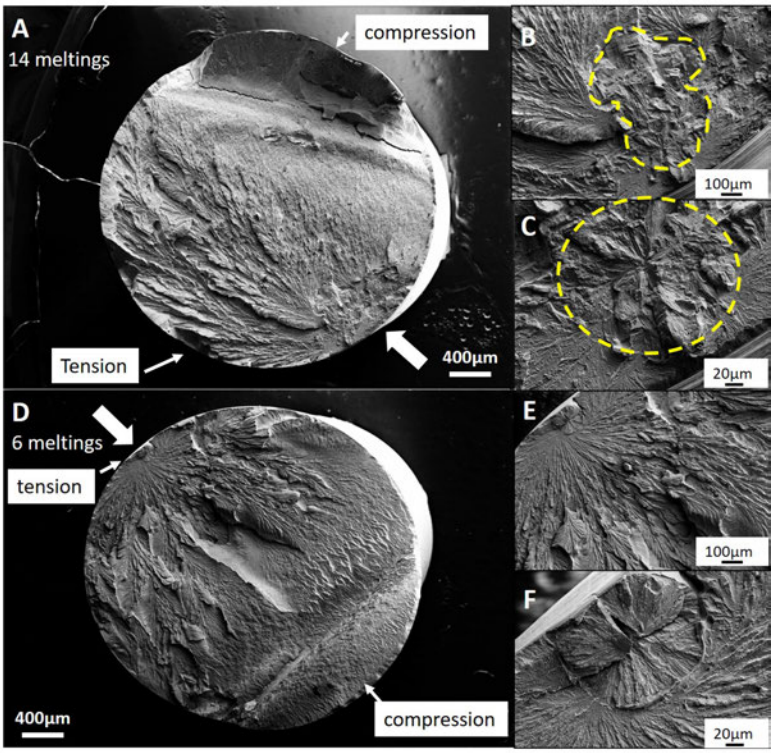

FIGURE 3.6 – SEM pictures of the fracture surface obtained by four-point bending. A/B/C were taken on a specimen that had been melted 14 times before casting and broke at 2405 MPa. D/E/F were taken on a specimen that had been melted 6 times before casting and broke at 1972 MPa. On both of the samples, there is a spherulite easy to identify which is the starting point of the fracture (big white arrow).

Fig. 3.6 shows the surface fracture of two specimens tested in four-point bending test. On these two samples, it is easy to determine the starting point of the main crack. In both cases, it can be seen that one or more spherulites are the starting points of the main crack. Unfortunately, the four-point bending tests are carried out on cylindrical specimens in a hard material (no trace left by the rollers) which did not allow us to locate with full confidence the tensile and compressive faces and the relative position of the defect with respect to these. But according to the surface profile it is possible to identify the faces in compression and tension. In most cases, the initial crack appears at 90° to the surface of the specimen on the tensile side. It then propagates in this way until it reaches the compression stress area which deflects the main crack before complete failure (as illustrated in Fig. 3.5C). For the condition 14 melts (in Fig. 3.6C), the initial defect has a surface of about 0.13mm^2 and about 550 μm in equivalent diameter, its position is not exactly in the maximum stress area. For this sample, failure occurred at a stress of 2405 MPa. For the samples with 6 melts (Fig. 3.6D,E,F), the initial defect has a surface of approximately 0.016mm^2 and 125μm in diameter, its position is believed to be in the exact area of maximum stress. For this sample, failure occurred at 1972 MPa. Those results will be further addressed in the discussion.

3.2.3 Influence of hydrogen

Following the previous results, apart from the cooling speed (related to the size of the mold), the heating mode (arc intensity and the number of melts) did not have a significant influence on the number and size of spherulites observed. Another possible explanation is impurities present inside the raw materials. To assess this hypothesis, TOF SIMS (Time Of Flight - Secondary Ion Mass Spectrometry) mapping is carried out. The TOF-SIMS map is a quantitative elemental surface analysis that can be done in two different polarizations. The positive polarization to quantify the heavy elements and the negative polarization for the light elements.

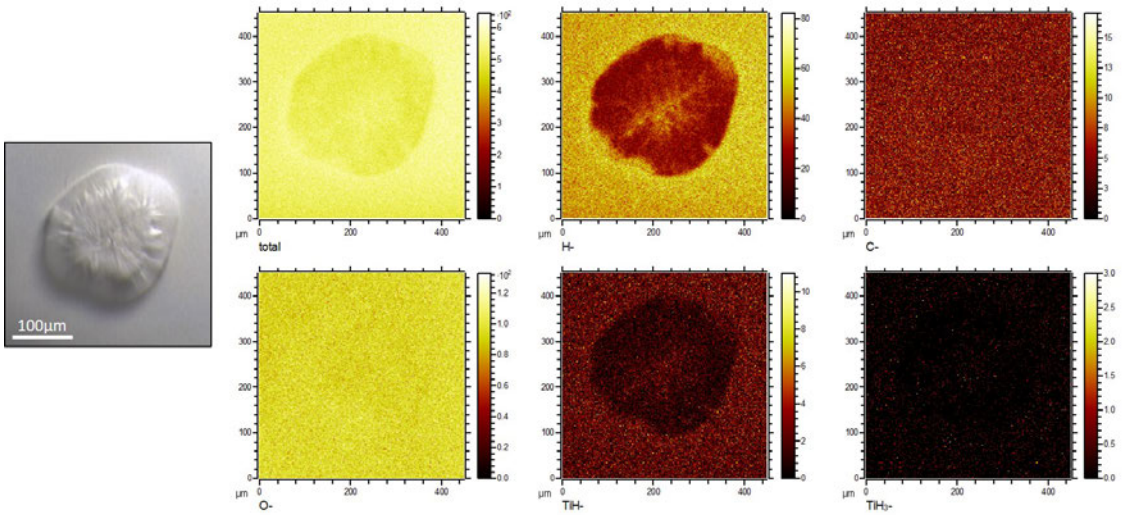

FIGURE 3.7 – TOF-SIMS (Time Of Flight - Secondary Ion Mass Spectrometry) analysis resulting in ion intensity images obtained in microprobe mode. This is a very high sensitivity method for elemental analysis of extreme surface. On this figure, on the left there is a picture of the targeted spherulite for the analysis. On the right, are presented the ionic images in negative polarity: H, C, O, TiH and TiH_3.

In positive polarization (results not shown here), there is no particular change in intensity observed for the elements Ti, Cu, Zr and Pd between the amorphous matrix and spherulites. However, under negative polarization shown in Fig. 3.7, a strong change in intensity is visible with hydrogen and TiH maps. It appears that the needles in the core of the spherulites and the amorphous matrix are richer in hydrogen ions than the periphery of the spherulites (local depletion). These results suggest that the presence of spherulites is probably not linked to oxygen or carbon pollution of the initial raw metals but highlights the potential involvement of hydrogen in this phenomenon. To determine the influence of hydrogen on the amount of crystallized matter in the rods, 3mm rods were made with and without the addition of H_2 in the arc melt chamber during the preparation of the master alloy and casting.

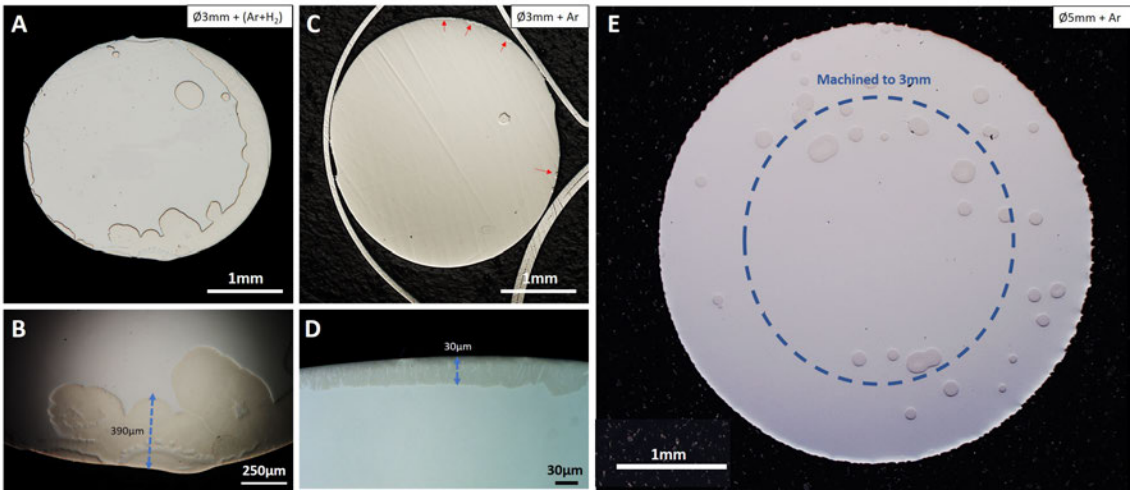

FIGURE 3.8 – Pictures of representative polished cuts of the microstructure inside the rods manufactured under different conditions. A, specimens casted in a 3mm diameter mold in an Argon + 3%H_2 atmosphere. B, zoom on the lower part at the copper mold interface of the as cast rod of 3mm diameter in Argon + 3%H_2 atmosphere. C, specimens casted in a 3mm diameter mold (pure argon atmosphere). D, zoom on the lower part at the copper mold interface of the as cast rod of 3mm diameter (pure argon atmosphere) E, specimens casted in a 5mm diameter mold (pure argon atmosphere) and machined down to 3mm diameter.

Fig. 3.8 shows optical microscopies of polished sections representative of each previous casting condition tested under compressive stress (3mm+Ar, 3mm + Argon + 3%H_2 and 5mm+ Ar). For each case the "least amorphous" section is shown (out of 15 observations for each condition). For the ⌀3mm-as cast condition (Ar +H_2) shown in A, there are few individual spherulites, so it is difficult to make the same statistical analysis (number of spherulite and surface) as in Fig. 3.2. However, it can be seen that the surface fraction (and therefore probably the volume fraction) of crystallized material is much higher for the Argon + H_2 casting (photos A and B) than with pure Argon (photos C and D). At the interface zones with the mold (B and D), the thickness of the crystallized zone is about ten times greater in the presence of hydrogen than without it (respectively 390µm and 30μm). In addition, during the rods casting, it was noticed that the surface of the rods prepared in the presence of hydrogen had a generally less smooth surface. In the rods prepared in a 5mm diameter mold there are significantly more and larger spherulites than in the rods prepared in the 3mm diameter mold (Same as in Fig. 3.1). The spherulites are randomly distributed, with a preferential crystallization at the interface with the mold (which is eliminated when the diameter is rectified to 3mm for the following compressive tests show in Fig. 3.9). Then the rods are tested in compression to evaluate their mechanical properties (compromise between number of samples and limited amount of material).

Fig. 3.9A shows the stress-strain curves under compressive stress for three casting conditions: 1) specimens casted in a 5mm diameter mold under pure argon atmosphere and machined down to 3mm diameter (blue curves). 2) specimens casted in a 3mm diameter mold under pure argon atmosphere (green curves). 3) specimens casted in a 3mm diameter

mold in an Argon + 3%H_2 atmosphere (red curves). The conditions 1) and 2) are chosen to determine the influence of the cooling rate on the compressive mechanical properties. The conditions 2) and 3) are chosen to determine the influence of hydrogen on the compressive mechanical properties. The graph shows good reproducibility for conditions 1) and 2) but a wide dispersion of results for condition 3). The mean values and standard deviations of the Young's modulus and maximum stress for each condition are summarized in Tab. 3.5.

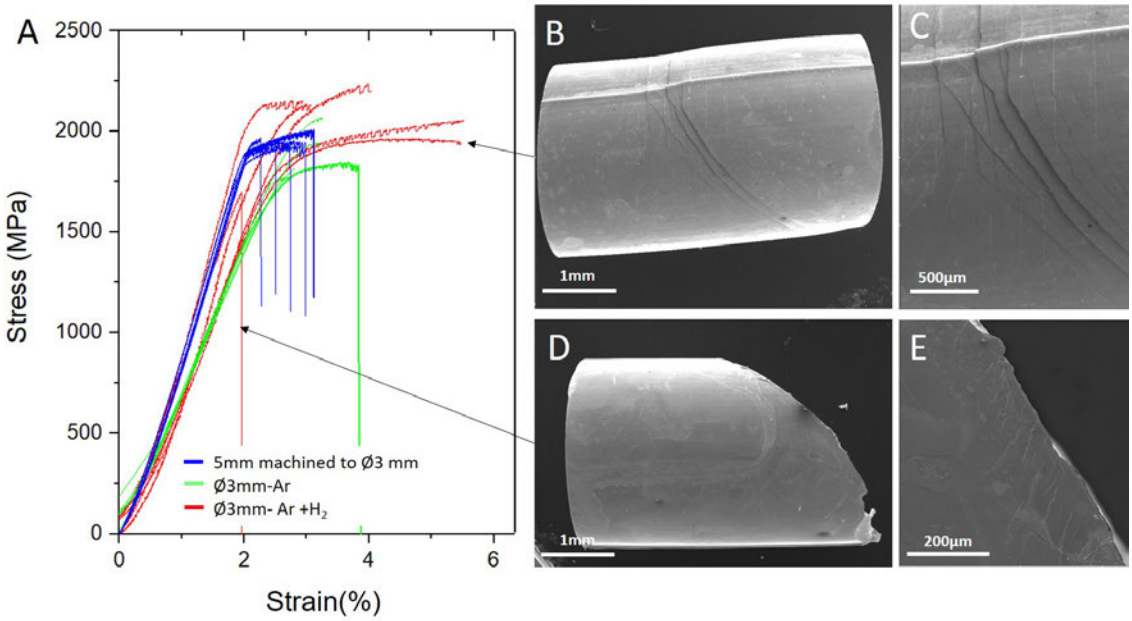

FIGURE 3.9 – Compressive stress-strain curves of three sample populations. In blue, specimens casted in a 5mm diameter mold (pure argon atmosphere) and machined down to 3mm diameter. In green, specimens casted in a 3mm diameter mold (pure argon atmosphere). In red, specimens casted in a 3mm diameter mold in an Argon + 3%H_2 atmosphere. B/C/D/E are SEM picture of one ductile sample (B and C) and one brittle sample (D and E).

TABLE 3.5 – Summary table of Young's modulus (GPa), mechanical strength (MPa) and plastic deformation (%) for the three manufacturing conditions (5mm as cast, 3mm as cast and 3mm as cast Argon + H_2).

Compressive test	E(GPa)	σ_{max} (MPa)	ϵ_p (%)	Hardness Vickers (0,5kgF)
⌀5mm as cast machined to ⌀3mm	100±5	2010±15	0,3 - 0,7	556±4,5
⌀3mm-as cast	75±5	1760 - 2060	0,4 - 1,3	543±8
⌀3mm-as cast (Ar +H_2)	93±12	1700- 2230	0 – 2,9	547±7

From these compression tests, there is a significant decrease (25%) in Young's modulus values following a change of mold diameter (cooling rate), from approximately 100 GPa for 5mm as cast rods to approximately 75 GPa for 3mm as cast rods. Similarly, the σ_{max} supported are on average higher for 5mm as cast than for 3mm as cast. However, a significant higher plastic deformation is seen for 3mm as cast rods.

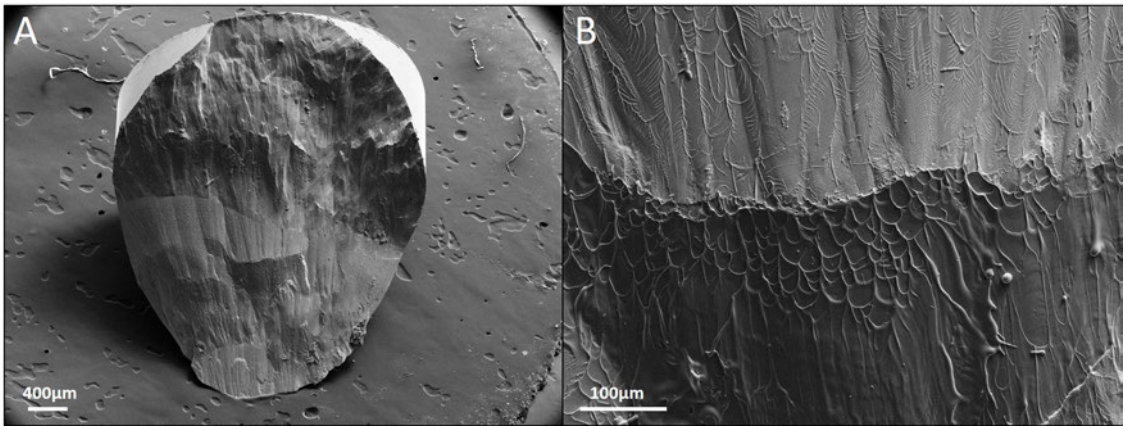

FIGURE 3.10 – Surface fracture of a compressive test specimen. A is a typical brittle fracture surface. B is typical vein pattern on the same sample.

Regarding the ⌀3mm as cast (Ar $+H_2$) condition, the behavior is more scattered exhibiting sometimes a brittle fracture and sometimes some surprising ductility as shown in Fig. 3.9 A (red curves). This leads to some difficulties in understanding the exact effect of hydrogen on the mechanical properties. The fracture surfaces exhibit features typical of a brittle fracture with vein pattern in mode II (shown in Fig. 3.10), but not clear difference is observed between the different conditions. However, looking at the profile of the test specimens in Fig. 3.9B and C, it can be seen that the specimens showing macroscopic plastic deformation show numerous shear bands along the maximum stress axis. The area with shear bands is approximately 1mm thick. In contrast, in Fig. 3.9D and E for specimens with macroscopic brittle behavior, there are far fewer shear bands in a much narrower area (180μm on one half of the specimen and probably about 360μm in total).

3.2.4 Influence of post-casting heat treatment

After trying to modify the spherulite's amount and/or size inside the rods during heating and cooling steps, the role of the post casting heat treatments in salt bath is investigated. The main enquiry is to test if the spherulite are stable structure or not and if it is possible to make it grow after casting. The heat treatment temperatures are based on a previous DSC analysis which results are presented in Fig. 3.11.

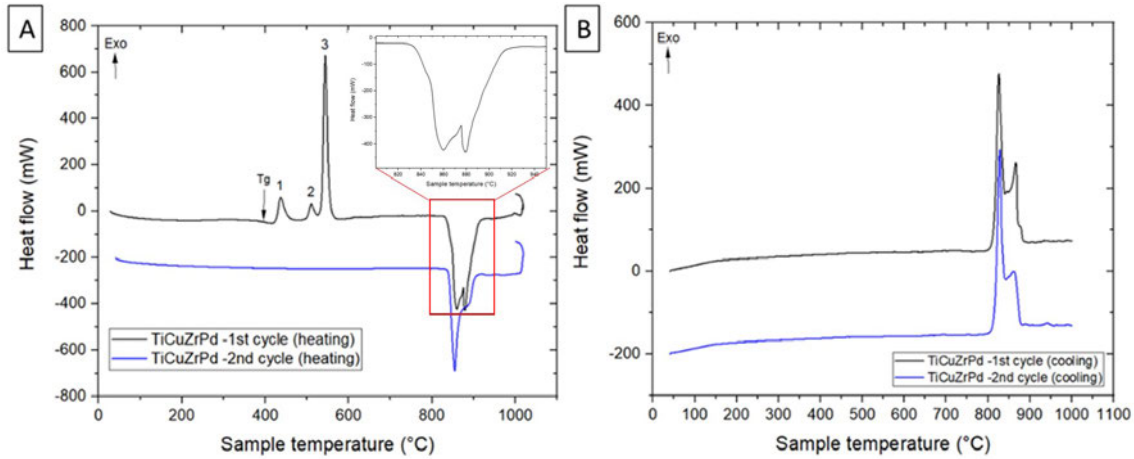

FIGURE 3.11 – DSC curves heat flow (mW) as function of sample's temperature. A, shows the two heating cycles and isothermal curve. B, shows the two cycles cooling curves.

Fig. 3.11 shows the heating and cooling curves of two consecutive cycles in DSC at 10°C/min. On Fig. 3.11A (heating), on the black curve (1st cycle), the glass transition temperature had been determined to be at 395°C. Then, there are three successive exothermic peaks respectively at 438, 513 and 543°C which correspond to crystallisation peaks. Above 836°C, there are probably three endothermic peaks (see inset in A) which correspond to the melting peaks of the alloy. The liquidus temperature of the grade is estimated here at 910°C. During cooling Fig. 3.11B (black curve) there are at least two solidification peaks at 882 and 828°C (a deconvolution analysis could lead to a more accurate analysis of the number of peaks actually present). During the 2nd cycle (blue curve on A and B), neither the T_g nor the crystallization peaks are visible which is logical since the sample is fully crystallized at the end of the 1st cycle. The melting and solidification peaks of the 2nd cycle is almost equivalent to those of the first cycle. It is likely that the small differences are due to a reaction between the sample and the alumina crucible used for the analysis. The DSC data obtained will allow GFA calculation of the $Ti_{40}Cu_{36}Zr_{10}Pd_{14}$ grade in discussion.

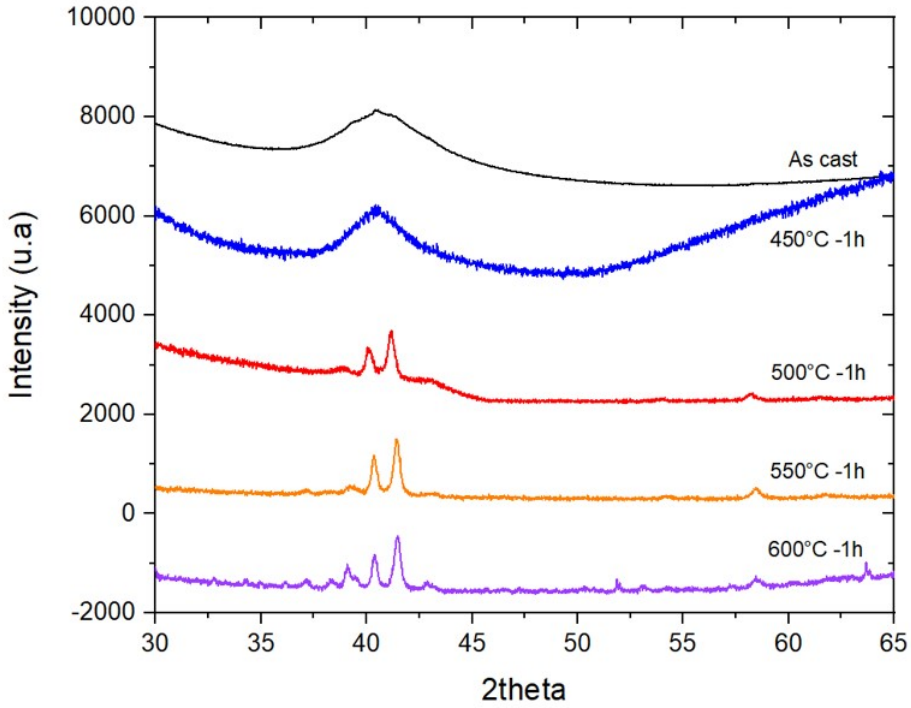

FIGURE 3.12 – X-ray diffraction of specimens casted in a 3mm diameter mold (pure argon atmosphere) heat treated in a salt bath. The times and temperatures are shown directly on the graph.

The Fig. 3.12 shows X-Rays diffractograms corresponding to the influence of heat treatments in salt bath on the crystalline state of the 3mm as cast rods (initially almost 100% amorphous rod). It can be seen that after a heat treatment at 450°C for 1h (above T_g and the first crystallization peak at 438°C) according to the DSC (curves presented in Fig. 3.11A), there is no visible peak in XRD. On the other hand, for all the other treatments, the higher the temperature, the more crystallized the samples are and the more intense and narrow the peaks are. The aspect of the peaks reflecting the presence of larger and more numerous crystalline grains. It is interesting to note that the peaks visible in this diffractogram are close to the one obtained in the XRD diffractogram on a cluster of spherulites given in Chapter 2, Figure 1. It is therefore likely that these peaks are not related to an increase of the size of the spherulites in the rods. Especially since the peaks obtained in Fig. 3.12 can be identified here as CuTi which is the main spherulite phase.

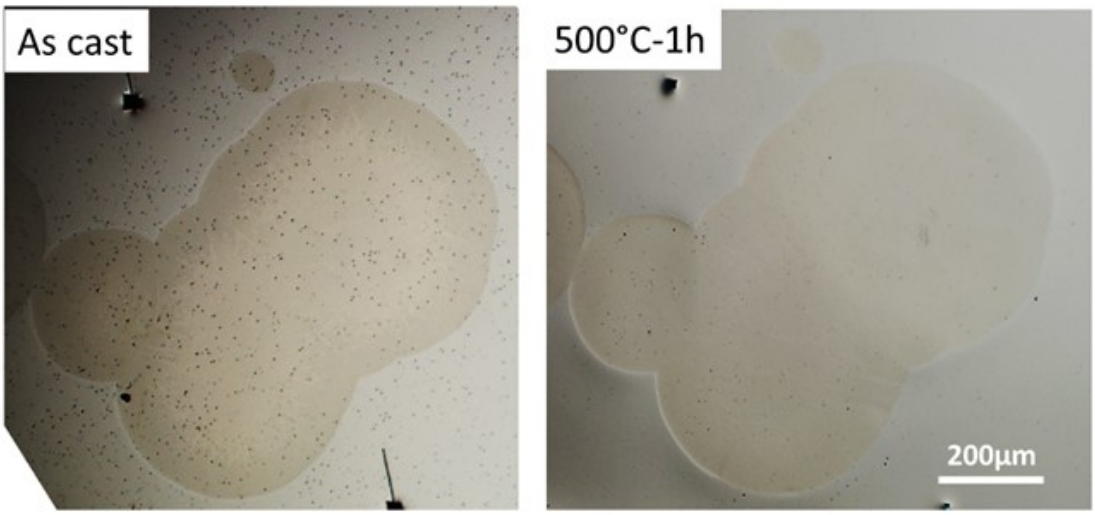

FIGURE 3.13 – Optical pictures of the same spherulite before (as cast) and after a 1h heat treatment at 500°C (left picture).

Fig. 3.13 shows pictures of the same spherulite before and after a salt bath treatment (500°C-1h). These observations show that the spherulites do not grow during the heat treatments tested in this study. Furthermore, no visible change in the amorphous matrix was observed in optical and SEM observations in the amorphous matrix (results not showed here). Some hardness measurements (Vickers at 0.5kgF) were made on the amorphous matrix of a sample which spent 1h at 550°C in the salt bath (orange curve in XRD Fig. 3.12). On average, the hardness measured was 726 HV after 1h at 550°C, i.e. an increase of about 35% compared to an as cast sample (550 HV). This change in hardness is indicative of the evolution of the amorphous structure, which will be discussed in the next section.

3.3 Discussion

Since their discovery, spherulites were initially considered as defects that could affect mechanical properties before being considered as potential reinforcements by obtaining composite BMG. In previous study, it was shown that they may have a negative influence on tensile strength, fatigue and potentially corrosion resistance [GAU 22]. Several parameters of the copper mold suction casting were tested here to assess their influence on size and repartition of spherulite on mechanical properties of the resulting rods. As it is not possible to directly visualize spherulites in 3D in the rods by using X-ray tomography due to the absence of chemical difference between amorphous matrix and spherulite. The statistical analyses used in this study appeared to be the best method to quantify spherulite evolution but they have limitations: first, they are based on observations of 2D sections to characterize 3D objects (spherulites) which are only estimations (minimizing the real

values [SAL 58]) of the actual diameter/surface of the spherulites. Moreover, the number of observations is relatively limited for each condition, some results are appearing insignificant with the chosen parameters and could become significant with a larger sampling but it is particularly difficult to achieve from an experimental point of view (quantity of samples limited by the price, its elaboration time and preparation and observation of the samples).

3.3.1 Effect of cooling rate

It is commonly accepted in the literature that the cooling rate has a fundamental importance on the state and properties of the obtained glasses [TUR 69][DAV 75][INO 00] . In the case of $Ti_{40}Cu_{36}Zr_{10}Pd_{14}$ alloy, there is no exception to this principle and Fig. 3.1 and Tab. 3.1 well illustrate this statement. By decreasing the size of the mold (to ⌀3mm), the cooling rate is directly increased, the rods are then cooled faster and resulting in a different amorphous/crystalline ratio compared to the ⌀5mm rods. In the case of a mold with ⌀3mm, the sample is almost completely amorphous (rare and small spherulites), whereas in the case of a mold with a ⌀5mm, numerous and large spherulites are visible. This was well illustrated in the study of [HAA 18] were they monitor the alloy temperature in a "V" shaped mold during solidification. Beyond the microstructure alone, which is impacted by the mold diameter, it is likely that the amount of free volume also depends on the cooling rate [XIA 10], [ZHU 14]. The theory of free volume [TUR 69] [ARG 79][SPA 77], defines the amount of free space available for the movement of the atoms in the frozen amorphous alloy. Following this assumptions, the compressive tests curves presented in Fig. 3.9 showed an decrease in Young's modulus for a ⌀3mm as cast rod, which is surprising compared to [XIA 10] where all the samples keep the same young modulus (only the amount of plastic deformation change). However, the faster cooled samples showed more plastic deformation than the others as in literature. Moreover, there is a higher amount of crystalline material in the 5mm diameter rod than in a 3mm diameter rod. If we assume that we are in a composite material with various amorphous/spherulite ratio: in the case of ⌀5mm rods there are larger and numerous spherulite in addition of a limited amount of free volume in the amorphous matrix. Maybe in the case of 3mm rods, there are less spherulite with more free volume available. The microscopically observed Young Modulus then can be higher for ⌀5mm rods than for the ⌀3mm rods. The plastic deformation is greater on the 3mm diameter as-cast specimens because it contains probably more free volume which allow the creation of more shear bands along the main shear axis on the highly deformed specimens prior to failure. In the future it would be interesting to perform tensile tests on specimens taken from 3mm rods as the size of the spherulite is on average smaller ($\approx 76\mu$m) than the size of the estimated plastic zone of (about 100μm) in this alloy [GAU 22]. In this configuration maybe, some ductility could be seen under mode I.

3.3.2 Effect of melting parameters

As the starting point for spherulite nucleation has not been formally identified yet, there are two main hypotheses about initial nucleation. The first one is: insufficient heating temperature and the second one: a lack of chemical homogeneity. It can be seen that even on the 3mm as cast samples there are some spherulites (in the core and at the interface with the mold) whereas this grade is claimed with a critical diameter of 6mm [ZHU 07a][OAK 07]. It is therefore likely that during the preparation of the rods, some areas of the master alloy are maybe not fully melt [LIU 12a]. In the arc furnace, the heat generated by the electric arc is not homogeneous but rather exhibits a gradient leading to some cold spots where the master alloy can stay solid. This assumption is schematically represented in Fig. 3.14. Furthermore, the part of the material in contact with the mold is necessarily colder than the part in contact with the argon atmosphere in the furnace chamber [GUE 20]. Then the rod will be casted, and the nucleus according to its position in the liquid (in contact with the mold or in rod's core) will be the starting point for crystallization which will lead to the apparition of spherulites of varying size depending on the cooling time, number of nucleus in the rod but also needle-like structures in the case of an isolated nucleus.

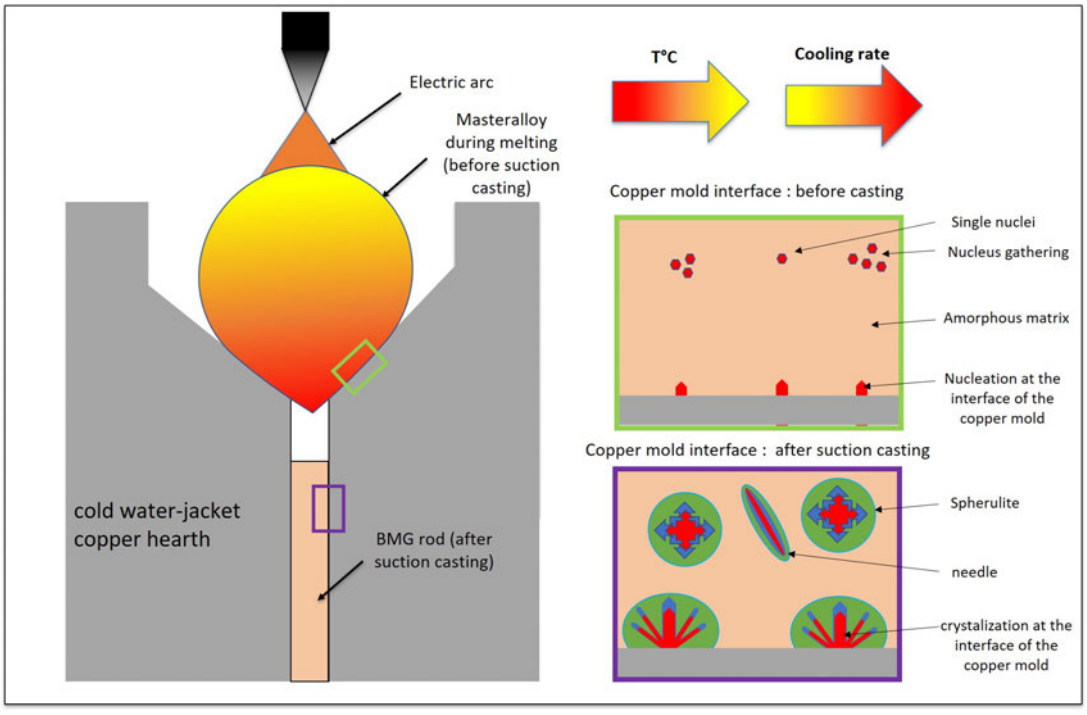

FIGURE 3.14 – Schematic illustration of the interface with the copper mold. At the proximity of copper crucible (green square) there still can be non-melted zones which will serve as nucleus, and which will maybe grow during the solidification step (purple square).

To test this hypothesis of potential, unmelt areas, two experiments were carried out in this study. The first one is the casting tests with different electric arc intensities. However, the results in Fig. 3.2 and its associated statistical analysis showed that there is no significant influence of arc intensity on the number and size of spherulites observed inside the rods. It is therefore probable that even at 200A the alloy temperature is above the liquidus temperature (estimated at 910°C by DSC analysis) so this hypothesis is not confirmed. Others have investigated the influence of arc intensity on a Zr based BMG [LIU 18][TAN 11]. In [LIU 18], they concluded that there is a direct correlation between the intensity and microstructure on their samples. The lower the arc intensity used, the more likely the sample was to be crystallized. They also mention the occurrence of phase separation in the liquid phase, which has a considerable influence on the mechanical properties under compressive stress. Maybe there were no visible difference in microstructure but at a finer scale the difference in free volume could have been changed via the arc intensity. It is also possible that the diameter of 3mm was too thin and the cooling too high to see a significant change according to the arc intensity. The amount of master alloy is greater for the preparation of a ⌀5mm rod than for a ⌀3mm rod. Therefore it is likely that the greater the amount of master alloy the more the heating step may influence the rods crystalline/amorphous ratio. Future investigations using ⌀5mm rods can definitely could will help to conclude on the effect of arc intensity on this BMG.
The second one is the number of melts/flips required to obtain the better ratio amorphous/crystalized material volume to improve mechanical properties. For one composition, the ZrCuAl system, the more the master alloy is re-melt, the less B2 crystalline phase is present but its repartition is more and more homogeneous, they find that 12 melts/flipping of 1min each at 410 A is the optimal condition to show plasticity and strain hardening in tensile test [LIU 12a]. In summary, according to these experiments, the hypothesis is that the number of melts can reduce heterogenous nucleation and growth by oxides and nitride dissolution associated with a better chemical homogeneity of the master alloy. Obtaining a very homogeneous master alloy should limit the presence of unmelt areas which are preferential nucleation sites. The results of four-point bending tests on 14 and 6 melts/flips proved to be very poorly reproducible (Fig. 3.5) but hints the incredible properties that this BMG composition $Ti_{40}Cu_{36}Zr_{10}Pd_{14}$ can reach (maximum mechanical strength of 3700 MPa for one sample). The lack of repeatability in compressive and tensile tests has been already discussed in [GAO 11], admitting that the casting process should be improved. Our experiment illustrates the difficulty of mastering the suction casting process for the manufacturing of metallic glasses. Statistically, no difference in distribution of the crystallized material could be determined between 14 and 6 melts/flips (Fig. 3.4). However, it appears that the less crystallized rods have lower mechanical strength (orange and dark blue curves in Fig. 3.5) than those containing more spherulites (red and dark blue curves). The observations of the fracture surfaces, the measurement of the fracture angles, the size and position of the starting crack point in specimens after failure allow

to give some general trends to the wide spread of the mechanical strengths. It seems that more the starting defect (here spherulite) is big and close to the maximum tensile area of the specimen, the more likely it is that the specimen will break prematurely (at small load). On the contrary, if there is no spherulite near the tensile surface, then very high stresses can be reached and the specimens can be plastically deformed before failure. Indeed, it was noticed that on the highest strength specimens (3200 and 3700 MPa), there is an absence of clear starting point on the fracture surfaces (Fig. 3.5D). The scattering of results of four point-bending test therefore indicate that there is a statistical randomness in the results which rely on the spherulite nucleation position.

Finally, it seems that the spherulites are not likely to be the result of unmelt areas or a lack of homogeneity during casting, their presence seems to be more influenced by the cooling rate than the heating step.

3.3.3 Influence of hydrogen

The other main origin of spherulite nucleation can be the purity of the raw pure metals used for the sample's manufacturing. Spherulites may be the result of external element contamination of the pure metals before (in the raw metals) or during casting (air leak in furnace chamber or insufficient primary and secondary vacuum). The difference in purity of the metals can be considered as a plausible explanation for the varying mechanical properties obtained for the same alloy composition in equivalent manufacturing processes in literature. For example, [LIU 02], [KER 06] oxygen contamination during cooper mold casting process has been proved to provoke an embrittlement of the BMG and a decrease of its GFA. In an attempt to determine whether the $Ti_{40}Cu_{36}Zr_{10}Pd_{14}$ grade is contaminated by one or more elements, a surface analysis based on mass spectroscopy method was carried out on a rod. The only contrast visible in Fig. 3.7, suggested that hydrogen may be involved in the nucleation of spherulites. Observations on rods fabricated in the presence of hydrogen suggest that the crystalline layer at the mold interface is larger than when fabricated without hydrogen and spherulites are maybe larger (see Fig. 3.8).Compressive tests carried out on samples casted with hydrogen show a wide spread of results. In compression, the fracture surfaces did not show any difference between the specimens that showed plastic deformation and those that did not, but the observations of the length and density of the shear bands on the profile view of the specimens after the test seems to be an important element. This method was also used by others in [NAR 18]. It would appear that the specimens that showed the most important plastic deformation also developed more shear bands than those with brittle behavior. Those results are rather surprising, indeed in literature the hydrogen is mostly considered as an alloying element which increase GFA, free volume amount which result in improved ductility (promote multiple shear bands development)[GRA 15] [SU 12][DON 12][SUH 00]. According to this result, it is believed that hydrogen is, in the case of the $Ti_{40}Cu_{36}Zr_{10}Pd_{14}$ grade, depending on where

it is absorbed (spherulite or amorphous) have a different influence. Inside the spherulite it seems to promote their growth and/or nucleation, on the contrary in the amorphous matrix maybe it increases free volume. The large scatter of mechanical behavior under compressive stress (from brittle to ductile) rely maybe again on the spherulite position inside the specimen. If the spherulite (which is bigger than usual) is on the maximum compressive axis, it can act as a critical defect, then the sample is probably going to break with a brittle behavior (Fig. 3.9D). On the contrary, if there is no spherulite in the maximum compressive axis, the sample will deform plastically before failure by forming numerous shear bands (Fig. 3.9B) in the amorphous matrix (alloyed with hydrogen). Because, we suspect hydrogen to promote spherulite growth inside the rods and linked to rather unpredictable mechanical behavior, it is therefore best to avoid hydrogen during casting. To confirm those assumptions, as suggested in [SUH 00], simple DSC measurements could have been done on the 5mm as cast rods and 3mm as cast Ar+H_2 to highlight the evolution free volume through change in T_g and T_x to better explain the difference of Young modulus between 3 and 5mm rods.

3.3.4 Influence of heat treatments

The thermal stability of the alloy was studied using DSC analysis mainly to determine the T_g (glass transition temperature), T_x (crystallization temperature) and T_l (liquidus temperature) to calculate the GFA of the alloy. According to [ZHU 07a], there is two parameters γ and δ which are able to give information on the GFA of the alloy studied. The higher γ and δ are, the higher the GFA. According to characteristics temperatures extracted from Fig. 3.11 :

$$\gamma = \frac{T_x}{(T_g + T_l)} = 0.384$$

$$\delta = \frac{T_x}{(T_l - T_g)} = 1.38$$

And according to [INO 08] it is possible to estimate a theoretical critical diameter by following the below formula:

$$D_c = 10^{-2.57+6.16(\frac{T_g}{T_l})} = 8.1mm$$

The results obtained for γ and δ are in full agreement with the values given in the literature [ZHU 07a][CZE 16] [SYP 16] [GAO 11][NAR 18]. But the estimation of the critical diameter of 8 mm for this composition is not really representative of what can be obtained experimentally with a laboratory arc melting suction casting, because even with 3 mm rods there are spherulites.
Perhaps here again, the supply and purity of the pure metals used to make the alloy are of such importance that they can strongly influence crystallization during casting. It would

be interesting in the future to separate the quality of the raw materials from the manufacturing process and to identify the influence of each of these parameters. Furthermore, the characteristic temperatures of the alloy allowed us to try different heat treatments (from 400 to 600°C for 1h, see Fig. 3.12). The spherulites are not sensitive to the heat treatments and retain their as cast size (Fig. 3.13). It appears that the 450°C treatment is equivalent to a structural relaxation treatments and that the higher temperature treatments induce a crystallization of the initially amorphous matrix exactly as in [QIN 07a]. The heat treatments were all carried out over a period of 1 hour and the importance of testing other temperatures and durations to evaluate the changes of the microstructure cannot be excluded. Future tests in this direction could lead to the determination of the TTT (time-temperature-transformation) diagram of the TiCuZrPd grade, which will probably help to better understand $Ti_{40}Cu_{36}Zr_{10}Pd_{14}$ mechanical properties. It is also likely that the enthalpy of crystallization of this grade is so low that obtaining this grade in bulk and perfectly amorphous state appears difficult or for very small diameter. Doping with elements such as Si, Sn and Nb has already been tested [SYP 16], [FOR 13][ZHU 12][LIE 20] there were no more spherulites and an increase in GFA but there was a decrease in mechanical properties. In this context, it seems legitimate to consider staying in the same system but perhaps changing the atomic distributions. Perhaps the only way to get amorphous bulk parts of the $Ti_{40}Cu_{36}Zr_{10}Pd_{14}$ alloy would be to atomize the alloy in powder and sinter it for example, by SPS (spark plasma sintering), which could allow an even better assessment of the need to get rid of the spherulites or not.

3.4 Conclusion

Various investigation based on the arc melt suction casting process of the $Ti_{40}Cu_{36}Zr_{10}Pd_{14}$ grade have been studied in this chapter. The parameters studied made it possible to rule out certain hypotheses for the appearance of spherulites and to evaluate the capacity of this alloy to have customized micro-amorphous/crystalline ratio to meet the requirements of the medical sector (improvement in toughness, fatigue endurance and plasticity under tension). The main trends and results of this study are as follows:

- The larger the size of the mold used, the lower the cooling rate and the more crystallized the sample will be (spherulites will be larger and many more numerous). Unfortunately, even with a mold of 3mm in diameter, rods are never 100% amorphous. But spherulites could eventually be small enough to prevent premature brittle failure under tensile stress.
- The change in intensity of the arc (between 200 and 400A) does not seem to have any influence on the number and size of spherulites, so the hypothesis that the spherulites would come from unmelt areas during casting is not confirmed, at least in the conditions chosen in our study.

- The number of melts/flips of the master alloy prior to the rods casting does not seem to have any influence on the number and size of spherulites, so the believed presence of non-homogeneous areas in the rods is not confirmed.
- It seems that the heating step do not have significant influence of the casted rods but the cooling step is crucial.
- Surface analysis by mass spectrometry indicated that hydrogen can be involved in the growth of spherulites. The casting in an H_2 enriched Argon atmosphere showed an increase in the crystallization of the core's rods at the periphery (interface with the copper mold), which makes the mechanical properties of the alloy particularly unpredictable even in compressive tests.

Chapter 4

Exploring the $Ti_{40}Cu_{36}Zr_{10}Pd_{14}$ alloy in its equilibrium state and potential new compositions derived from the basic grade

4.1 Introduction

Since two decades, Bulk Metallic Glasses (BMG) are often described as very promising materials for biomedical applications. They may exhibit effectively astonishing mechanical and corrosion properties [ECK 07], especially when they are processed in the form of very small samples. The $Ti_{40}Cu_{36}Zr_{10}Pd_{14}$ grade for example has already been proved to be biocompatible and presents a yield strength up to 2 GPa[LIE 18][GAU 22][ZHU 07a]. This, in addition to a theoretical improvement of corrosion resistance related to its amorphous nature, would open the door to minimally invasive implants and small dental products. However, we have recently shown that crystallized casting defects (referred as spherulites) in this specific composition have a detrimental influence on the mechanical and electrochemical properties [GAU 22]. They are particularly numerous and large in few millimetres bulk samples, which are relevant to produce dental implants. While the exact origin of the spherulites has not yet been determined, their morphology, chemistry, crystallography based on Cu-Ti binary diagram and a growth mechanism have been detailed previously (Chapter 2). It is assumed that if the microstructure (content and size of such spherulites) of this BMG can be better controlled through processing it can lead to a significant improvement in the mechanical properties. Unfortunately after several tests, it seems that even under the best believed manufacturing conditions the suction casting limits were reached without succeeding in obtaining 3mm rods without spherulites or with size controlled spherulites (chapter 3). It appears that this alloy has probably a too large capacity to crystallize to hope to manufacture it in amorphous state without spherulites. Furthermore, the corrosion resistance of the $Ti_{40}Cu_{36}Zr_{10}Pd_{14}$ grade is limited [LIE 18] [QIN 07b][OAK 09] which is a problem for dental implant application. Moreover, according to the results of Chapter 3, spherulites do not seem to be sensitive to heat treatments (up to 600°C), it appeared that the amorphous matrix relaxed before crystallizing without change for spherulites size or crystallography. So, it is questionable whether the phases inside the spherulites are equilibrium state phases or not. The first part of this chapter focuses on the master alloy of the $Ti_{40}Cu_{36}Zr_{10}Pd_{14}$ grade. The master alloy has been chosen because it is the closest state to thermodynamic equilibrium (crystalline) afford-

able at the laboratory. The main goal of the study of the master alloy was to determine if the spherulite's phases are identical to those of the master alloy or not by using X rays diffraction. In addition to these results, the microstructure organization of the master alloy is observed by optical and electronic microscopies and some potentiodynamic tests in the same conditions as for metallic glass previously (chapter 1), in NaCl 0.9% at 37°C were performed for comparison of the amorphous state alloy.
In the second part of this chapter, admitting that, for composition $Ti_{40}Cu_{36}Zr_{10}Pd_{14}$, spherulites are particularly difficult to avoid in suction casting and given the very modest global corrosion resistance of this composition, probably due to its high copper and palladium content, its future as a biomaterial seems increasingly compromised. In order to address these two main problems, there are two possible strategies. First, to get rid of spherulites there is a need to improve GFA, the most common strategy which has already been tried in literature is adding or substitute small amount of extra elements. In the specific case of $Ti_{40}Cu_{36}Zr_{10}Pd_{14}$, it has already been demonstrated that additional components make it possible to reduce or even eliminate the presence of spherulites (for Sn and Sn+Si addition), but they also considerably reduce the mechanical properties and do not really improve the corrosion resistance or have a limited critical diameter (D_c). A summary of the main literature results of the extra elements addition is available in Tab. 4.1 below.

The second approach is to remain in the TiCuZrPd system and change the atomic distribution in an attempt to avoid spherulites and improve corrosion resistance. It was therefore decided to carry out casting tests without prior specific thermodynamic calculations, with compositions never mentioned in literature and from the $Ti_{40}Cu_{36}Zr_{10}Pd_{14}$ master alloy phases chemistries analysis resulting from the part 1 study. The derived alloy compositions were selected considering two chemistries that were thought to be more resistant to corrosion ($Ti_{65}Cu_{21}Zr_4Pd_{10}$ and $Ti_{51}Cu_{38}Zr_3Pd_8$) than the basic grade $Ti_{40}Cu_{36}Zr_{10}Pd_{14}$ and one chemistry that was expected to be very sensitive to corrosion ($Ti_{26}Cu_{43}Zr_{15}Pd_{16}$).Those chemistries are considered to comply with most of the laws stated by Inoue [INO 00], with a hope of obtaining these partially amorphous rods. All the obtained results will be described and followingly discussed.

[ ]

TABLE 4.1 – A summary of additional elements tested on $Ti_{40}Cu_{36}Zr_{10}Pd_{14}$ published in the literature.

Tested extra element on $Ti_{40}Cu_{36}Zr_{10}Pd_{14}$	Tested composition	GFA /Critical diameter (D_c)/ Reduced glass transition ($T_{rg} = T_g / T_l$)	General trends	Ref
Sn	$Ti_{40}Zr_{10}Cu_{36-x}Pd_{14}Sn_x$ (x = 0, 2, 4, 6 at.%)	Trg is the highest for Sn =2at.%, Dc = 10mm	Compressive, tensile and fatigue tests exhibit lower performance than the $Ti_{40}Cu_{36}Zr_{10}Pd_{14}$ grade	[ZHU 08a] [ZHU 12]
Sn + Ta and Sn+Nb	$Ti44.55Zr9.9Pd9.9Cu30.69Sn3.96Ta1$ $Ti44.1Zr9.8Pd9.8Cu30.38Sn3.92Ta2$ $Ti43.65Zr9.7Pd9.7Cu30.07Sn3.88Ta3$ $Ti43.2Zr9.6Pd9.6Cu29.76Sn3.84Ta4$ $Ti42.75Zr9.5Pd9.5Cu29.45Sn3.8Ta$ $Ti44.55Zr9.9Pd9.9Cu30.69Sn3.96Nb1$ $Ti44.1Zr9.8Pd9.8Cu30.38Sn3.92Nb2$ $Ti43.65Zr9.7Pd9.7Cu30.07Sn3.88Nb3$ $Ti43.2Zr9.6Pd9.6Cu29.76Sn3.84Nb4$ $Ti42.75Zr9.5Pd9.5Cu29.45Sn3.8Nb5$	Dc in the range of 3 to 5mm	Mechanical properties are worse than the basic composition and the corrosion resistance is not significantly improved	[OAK 09]
Si	$Ti_{40}Zr_{10}Cu_{40-x}Pd_{10}Si_x$ (x = 0, 1, 2 at.%)	Dc = 5mm	1900MPa and lower Young's modulus under 85 GPa (compression)	[ZHU 07c] [ZHU 08b]
Fe+Sn+Si+Ag	$Ti_{47}Cu_{38-x}Zr_{7.5}Fe_{2.5}Sn_2Si_1Ag_2Pd_x$ (x = 1, 2, 3, and 4 at.%)	Dc = 5mm	Up to 2340 MPa in compression, pitting potential around 1V in Hank solution at 37°C, proven biocompatibility but contains potentially harmful elements Ag and Fe	[WAN 21]
Ga	$Ti_{40}Zr_{10}Cu_{40-x}Pd_{10}Ga_x$ (x = 0, 1, 2, 4, 8, 10 at.%)	It is mentioned "can improve GFA" but not available data	Ga levels up to 10% have no significant effect on passive current density, pitting potential or cathodic reactivity in 0.9% NaCl at 37°C. No data on mechanical properties.	[WEI 19]
Pt	$Ti_{41}Zr_{10}Cu_{31}Pd_{1-x}Pt_x$ (x= 1; 2, 3,4 at.%)	Dc = 4mm	Same yield strength as the basic alloy but greater plastic deformation under compression	[JIA 18a]
Ni	$Ti_{41}Zr_{10}Cu_{31}Pd_{13-x}Ni_x$ (x= 1; 2, 3,4 at.%)	Dc = 5mm (1 and 2 Ni at.%)	Ni=3 at.% has the same compressive behavior than the basic grade but contains potentially harmful element (Ni)	[JIA 18a]
Co	$(Ti_{40}Zr_{10}Cu_{34}Pd_{14})_{100-x}Co_x$ (x = 0, 1, 2, 3, and 4at.%)	Dc = 10mm	Good plasticity under a compressive stress , a high fracture strength of about 1960 MPa, small improvement in corrosion resistance in simulated body fluid. But contain potentially harmful element (Co)	[WAN 13a]
Nb	$(Ti_{40}Zr_{10}Cu_{34}Pd_{14})_{100-x}Nb_x$ (x=0, 2, 3, 4at.%)	/	Addition of Nb promotes the formation of nanocrystals. significant increase in compressive plasticity (total strain over 13%) is achieved in the sample with 3% of Nb without compromising the strength/slightly delayed pitting corrosion potential	[FOR 13]

4.2 Results and discussion

4.2.1 Study of the $Ti_{40}Cu_{36}Zr_{10}Pd_{14}$ master alloy: microstructure and electrochemical properties

The first part of this chapter focuses on the characterization of the $Ti_{40}Cu_{36}Zr_{10}Pd_{14}$ master alloy. In order to determine whether the spherulites have phases identical to that of the alloy in its close to equilibrium state. The master alloy was cut and polished as described in the Materials and Methods, the diffractogram of which is shown in Fig. 4.1 (compared to the one obtained on spherulite aggregate already showed in Chapter 2 Fig 2.1).

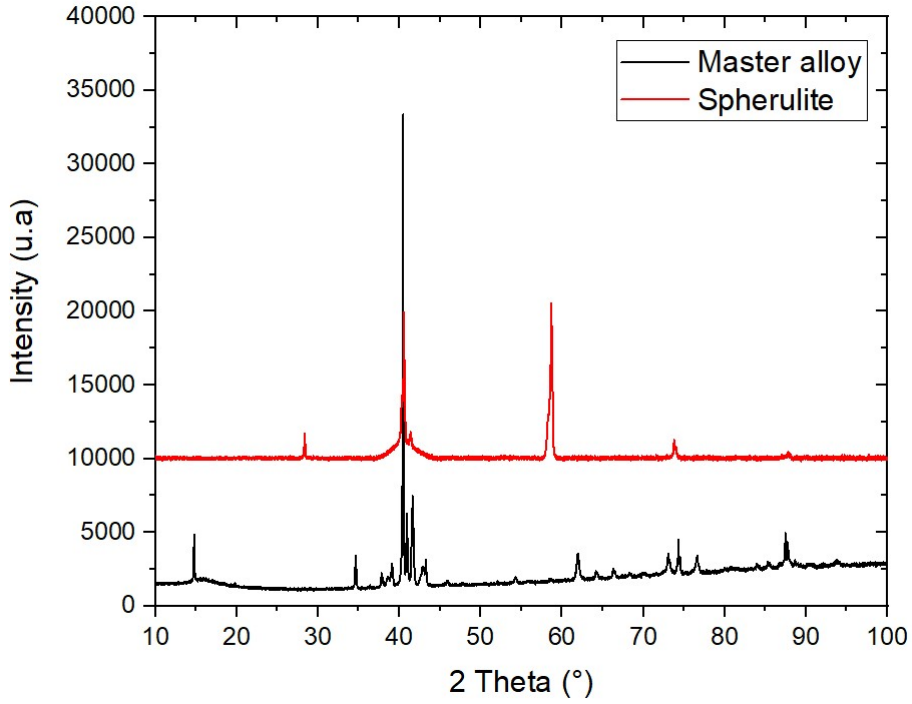

FIGURE 4.1 – XRD diffractogram of the $Ti_{40}Cu_{36}Zr_{10}Pd_{14}$ master alloy (black curve) compared to the one of the spherulite aggregate (red curve) (already presented in Chapter 2, Fig 2.1).

The two diffractograms in Fig. 4.1 are quite different, the master alloy one contains many more peaks than the one of the spherulites. This multitude of peaks goes in the direction of the presence of a large number of different phases in the material. Formally identifying the phases present in the master alloy through XRD analysis is a major challenge given the complexity of the signal, it was tried to performed the Rietveld method with phases based on the binary Cu-Ti diagram but we have not been able to formally identify the present phases. It was noticed that there are some peaks in common with the spherulite diffractogram, such as the double peak at 40.4 and 41.5° and the peaks at 74° and 88°. However, it would appear that the CuTi-B2 phase identified in XRD for the

spherulites is not formally identified on the $Ti_{40}Cu_{36}Zr_{10}Pd_{14}$ master alloy diffractogram. The master alloy diffractogram is coherent with the work of Qin [QIN 07b], where they present a diffractogram of $Ti_{40}Cu_{36}Zr_{10}Pd_{14}$ cooled at 823K/10min which is almost identical to the one in Fig. 4.1, they identified those peaks with Ti_3Cu_4, Ti_2Pd_3 and Ti_2Pd. However in the work of Czeppe [CZE 16], they present a diffractogram of $Ti_{40}Cu_{36}Zr_{10}Pd_{14}$ cooled at 60K/min, they found the signal of a single CuTi phase, which is tetragonal with lattice parameters a = 3.115 Å and c = 5.947 Å. It seems that there is no consensus on the crystalline phases present in $Ti_{40}Cu_{36}Zr_{10}Pd_{14}$ alloy probably because its depends on thermal history of the alloy. It would probably be necessary to carry out TEM analyses but this was not performed yet, as not being the main objective of this chapter. But at this point, it can not be excluded that there could be common phases between spherulites and master alloy.

- How is the master alloy organized?

The sample are then observed under optical microscopy, the pictures are presented below in Fig. 4.2.

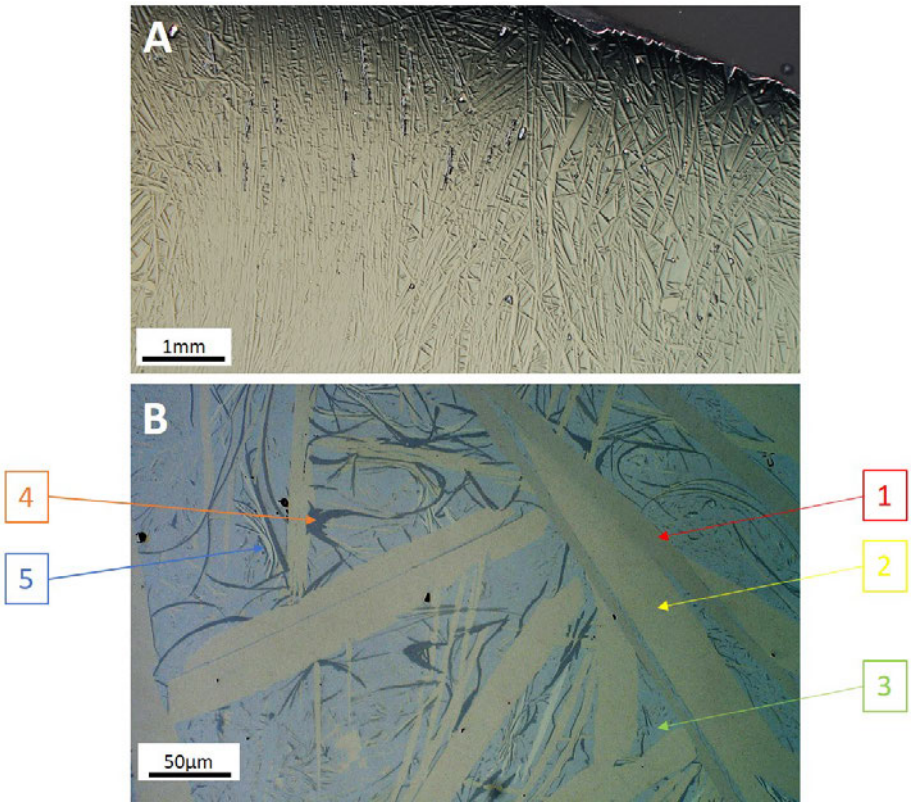

FIGURE 4.2 – Optical microscopy pictures of the microstructure of the polished $Ti_{40}Cu_{36}Zr_{10}Pd_{14}$ master alloy. A, at low magnification we see large laths oriented from bottom to top of the alloy. In B, at higher magnification, 5 phases can be seen with their morphology and different colors. Numbers and colors (red, yellow, green,orange and blue) are indicators given to each phase for the rest of the study.

The optical microscopy images in Fig. 4.2 show a complex microstructure with large laths. At higher magnification (B), five different color shades are visible in optical microscopy (OM). This difference in color under OM suggests that they may be 5 crystallographically and chemically distinct phases. The orientation of the laths in the master alloy appears to be directly related to the configuration of the arc furnace chamber. As illustrated in Fig. 4.3, the top zone (with respect to the electric arc) of the master alloy during melting is the one that reaches the highest temperature but cools down the slowest as it is the furthest from the water-cooled copper plate. Conversely, the bottom zone is further away from the arc and reaches slightly lower temperatures while being in contact with the cooled Copper plate and therefore cools down faster. This schematic view explains why on the bottom side of the master alloy the microstructure is finer (less time for grain growth).

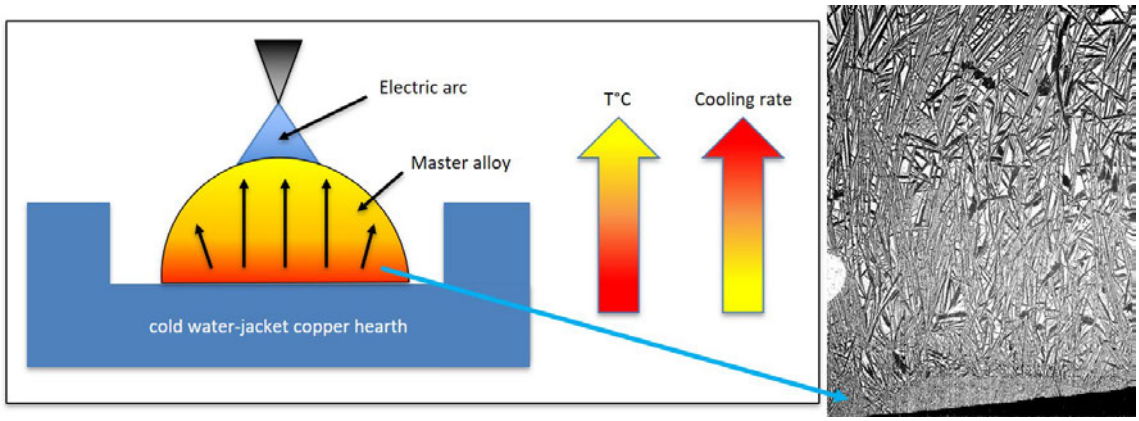

FIGURE 4.3 – Scheme of the master alloy in the arc furnace chamber. The temperature and cooling rate are shown during the heating of the alloy. On the SEM picture on the right, the microstructure evolution of the master alloy can be seen. In the immediate vicinity of the copper plate the microstructure is much finer than in the rest of the alloy.

After the previous coarse observations of the $Ti_{40}Cu_{36}Zr_{10}Pd_{14}$ master alloy in OM, some SEM are performed in BSE mode presented in Fig. 4.4. Five different grey shades can be seen which agrees with the previous observations in OM in Fig. 4.2. The colored numbers shown in Fig. 4.4 correspond to the areas on which the chemical compositions were measured by EDXS. Five different chemisteries can be distinguished, which compositions (in at.%) are summarized in Tab. 4.2. These analyses allow us to establish a numbering (from 1 to 5) and a color code (red, yellow, green, orange and blue) for each phase, accordingly to Fig. 4.2.
In Tab. 4.2, it can be seen that the phases 1, 2 and 4 are particularly rich in Ti and phases 2, 4 and 5 are particularly rich in Copper. Phases 1, 2 and 4 are low in Zirconium, while phases 3 and 5 are high in Zirconium. Excepted for phase 5, the amount of Pd is around 10 at.%. for all the phases. All these compositions offer a large panel of chemistries from the same quaternary atomic system. It is noticed that the master alloy chemisteries have

significantly different chemical compositions from the phases identified on the spherulites (Chapter 2, Tab 2.1).

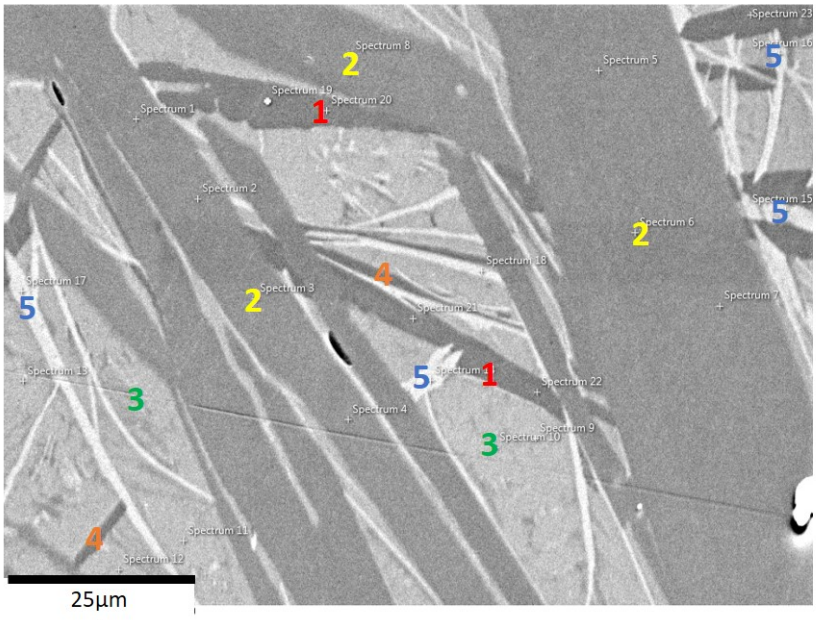

FIGURE 4.4 – SEM-BSE picture of the $Ti_{40}Cu_{36}Zr_{10}Pd_{14}$ master alloy in high magnification. The numbers and their colors refer to the exact position of the EDXS measurement to determine each phase's composition.

TABLE 4.2 – Summary of the atomic composition for the five previously identified phases in EDXS took on the areas pointed in Fig. 4.4.

Phase/at.%	Phase 1	Phase 2	Phase 3	Phase 4	Phase 5
Ti	65	51	35	45	26
Cu	21	38	32	38	43
Zr	4	3	21	8	15
Pd	10	8	11	9	16

- Do all of these phases have the same corrosion resistance?

The $Ti_{40}Cu_{36}Zr_{10}Pd_{14}$ BMG has relatively weak corrosion resistance, the master alloy provides us with different phases and chemistries of the TiCuZrPd system. It was wondered out of curiosity if some of the master alloy's phases are more sensitive to corrosion than others. Some classical electrochemical tests with a 3-electrodes set-up in a 0.9% NaCl solution (pH=7) at 37°C (as described in details in the Materials and Methods Chapter) are performed to see if it is possible to make a link with their chemical compositions. The

open circuit potential (OCP) and potentiodynamic curves are presented in Fig. 4.5 (in comparison with TA6V and $Ti_{40}Cu_{36}Zr_{10}Pd_{14}$ BMG curves).

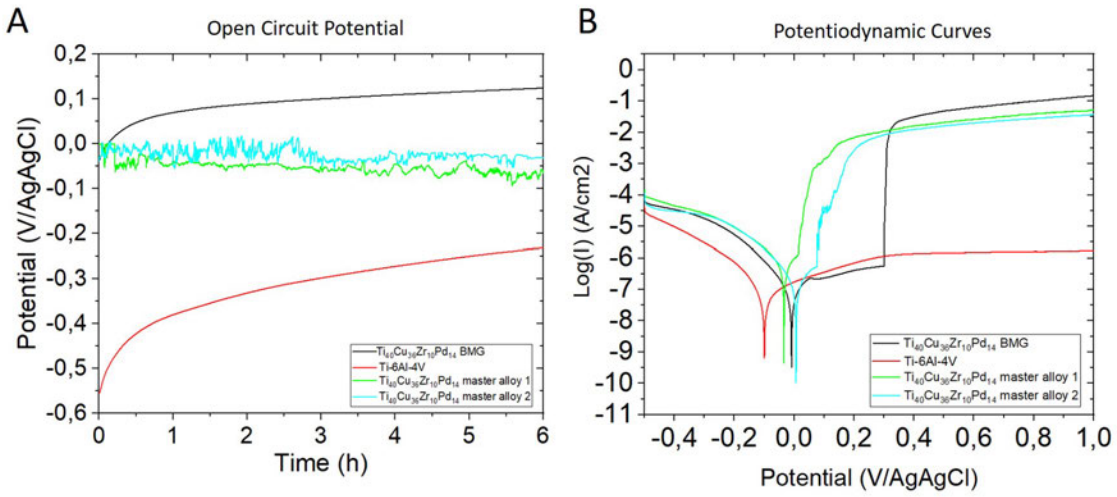

FIGURE 4.5 – 6h Open circuit potential curves (A) and potentiodynamic curves from -0.5 to 1V (B) of two similar measurements on the $Ti_{40}Cu_{36}Zr_{10}Pd_{14}$ master alloy (light blue and green curves) compared to two references: $Ti_{40}Cu_{36}Zr_{10}Pd_{14}$ amorphous state (black curve) and a TA6V(red curve). The tests were done in 0,9%NaCl, pH=7 at 37°C.

Fig. 4.5A shows two OCP curves for the master alloy (green and light blue curves) compared to the OCP measured for the $Ti_{40}Cu_{36}Zr_{10}Pd_{14}$ BMG (black curve) and the TA6V reference curve (red curve). The master alloy curves are much less stable than the $Ti_{40}Cu_{36}Zr_{10}Pd_{14}$ BMG and TA6V curves, it seems that many small events occurred throughout the 6h of immersion. Excepted the presence of these small fluctuations, the OCP of the master alloy reaches quickly a stable value compared to the other systems showing an asymptotic increase. The stable potential of the amorphous is around 0.13V while that of the master alloy is a little lower ($\approx$ -0.05V). In Fig. 4.5B shows the corresponding potentiodynamic curves from -0.5 to 1V. The corrosion potentials (E_{corr}) appear to be close between the master alloys and the BMG of the same composition, however, once the anodic part of the curve is reached, the BMG exhibits a passivation plateau until 0.3V whereas for the master alloy the current density increases immediately and sharply which corresponds to dissolution phenomenon (between 0 and 0.1V). TA6V, on the other hand, is an exceptional passive material and does not suffer from pitting corrosion or dissolution in these experimental conditions. From these curves, it appears that the amorphous state alloy exhibits a slightly higher corrosion resistance compared to the master alloy but both are sensitive to pitting and dissolution, respectively. This trend is probably observed because amorphous material is theoretically composed of one solid solution (no secondary phases), or much more chemically homogeneous and does not have crystalline defects that are preferential pitting sites.

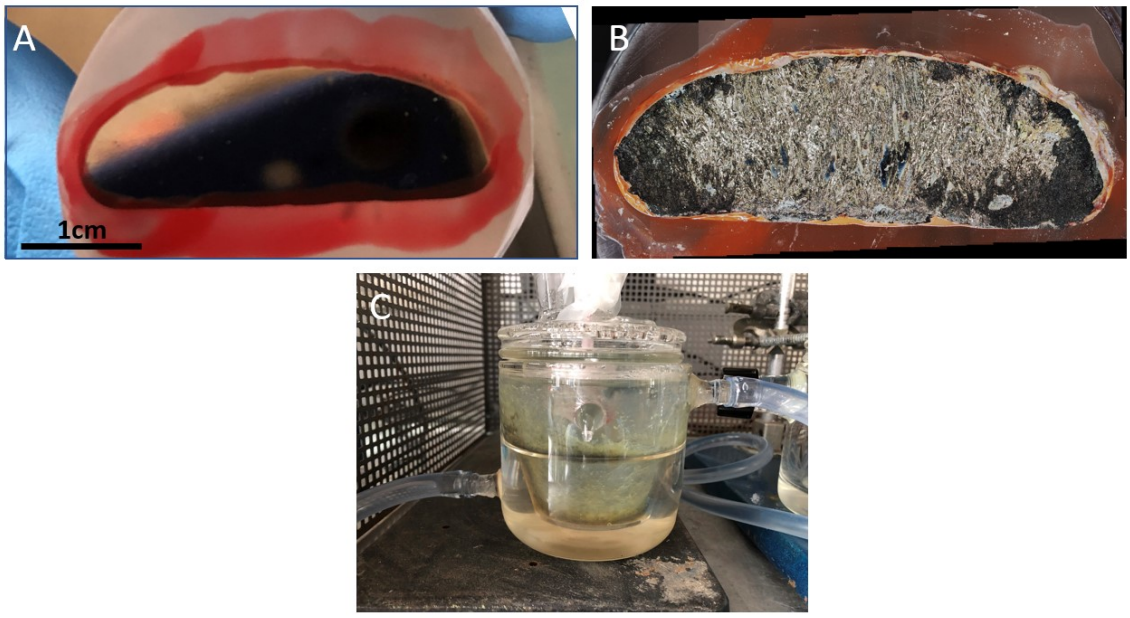

FIGURE 4.6 – View of the sample $Ti_{40}Cu_{36}Zr_{10}Pd_{14}$ master alloy surface before (A) and after (B) the potentiodynamic test in NaCl 0.9% at 37°C. C is a picture of the NaCl test solution after the test with a large amount of green precipitates.

Fig. 4.6 shows the appearance of the sample's surface ($Ti_{40}Cu_{36}Zr_{10}Pd_{14}$ master alloy) before (A) and after (B) the potentiodynamic tests, the curves of which are shown in Fig. 4.5. The initial surface is mirror polished before the test and in B, after the test needles can be guessed on the whole surface which has become very rough. Part of the surface appears black because it is covered with corrosion products. In C, the appearance of the electrochemical cell containing the 0.9% NaCl solution after the test can be seen, there is a large green precipitate which reflects a very strong dissolution of the sample during the test. The surface of the sample is also observed in the SEM after it had been cleaned in an ultrasonic bath to remove as much corrosion products as possible. SEM pictures of the surface are shown in Fig. 4.7.

Fig. 4.7A shows that the surface of the $Ti_{40}Cu_{36}Zr_{10}Pd_{14}$ master alloy is very heavily degraded during the test and that almost the entire surface is impacted except for small areas circled in orange. Image B is an enlargement of one of these areas which was spared during the test, the surface is still polished and the morphology of the master alloy described in Fig. 4.2 and Fig. 4.4 can still be seen. It is likely that if the test had been carried out for longer duration or at higher anodic potential then the entire surface would have been attacked. One explanation can be that statistically there are some kind of islands (containing phases 3, 4 and 5) which prevent the pitting to spread horizontally but not in depth. Another possibility would be a preferential crystallographic orientation which influences the corrosion sensitivity.

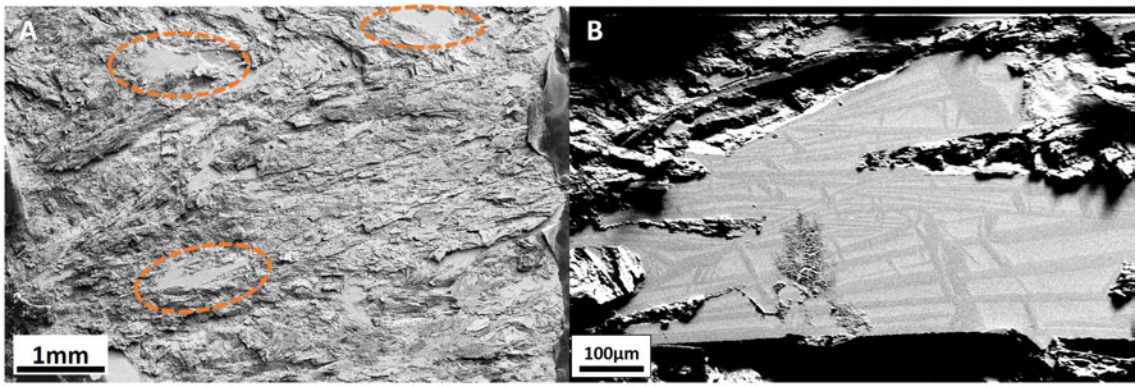

FIGURE 4.7 – A, is a SEM picture of $Ti_{40}Cu_{36}Zr_{10}Pd_{14}$ master alloy after the previous corrosion test, all the surface has been corroded except small areas circled in orange. B, is a picture taken on one of the unaffected areas, on this picture the surface is still polished and the microstructure of the alloy is still visible.

Those previous coarse tests did not allow to know whether phases of the master alloy are more sensitive than others (given the present range of chemical compositions). To determine where are the starting points a cyclic polarization test is carried out in the same experimental condition. The test simply consists of lowering the potential once the current density threshold value has been reached (in this case $1mA/cm^2$ was chosen) to identify the pitting nucleation site(s) and the associated phase(s).

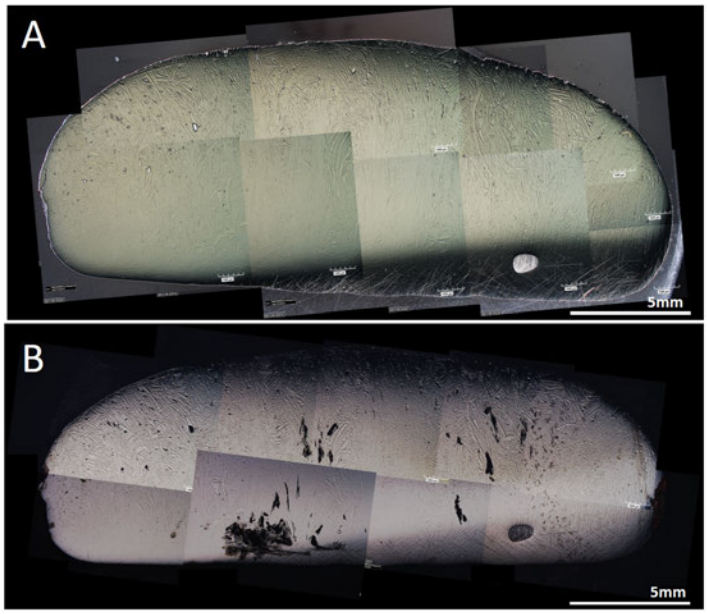

FIGURE 4.8 – A and B are photographic stitchings taken in optical microscopy on $Ti_{40}Cu_{36}Zr_{10}Pd_{14}$ master alloy before(A) and after(B) a test in cyclic polarization (the potential drops when it reaches a threshold value, here 1mA/cm2) in NaCl 0.9% at 37°C.

Fig. 4.8 shows the entire sample surface of $Ti_{40}Cu_{36}Zr_{10}Pd_{14}$ master alloy before (A)

and after (B) the cyclic polarization test. In picture B, it can be seen that the corrosion only occurred in certain specific areas so the current density threshold value has been well chosen. In an attempt to determine the phase at the origin of the anodic dissolution, an altered area is targeted and is found in SEM imaging before and after cyclic polarization.

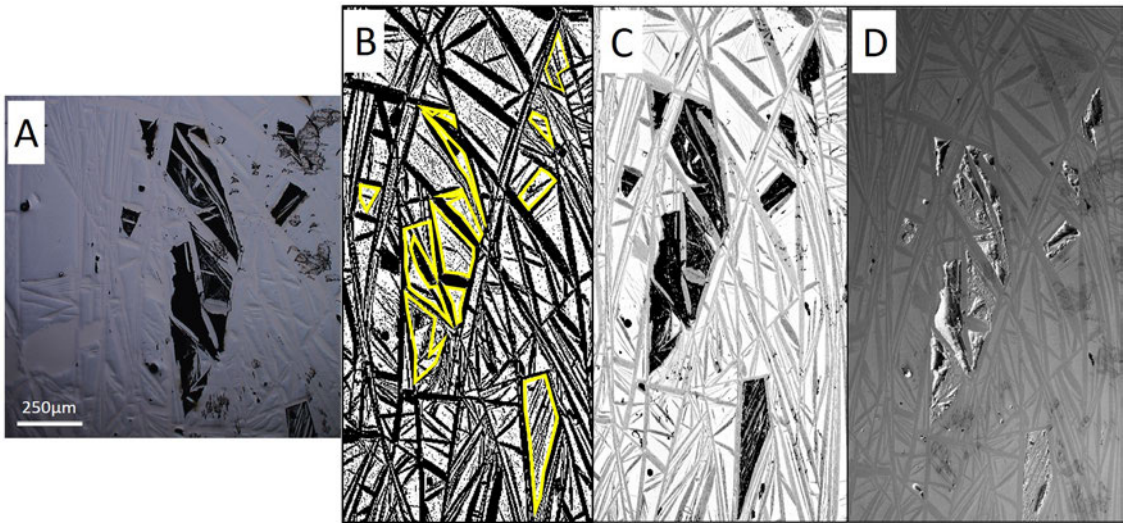

FIGURE 4.9 – A, is a picture of a specific area of $Ti_{40}Cu_{36}Zr_{10}Pd_{14}$ master alloy in optical microscopy after the cyclic polarization. B is the SEM- BSE picture corresponding to the same area before the test (the areas sensitive to dissolution are highlighted in yellow). C, is the SEM–BSE picture corresponding to the same area after the test. D, is SEM picture in secondary electrons of the same area after the test.

Fig. 4.9 shows the same attacked zone in four different modes, optically (A), SEM-BSE before the test (B), SEM-BSE after the test (C) and secondary electrons after the test (D). In picture D, it is clear that the surface of the sample has been strongly and specifically attacked during the test. It can also be seen that it is not the phases with lath morphology (phases 1 and 2) that are affected, but the entire space between several large laths (phases 3, 4 and 5).

At higher magnification of the interface between an attacked and non-attacked area as shown in Fig. 4.10A, EDXS measurements is made to identify which phases were present or missing in this area. As suspected from the images in Fig. 4.9, phases 1 and 2 are found as large laths around the altered area (B). In a non-attacked area (D), the five phases of the master alloy are still easily identified by their chemical signature, while inside the etched area (C), phases 1, 2 and 4 are present as well as residues of phase 3, but no trace of phase 5 can be found.
Phases 5 and 3, which contain the smallest amount of Ti (see Tab. 4.2) and the higher Cu and Pd contents, seem to be the most sensitive to dissolution while phases 1, 2 and 4, which are the most Ti-rich, seem to be more resistant.

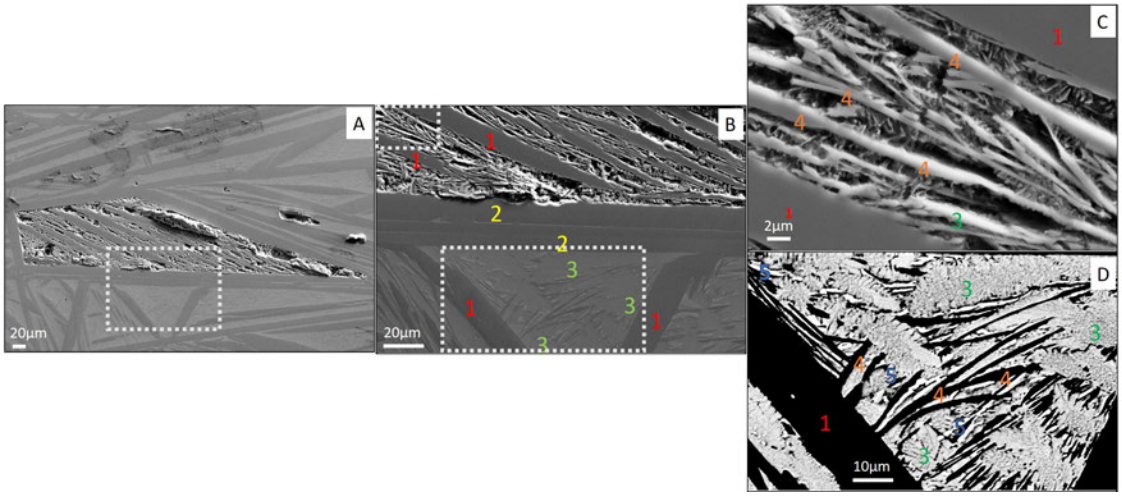

FIGURE 4.10 – A is a SEM picture in secondary electrons of the area study in EDXS. B, SEM picture in secondary electrons of the dotted rectangle in image A, on this area the EDXS analysis shows the presence of the phases 1, 2 and 3. C, SEM picture of the upper dotted rectangle in picture B. This area has suffered from the dissolution, the EDXS measurements still show the presence of the phases 1, 3 and 4. D, SEM-BSE picture of the lower dotted rectangle in picture B. This area hasn't suffered from the dissolution, the EDXS measurements show the presence of the phases 1, 3, 4 and 5 (the phase 2 phase not present in the picture but it is visible in B). .

It is possible that galvanic coupling occurs between the most and the lowest noble phases. Furthermore, according to the results presented in Fig. 4.8, Fig. 4.9 and Fig. 4.10, phases 1, 2 and 4, which are the richest in Ti and Zr, are assumed to passivate and to be the less sensitive to corrosion and that phases 3 and 5 are the most sensitive. The latter two phases are the poorer in Ti and relatively Cu-rich. It is highly probable that dissolution will occur in phase 5 first, which is the only one with a Ti + Zr (at.%) ratio of less than 50 at.%. Furthermore, Pourbaix diagrams where generated for the experimental conditions used here (available in appendix Fig. 4.18), it is known that in the potential range of -0.5 to 1 V for a pH = 7 (NaCl solution used for the tests) Cu and Pd will preferentially form soluble complexes with Cl^- ions rather than form oxides which would play a protective role against corrosion. Titanium and Zirconium are not at all sensitive to the presence of Cl^- in this potential range and form oxides which constitute a passive protective film. The phases richest in Pd and Cu are the most sensitive to dissolution as they form soluble chlorides complex and consequently they will act as anodic site. Conversely, the phases richest in Titanium and Zirconium dissolve less easily in the test conditions and play the role of cathodic site in the corrosion galvanic process. It is observed in Fig. 4.6C that in the NaCl solution after the test there is a green precipitate which is not identified yet. This precipitate could be put back in solution in HCl for ICP (inductively coupled plasma) measurements which can provide further quantitative evidence of which atomic species is sensitive to chlorides complex or precipitate formation. In the work of Gostin et al. [GOS 18] they study the corrosion products formed in saline solution in artificial

pits of the $Ti_{40}Cu_{34}Zr_{10}Pd_{14}Sn_2$ which are really close to the composition studied here. They find out that the mains species released were Pd nanoparticles, and $PdCl_2$ and CuCl while few amounts of free cationic form of Zr and Ti was detected. It is highly probable to find those species in green precipitate obtained in this study especially since $PdCl_2$ is not soluble in water.

Key point of part 1:

- The $Ti_{40}Cu_{36}Zr_{10}Pd_{14}$ master alloy has a multiphase microstructure, five of which have been identified by their chemical signature in SEM-EDXS.
- The phases of the $Ti_{40}Cu_{36}Zr_{10}Pd_{14}$ master alloy seems to be different acoording to EDXS and XRD from those of the spherulites ($Ti_{40}Cu_{36}Zr_{10}Pd_{14}$ BMG) which are probably transition phases frozen during casting.
- The $Ti_{40}Cu_{36}Zr_{10}Pd_{14}$ master alloy is a little bit more sensitive to corrosion than its amorphous counterpart.
- The $Ti_{40}Cu_{36}Zr_{10}Pd_{14}$ master alloy's phases which richest in Cu and Pd are found to be the most sensitive to dissolution because these two elements easily form chloride complexes under the test conditions.

4.2.2 Casting attempts of three new grades of the system TiCuZrPd

As mentioned in introduction, even after numerous attempts to get rid of the spherulites in suction casting no prospects for improvement could be identified (Chapter 3 of the manuscript), leaving little hope for the use of $Ti_{40}Cu_{36}Zr_{10}Pd_{14}$ grade in the manufacture of dental implants. To overcome the problem of nucleation when increasing the GFA of certain alloys, the BMG community relies heavily on the use of additive elements. However, it is acknowledged that in the case of $Ti_{40}Cu_{36}Zr_{10}Pd_{14}$ grade, if there is a reduction or even an absence of spherulites, it will be at the expense of the mechanical properties and probably not significantly improves corrosion resistance (see Tab. 4.1). In the case of $Ti_{40}Cu_{36}Zr_{10}Pd_{14}$ grade, it is probably the high content of Cu and Pd that makes it tends to dissolve in saline solution. In this part we choose another approach: to stay in the TiCuZrPd system without adding any others element. Considering the electochemical results of part 1, it is believed that in order to have a Ti-based metallic glass that is biocompatible and has a better corrosion resistance than $Ti_{40}Cu_{36}Zr_{10}Pd_{14}$, it would be necessary to target compositions richer in Ti and Zr. The chemical compositions of phases 1 and 2 identified in the $Ti_{40}Cu_{36}Zr_{10}Pd_{14}$ master alloy are chosen because there are the most corrosion resistant phases and the phase 5 with the most corrosion-sensitive chemistry as a counter example to perform casting tests. The targeted compositions are summarized in Tab. 4.3. It is believed that the three chemical compositions could maybe be casted in bulk amorphous state because respecting at least two of the three principles stated by Inoue [INO 00], i.e.:

- three or more different atomic species (the more, the better)

- large atomic radius mismatch between species (at least 12%)
- mixing enthalpies between species as negative as possible (this one has not been calculated)

TABLE 4.3 – Summary of the three chemical compositions targeted for the remaining part of the study. The phases 1 and 2 seems to be more resistant to corrosion and as counter example the phase 5 has been picked.Their $\frac{(Ti+Zr)}{(Cu+Pd)}$ ratio were calculated.

(at.%)/Phase	**Basic compo**	**$Ti_{65}Cu_{21}Zr_4Pd_{10}$**	**$Ti_{51}Cu_{38}Zr_3Pd_8$**	**$Ti_{26}Cu_{43}Zr_{15}Pd_{16}$**
Ti	40	65	51	26
Cu	36	21	38	43
Zr	10	4	3	15
Pd	14	10	8	16
$(Ti+Zr)_X(Cu+Pd)_Y$	$(Ti+Zr)_{50}(Cu+Pd)_{50}$	$(Ti+Zr)_{69}(Cu+Pd)_{31}$	$(Ti+Zr)_{54}(Cu+Pd)_{46}$	$(Ti+Zr)_{41}(Cu+Pd)_{59}$
$\frac{(Ti+Zr)}{(Cu+Pd)}$	1	2.2	1.2	0.7

The casting attempts were performed with the suction casting routine protocol without specific parameters but with a rods Copper mold ranging from 1 to 6mm in diameter.

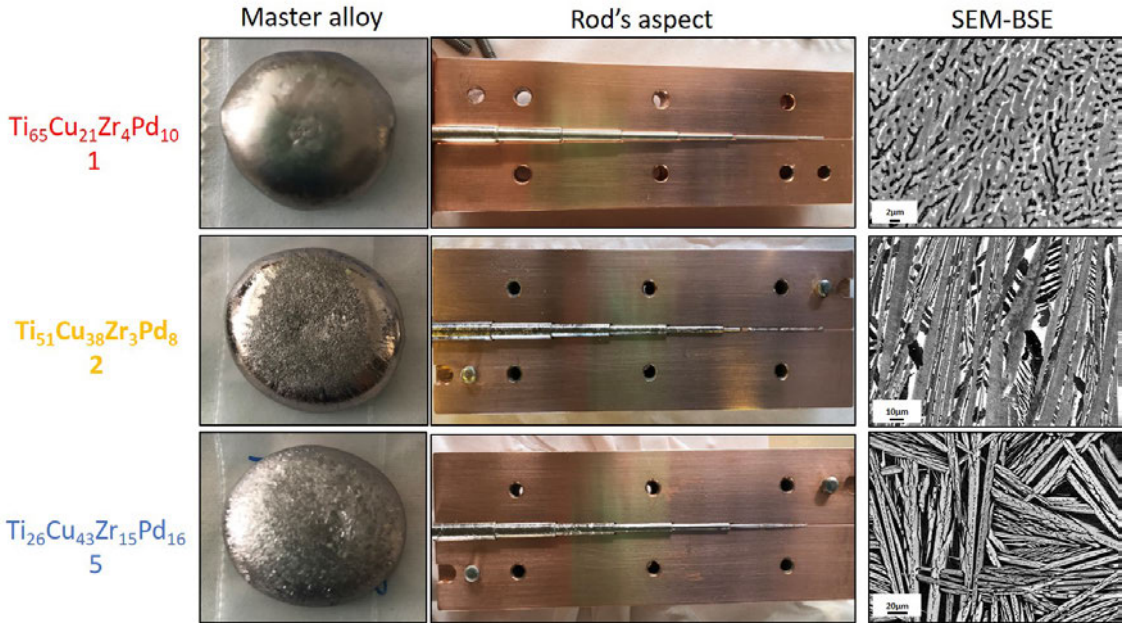

FIGURE 4.11 – The three targeted compositions have been prepared first into master alloys (1st column) before being casted in a copper mold with various diameters (from 1 to 6mm) (2nd column). Some slices of the several alloys have been cut and polished before SEM observations in BSE mode (3rd column).

In Fig. 4.11, the 1st column illustrates the appearance of each of the 3 derived alloys after 4 melts/flips. It can be seen that all three have very different surface aspects, $Ti_{65}Cu_{21}Zr_4Pd_{10}$ alloy (1) is very mat while $Ti_{51}Cu_{38}Zr_3Pd_8$ alloy (2) has needles on the upper part and $Ti_{26}Cu_{43}Zr_{15}Pd_{16}$ alloy (5) has needles on the whole surface. The 2nd column in Fig. 4.11, shows the appearance of the cast rods, $Ti_{65}Cu_{21}Zr_4Pd_{10}$ rod (1) has

a rather smooth and shiny appearance whereas $Ti_{51}Cu_{38}Zr_3Pd_8$ (2) and $Ti_{26}Cu_{43}Zr_{15}Pd_{16}$ (5) rods have rather rough surfaces which probably reflects the presence of non-amorphous state. The 3rd column of Fig. 4.11 shows SEM-BSE pictures of polished 3mm rods section for each of the three compositions studied. The microstructure of the three compositions are very different from each other's. For $Ti_{65}Cu_{21}Zr_4Pd_{10}$ (1), the sample is crystalline even at ⌀1mm and three phases can be seen, two of which are in the shape of small micrometric dendrites. There is the beginning of chemical segregation in this alloy. For $Ti_{51}Cu_{38}Zr_3Pd_8$ (2), the microstructure is very close to that of the $Ti_{40}Cu_{36}Zr_{10}Pd_{14}$ master alloy (see Fig. 4.4) with at least three phases. Finally, $Ti_{26}Cu_{43}Zr_{15}Pd_{16}$ (5) alloy has needles all over the rod and oriented in all directions, they are several hundred microns long and about 15µm wide, around these needles another phase (interstitial) which appears in black.

To demonstrate the crystalline state of every composition processed by suction casting and eventually to identify the common phases in these new compositions, a XRD analysis is carried out, the results are shown in Fig. 4.12.

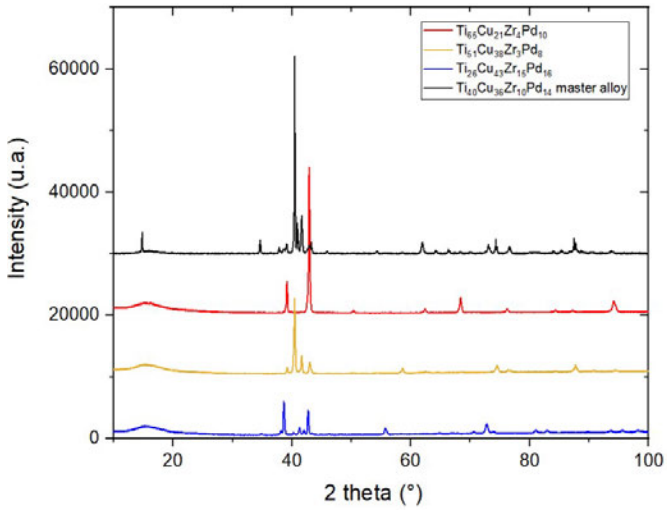

FIGURE 4.12 – XRD diffractograms of each of the new three casted compositions (red, yellow and blue curves) compared to the master alloy diffractogram of $Ti_{40}Cu_{36}Zr_{10}Pd_{14}$ master alloy (black curve, reported from Fig. 4.4).

All three compositions show fine and intense peaks which reflects definitely their crystalline state, however a small broad halo around 15° could correspond to the presence of a small fraction of still amorphous matter in the rods. All three compositions present several phases which is consistent with the SEM -BSE pictures in Fig. 4.11. The identification of these phases would require much more work for a system such as complex as TiCuZrPd. However, it can be noticed a certain similarity between the diffractogram of the $Ti_{40}Cu_{36}Zr_{10}Pd_{14}$ master alloy (black curve) and the one of the $Ti_{51}Cu_{38}Zr_3Pd_8$ rod (2) (yellow curve).

- Are those compositions really bad suitors to make metallic glass?

Currently, absolutely all the grades of the TiCuZrPd quaternary system present in the literature respect a ratio of $(Ti+Zr)_{50}(Cu+Pd)_{50}$. Most of these grades have been studied by Zhu and Al [ZHU 07b] with a summary diagram of every tested composition and critical amorphous diameter produced of 6mm (available in the appendix Fig. 4.17). None of the three compositions above respect this trend (see Tab. 4.3), is that why they are crystallized? If we follow this principle, composition 2 has the best chance to be obtained in amorphous state.
Moreover, the mixing enthalpies of palladium are negative with the three other elements: -14kJ/mol for Cu, -65kJ/mol for Ti and -91 kJ/mol for Zr. And Zr has the largest atomic radius (0.160nm) and the most different to the others atomic radii (14% with Pd and 20% with Cu), so should we respect the (Ti+Zr)= 50 at.% while replacing Ti with Zr to increase the GFA? Moreover, given the deleterious influence of Cu and Pd on the corrosion resistance, we are still very tempted to change the ratio $(Ti+Zr)_{50}(CuPd)_{50}$ as for compositions 1 and 2 (see Tab. 4.3).
In order to make a rough estimation of the mechanical properties of these compositions without the need for a lot of material or specimens, Vickers hardness measurements are carried out, the results are gathered in Tab. 4.4.

TABLE 4.4 – Summary of the mean and standard deviation of Vickers hardness values for each of the three chemical compositions tested in casting. For the last composition other measurements at 1kgF have been made in order to average the hardness of the sample in particular, given to its microstructure.

	$Ti_{65}Cu_{21}Zr_4Pd_{10}$	$Ti_{51}Cu_{38}Zr_3Pd_8$	$Ti_{26}Cu_{43}Zr_{15}Pd_{16}$	$Ti_{26}Cu_{43}Zr_{15}Pd_{16}$
Hardness Vickers	1 0,3kgF	2 0,3kgF	5 0,3kgF	5 1kgF
Mean	327	339	472	525
SD	8	18	34	51

The average hardnesses are 324, 339 and 472 HV (at 0.3kgF) for $Ti_{65}Cu_{21}Zr_4Pd_{10}$ (1), $Ti_{51}Cu_{38}Zr_3Pd_8$ (2) and $Ti_{26}Cu_{43}Zr_{15}Pd_{16}$ (5), respectively. It can be seen that the hardness of $Ti_{26}Cu_{43}Zr_{15}Pd_{16}$ alloy (5) is really high for a titanium alloy or even Cu based alloy. For further evaluation, additional measurements with a load of 1kgF were made on the composition (5), which exhibit mean value of 525 HV with a relatively large standard deviation of 51 HV (probably due to the presence of porosities see picture A in Fig. 4.14). For comparison, TA6V and CpTi grade 2 have a mean hardness of 330 HV and 200 HV, respectively [POO 09]. The hardness of this alloy is widely higher than most of the Cu alloys (which is in this case the principal element) [BAR 91]. The yield strength (σ_y) is estimated by use well-known approximate scaling relation $\sigma_y = 3.HV$ [TAB 00], [JON 12]. It gives a σ_y about 1.5 GPa, which is very high for a Titanium alloy (much higher than that of TA6V). However, in order to better characterize the mechanical properties of this composition, it will be necessary to improve the manufacturing process in order to remove

porosities and cracks without modifying the microstructure of the alloy too much. The microstructure of the alloy is found to be multiphased, with at least two distinct phases. One is needles oriented in all directions and the second is an interstitial phase filling the space between these needles. It is likely that these defects (porosities and cracks) in the material are due to excessive cooling rate during casting, insufficient to maintain the structure of a metastable liquid (amorphous state) but high enough to cause contraction of the material during crystallization shrinkage phenomenon (see Fig. 4.14A). To eliminate these defects, there is several ways:

- Perform a DSC analysis to find out the melting and crystallization temperatures of the alloy and to choose the temperature and duration to perform a HIP (Hot Isostatic Pressing) treatment, this treatment commonly used in additive manufacturing to eliminate porosities [DUP 20].
- Find a way to cool the material a little bit slower to avoid the appearance of these defects.

The final application of these different alloys remains to obtain a biomaterial that can be used for dental implant manufacturing. In this context, the electrochemical properties of the materials are of great interest. To evaluate the corrosion resistance of the $Ti_{26}Cu_{43}Zr_{15}Pd_{16}$ composition, tests were carried out in a 0.9% NaCl solution at 37°C (Fig. 4.13 and Fig. 4.14). It is very likely from the results of part 1 that this grade with high content in Copper and Palladium will have a limited corrosion resistance.

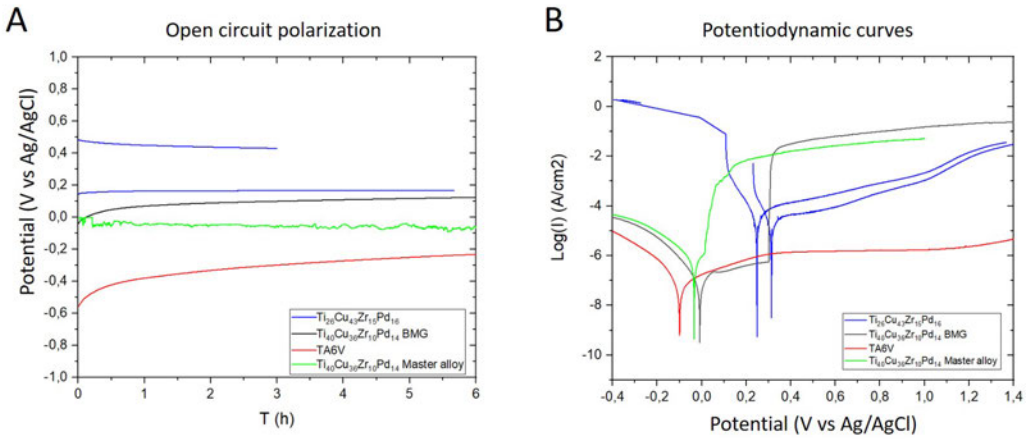

FIGURE 4.13 – 6h or 3h Open circuit potential curves (A) and potentiodynamic curves from -0.5 to 1.4V (B) of 5mm in diameter disc of $Ti_{26}Cu_{43}Zr_{15}Pd_{16}$ alloy (blue curves) exposed to NaCl 0.9% solution at 37°C compared to $Ti_{40}Cu_{36}Zr_{10}Pd_{14}$ BMG and master alloy (black and green curves) and a TA6V (red curve).

Fig. 4.13 shows the OCP (A) and potentiodynamic (B) curves of the $Ti_{26}Cu_{43}Zr_{15}Pd_{16}$ alloy compared to that of TA6V and $Ti_{40}Cu_{36}Zr_{10}Pd_{14}$ BMG. For OCPs (A), the potential reaches stable value quite quickly for the $Ti_{26}Cu_{43}Zr_{15}Pd_{16}$ alloy and it is slightly

higher than that of the reference materials. The potentiodynamic curves (B) for the $Ti_{26}Cu_{43}Zr_{15}Pd_{16}$ alloy show, as anticipated, that the current densities are higher than those of TA6V and the initial composition $Ti_{40}Cu_{36}Zr_{10}Pd_{14}$ (amorphous or crystalline), which probably reflects the absence of genuine passivation (values above $1\mu A/cm^2$). On the anodic part of the curves, there are no sudden increase in the current density for $Ti_{26}Cu_{43}Zr_{15}Pd_{16}$ unlike those for $Ti_{40}Cu_{36}Zr_{10}Pd_{14}$. The curves for the $Ti_{26}Cu_{43}Zr_{15}Pd_{16}$ composition correspond more to a slow and progressive dissolution rather than a very strong and fast active corrosion or pitting events.

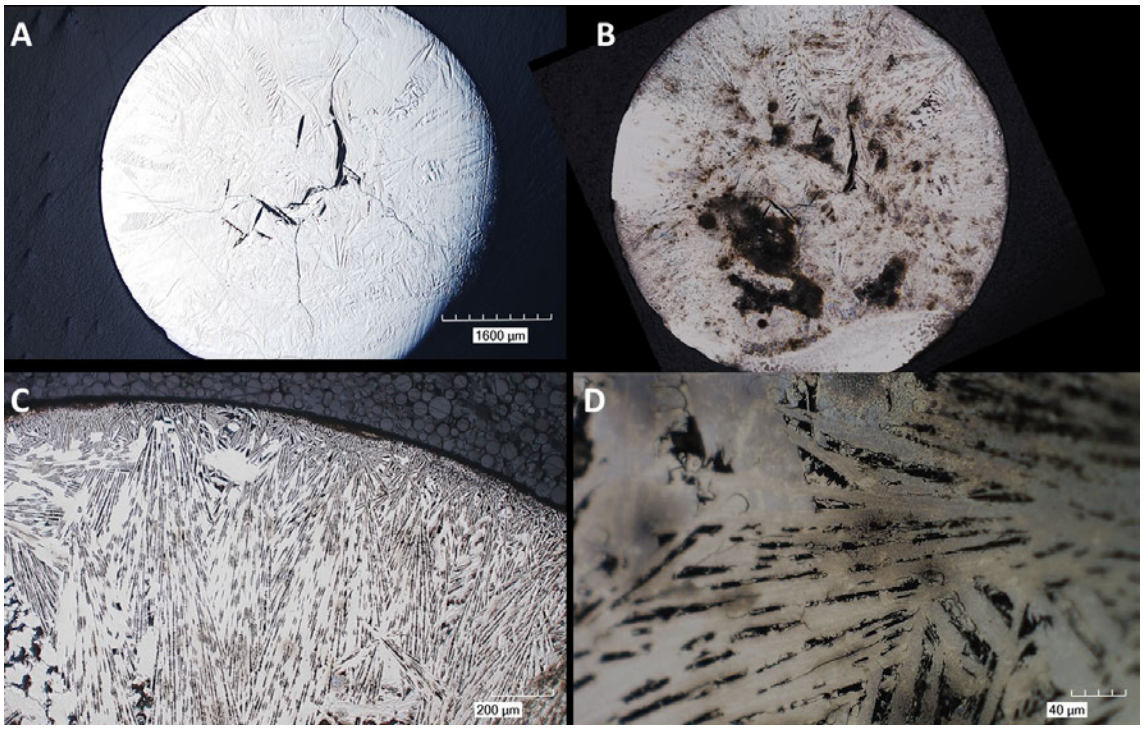

FIGURE 4.14 – Optical pictures of the sample $Ti_{26}Cu_{43}Zr_{15}Pd_{16}$ alloy before (A) and after (B) the electrochemical test in NaCl 0.9% at 37°C. C and D are higher magnifications of the sample surface after corrosion test.

Fig. 4.14 shows the surface appearance of the $Ti_{26}Cu_{43}Zr_{15}Pd_{16}$ 5mm rod before (A) and after (B) the corrosion test in 0.9% NaCl. It can be seen that in the initial state in a 5mm diameter rod there are large porosities or even cracks which are undoubtedly related to the manufacturing process (shrinkage porosity, see Appendix A.5). After the test, the surface does not appear to be significantly damaged (if we exclude the black corrosion products in the photo). In picture C, after the test, the needles stand out particularly well, as if the test had the same effect as a chemical etching on one of the two phases present in this alloy. On picture D, it is easy to see that it is the phase between the needles that was preferentially dissolved during the test. To better understand why one of the two phases dissolved preferentially, EDXS-SEM analysis is carried out and the results

are presented in Fig. 4.15.

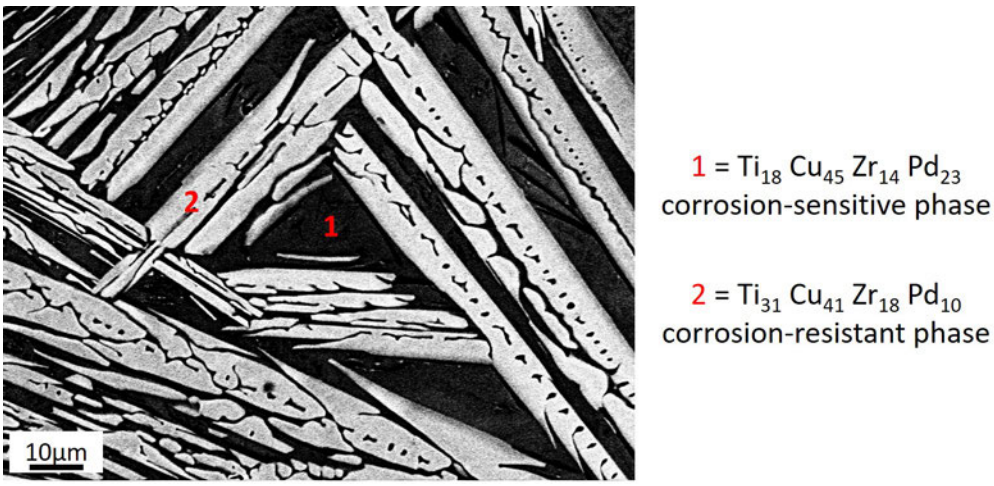

FIGURE 4.15 – SEM-BSE picture of the $Ti_{26}Cu_{43}Zr_{15}Pd_{16}$ alloy. 1 and 2 represent chemical compositions of both phases of the alloy determined by EDXS.

Fig. 4.15 shows a picture of the microstructure of the $Ti_{26}Cu_{43}Zr_{15}Pd_{16}$ alloy in SEM-BSE. As previously mentioned in Fig. 4.11, there are large needles on one side and an interstitial phase on the other which fill the space between the needles. Chemical analysis reveals that the (white) needles have the following composition $Ti_{31}Cu_{41}Zr_{18}Pd_{10}$ and that the interstitial phase (black) corresponds to a chemical composition of $Ti_{18}Cu_{45}Zr_{14}Pd_{23}$. The interstitial phase is very rich in Copper and Palladium while the needles are richer in Titanium and Zirconium. The chemical analysis indicates that, as for the $Ti_{40}Cu_{36}Zr_{10}Pd_{14}$ master alloy, it is the phase containing the most Cu and Pd that is the most prone to form chlorides complexes and therefore to dissolve. In this case, it is assumed that the same mechanism occurred. The $Ti_{26}Cu_{43}Zr_{15}Pd_{16}$ alloy can be considered as a "composite" material with two phases with different chemistries. One phase rich in Ti and Zr (the needles) tends to passivate and is less sensitive to corrosion whereas the second phase (interstitial phase) is rich in Cu and Pd is much more sensitive (see Pourbaix diagrams Fig. 4.18 in the appendix). The potentiodynamic curve is therefore probably a mixture of the signals from the two phases, which is illustrated in Fig. 4.16 below.

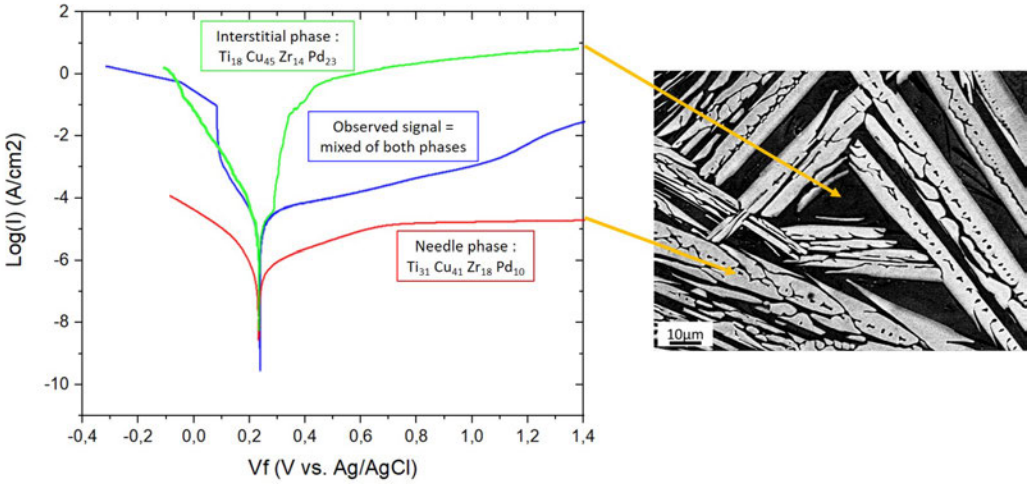

FIGURE 4.16 – Schematic illustration of probable potentiodynamic curves of both the needle phase (in red) and the interstitial phase (in green) compared to the measurement reproduced from Fig. 4.13 of $Ti_{26}Cu_{43}Zr_{15}Pd_{16}$ alloy in NaCl 0.9% at 37°C. Both phases are directly represented on the SEM-BSE picture on the right of the figure.

Key point of part 2:

- By remaining in the same quaternary system (TiCuZrPd) with general respects of Inoue's laws and by changing the atomic distributions, it is not trivial to succeed in making bulk amorphous rods.
- Among the compositions studied here, the composition: $Ti_{26}Cu_{43}Zr_{15}Pd_{16}$ has a very high hardness up to 525 HV even under crystallized state but as anticipated a poor corrosion resistance. This grade should be further investigated to assess its mechanical properties and its ability to be produced in amorphous state.
- An estimation of the enthalpy should be made to better understand if those composition are favorable for making BMG to justify further attempt of casting under different parameters.

4.3 Conclusion

In this last chapter of the manuscript, an exploratory approach has been adopted to propose some perspectives for the future work to be carried out on Ti-based metallic glasses. The main trends highlighted in this chapter are:

- The spherulites are probably not stable structure and the study of the master alloy can't confirm the findings of the Chapter 2 because of the lack of similarity between spherulite and master alloy.
- We are now sure that the high Cu and Pd content of the basic composition is responsible of its limited corrosion resistance.

- It is believed that, with some changes in the composition, spherulite formation could be prevented and corrosion resistance could be improved by increasing the $\frac{(Ti+Zr)}{(Cu+Pd)}$ ratio.

4.4 Chapter 4 - Appendix

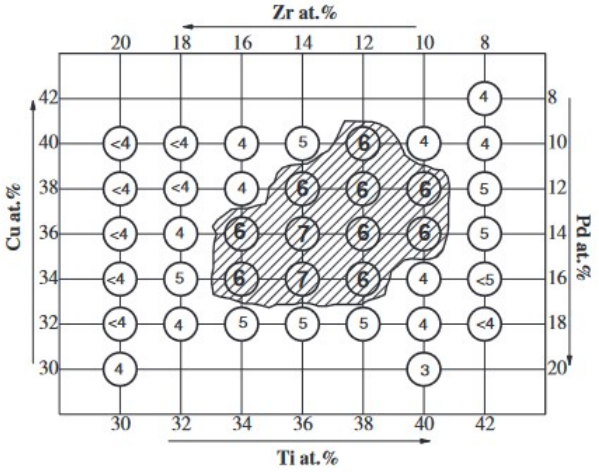

Fig. 2 Critical diameters (mm) of $(TiZr)_{50}(CuPd)_{50}$ glassy alloy rods produced by copper mold casting.

FIGURE 4.17 – reproduced from [ZHU 07b] with only compositions that respect $(Ti+Zr)_{50}(Cu+Pd)_{50}$.

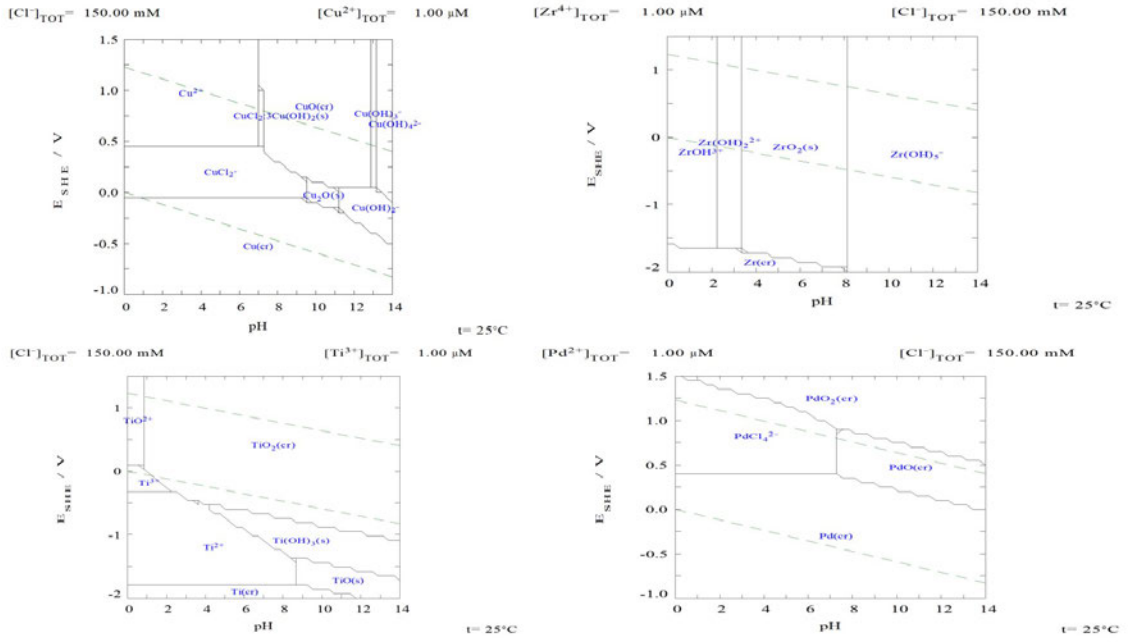

FIGURE 4.18 – Pourbaix plots of Cu, Pd,Ti and Zr in presence of Cl^- ions of the applied potential according to the pH at 25°C. In this chapter all the electrochemical tests have been done in NaCl solution of 0.9% at pH =7 at 37°C. Those plots give ideas of which species could be present during the potentiodynamic tests.

Conclusion and Perspectives

Conclusion

In this manuscript, the work was carried out on the BMG $Ti_{40}Cu_{36}Zr_{10}Pd_{14}$ grade. This grade appeared in the literature for the first time in 2007 by Zhu et al and soon described as very promising as a biomaterial in numerous published works. Most of these articles describe this material as particularly well suited for biomedical implants. It is true that $Ti_{40}Cu_{36}Zr_{10}Pd_{14}$ BMG has astonishing mechanical properties and it has been proved to be biocompatible. Despite all these promising studies, neither $Ti_{40}Cu_{36}Zr_{10}Pd_{14}$ BMG nor any other BMG grade have been marketed as a biomaterials to date. Two PhD works (including this one) carried out at MATEIS laboratory, were thus devoted to the potential use of this material as dental implants. In her manuscript, Aléthea Liens already highlighted the two main obstacles concerning the $Ti_{40}Cu_{36}Zr_{10}Pd_{14}$ BMG:

- The presence of un-identified crystalline casting defects (spherulites), likely involved in the premature failure of the samples in tension and fatigue (seen for the first time on the fracture surfaces),
- The moderate corrosion resistance of the alloy compared to most of the BMGs, with potential involvement of those spherulites but also the presence of Copper.

The first chapter of the manuscript was focused on a general description of the spherulites and their role on mechanical and corrosion properties. It was found that the spherulites are not easy to observe and often go unnoticed. The spherulites are large and randomly distributed on the rods. They have specific microstructures, with needles in the core and a polycrystalline shell at the interface with the amorphous matrix. The spherulites were proved to have significant impact on failure under mode I solicitation. Their diameter is greater than the calculated plastic zone (d_y), which induces premature brittle fracture in tension or fatigue following ISO 14801 standard. The corrosion resistance of the alloy was also investigated. It showed moderate resistance to corrosion in saline solution, even if spherulites were not the pitting starting points.

The second chapter focused in detail on the spherulites microstructure. The main goal was to describe, identify the phases present and propose a nucleation-growth scenario dur-

ing cooling from the melt state. It was determined that the Cu_3Ti_2 phase appears first in primary needles, then surrounded by CuTi tetragonal secondary needles. Later, the CuTi B2 appears and gives the round shape to the spherulite. More details in spherulite's microstructure were observed in the TEM observations. Observations of spherulites at different stages of their organization (early, intermediate and mature) allowed us to propose a detailed and robust growth scenario of spherulites in the BMG $Ti_{40}Cu_{36}Zr_{10}Pd_{14}$, which was never described before in the literature. This study concluded that it is the Cu_3Ti_2 phase that nucleates first in the liquid state metal and that it is probably the nucleus number that determines the final shape of the spherulite.

In the third chapter, various assumptions concerning the arc melting suction casting process were tested. Indeed, the copper mold diameter has a direct influence on the cooling rate and therefore a direct influence on the number and size of the spherulites. Then, it was believed that the heating steps of BMG preparation could have an influence on spherulites. This assumption was tested by varying the arc intensity between 200, 300 and 400 A and then by casting rods that had been melts/turn 6 or 14 times before casting. Neither the arc intensity nor the number of melts/turns had a significant factor in changing the distribution of spherulites in number and size or mechanical properties tested in 4-point bending. The bending strength values were in all cases very dispersed, with mostly brittle failure at a maximal stress dependent on the largest spherulite and its position. A chemical analysis of the surface (TOF-SIMS) revealed a contrast with hydrogen: there is more hydrogen in spherulite core and in the amorphous matrix than in the spherulite's periphery. Spherulites appears to be bigger and more numerous with H_2 addition in the chamber during casting. The rods were then tested by compressive tests. The results very poorly reproducible again (from brittle to ductile), so it is assumed that hydrogen facilitates the appearance of spherulites or promote their growth and that it is therefore preferable to avoid it. Final part of chapter 3 concludes that spherulite structure seems to be quite stable, because heat treatments even at 600°C do not change their size/structure.

The fourth and last chapter is more exploratory: it presents the study of the master alloy, which revealed complex microstructure with at least five phases which all have different chemical compositions. The phases of the master alloy and the spherulites appear to be different according the DRX and EDXS analyses. Among master alloy phases, two phases were found to be more resistant to corrosion than the others and one was found to be really sensitive to dissolution. It was concluded that it is the amount of Cu and Pd that influences the corrosion resistance because Cu and Pd atoms are able to form chloride complexes at pH tested. So, the more the alloy contains Cu and Pd, the more it is sensitive to corrosion. The three previous compositions were cast and were found to be fully crystalline, their GFA likely lower that the initial composition. However, one composition $Ti_{26}Cu_{43}Zr_{15}Pd_{16}$, with a particularly high hardness could be worth of deeper

investigation.

In conclusion, a lot of efforts and resources have been put into identifying and describing precisely the casting defects of BMG $Ti_{40}Cu_{36}Zr_{10}Pd_{14}$. We are now certain of their deleterious influence on the mechanical properties of the alloy. Despite several different approaches, we were not able to produce BMGs without any spherulite. Furthermore, the corrosion resistance of the BMG remains a problem in view of the intended application. It seems that the amount of Cu and Pd is too high to have a good corrosion resistance, even without spherulite. For us, this dampens profoundly the potential of the BMG $Ti_{40}Cu_{36}Zr_{10}Pd_{14}$ as a biomaterial. The mastering of its manufacturing process remains a source of uncertainty regarding the quality of the rods produced. The metallic glass community rarely mentions these drawbacks, which need to be further studied in order to better address the problems encountered to finally end up with a marketed product.

What is the future for metallic glasses in the biomedical industry?

Perspectives

Relation between manufacturing process and microstructure

Other suction casting parameters which have not been tested yet still have chance to change the spherulite/free volume quantity. For example, removing the cooling circuit of the copper mold and favoring a spontaneous pouring of the alloy rather than suction could be interesting. Indeed, it is likely that during suction, a flow of liquid metal surrounded by Argon gas would be drawn into the copper mold. The interface with the mold would therefore not be BMG/Copper but rather BMG/Argon/Copper, which would be detrimental to good heat conduction (and therefore to very fast cooling of the alloy). In addition, it seems that fluid mechanics is a key element in understanding the casting parameters. We should probably take a deeper look along that line to find answers. It is possible that the atomic movement due to suction can have influence on the Cu_3Ti_2 phase nucleation.
Currently, we do not know what cooling rates are actually achieved in the laboratory arc melter. It would be interesting to make thermal calculations on the copper mold used in this work (⌀3 and ⌀5mm) to have supplementary elements to explain spherulite evolution according to the cooling rate.
Thanks to the information gathered in chapter 2, a synchrotron proposal has been drafted and submitted to ESRF. A feasibility test (see Appendix B) proved that the use of Phase Contrast Tomography (PCT) coupled with Diffraction Contrast tomography (DCT) allows to observe clearly the spherulites and their distribution, in 3D and in a non-destructive manner. These analyses could provide more quantitative evidences that the size of the spherulites depends on the cooling rate, which is related to the size of the mold. In-situ mechanical tests in traction and compression should also provide information on the crack

propagation regime as a function of the solicitation mode.
Finally, it worth trying completely amorphous parts (even more than 5 mm pieces) by atomizing the master alloy of the $Ti_{40}Cu_{36}Zr_{10}Pd_{14}$ grade followed by Spark Plasma Sintering (SPS), so that mechanical and electrochemical tests can be carried out again without being hampered by spherulites and thus confirming the previous results.

Relation between microstructure and mechanical properties

It would be interesting to establish a TTT diagram of the $Ti_{40}Cu_{36}Zr_{10}Pd_{14}$ alloy using isothermal heat treatment using DSC to determine the position of the crystallization and relaxation noses to know if we are in the case of a type I or type II BMG (see introduction,[KUM 13])[KET 18]). The DSC can also be used to study the free volume according to casting parameters.
To better estimate the importance of the size and distribution of spherulites and their role in the failure mechanisms (in tension and compression for example), and because the synchrotron is not a very available facility, it would be interesting to develop a finite element model of an amorphous matrix containing crystalline spherulites, their mechanical properties being both known. It would be possible to simulate variation of the position and size of spherulites. Thus, it would be possible to confirm the critical diameter of the spherulites that should not be exceeded according to the solicitation mode.

Combinatorial metallurgy

Since we are likely to be in the case of an HEA in the quaternary TiCuZrPd, some compositions could have interesting mechanical properties even in their crystalline form (as illustrated in chapter 4). The question arises what is the “best” composition according to mechanical properties. To do this, based on the principle of combinatorial metallurgy, four alloys could be prepared (each of which could be particularly enriched in one of the 4 elements of the system). Then thermal treatments would be applied to the SPS to start diffusion of the elements. Finally, nano-indentation mapping could be done to identify the alloys with the best mechanical properties. Similarly, electrochemical tests on the same type of samples could highlight the most corrosion-resistant chemical compositions. The intersection of these two types of screening would make it possible to highlight the most promising alloy compositions as biomaterials in the TiCuZrPd system.
Among the three new compositions studied in Chapter 4, it would appear that composition $Ti_{26}Cu_{43}Zr_{15}Pd_{16}$ has a particularly high hardness (so likely high yield strength) even in crystalline state. In the future, we should find a way to produce rods without porosities to allow a robust evaluation of its mechanical properties. It would also be interesting to perform tomography to better estimate and understand the presence of those porosities and cracks in the “as cast” samples (see Appendix A.5). The use of a HIP treatment is a possible way to get rid of defects with time and temperature based on a previous DSC

analysis.

Modelling of spherulite nucleation in a BMG

The palladium present in the alloy is suspected to be the origin of the Cu_3Ti_2 phase nucleation. This assumption is particularly difficult to investigate experimentally but some molecular dynamics simulations could help us to better understand the nucleation phenomenon. Similarly, to go further, hydrogen could be introduced into the model to better understand its involvement in BMG crystallization. To do so, the first step will be to do some ab initio modelling in the initial BMG composition to find the binding energies between the atoms of the system. The next step will be to perform molecular dynamic simulation to access the phases enthalpies of the system and simulate the Cu_3Ti_2 phase nucleation. Finally, the ultimate goal would be to perform simulation on various chemical composition of the TiCuZrPd system to find the best GFA to avoid spherulite (and maybe have a better corrosion resistance).

Corrosion resistance

Pitting that occurs on the BMG $Ti_{40}Cu_{36}Zr_{10}Pd_{14}$ appears at very high potentials that are only slightly representative of what can happen in a patient's mouth. Several solutions can be imagined to overcome its sensitivity to dissolution of the alloy, such as the use of a coating that would cover all the parts to prevent pitting (some tests with DLC coatings have been performed already). Another approach could be to reinforce the surface oxide layer of the alloy to better protect it. Anodization or even Micro-Arc Oxidation (MAO, anodization at higher currents), which allow the surface oxide layer to grow, may allow in theory to have a denser and thicker layer of titanium and zirconium oxides to prevent pitting. In addition, MAO can provide controlled and reproducible surface states/morphologies, which is of particular interest for an application such as dental implants.

What is the future for metallic glasses in the biomedical industry?

Even though the $Ti_{40}Cu_{36}Zr_{10}Pd_{14}$ grade is probably not ultimately suitable for dental implants manufacturing, bulk metallic glasses in general remain materials with fascinating properties. It cannot be excluded that other grades (whether already known or not yet) could someday be used as dental implants. This category of materials is very young in the history of metallurgy, with more unanswered questions than for conventional metals. For example, what about the ageing of BMGs? At this point, we have no idea how the structure of an amorphous metal evolves over the long term, especially in an environment as complex as the human body. Despite their potential, the lack of global control of the manufacturing process(es) represents a major obstacle for industrial applications and particularly in the medical field. It is possible that if substantial investment in research

and development is put forward, then answers to most of the questions could be found and the problems we are currently facing could be solved in the future. Nevertheless, metallic glasses contain mostly noble and precious elements which are expensive and in limited quantities in the environment. It seems highly unlikely that even the hypothetical best performing BMG implants will ever completely replace TA6V implants. These products will be destined for a limited (niche) market in the dental sector, given the manufacturing costs of such implants. However, metallic glasses could become more widely available for other engineering applications.

The quaternary TiCuZrPd system and High Entropy Alloys (HEA)

Metallic glasses share some similarities with High Entropy Alloys (HEA). They are both recent categories of materials that have seen increasing interest over the last two decades. Indeed, HEA are composed of several atomic species (in theory minimum five) in equimolar or almost equimolar concentration (between 5 and 35 at.%). The principle of HEAs is that they do not form intermetallics, but on the contrary they organize themselves into a stable solid solution. Unlike amorphous metallic glasses, they are crystalline and organized in a single phase (sometimes with additional secondary phases) with a simple organization (CC or CFC). The promises of high entropy alloys would lie in their mechanical properties, with a combination of high yield strength and hardness together with high plastic strain and toughness. They are also promising in terms of thermal stability. The TiCuZrPd system investigated in this work, despite being 'only' quaternary, could match HEA compositions. In Chapter 4, several compositions of this quaternary system were tested and it was observed that $Ti_{26}Cu_{43}Zr_{15}Pd_{16}$ had a particularly high hardness and a two-phase microstructure that could probably be modified by heat treatments or other processing methods. A simple calculation of configurational entropy for the compositions mentioned in the manuscript gives, by using the following formula:

$$\Delta S_{mix} = \sum_{i=1}^{N} c_i ln(c_i)$$

N is the number of element, c_i atomic fraction of element i. R is the universal gas constant ($R = 8.314$). ΔS_{mix} for the four composition studied are gathered in Tab. 4.5.

Table 4.5

c_i (atomic fraction)	Ti	Cu	Zr	Pd	ΔS_{mix}
$Ti_{40}Cu_{36}Zr_{10}Pd_{14}$	0.4	0.36	0.1	0.14	6.77
$Ti_{65}Cu_{21}Zr_4Pd_{10}$	0.65	0.21	0.04	0.1	8.04
$Ti_{51}Cu_{38}Zr_3Pd_8$	0.51	0.38	0.03	0.08	8.47
$Ti_{26}Cu_{43}Zr_{15}Pd_{16}$	0.26	0.43	0.15	0.16	10.73

It is indeed $Ti_{26}Cu_{43}Zr_{15}Pd_{16}$ which has the highest entropy (but does not officially fall into the high entropy category $\Delta S_{mix} > R \times 1.61 = 13.38$). Again, an attempt to eliminate porosities (Appendix A.5) in the $Ti_{26}Cu_{43}Zr_{15}Pd_{16}$ rod or a change in the processing method could allow us to study this composition in more details and better draw the parallel between metallic glasses and HEA.

Appendix A

Use of X-ray tomography to detect defects in metallic glass rods

A.1 Porosities

Laboratory X-Rays tomography was used to check the absence of porosities in the rods before mechanical tests (Chapter 3). The precaution was useful, some isolated, but large porosities were observed (Fig. A.1). They were easy to spot and avoid when cutting the specimens.

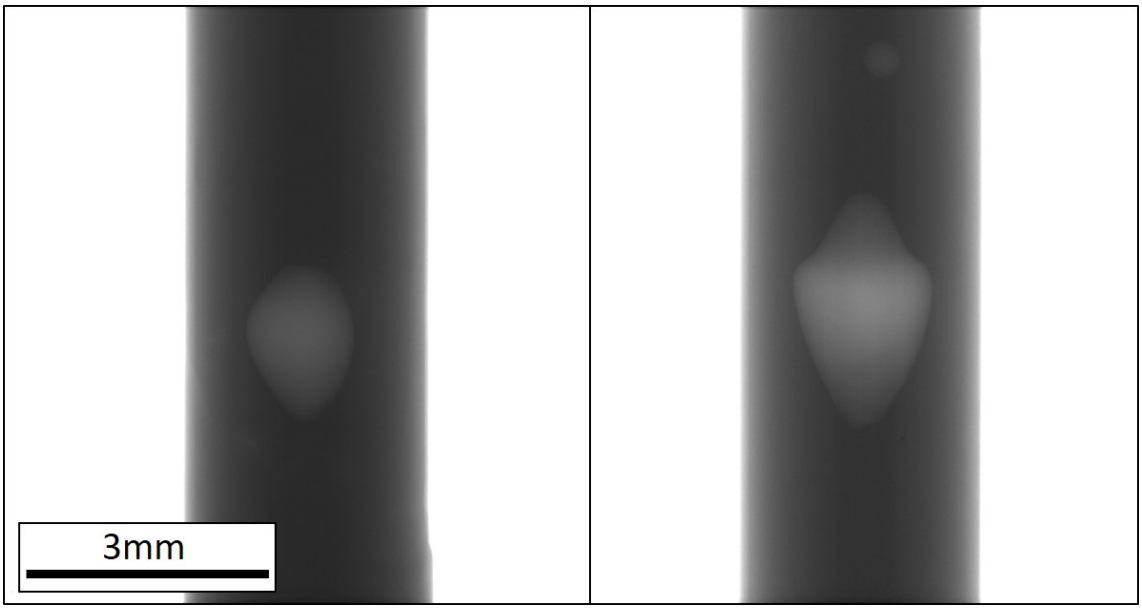

FIGURE A.1 – X-Rays radiography of 3mm rods with large porosities(left : 1.3 x 1.9 mm, right: 3 x 1.7 mm).

A.2 Unmelted Palladium granules

Another type of defect was observed thanks to X-rays tomography.Some massive granules could be observed in some rods, as illustrated in Fig. A.2. These granules strongly absorbed X-Rays, which suggested they were composed of heavy elements. SEM analysis was performed on cross sections Fig. A.3

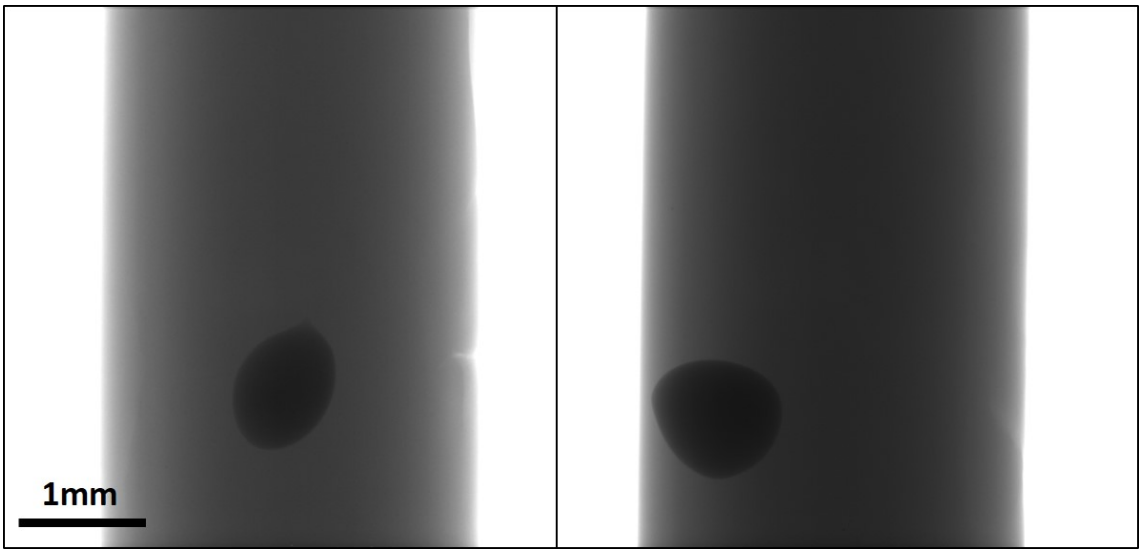

FIGURE A.2 – X-Rays radiography of 3mm rods with heterogeneous massive granules (strongly absorbing X-rays).

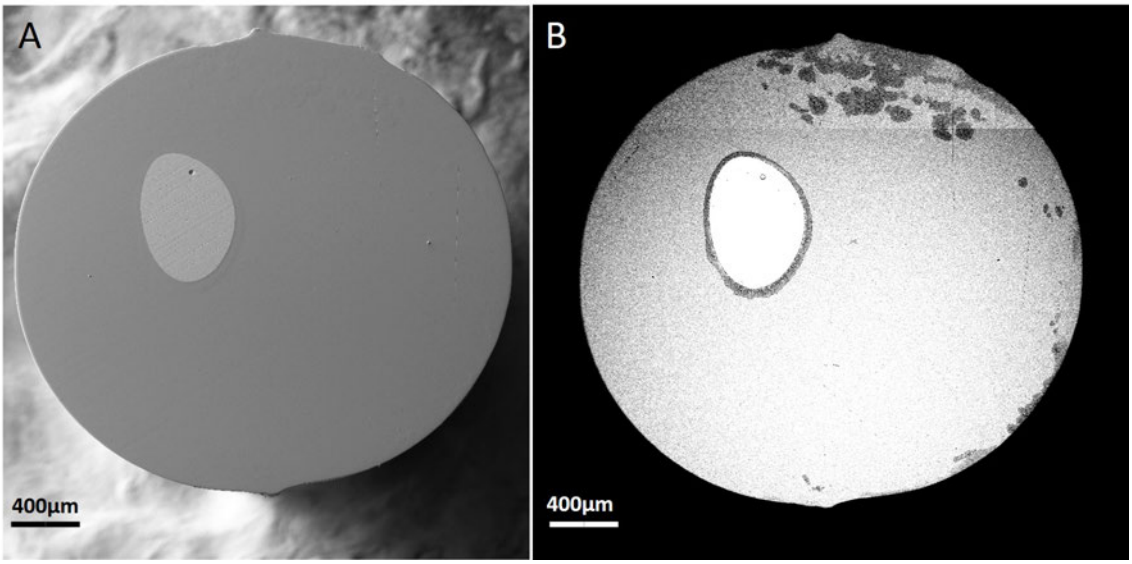

FIGURE A.3 – A, SEM picture in secondary electron mode of a granule. B, SEM-BSE picture of the same sample.

The large granule appears in white (heavy element) and is surrounded by a poly-

crystalline interface . Some spherulites can also be observedin the middle of the amorphous matrix.

The EDXS measurements confirmed that the granules are made of Palladium. The interface between granule and amorphous matrix has the exact same morphology than the copper mold interface crystallization. Some EDXS measurements were performed at the interface as illustrated in Fig. A.4.

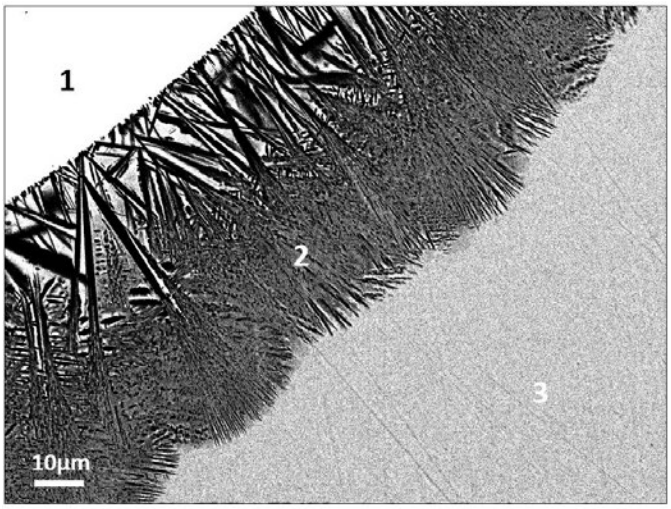

Label	1	2	3
Ti (at%)	0	41	42
Cu (at%)	0	38	37
Zr (at%)	0	10	11
Pd (at%)	100	10	10

FIGURE A.4 – SEM-BSE picture focusing on the interface granule/crystaline shell/amorphous matrix. Numbers are the postions were the EDXS measurements were done.On the left, table with EDXS quantification.

An EBSD map was performed at the interface too Fig. A.5. It confirms the presence of pure (unmelted) Palladium and that the interface is identical to the spherulite (same phases and same organization).

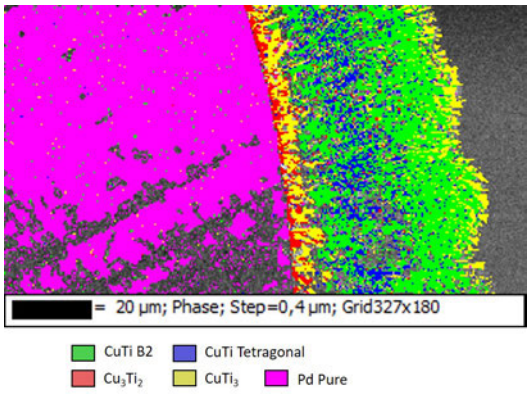

FIGURE A.5 – EBSD map of the interface granule/crystaline shell/amorphous matrix.

These results confirm that the alloy crystallizes preferentially at interfaces (heterogeneous nucleation).

A.3 Surface irregularities

Another type of surface defect was observed thanks to X-ray tomography. On 3mm BMG rods as illustrated in Fig. A.6.

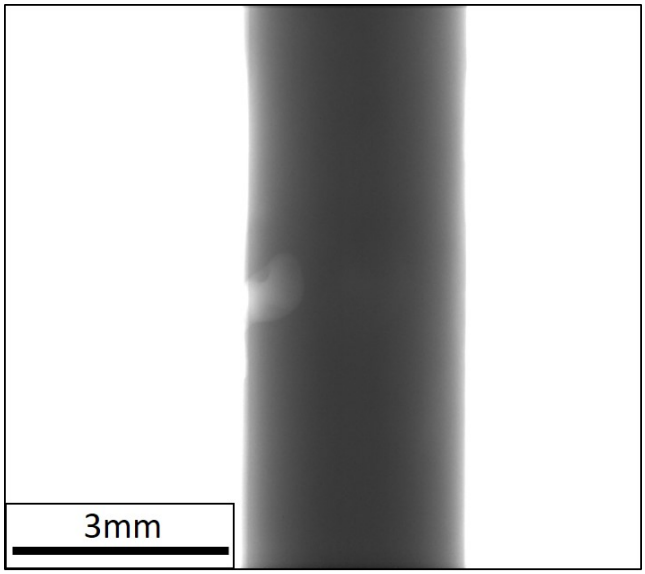

FIGURE A.6 – X-Rays radiography of 3mm rods with surface irregularities.

Fig. A.7 show the same type of surface irregularities but in SEM (secondary electron mode). In A, this is the surface of a "perfect" rod after casting, really shiny and smooth. On the contrary, in B, a surface irregularity can be seen. We don't really know if this is a fluid mechanics problem that prevents the liquid metal from coming into direct contact with the copper mold (a problem of wettability) or if it is an area where the argon to form a pocket during casting.

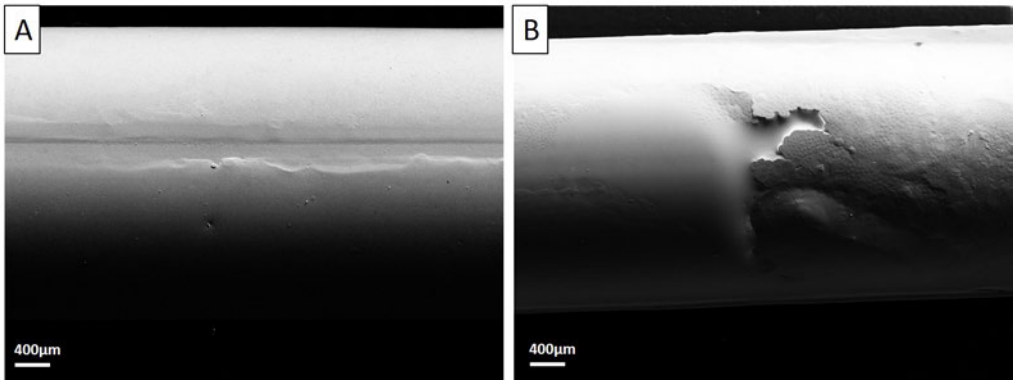

FIGURE A.7 – SEM pictures of 3mm rods surfaces. A, shiny and smooth, synonym of amorphous state. B, mat and rough, probably synonym of crystalline.

Higher magnification observations allow us to see additional detail on the rough area

in Fig. A.8. On those pictures, many small structures are visible. There are numerous and measure about 40 μm in diameter. These structures seem crystalline and have needle shaped details in the center. The surface crystallization is directly visible in SEM. It is possible that during casting if there is a Copper/Argon/alliy interface instead of Copper/alloy interface, then the heat transfer is much poorer and the cooling rate lower. The importance of argon flow on the final appearance of the rods and perhaps on their mechanical properties should be further investigated.

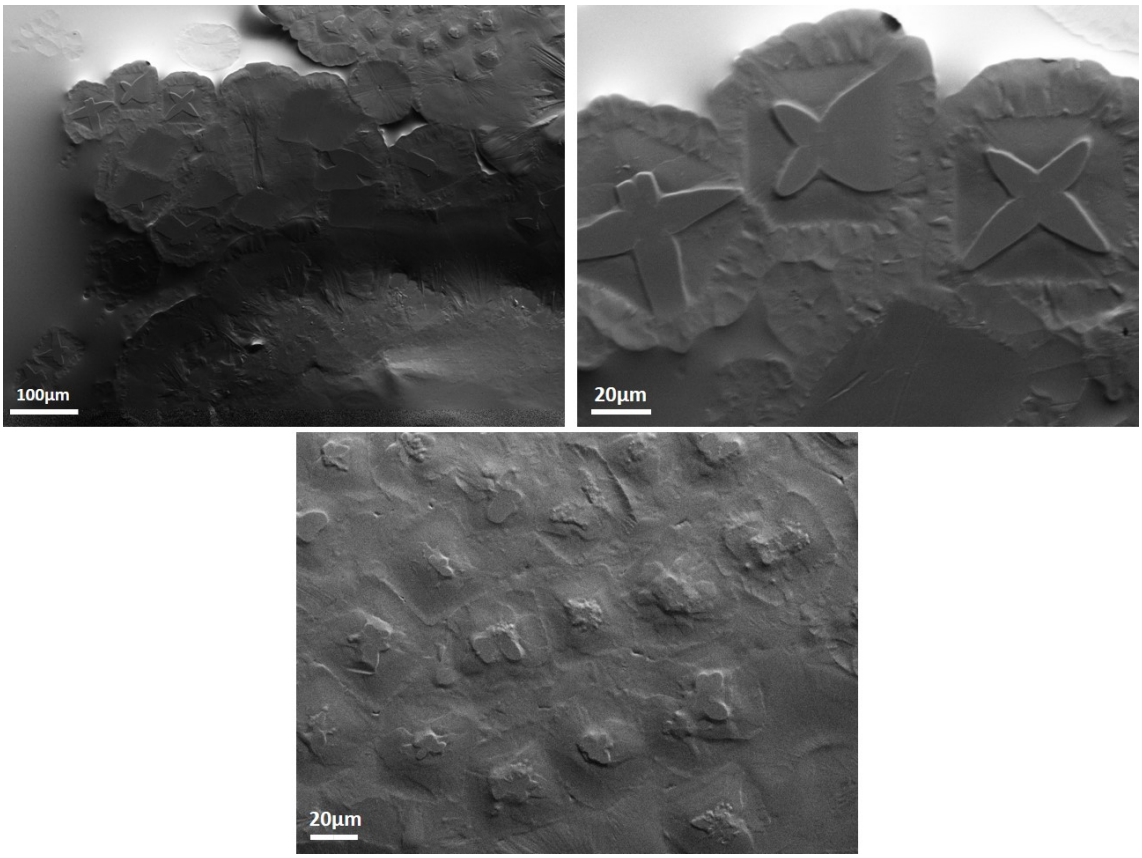

FIGURE A.8 – High magnification SEM pictures of surface irregularities. On the left picture, it is the mark of the interface between the two parts of the mold

A.4 Crystallization at the interface with the mold

In Fig. A.9, the crystallization at the periphery of the rod (at the interface with the mold) is particularly clear. The crystallization has a morphology identical to that of spherulites. It is not in sphere shape but in the shape of a crown all around the rod, since it is obviously the interface that favors the crystallization of the alloy. In this case also, one has the impression of primary and secondary needles and a globular phase that grows afterwards (chapter 2). The phenomenon is more or less accentuated depending on the diameter of the mold used and the use of hydrogen (Chapter 3). These observations suggest that some tests should be carried out without using suction and to see whether or not the surface condition of the as cast rods is better or not (smooth and therefore free of crystals).

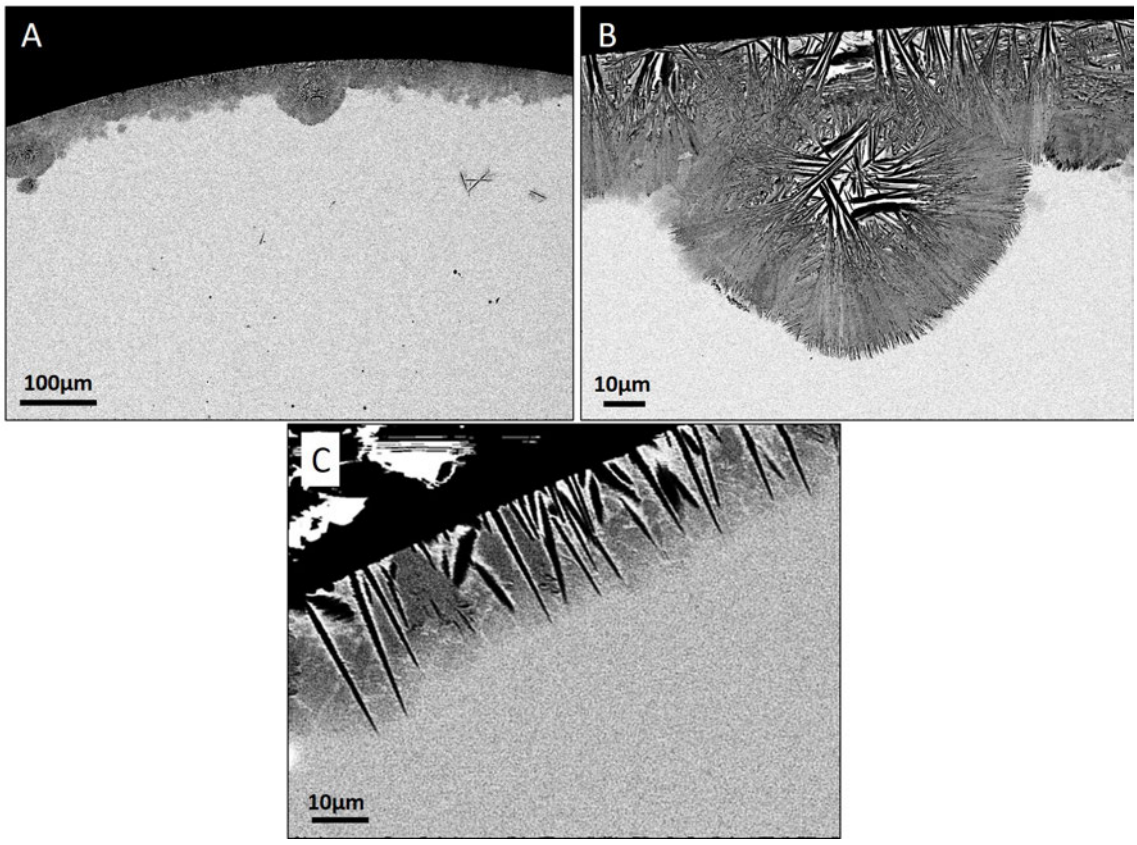

FIGURE A.9 – SEM-BSE pictures of crystalline interface with the copper mold.

A.5 Porosities evolution in $Ti_{26}Cu_{43}Zr_{15}Pd_{16}$ polycristalline according to sample diameter

As mentioned in **Chapter 4** (see Fig 4.14), the $Ti_{26}Cu_{43}Zr_{15}Pd_{16}$ shows massives porosities and cracks. In order to observe their shape and repartition according to the rod's diameters some acquisitions were performed the main results are presented in figure Fig. A.10 and Fig. A.11.

The following figures show that the larger the diameter, the larger the number of pores. For a diameter of 2mm, there are hardly any and very small. For the 3mm diameter, they are punctual but a bit bigger. For diameter 4mm, there are many more porosities in the rod's core, in the shape of "small plates" (flat and extended). It is assumed that this shape corresponds to the contraction of the material during crystallization. For the 5mm diameter, the porosities are even more numerous and more extensive, one can even distinguish cracks.Those cracks and porosities are probably due to shrinkage phenomenon during material processing.

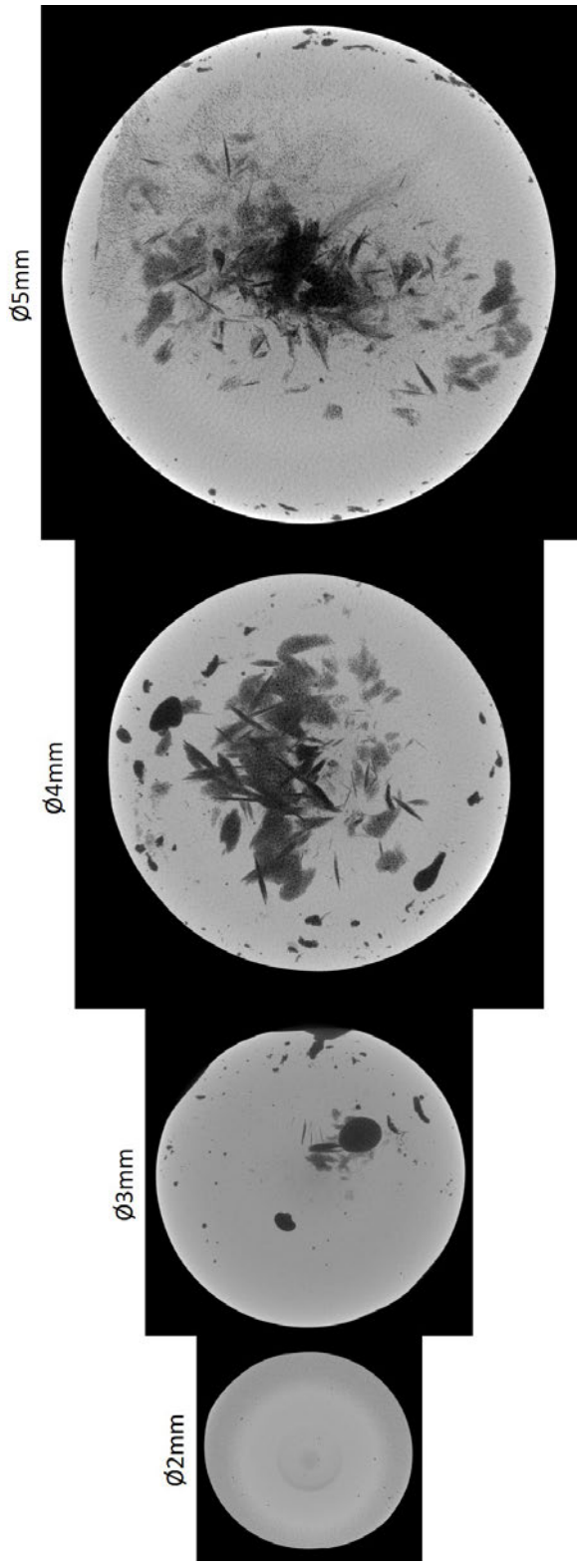

FIGURE A.10 – Projection of porosities on z axis for rod diameters from 2 to 5mm of $Ti_{26}Cu_{43}Zr_{15}Pd_{16}$ alloy.

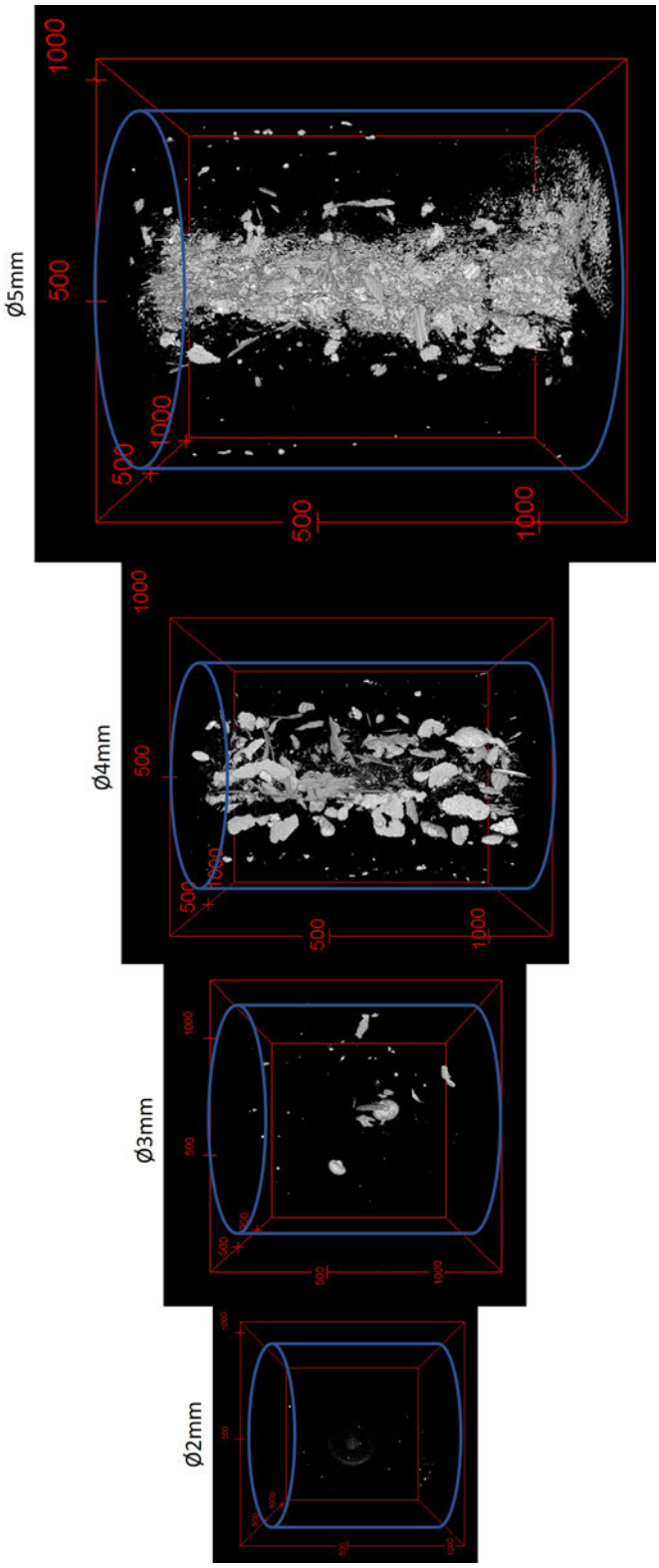

FIGURE A.11 – 3D view of the prorosities inside the same rods form 2mm to 5mm of $Ti_{26}Cu_{43}Zr_{15}Pd_{16}$ alloy.

A.6 Using PCT and DCT test to view spherulites in 3D

A mini cylinder (800 μm diameter) of the alloy studied here has already been characterized at ID11 (ESRF beamline) to test. the feasibility of DCT en PCT experiments on our BMG. Both, DCT and PCT have been tested to visualize for the first time and in 3D the spherulites and their distribution in a bulk specimen. the results are presented in Fig. A.12.

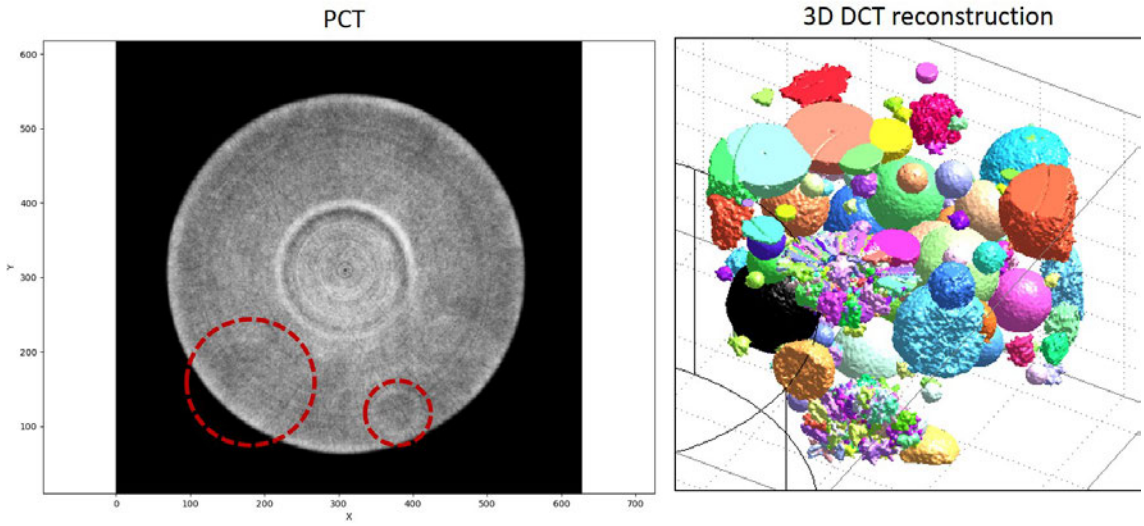

FIGURE A.12 – PCT(left) and DCT(right) acquisitions on a $Ti_{40}Cu_{36}Zr_{10}Pd_{14}$ small cylinder. The DCT reconstruction was done using a CuTi-B2 lattice parameters.

The contrast in PCT is not important enough to see well the spherulite. On the contrary, the DCT reconstruction using CuTi B2 crystal lattice seems to work very well to see the spherulite in 3D. These good results allowed us to apply to ESRF for beam time, the details of which are presented in Appendix B.

Appendix B

Towards a quantitative 3D analysis of sperulites population by DCT - Application for beam time at ESRF

EUROPEAN SYNCHROTRON RADIATION FACILITY

ESRF User Office
CS 40220, F-38043 GRENOBLE Cedex 9, France
Delivery address: 71 avenue des Martyrs, 38000 GRENOBLE, France
Tel: +33 (0)4 7688 2552; fax: +33 (0)4 7688 2020; email: useroff@esrf.fr; web: http://www.esrf.fr

Application for beam time at ESRF – Experimental Method

Template for ESRF Standard proposals, CRG proposals, MX Rolling Crystallography and MX Rolling BioSAXS proposals.
This document should consist of a **maximum** of **two A4 pages** (including references) with a minimal font size of **12 pt**.

Proposal Summary (should state the aims and scientific basis of the proposal) :

The BMG $Ti_{40}Cu_{36}Zr_{10}Pd_{14}$ grade has already been demonstrated as a material with very high potential for biomedical applications [1], [2] (mainly the manufacturing of dental implants). However, recently the presence of crystalline defects (called 'spherulite') has been observed in this alloy and it now appears essential to know the actual 3D distribution of spherulites in the manufactured parts. Indeed, we believe there is a critical spherulite diameter beyond which the parts break prematurely with a fully brittle behavior. It is assumed that the control of their size and distribution in massive parts can improve the mechanical strength and plastic behavior before failure[3].

So first the aim of the study is to check the 3D distribution of the spherulite in PCT (phase contrast tomography) and the phases repartition inside one spherulite thanks to the nanoscope device in different samples (casted with different parameters). Some thermic treatment are also planned to study the influence of temperature on the size and some change of phase of these defects [4].

This proposal is finally aimed to study the effect of the stress on the spherulite microstructure and deformation mode [5]. Mechanical tests in compression should allow us to determine whether stress can induce changes in the microstructure of these defects and determine whether the spherulites deform and slow down the propagation of cracks or whether the cracks pass through them and cause brittle behavior.

These experiments should give us elements to rule on the influence of spherulites on mechanical strength: are they deleterious or advantageous? And they should give us clues as to the cooling rates to be reached or the heat treatment to control their size/distribution. This study is intended to overcome the technical barriers to the development of this grade for the manufacture of implants on an industrial scale.

Scientific background :

A mini cylinder (800 µm diameter) of the alloy studied here has already been characterized at ID11 to test the feasibility of the experiments described in this form. Both, DCT and PCT have been used to visualize for the first time – and in 3D - the spherulites and their distribution in a bulk specimen.

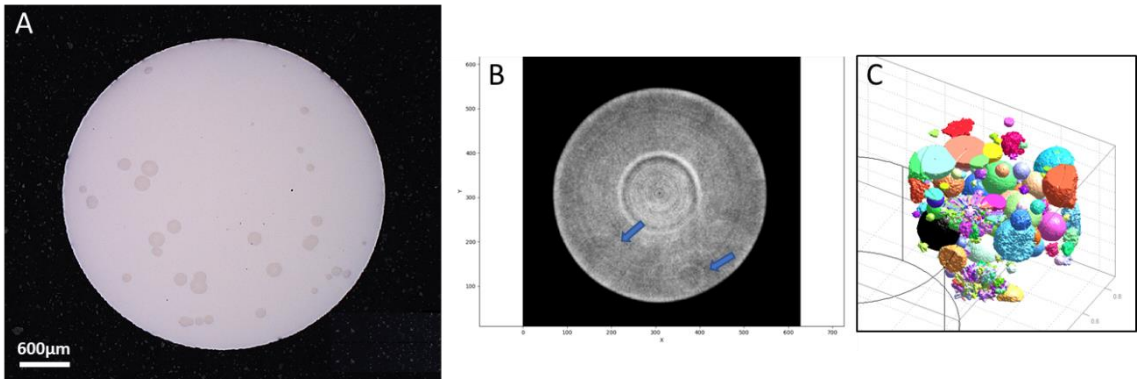

Figure 1 : A) SEM picture of 3mm diameter random rod's cut. B) Phase contrast tomography (PCT) slice showing faint contrast at the interface layer between the spherulites and the amorphous matrix. C) 3D reconstruction of spherulites (using a single, cubic phase) using DCT.

Thanks to previous works, we were able to study spherulites in particular through their complex microstructure and their influence on mechanical properties and corrosion resistance. A recent laboratory study, including TEM/SEM/EDS/EBSD allowed us to identify several phases, their organization and even to propose a growth scenario, recently confirmed by ASTAR TEM experiments done in SIMAP Laboratory [6]. This information will be valuable input for the 3D reconstruction of the complex, multiphase

microstructure of spherulites using the scanning-3DXRD approach. It appears that the crystallisation in this alloy has similarities with CuZr based alloys [7]. We wish to know the size and distribution of spherulites in solid parts in order to know the influence of the manufacturing process parameters on the final state of the parts produced. This information is essential for the potential industrial application of dental implant manufacturing which depends directly on it. Similarly, mechanical tests and the study of crack propagation in this BMG composite could make it very competitive and innovative in the dental sector. The interest of choosing this material for the manufacture of dental implants is their miniaturization and the reduction of damage to the implantation site in patients (reduction of pain, healing time and complications) and the minimization of the phenomenon of stress shielding.

Experimental technique(s), required set-up(s), measurement strategy, sample details (quantity...etc) :

1. PCT characterization of the 3D repartition and volume fraction of spherulites in samples made from different rods: a 3mm rod made under pure Ar, a 5mm rod made under pure Ar and a 3mm rod made under hydrogenated Ar. The aim of this part of the study is to improve the manufacturing process.
2. In situ observation of one sample (alternating PCT and 3DXRD scans) at increasing temperatures (from 20 to 700°C with a slow ramp of about 1 °C per minute) to observe the growth of spherulites (PCT) and to study the order of appearance of the phases during the casting process (3DXRD). Moreover, this test will provide information on the temperature of crystallisation and the theoretical cooling rates to reach to avoid them.
3. Interrupted compression tests on specimens with dimensions representative of the dental implants and with different spherulite content in order to prove the influence of spherulites on the stress/strain field and to observe the possible occurrence of martensitic phase transformation (3DXRD).
4. 3D crystallite shapes and phase identification in individual spherulites using the scanning-3DXRD technique (150 nm beam) on the nanoscope endstation.

Beamline(s) and beam time requested with justification :

ID11 is the only beamline offering the required combination of X-ray phase and X-ray diffraction contrast tomography and scanning-3DXRD characterization.
Preliminary tests (DCT & PCT) have already been successfully conducted (Fig 1). We estimate the time needed to perform the proposed experimental program to be: 1 day for the ex-situ and in-situ PCT observations at increasing temperature. 2 days for the in-situ compression tests (using a tomographic stress rig provided by INSA Lyon). 2 days for the high-resolution measurements by s-3DXRD on the nanoscope endstation.

Results expected and their significance in the respective field of research :

Quantification of spherulite volume fraction as function of the processing route (5mm versus 3mm rods, forming gas). For the temperature tests, we think we can determine the growth rate as a function of temperature and deduce the theoretical cooling speed necessary to avoid/reduce their formation. The mechanical tests should allow us to test the hypothesis that if the spherulites are sufficiently small, numerous and randomly distributed, then the parts could undergo some plastic deformation before breaking. The results obtained should allow us to ensure the possibility of industrialisation of this alloy.

References

[1] A. Liens *et al.*, « On the potential of Bulk Metallic Glasses for dental implantology: Case study on Ti 40 Zr 10 Cu 36 Pd 14 », *Materials*, vol. 11, nº 2, Art. nº 2, 2018, doi: 10.3390/ma11020249.

[2] A. Liens *et al.*, « Effect of alloying elements on the microstructure and corrosion behavior of TiZr-based bulk metallic glasses », *Corros. Sci.*, vol. 177, p. 108854, déc. 2020, doi: 10.1016/j.corsci.2020.108854.

[3] L. Gautier *et al.*, « Impact of spherulite-type crystalline defects on the mechanical and electrochemical properties of TiCuZrPd metallic glasses », *Materialia*, p. 101353, févr. 2022, doi: 10.1016/j.mtla.2022.101353.

[4] A. Sypien, K. Badura, P. Fima, et K. Miernik, « Effect of Pd, temperature and time on wetting and interfacial microstructure of bulk metallic glasses TiCuZrPd on Ti-6Al-4V substrate », *J. Alloys Compd.*, vol. 695, p. 962-970, févr. 2017, doi: 10.1016/j.jallcom.2016.10.216.

[5] C. Bernard et V. Keryvin, « Crystalline defects in bulk metallic glasses: consequences on fracture toughness determination and ductility », *J. Phys. Condens. Matter*, vol. 32, nº 48, Art. nº 48, nov. 2020, doi: 10.1088/1361-648X/abaa7f.

[6] E. F. Rauch et M. Véron, « Automated crystal orientation and phase mapping in TEM », *Mater. Charact.*, vol. 98, p. 1-9, déc. 2014, doi: 10.1016/j.matchar.2014.08.010.

[7] S. Pauly, G. Liu, G. Wang, U. Kühn, N. Mattern, et J. Eckert, « Microstructural heterogeneities governing the deformation of Cu47.5Zr47.5Al5 bulk metallic glass composites », *Acta Mater.*, vol. 57, nº 18, Art. nº 18, oct. 2009, doi: 10.1016/j.actamat.2009.07.042.

References

[ABU 10] Abuhussein H., Pagni G., Rebaudi A., Wang H.-L.
The Effect of Thread Pattern upon Implant Osseointegration. *Clinical Oral Implants Research*, vol. 21, n° 2, 2010, p. 129–136.

[ALB 05] Albrektsson T., Wennerberg A.
The Impact of Oral Implants — Past and Future, 1966–2042. *Journal of the Canadian Dental Association*, vol. 71, n° 5, 2005, Page 5.

[ALB 17] Albrektsson T., Chrcanovic B., Östman P.-O., Sennerby L.
Initial and Long-Term Crestal Bone Responses to Modern Dental Implants. *Periodontology 2000*, vol. 73, n° 1, 2017, p. 41–50.

[AND 16] Andreatta F., Fedrizzi L.
The Use of the Electrochemical Micro-Cell for the Investigation of Corrosion Phenomena. *Electrochimica Acta*, vol. 203, 2016, p. 337–349.

[ANS 10] Anselme K., Ploux L., Ponche A.
Cell/Material Interfaces: Influence of Surface Chemistry and Surface Topography on Cell Adhesion. *Journal of Adhesion Science and Technology*, vol. 24, n° 5, 2010, p. 831–852.

[ANS 18] Anselme K., Wakhloo N. T., Rougerie P., Pieuchot L.
Role of the Nucleus as a Sensor of Cell Environment Topography. *Advanced Healthcare Materials*, vol. 7, n° 8, 2018, Page 1701154.

[ARG 79] Argon A. S.
Plastic Deformation in Metallic Glasses. *Acta Metallurgica*, vol. 27, n° 1, 1979, p. 47–58.

[ASH 93] Ashby M. F., Cebon D.
Materials Selection in Mechanical Design. *Le Journal de Physique IV*, vol. 03, n° C7, 1993, p. C7-1-C7-9.

[ASH 06] Ashby M., Greer A.
Metallic Glasses as Structural Materials. *Scripta Materialia*, vol. 54, n° 3, 2006, p. 321–326.

[BAD 07] Badrinarayanan P., Zheng W., Li Q., Simon S. L.
The Glass Transition Temperature versus the Fictive Temperature. *Journal of Non-Crystalline Solids*, vol. 353, n° 26, 2007, p. 2603–2612.

[Bag 97] Bagedahl-Strindlund M., Hie M., Furhotf A.-K., Tomson Y., Larsson K., Sandborgh-Englund G., Torstenson B., Wretlind K.
A Multidisciplinary Clinical Study of Patients Suffering from Illness Associated with Mercury Release from Dental Restorations: Psychiatric Aspects. *Acta Psychiatrica Scandinavica*, vol. 96, n° 6, 1997, p. 475–482, Wiley Online Library.

[BAG 08] Baggi L., Cappelloni I., Di Girolamo M., Maceri F., Vairo G.
The Influence of Implant Diameter and Length on Stress Distribution of Osseointegrated Implants Related to Crestal Bone Geometry: A Three-Dimensional Finite Element Analysis. *The Journal of Prosthetic Dentistry*, vol. 100, n° 6, 2008, p. 422–431.

[BAP 18] Baptista A., Silva F. J. G., Porteiro J., Míguez J. L., Pinto G., Fernandes L.
On the Physical Vapour Deposition (PVD): Evolution of Magnetron Sputtering Processes for Industrial Applications. *Procedia Manufacturing*, vol. 17, 2018, p. 746–757.

[BAR 91] Barbery J.
Traitements thermiques du cuivre et de ses alliages. *Techniques de l'ingenieur*, vol. M1295 V2, 1991, Page 23.

[BAZ 20] Bazli L., Chahardehi A. M., Arsad H., Malekpouri B., Jazi M. A., Azizabadi N. et al.
Factors Influencing the Failure of Dental Implants: A Systematic Review. *Journal of Composites and Compounds*, vol. 2, n° 2, 2020, p. 18–25.

[BEA 17] Beausir B., Fundenberger J.-J.
. "Analysis Tools for Electron and X-ray Diffraction, ATEX - Software'', 2017.

[BEH 20] Behnia H., Sharifzadeh N., Behnia P.
Aesthetic Dental Implant Complications. Bagheri S. C., Khan H. A., Stevens M. R., Eds., *Complex Dental Implant Complications*, p. 73–102 Springer International Publishing, Cham, 2020.

[BER 17] Bera S., Sarac B., Balakin S., Ramasamy P., Stoica M., Calin M., Eckert J.
Micro-Patterning by Thermoplastic Forming of Ni-free Ti-based Bulk Metallic Glasses. *Materials and Design*, vol. 120, 2017, p. 204–211, Elsevier Ltd.

[BER 20] Bernard C., Keryvin V.
Crystalline Defects in Bulk Metallic Glasses: Consequences on Fracture Toughness Determination and Ductility. *Journal of Physics: Condensed Matter*, vol. 32, n° 48, 2020, Page 483001.

[BHA 98] Bhatnagar A. K., Seshu B., Rathnayaka K. D. D., Naugle D. G.
Changes in Resistivity Behavior of Metallic Glass Fe70Ni12B16Si2 Due to Molybdenum

Substitution for Nickel. *Journal of Applied Physics*, vol. 76, n° 10, 1998, Page 6107, American Institute of PhysicsAIP.

[BIG 11] Bigerelle M., Giljean S., Anselme K.
Existence of a Typical Threshold in the Response of Human Mesenchymal Stem Cells to a Peak and Valley Topography. *Acta Biomaterialia*, vol. 7, n° 9, 2011, p. 3302–3311, Acta Materialia Inc.

[BOC 19] Bochtler B.
Thermophysical and Structural Investigations of a CuTi- and a Zr-based Bulk Metallic Glass, the Influence of Minor Additions, and the Relation to Thermoplastic Forming. 2019.

[BRA 86] Branemark P.-I., Zarb G. A., Albrektsson T., Rosen H. M.
Tissue-Integrated Prostheses. Osseointegration in Clinical Dentistry. *Plastic and Reconstructive Surgery*, vol. 77, n° 3, 1986, p. 496–497.

[BRU 88] Brunski J. B.
Biomaterials and Biomechanics in Dental Implant Design. , 1988, Page 30.

[BUS 07] Busch R., Schroers J., Wang W. H.
Thermodynamics and Kinetics of Bulk Metallic Glass. *MRS Bulletin*, vol. 32, n° 8, 2007, p. 620–623.

[CAL 03] Calin M., Eckert J., Schultz L.
Improved Mechanical Behavior of Cu–Ti-based Bulk Metallic Glass by in Situ Formation of Nanoscale Precipitates. *Scripta Materialia*, vol. 48, n° 6, 2003, p. 653–658.

[CAL 13] Calin M., Gebert A., Ghinea A. C., Gostin P. F., Abdi S., Mickel C., Eckert J.
Designing Biocompatible Ti-based Metallic Glasses for Implant Applications. *Materials Science and Engineering C*, vol. 33, n° 2, 2013, p. 875–883, Elsevier B.V.

[CHA 10] Chang P.-C., Lang N. P., Giannobile W. V.
Evaluation of Functional Dynamics during Osseointegration and Regeneration Associated with Oral Implants. *Clinical Oral Implants Research*, vol. 21, n° 1, 2010, p. 1–12.

[CHA 17] Chavan N., Onkar
. "Dental Implants and Prosthetics Market Size and Share by 2023 | AMR''. https://www.alliedmarketresearch.com/dental-implants-and-prosthetics-market, 2017.

[CHE 06] Chen Q., Shen J., Zhang D., Fan H., Sun J., McCartney D. G.
A New Criterion for Evaluating the Glass-Forming Ability of Bulk Metallic Glasses. *Materials Science and Engineering: A*, vol. 433, n° 1, 2006, p. 155–160.

[CHE 07] Chevalier J., Gremillard L., Deville S.
Low-Temperature Degradation of Zirconia and Implications for Biomedical Implants. *Annual Review of Materials Research*, vol. 37, n° 1, 2007, p. 1–32.

[CHE 11] Chen M.
A Brief Overview of Bulk Metallic Glasses. *NPG Asia Materials*, vol. 3, n° 9, 2011, p. 82–90, Nature Publishing Group.

[CHE 21] Chen Y., Tang C., Jiang J.-Z.
Bulk Metallic Glass Composites Containing B2 Phase. *Progress in Materials Science*, , 2021, Page 100799.

[COR 04] Cortizo M. C., de Mele M. F. L.
Cytotoxicity of Copper Ions Released from Metal: Variation with the Exposure Period and Concentration Gradients. *Biological Trace Element Research*, vol. 102, n° 1-3, 2004, p. 129–142.

[CRU 11] Cruz H. V., Souza J. C. M., Henriques M., Rocha L. A.
Tribocorrosion and Bio- Tribocorrosion in the Oral Environment: The Case of Dental Implants. , 2011, Page 34.

[CZE 16] Czeppe T., Sypien A., Wierzbicka-Miernik A.
Modification of the Ti40Cu36Zr10Pd14 BMG Crystallization Mechanism with Heating Rates 10-140 K/Min. *Journal of Materials Engineering and Performance*, vol. 25, n° 12, 2016, p. 5289–5301.

[DAM 96] Damani R., Gstrein R., Danzer R.
Critical Notch-Root Radius Effect in SENB-S Fracture Toughness Testing. *Journal of the European Ceramic Society*, vol. 16, n° 7, 1996, p. 695–702.

[DAV 75] Davies H. A., Lewis B. G.
A Generalised Kinetic Approach to Metallic Glass Formation. *Scripta Metallurgica*, vol. 9, n° 10, 1975, p. 1107–1112.

[DAV 00] Davis J. R.
Corrosion: Understanding the Basics. ASM International, 2000.

[DEB 12] Debnath M. R., Kim D.-H., Fleury E.
Dependency of the Corrosion Properties of In-Situ Ti-based BMG Matrix Composites with the Volume Fraction of Crystalline Phase. *Intermetallics*, vol. 22, 2012, p. 255–259.

[DEB 14] Debnath M. R., Chang H.-J., Fleury E.
Effect of Group 5 Elements on the Formation and Corrosion Behavior of Ti-based BMG Matrix Composites Reinforced by Icosahedral Quasicrystalline Phase. *Journal of Alloys and Compounds*, vol. 612, 2014, p. 134–142.

[DEM 10] Demetriou M. D., Wiest A., Hofmann D. C., Johnson W. L., Han B., Wolfson N., Wang G., Liaw P. K.
Amorphous Metals for Hard-Tissue Prosthesis. *JOM*, vol. 62, n° 2, 2010, p. 83–91.

[DEM 11] Demetriou M. D., Launey M. E., Garrett G., Schramm J. P., Hofmann D. C., Johnson W. L., Ritchie R. O.
A Damage-Tolerant Glass. *Nature Materials*, vol. 10, n° 2, 2011, p. 123–128.

[DON 12] Dong F., Su Y., Luo L., Wang L., Wang S., Guo J., Fu H.
Enhanced Plasticity in Zr-based Bulk Metallic Glasses by Hydrogen. *International Journal of Hydrogen Energy*, vol. 37, n° 19, 2012, p. 14697–14701.

[DUA 07] Duan G., Wiest A., Lind M. L., Li J., Rhim W. K., Johnson W. L.
Bulk Metallic Glass with Benchmark Thermoplastic Processability. *Advanced Materials*, vol. 19, n° 23, 2007, p. 4272–4275.

[DUP 20] Du Plessis A., Macdonald E.
Hot Isostatic Pressing in Metal Additive Manufacturing: X-ray Tomography Reveals Details of Pore Closure. *Additive Manufacturing*, vol. 34, 2020, Page 101191.

[DUR 15] Duraccio D., Mussano F., Faga M. G.
Biomaterials for Dental Implants: Current and Future Trends. *Journal of Materials Science*, vol. 50, n° 14, 2015, p. 4779–4812.

[ECK 07] Eckert J., Das J., Pauly S., Duhamel C.
Mechanical Properties of Bulk Metallic Glasses and Composites. *Journal of Materials Research*, vol. 22, n° 2, 2007, p. 285–301.

[ELA 18] Elani H., Starr J., Da Silva J., Gallucci G.
Trends in Dental Implant Use in the U.S., 1999–2016, and Projections to 2026. *Journal of Dental Research*, vol. 97, n° 13, 2018, p. 1424–1430.

[ERE 66] Eremenko V. N., Buyanov Y. I., Prima S. B.
Phase Diagram of the System Titanium-Copper. *Soviet Powder Metallurgy and Metal Ceramics*, vol. 5, n° 6, 1966, p. 494–502.

[ESC 19] Escher B.
Stability of the B2 CuZr Phase in Cu-Zr-Al-Sc Bulk Metallic Glass Matrix Composites. *Journal of Alloys and Compounds*, , 2019, Page 9.

[ETI 17] Etiemble A., Loughian C. D., Apreutesei M., Langlois C., Cardinal S., Pelletier J. M., Pierson J. F., Steyer P.
Innovative Zr-Cu-Ag Thin Film Metallic Glass Deposed by Magnetron PVD Sputtering for Antibacterial Applications. *Journal of Alloys and Compounds*, vol. 707, 2017, p. 155–161, Elsevier B.V.

[FEL 15] Feller L., Jadwat Y., Khammissa R. A. G., Meyerov R., Schechter I., Lemmer J.
Cellular Responses Evoked by Different Surface Characteristics of Intraosseous Titanium Implants. *BioMed Research International*, vol. 2015, 2015, p. 1–8, Hindawi Publishing Corporation.

[Flo 15] Florencio-Silva R., Sasso G. R. d. S., Sasso-Cerri E., Simões M. J., Cerri P. S.
Biology of Bone Tissue: Structure, Function, and Factors That Influence Bone Cells. *BioMed research international*, vol. 2015, 2015, Hindawi.

[FOR 11] Fornell J., Van Steenberge N., Varea A., Rossinyol E., Pellicer E., Suriñach S., Baró M., Sort J.
Enhanced Mechanical Properties and in Vitro Corrosion Behavior of Amorphous and Devitrified Ti40Zr10Cu38Pd12 Metallic Glass. *Journal of the Mechanical Behavior of Biomedical Materials*, vol. 4, n° 8, 2011, p. 1709–1717.

[FOR 13] Fornell J., Pellicer E., Van Steenberge N., González S., Gebert A., Suriñach S., Baró M. D., Sort J.
Improved Plasticity and Corrosion Behavior in Ti–Zr–Cu–Pd Metallic Glass with Minor Additions of Nb: An Alloy Composition Intended for Biomedical Applications. *Materials Science and Engineering: A*, vol. 559, 2013, p. 159–164.

[GAO 11] Gao H.-L., Shen Y., Xu J.
Weibull Analysis of Fracture Strength for Zr55Ti2Co28Al 15 Bulk Metallic Glass: Tension–Compression Asymmetry and Porosity Effect. *Journal of Materials Research*, vol. 26, n° 16, 2011, p. 2087–2097.

[GAR 75] Garvie R. C., Hannink R. H., Pascoe R. T.
Ceramic Steel? *Nature*, vol. 258, n° 5537, 1975, p. 703–704, Nature Publishing Group.

[GAR 13] Gargarella P., Pauly S., Song K. K., Hu J., Barekar N. S., Samadi Khoshkhoo M., Teresiak A., Wendrock H., Kuhn U., Ruffing C., Kerscher E., Eckert J.
Ti–Cu–Ni Shape Memory Bulk Metallic Glass Composites. *Acta Materialia*, vol. 61, n° 1, 2013, p. 151–162.

[GAU 22] Gautier L., Liens A., Ter-Ovanessian B., Marcelin S., Douillard T., Richard H., Courtois N., Chevalier J., Fabrègue D.
Impact of Spherulite-Type Crystalline Defects on the Mechanical and Electrochemical Properties of TiCuZrPd Metallic Glasses. *Materialia*, , 2022, Page 101353.

[GEP 13] Gepreel M. A.-H., Niinomi M.
Biocompatibility of Ti-alloys for Long-Term Implantation. *Journal of the Mechanical Behavior of Biomedical Materials*, vol. 20, 2013, p. 407–415.

[GER 10] Gerritsen A. E., Allen P. F., Witter D. J., Bronkhorst E. M., Creugers N. H.
Tooth Loss and Oral Health-Related Quality of Life: A Systematic Review and Meta-Analysis. *Health and Quality of Life Outcomes*, vol. 8, n° 1, 2010, Page 126.

[GON 16] Gong P., Deng L., Jin J., Wang S., Wang X., Yao K.
Review on the Research and Development of Ti-Based Bulk Metallic Glasses. *Metals*, vol. 6, n° 11, 2016, Page 264, MDPI AG.

[GOS 18] Gostin P. F., Addison O., Morrell A. P., Zhang Y., Cook A. J. M. C., Liens A., Stoica M., Ignatyev K., Street S. R., Wu J., Chiu Y.-L., Davenport A. J.

In Situ Synchrotron X-Ray Diffraction Characterization of Corrosion Products of a Ti-Based Metallic Glass for Implant Applications. *Advanced Healthcare Materials*, vol. 7, n° 21, 2018, Page 1800338.

[GRA 15] Granata D., Fischer E., Löffler J. F.
Effectiveness of Hydrogen Microalloying in Bulk Metallic Glass Design. *Acta Materialia*, vol. 99, 2015, p. 415–421.

[GUE 20] Guerin E., Daudin R., Lenain A., Mendil N., Gravier S., Ter-Ovanessian B., Fabregue D., Blandin J.-J.
Effect of the Alloy/Mould Contact on Surface Crystallisation of a Biocompatible Zr-CoAl Bulk Metallic Glass. *Journal of Physics: Condensed Matter*, vol. 32, n° 21, 2020, Page 214008.

[GUG 19] Guglielmotti M. B., Olmedo D. G., Cabrini R. L.
Research on Implants and Osseointegration. *Periodontology 2000*, vol. 79, n° 1, 2019, p. 178–189.

[HAA 18] Haag F., Geisel S., Kurtuldu G., Löffler J. F.
Bulk Metallic Glass Casting Investigated Using High-Speed Infrared Monitoring and Complementary Fast Scanning Calorimetry. *Acta Materialia*, vol. 151, 2018, p. 416–423.

[HAN 03] Hanawa T.
Reconstruction and Regeneration of Surface Oxide Film on Metallic Materials in Biological Environments. *Corrosion Reviews*, vol. 21, n° 2-3, 2003, p. 161–182.

[HAR 94] Hari Kumar K. C., Wollants P., Delacy L.
Thermodynamic Assessment of the Ti-Zr System and Calculation of the Nb-Ti-Zr Phase Diagram. *Journal of Alloys and Compounds*, vol. 206, n° 1, 1994, p. 121–127.

[HAR 09] Harimkar S. P., Paital S. R., Singh A., Aalund R., Dahotre N. B.
Microstructure and Properties of Spark Plasma Sintered Fe–Cr–Mo–Y–B–C Bulk Metallic Glass. *Journal of Non-Crystalline Solids*, vol. 355, n° 43, 2009, p. 2179–2182.

[HAS 14] Hasan I., Bourauel C., Mundt T., Stark H., Heinemann F.
Biomechanics and Load Resistance of Small-Diameter and Mini Dental Implants: A Review of Literature. *Biomedizinische Technik/Biomedical Engineering*, vol. 59, n° 1, 2014, p. 1–5.

[HIN 19] Hin S., Bernard C., Doquet V., Yokoyama Y., Magueresse A., Keryvin V.
Influence of As-Cast Spherulites on the Fracture Toughness of a Zr 55 Cu 30 Al 10 Ni 5 Bulk Metallic Glass. *Materials Science and Engineering: A*, vol. 740–741, 2019, p. 137–147.

[HOF 08] Hofmann D. C., Suh J.-Y., Wiest A., Duan G., Lind M.-L., Demetriou M. D., Johnson W. L.

Designing Metallic Glass Matrix Composites with High Toughness and Tensile Ductility. *Nature*, vol. 451, n° 7182, 2008, p. 1085–1089.

[HOF 13] Hofmann D. C.
Bulk Metallic Glasses and Their Composites: A Brief History of Diverging Fields. *Journal of Materials*, vol. 2013, 2013, p. 1–8.

[HOM 15] Hommada A.
La perte des dents, une menace pour l'identité? 2015.

[HON 18] Hong S. H.
Mechanical, Deformation and Fracture Behaviors of Bulk Metallic Glass Composites Reinforced by Spherical B2 Particles. *Progress in Natural Science*, , 2018, Page 7.

[HOT 16] Hotchkiss K. M., Reddy G. B., Hyzy S. L., Schwartz Z., Boyan B. D., Olivares-Navarrete R.
Titanium Surface Characteristics, Including Topography and Wettability, Alter Macrophage Activation. *Acta Biomaterialia*, vol. 31, 2016, p. 425–434, Acta Materialia Inc.

[HU 09] Hu Y., Li J., Lin T., Zhou Y.
Plasticity Improvement of Zr55Al10Ni5Cu30 Bulk Metallic Glass by Remelting Master Alloy Ingots. *Journal of Materials Research*, vol. 24, n° 12, 2009, p. 3590–3595.

[HUA 12] Huang L., Yokoyama Y., Wu W., Liaw P. K., Pang S., Inoue A., Zhang T., He W.
Ni-Free Zr–Cu–Al–Nb–Pd Bulk Metallic Glasses with Different Zr/Cu Ratios for Biomedical Applications. *Journal of Biomedical Materials Research Part B: Applied Biomaterials*, vol. 100B, n° 6, 2012, p. 1472–1482.

[HUA 20] Hua N., Hong X., Lin L., Liao Z., Zhang L., Ye X., Wang Q.
Mechanical, Corrosion, and Wear Performances of a Biocompatible Ti-based Glassy Alloy. *Journal of Non-Crystalline Solids*, vol. 543, 2020, Page 120116.

[HUI 93] Huiskes R.
Stress Shielding and Bone Resorption in THA: Clinical versus Computer-Simulation Studies. *Acta Orthopaedica Belgica*, vol. 59 Suppl 1, 1993, p. 118–129.

[IDA 18] Ida H., Seiryu M., Takeshita N., Iwasaki M., Yokoyama Y., Tsutsumi Y., Ikeda E., Sasaki S., Miyashita S., Sasaki S., Fukunaga T., Deguchi T., Takano-Yamamoto T.
Biosafety, Stability, and Osteogenic Activity of Novel Implants Made of Zr70Ni16Cu6Al8 Bulk Metallic Glass for Biomedical Application. *Acta Biomaterialia*, vol. 74, 2018, p. 505–517.

[INO 93] Inoue A., Zhang T., Masumoto T.
Glass-Forming Ability of Alloys. *Journal of Non-Crystalline Solids*, vol. 156–158, 1993, p. 473–480.

[INO 95] Inoue A.
High Strength Bulk Amorphous Alloys with Low Critical Cooling Rates (*Overview*). *Materials Transactions, JIM*, vol. 36, n° 7, 1995, p. 866–875.

[INO 00] Inoue A.
Stabilization of Metallic Supercooled Liquid and Bulk Amorphous Alloys. *Acta Materialia*, vol. 48, n° 1, 2000, p. 279–306.

[INO 01] Inoue A.
Bulk Amorphous and Nanocrystalline Alloys with High Functional Properties. *Materials Science and Engineering: A*, vol. 304–306, 2001, p. 1–10.

[INO 08] Inoue A., Wang X. M., Zhang W.
Development and Applications of Late Transition Metal Bulk Metallic Glasses. , 2008, Page 10.

[ION 20] Ionita D., Pirvu C., Stoian A. B., Demetrescu I.
The Trends of TiZr Alloy Research as a Viable Alternative for Ti and Ti16 Zr Roxolid Dental Implants. *Coatings*, vol. 10, n° 4, 2020, Page 422, Multidisciplinary Digital Publishing Institute.

[JAB 14] Jabbari Y. S. A.
Physico-Mechanical Properties and Prosthodontic Applications of Co-Cr Dental Alloys: A Review of the Literature. *The Journal of Advanced Prosthodontics*, vol. 6, n° 2, 2014, p. 138–145, The Korean Academy of Prosthodontics.

[JAR 08] Jarmar T., Palmquist A., Bråmark R., Hermansson L., Engqvist H., Thomsen P.
Characterization of the Surface Properties of Commercially Available Dental Implants Using Scanning Electron Microscopy, Focused Ion Beam, and High-Resolution Transmission Electron Microscopy. *Clinical Implant Dentistry and Related Research*, vol. 10, n° 1, 2008, p. 11–22.

[JIA 18a] Jia H., Xie X., Zhao L., Wang J., Gao Y., Dahmen K. A., Li W., Liaw P. K., Ma C.
Effects of Similar-Element-Substitution on the Glass-Forming Ability and Mechanical Behaviors of Ti-Cu-Zr-Pd Bulk Metallic Glasses. *Journal of Materials Research and Technology*, vol. 7, n° 3, 2018, p. 261–269.

[JIA 18b] Jiang S.-S.
A CuZr-based Bulk Metallic Glass Composite with Excellent Mechanical Properties by Optimizing Microstructure. , 2018, Page 5.

[JIN 09] Jindal V., Srivastava V., Uhlenwinkel V.
On the Role of Liquid Phase Stability and GFA Parameters. *Journal of Non-Crystalline Solids*, vol. 355, n° 28-30, 2009, p. 1552–1555.

[JON 12] Jones D. R., Ashby M. F.
Engineering Materials 2: An Introduction to Microstructures and Processing. Butterworth-Heinemann, 2012.

[KAN 20] Kanto M.
Radiological Evaluation of the Relationship Between Cortical Hypertrophy and Stress Shielding After Total Hip Arthroplasty Using a Cementless Stem. *Arthroplasty Today*, , 2020, Page 7.

[KAR 51] Karlsson N.
An X-Ray Study of the Phases in the Copper-Titanium System. *J Inst Met*, vol. 79, 1951, p. 391–405.

[KAU 19] Kaur M., Singh K.
Review on Titanium and Titanium Based Alloys as Biomaterials for Orthopaedic Applications. *Materials Science and Engineering: C*, vol. 102, 2019, p. 844–862.

[KEL 03] Keller J. C., Schneider G. B., Stanford C. M., Kellogg B.
Effects of Implant Microtopography on Osteoblast Cell Attachment. *Implant Dentistry*, vol. 12, n° 2, 2003, p. 175–181.

[KER 06] Keryvin V., Bernard C., Sanglebœuf J. C., Yokoyama Y., Rouxel T.
Toughness of Zr55Cu30Al10Ni5 Bulk Metallic Glass for Two Oxygen Levels. *Journal of Non-Crystalline Solids*, vol. 352, n° 26, 2006, p. 2863–2868.

[KET 18] Ketkaew J., Chen W., Wang H., Datye A., Fan M., Pereira G., Schwarz U. D., Liu Z., Yamada R., Dmowski W., Shattuck M. D., O'Hern C. S., Egami T., Bouchbinder E., Schroers J.
Mechanical Glass Transition Revealed by the Fracture Toughness of Metallic Glasses. *Nature Communications*, vol. 9, n° 1, 2018, Page 3271, Nature Publishing Group.

[KIM 18] Kim B. J., Yun Y. S., Kim W. T., Kim D. H.
Microstructure Evolution During Solidification of Cu–Zr–Ti Alloy Forming B2 Phase Particles Embedded in a Glassy Matrix. *Metals and Materials International*, vol. 24, n° 5, 2018, p. 926–933.

[KOP 15] Kopf B. S., Schipanski A., Rottmar M., Berner S., Maniura-Weber K.
Enhanced Differentiation of Human Osteoblasts on Ti Surfaces Pre-Treated with Human Whole Blood. *Acta Biomaterialia*, vol. 19, 2015, p. 180–190, Acta Materialia Inc.

[KOZ 15] Kozieł T.
Estimation Of Cooling Rates In Suction Casting And Copper-Mould Casting Processes. *Archives of Metallurgy and Materials*, vol. 60, n° 2, 2015, p. 767–771.

[KRU 11] Kruzic J. J.
Understanding the Problem of Fatigue in Bulk Metallic Glasses. *Metallurgical and Materials Transactions A*, vol. 42, n° 6, 2011, p. 1516–1523.

[KRU 16] Kruzic B. J. J.
Bulk Metallic Glasses as Structural Materials : A Review. , n° 8, 2016.

[KUM 13] Kumar G., Neibecker P., Liu Y. H., Schroers J.
Critical Fictive Temperature for Plasticity in Metallic Glasses. *Nature Communications*, vol. 4, n° 1, 2013, Page 1536, Nature Publishing Group.

[LAU 08] Launey M. E., Busch R., Kruzic J. J.
Effects of Free Volume Changes and Residual Stresses on the Fatigue and Fracture Behavior of a Zr–Ti–Ni–Cu–Be Bulk Metallic Glass. *Acta Materialia*, vol. 56, n° 3, 2008, p. 500–510.

[LEG 07] Le Guehennec L., Soueidan A., Layrolle P., Amouriq Y.
Surface Treatments of Titanium Dental Implants for Rapid Osseointegration. *Dental Materials*, vol. 23, n° 7, 2007, p. 844–854.

[LEV 51] Leventhal G. S.
Titanium, a Metal for Surgery. *JBJS*, vol. 33, n° 2, 1951, p. 473–474.

[LEW 05] Lewandowski J. J., Wang W. H., Greer A. L.
Intrinsic Plasticity or Brittleness of Metallic Glasses. *Philosophical Magazine Letters*, vol. 85, n° 2, 2005, p. 77–87, Taylor & Francis.

[Ley 20] Leyva-Porras C., Cruz-Alcantar P., Espinosa-Solís V., Martínez-Guerra E., Piñón-Balderrama C. I., Compean Martínez I., Saavedra-Leos M. Z.
Application of Differential Scanning Calorimetry (DSC) and Modulated Differential Scanning Calorimetry (MDSC) in Food and Drug Industries. *Polymers*, vol. 12, n° 1, 2020, Page 5, Multidisciplinary Digital Publishing Institute.

[LI 19] Li K., Xia C., Qiao Y., Liu X.
Dose-Response Relationships between Copper and Its Biocompatibility/Antibacterial Activities. *Journal of Trace Elements in Medicine and Biology*, vol. 55, 2019, p. 127–135, Urban & Fischer.

[LIE 18] Liens A., Etiemble A., Rivory P., Balvay S., Pelletier J. M., Cardinal S., Fabrègue D., Kato H., Steyer P., Munhoz T., Adrien J., Courtois N., Hartmann D. J., Chevalier J.
On the Potential of Bulk Metallic Glasses for Dental Implantology: Case Study on Ti 40 Zr 10 Cu 36 Pd 14. *Materials*, vol. 11, n° 2, 2018.

[LIE 19] Liens A.
On the Potential of Ti-based Bulk Metallic Glasses and Ce-TZP Zirconia Composites for the Development of Innovative Dental Implants. 2019.

[LIE 20] Liens A., Ter-Ovanessian B., Courtois N., Fabregue D., Wada T., Kato H., Chevalier J.
Effect of Alloying Elements on the Microstructure and Corrosion Behavior of TiZr-based Bulk Metallic Glasses. *Corrosion Science*, vol. 177, 2020, Page 108854.

[LIM 10] Lim K., Na J., Park J., Kim W., Kim D.
Enhancement of Plasticity in Ti-based Metallic Glass Matrix Composites by Controlling Characteristic and Volume Fraction of Primary Phase. *Journal of Materials Research*, vol. 25, n° 11, 2010, p. 2183–2191.

[LIU 02] Liu C. T., Chisholm M. F., Miller M. K.
Oxygen Impurity and Microalloying Effect in a Zr-based Bulk Metallic Glass Alloy. *Intermetallics*, vol. 10, n° 11, 2002, p. 1105–1112.

[LIU 12a] Liu Z., Li R., Liu G., Song K., Pauly S., Zhang T., Eckert J.
Pronounced Ductility in CuZrAl Ternary Bulk Metallic Glass Composites with Optimized Microstructure through Melt Adjustment. *AIP Advances*, vol. 2, 2012.

[LIU 12b] Liu Z., Li R., Liu G., Su W., Wang H., Li Y., Shi M., Luo X., Wu G., Zhang T.
Microstructural Tailoring and Improvement of Mechanical Properties in CuZr-based Bulk Metallic Glass Composites. *Acta Materialia*, vol. 60, n° 6-7, 2012, p. 3128–3139.

[LIU 18] Liu S.-n., Dong W.-x., Lu C.-y., Lu Z.-w., Ge J.-c., Yuan C.-c., Sun B.-a., Feng T., Wang X.-l., Lan S.
Effects of Casting Current on Structure and Properties of a Nanostructured Zr–Cu–Fe–Al Bulk Metallic Glass. *Journal of Iron and Steel Research International*, vol. 25, n° 6, 2018, p. 630–636.

[LIU 20] Liu Y., Wang H.-J., Pang S.-J., Zhang T.
Ti–Zr–Cu–Fe–Sn–Si–Ag–Ta Bulk Metallic Glasses with Good Corrosion Resistance as Potential Biomaterials. *Rare Metals*, vol. 39, n° 6, 2020, p. 688–694.

[LOK 16] Loke C., Lee J., Sander S., Mei L., Farella M.
Factors Affecting Intra-Oral pH – a Review. *Journal of Oral Rehabilitation*, vol. 43, n° 10, 2016, p. 778–785.

[LOU 17] Lou B.-S., Yang Y.-C., Lee J.-W., Chen L.-T.
Biocompatibility and Mechanical Property Evaluation of Zr-Ti-Fe Based Ternary Thin Film Metallic Glasses. *Surface and Coatings Technology*, vol. 320, 2017, p. 512–519.

[LU 02] Lu Z. P., Liu C. T.
A New Glass-Forming Ability Criterion for Bulk Metallic Glasses. *Acta Materialia*, vol. 50, n° 13, 2002, p. 3501–3512.

[MAD 12] Madge S. V., Louzguine-Luzgin D. V., Lewandowski J. J., Greer A. L.
Toughness, Extrinsic Effects and Poisson's Ratio of Bulk Metallic Glasses. *Acta Materialia*, vol. 60, n° 12, 2012, p. 4800–4809.

[MAH 18] Mahbooba Z., Thorsson L., Unosson M., Skoglund P., West H., Horn T., Rock C., Vogli E., Harrysson O.
Additive Manufacturing of an Iron-Based Bulk Metallic Glass Larger than the Critical Casting Thickness. *Applied Materials Today*, vol. 11, 2018, p. 264–269.

[MAN 09] Manda M. G., Psyllaki P. P., Tsipas D. N., Koidis P. T.
Observations on an In-Vivo Failure of a Titanium Dental Implant/Abutment Screw System: A Case Report. *Journal of Biomedical Materials Research Part B: Applied Biomaterials*, vol. 89B, n° 1, 2009, p. 264–273.

[MAR 87] Marshall A. F., Lee Y. S., Stevenson D. A.
Crystallization Behavior of Amorphous Cu48Ti52: Formation of an Intermediate Long-Period Superlattice Phase. *Acta Metallurgica*, vol. 35, n° 1, 1987, p. 61–68.

[MAR 14] Marchetti E., Ratta S., Mummolo S., Tecco S., Pecci R., Bedini R., Marzo G.
Evaluation of an Endosseous Oral Implant System According to UNI EN ISO 14801 Fatigue Test Protocol. *Implant Dentistry*, vol. Publish Ahead of Print, 2014.

[MAR 16] Marchetti E., Ratta S., Mummolo S., Tecco S., Pecci R., Bedini R., Marzo G.
Mechanical Reliability Evaluation of an Oral Implant-Abutment System According to UNI EN ISO 14801 Fatigue Test Protocol. *Implant Dentistry*, vol. 25, n° 5, 2016, p. 613–618.

[MAR 17] Martin J. R., Watts C. D., Levy D. L., Kim R. H.
Medial Tibial Stress Shielding: A Limitation of Cobalt Chromium Tibial Baseplates. *The Journal of Arthroplasty*, vol. 32, n° 2, 2017, p. 558–562.

[MED 16] Medvedev A. E., Molotnikov A., Lapovok R., Zeller R., Berner S., Habersetzer P., Dalla Torre F.
Microstructure and Mechanical Properties of Ti–15Zr Alloy Used as Dental Implant Material. *Journal of the Mechanical Behavior of Biomedical Materials*, vol. 62, 2016, p. 384–398.

[MES 21] Messous R., Henriques B., Bousbaa H., Silva F. S., Teughels W., Souza J. C. M.
Cytotoxic Effects of Submicron- and Nano-Scale Titanium Debris Released from Dental Implants: An Integrative Review. *Clinical Oral Investigations*, vol. 25, n° 4, 2021, p. 1627–1640.

[MIS 14] Mishra S. K., Chowdhary R.
Heat Generated by Dental Implant Drills During Osteotomy—A Review. *The Journal of the Indian Prosthodontic Society*, vol. 14, n° 2, 2014, p. 131–143.

[NAR 15] Narayan R., Tandaiya P., Garrett G., Demetriou M., Ramamurty U.
On the Variability in Fracture Toughness of 'Ductile' Bulk Metallic Glasses. *Scripta Materialia*, vol. 102, 2015, p. 75–78.

[NAR 18] Narayan R. L., Raut D., Ramamurty U.
A Quantitative Connection between Shear Band Mediated Plasticity and Fracture Initiation Toughness of Metallic Glasses. *Acta Materialia*, vol. 150, 2018, p. 69–77.

[NII 98] Niinomi M.
Mechanical Properties of Biomedical Titanium Alloys. *Materials Science and Engineering: A*, vol. 243, n° 1, 1998, p. 231–236.

[OAK 07] Oak J.-J., Louzguine-Luzgin D. V., Inoue A.
Fabrication of Ni-free Ti-based Bulk-Metallic Glassy Alloy Having Potential for Application as Biomaterial, and Investigation of Its Mechanical Properties, Corrosion, and Crystallization Behavior. *Journal of Materials Research*, vol. 22, n° 5, 2007, p. 1346–1353.

[OAK 09] Oak J.-J., Louzguine-Luzgin D. V., Inoue A.
Investigation of Glass-Forming Ability, Deformation and Corrosion Behavior of Ni-free Ti-based BMG Alloys Designed for Application as Dental Implants. *Materials Science and Engineering: C*, vol. 29, n° 1, 2009, p. 322–327.

[OKA 13] Okamoto H.
Pd-Ti (Palladium-Titanium). *Journal of Phase Equilibria and Diffusion*, vol. 34, n° 1, 2013, p. 74–75.

[OSM 15] Osman R., Swain M.
A Critical Review of Dental Implant Materials with an Emphasis on Titanium versus Zirconia. *Materials*, vol. 8, n° 3, 2015, p. 932–958.

[PAL 14] Palmero P., Montanaro L., Reveron H., Chevalier J.
Surface Coating of Oxide Powders: A New Synthesis Method to Process Biomedical Grade Nano-Composites. *Materials*, vol. 7, n° 7, 2014, p. 5012–5037.

[PAN 15] Pang S., Liu Y., Li H., Sun L., Li Y., Zhang T.
New Ti-based Ti-Cu-Zr-Fe-Sn-Si-Ag Bulk Metallic Glass for Biomedical Applications. *Journal of Alloys and Compounds*, vol. 625, 2015, p. 323–327, Elsevier B.V.

[PAP 96] Papavasiliou G., Kamposiora P., Bayne S. C., Felton D. A.
Three-Dimensional Finite Element Analysis of Stress-Distribution around Single Tooth Implants as a Function of Bony Support, Prosthesis Type, and Loading during Function. *The Journal of Prosthetic Dentistry*, vol. 76, n° 6, 1996, p. 633–640.

[PAR 02] Pardo A., Otero E., Merino M. C., López M. D., Vázquez M., Agudo P., Escalera M. D., M'Hich A.
Influence of Chromium Additions on Corrosion Resistance of Co $_{75.5}$ Si $_{13.5}$ B $_{9}$ Nb $_{3}$ Cu $_{1}$ Metallic Glass in Marine Environment. *British Corrosion Journal*, vol. 37, n° 1, 2002, p. 69–75.

[PAU 09] Pauly S., Liu G., Wang G., Kühn U., Mattern N., Eckert J.
Microstructural Heterogeneities Governing the Deformation of Cu47.5Zr47.5Al5 Bulk Metallic Glass Composites. *Acta Materialia*, vol. 57, n° 18, 2009, p. 5445–5453.

[POO 09] Poondla N., Srivatsan T. S., Patnaik A., Petraroli M.
A Study of the Microstructure and Hardness of Two Titanium Alloys: Commercially

Pure and Ti–6Al–4V. *Journal of Alloys and Compounds*, vol. 486, n° 1, 2009, p. 162–167.

[QIN 07a] Qin F. X., Wang X. M., Inoue A.
Effect of Annealing on Microstructure and Mechanical Property of a Ti–Zr–Cu–Pd Bulk Metallic Glass. *Intermetallics*, vol. 15, n° 10, 2007, p. 1337–1342.

[QIN 07b] Qin F., Yoshimura M., Wang X., Zhu S., Kawashima A., Asami K., Inoue A.
Corrosion Behavior of a Ti-Based Bulk Metallic Glass and Its Crystalline Alloys. *MATERIALS TRANSACTIONS*, vol. 48, n° 7, 2007, p. 1855–1858.

[QUI 93] Quirynen M., Van Steenberghe D.
Bacterial Colonization of the Internal Part of Two-Stage Implants. *An in Vivo Study* .: Micro Leakage at Implant/Abutment Interface? *Clinical Oral Implants Research*, vol. 4, n° 3, 1993, p. 158–161.

[RAD 92] Radaj D.
Heat Effects of Welding. Springer Berlin Heidelberg, Berlin, Heidelberg, 1992.

[RAM 15] Ramya M., Sarwat S. G., Udhayabanu V., Subramanian S., Raj B., Ravi K. R.
Role of Partially Amorphous Structure and Alloying Elements on the Corrosion Behavior of Mg–Zn–Ca Bulk Metallic Glass for Biomedical Applications. *Materials & Design*, vol. 86, 2015, p. 829–835.

[RAU 14] Rauch E. F., Véron M.
Automated Crystal Orientation and Phase Mapping in TEM. *Materials Characterization*, vol. 98, 2014, p. 1–9.

[ROB 19] Robinson D., Aguilar L., Gatti A., Abduo J., Lee P. V. S., Ackland D.
Load Response of the Natural Tooth and Dental Implant: A Comparative Biomechanics Study. *The Journal of Advanced Prosthodontics*, vol. 11, n° 3, 2019, p. 169–178, The Korean Academy of Prosthodontics.

[RON 18] Rong C., Shen B.
Nanocrystalline and Nanocomposite Permanent Magnets by Melt Spinning Technique. *Chinese Physics B*, vol. 27, n° 11, 2018, Page 117502.

[SAL 58] Saltykov S.
Stereometric Metallography. Metallurgizdat, Moscow, 2nd edition édition, 1958.

[SAR 17] Sarac B., Bera S., Balakin S., Stoica M., Calin M., Eckert J.
Hierarchical Surface Patterning of Ni- and Be-free Ti- and Zr-based Bulk Metallic Glasses by Thermoplastic Net-Shaping. *Materials Science and Engineering C*, vol. 73, 2017, p. 398–405, Elsevier B.V.

[SCH 99] Schwartz Z., Lohmann C. H., Oefinger J., Bonewald L. F., Dean D. D., Boyan B. D.
Implant Surface Characteristics Modulate Differentiation Behavior of Cells in the Osteoblastic Lineage. *Advances in dental research*, vol. 13, 1999, p. 38–48.

[SCH 00] Schwarz M. S.
Mechanical Complications of Dental Implants. *Clinical Oral Implants Research*, vol. 11, n° s1, 2000, p. 156–158.

[SCH 07a] Schroers J., Lohwongwatana B., Johnson W. L., Peker A.
Precious Bulk Metallic Glasses for Jewelry Applications. *Materials Science and Engineering: A*, vol. 449–451, 2007, p. 235–238.

[SCH 07b] Schroers J., Pham Q., Desai A.
Thermoplastic Forming of Bulk Metallic Glass— A Technology for MEMS and Microstructure Fabrication. *Journal of Microelectromechanical Systems*, vol. 16, n° 2, 2007, p. 240–247.

[SCH 07c] Schuh C., Hufnagel T., Ramamurty U.
Mechanical Behavior of Amorphous Alloys. *Acta Materialia*, vol. 55, n° 12, 2007, p. 4067–4109.

[SCH 10] Schroers J.
Processing of Bulk Metallic Glass. *Advanced Materials*, vol. 22, n° 14, 2010, p. 1566–1597.

[SCH 18] Schwarz F., Derks J., Monje A., Wang H.-L.
Peri-Implantitis. *Journal of Clinical Periodontology*, vol. 45, n° S20, 2018, p. S246-S266.

[SCU 07] Scully J. R., Gebert A., Payer J. H.
Corrosion and Related Mechanical Properties of Bulk Metallic Glasses. *Journal of Materials Research*, vol. 22, n° 2, 2007, p. 302–313.

[SME 16] Smeets R., Stadlinger B., Schwarz F., Beck-Broichsitter B., Jung O., Precht C., Kloss F., Gröbe A., Heiland M., Ebker T.
Impact of Dental Implant Surface Modifications on Osseointegration. *BioMed Research International*, vol. 2016, 2016, p. 1–16, Hindawi Publishing Corporation.

[SNE 89] Snedecor G., Crochan W.
Statistical Methods, 8thEdn, vol. 54. Iowa State Univ., press iowa édition, 1989.

[SOI 11] Soinila E., Pihlajamäki T., Bossuyt S., Hänninen H.
A Combined Arc-Melting and Tilt-Casting Furnace for the Manufacture of High-Purity Bulk Metallic Glass Materials. *Review of Scientific Instruments*, vol. 82, n° 7, 2011, Page 073901, American Institute of Physics.

[SON 11] Song R.-b., Xiang J.-y., Hou D.-p.
Characteristics of Mechanical Properties and Microstructure for 316L Austenitic Stain-

less Steel. *Journal of Iron and Steel Research International*, vol. 18, n° 11, 2011, p. 53–59.

[SON 16] Song W., Wu Y., Wang H., Liu X., Chen H., Guo Z., Lu Z.
Microstructural Control via Copious Nucleation Manipulated by In Situ Formed Nucleants: Large-Sized and Ductile Metallic Glass Composites. *Advanced Materials*, vol. 28, n° 37, 2016, p. 8156–8161.

[SPA 77] Spaepen F.
A Microscopic Mechanism for Steady State Inhomogeneous Flow in Metallic Glasses. *Acta Metallurgica*, vol. 25, n° 4, 1977, p. 407–415.

[SU 12] Su Y., Dong F., Luo L., Guo J., Han B., Li Z., Wang B., Fu H.
Bulk Metallic Glass Formation: The Positive Effect of Hydrogen. *Journal of Non-Crystalline Solids*, vol. 358, n° 18, 2012, p. 2606–2611.

[SUH 00] Suh D., Dauskardt R. H.
Hydrogen Effects on the Mechanical and Fracture Behavior of a Zr-Ti-Ni-Cu-Be Bulk Metallic Glass. *Scripta Materialia*, vol. 42, n° 3, 2000, p. 233–240.

[SUN 13] Sun H., Flores K. M.
Spherulitic Crystallization Mechanism of a Zr-based Bulk Metallic Glass during Laser Processing. *Intermetallics*, vol. 43, 2013, p. 53–59.

[SYP 14] Sypien A., Czeppe T., Garzel G., Litynska-Dobrzynska L., Latuch J., Chinh N.
Thermal Stability and Mechanical Properties of the TiCuZrPd Glasses with 10, 14 and 20at.% Pd. *Journal of Alloys and Compounds*, vol. 615, 2014, p. S108-S112.

[SYP 16] Sypien A., Stoica M., Czeppe T.
Properties of the Ti40Zr10Cu36Pd14 BMG Modified by Sn and Nb Additions. *Journal of Materials Engineering and Performance*, vol. 25, n° 3, 2016, p. 800–808.

[SYP 17] Sypien A., Badura K., Fima P., Miernik K.
Effect of Pd, Temperature and Time on Wetting and Interfacial Microstructure of Bulk Metallic Glasses TiCuZrPd on Ti-6Al-4V Substrate. *Journal of Alloys and Compounds*, vol. 695, 2017, p. 962–970.

[TAB 00] Tabor D.
The Hardness of Metals. Oxford university press, 2000.

[TAK 11] Takeuchi S., Edagawa K.
Atomistic Simulation and Modeling of Localized Shear Deformation in Metallic Glasses. *Progress in Materials Science*, vol. 56, n° 6, 2011, p. 785–816.

[TAN 11] Tan J., Zhang Y., a. Sun B., Stoica M., Li C. J., Song K. K., Kühn U., Pan F. S., Eckert J.
Correlation between Internal States and Plasticity in Bulk Metallic Glass. *Applied Physics Letters*, vol. 98, n° 15, 2011, Page 151906, American Institute of Physics.

[TON 15] Tong Y., Iwashita T., Dmowski W., Bei H., Yokoyama Y., Egami T.
Structural Rejuvenation in Bulk Metallic Glasses. *Acta Materialia*, vol. 86, 2015, p. 240–246.

[TSA 12] Tsai P. H., Lin Y. Z., Li J. B., Jian S. R., Jang J. S. C., Li C., Chu J. P., Huang J. C.
Sharpness Improvement of Surgical Blade by Means of ZrCuAlAgSi Metallic Glass and Metallic Glass Thin Film Coating. *Intermetallics*, vol. 31, 2012, p. 127–131.

[TUR 69] Turnbull D.
Under What Conditions Can a Glass Be Formed? *Contemporary Physics*, vol. 10, n° 5, 1969, p. 473–488.

[Tur 14] Turon-Vinas M., Anglada M.
Fracture Toughness of Zirconia from a Shallow Notch Produced by Ultra-Short Pulsed Laser Ablation. *Journal of the European Ceramic Society*, vol. 34, n° 15, 2014, p. 3865–3870.

[Vel 06] Vela-Nebot X., Rodríguez-Ciurana X., Rodado-Alonso C., Segalà-Torres M.
Benefits of an Implant Platform Modification Technique to Reduce Crestal Bone Resorption. *Implant Dentistry*, vol. 15, n° 3, 2006, p. 313–320.

[WAN 89] Wang J., Stevens R.
Zirconia-Toughened Alumina (ZTA) Ceramics. , n° 24(10), 3421–3440., 1989, Page 20.

[WAN 09] Wang J.-X., Fan Y.-B., Gao Y., Hu Q.-H., Wang T.-C.
TiO2 Nanoparticles Translocation and Potential Toxicological Effect in Rats after Intraarticular Injection. *Biomaterials*, vol. 30, n° 27, 2009, p. 4590–4600.

[WAN 13a] Wang H., Park E. S., Oak J. J., Setyawan A. D., Zhu S. L., Wada T., Wang X. M., Takeuchi A., Kato H.
Effect of Cobalt Microalloying on the Glass Forming Ability of Ti–Cu–Pd–Zr Metallic Glass. *Journal of Non-Crystalline Solids*, vol. 379, 2013, p. 155–160.

[WAN 13b] Wang X., Zhenhua Dan Fengxiang Qin Guoqiang Xie S. Z.
Fabrication and Corrosion of Ti-based Metallic Glassses. *Titanium Alloys*, vol. 66, 2013, p. 701–707.

[WAN 14] Wang Y., Liu Y., Liu L.
Fatigue Behaviors of a Ni-free ZrCuFeAlAg Bulk Metallic Glass in Simulated Body Fluid. *Journal of Materials Science & Technology*, vol. 30, n° 6, 2014, p. 622–626.

[WAN 15] Wang Y., Zhang Y., Miron R. J.
Health, Maintenance, and Recovery of Soft Tissues around Implants: Soft Tissues around Implants. *Clinical Implant Dentistry and Related Research*, , 2015.

[WAN 21] Wang C., Hua N., Liao Z., Yang W., Pang S., Liaw P. K., Zhang T.
Ti-Cu-Zr-Fe-Sn-Si-Ag-Pd Bulk Metallic Glasses with Potential for Biomedical Applications. *Metallurgical and Materials Transactions A*, vol. 52, n° 5, 2021, p. 1559–1567.

[WEI 19] Wei Q., Gostin P. F., Addison O., Reed D., Calin M., Bera S., Ramasamy P., Davenport A.
The Influence of Partial Replacement of Cu with Ga on the Corrosion Behavior of Ti40Zr10Cu36Pd 14 Metallic Glasses. *Journal of The Electrochemical Society*, vol. 166, n° 14, 2019, p. C485-C491.

[WIL 17] Williams E., Lavery N.
Laser Processing of Bulk Metallic Glass: A Review. *Journal of Materials Processing Technology*, vol. 247, 2017, p. 73–91.

[WIR 08] Wirth C., Grosgogeat B., Lagneau C., Jaffrezic-Renault N., Ponsonnet L.
Biomaterial Surface Properties Modulate in Vitro Rat Calvaria Osteoblasts Response: Roughness and or Chemistry? *Materials Science and Engineering C*, vol. 28, n° 5-6, 2008, p. 990–1001.

[WU 10] Wu Y., Xiao Y., Chen G., Liu C. T., Lu Z.
Bulk Metallic Glass Composites with Transformation-Mediated Work-Hardening and Ductility. *Advanced Materials*, vol. 22, n° 25, 2010, p. 2770–2773.

[WU 12] Wu G., Li R., Liu Z., Chen B., Li Y., Cai Y., Zhang T.
Induced Multiple Heterogeneities and Related Plastic Improvement by Laser Surface Treatment in CuZr-based Bulk Metallic Glass. *Intermetallics*, vol. 24, 2012, p. 50–55.

[WU 14] Wu B., Hybels C., Liang J., Landerman L., Plassman B.
Social Stratification and Tooth Loss among Middle-Aged and Older Americans from 1988 to 2004. *Community Dentistry and Oral Epidemiology*, vol. 42, n° 6, 2014, p. 495–502.

[XIA 10] Xiao Y., Wu Y., Liu Z., Wu H., Lü Z.
Effects of Cooling Rates on the Mechanical Properties of a Ti-based Bulk Metallic Glass. *Science China Physics, Mechanics and Astronomy*, vol. 53, n° 3, 2010, p. 394–398.

[XIE 08] Xie S., George E.
Hardness and Shear Band Evolution in Bulk Metallic Glasses after Plastic Deformation and Annealing. *Acta Materialia*, vol. 56, n° 18, 2008, p. 5202–5213.

[YAM 14] Yamaura S.-i., Zhu S., Abe K., Xie G.
Ultrasonic Fatigue of Ti40Zr10Cu34Pd14Sn2 Glassy Alloy. *Open Journal of Metal*, vol. 4, n° September, 2014, p. 56–64.

[YAN 11] Yang Y., Zhou R., Wei S., Liu D., Xu H., Li S.
Microstructural Evolution of Slowly Solidified Cu-Ti-Zr-Ni Amorphous Alloy. *Journal of Non-Crystalline Solids*, vol. 357, n° 6, 2011, p. 1516–1521.

[YOK 15] Yokoyama Y.
Development of an Automatic Fabrication System for Cast Glassy Alloys. vol. 46, n° April, 2015, p. 893–905.

[Zha 94] Zhalko-Titarenko A. V., Yevlashina M. L., Antonov V. N., Yavorskii B. Y., Koval Y. N., Firstov G. S.
Electronic and Crystal Structure of the ZrCu Intermetallic Compound Close to the Point of Structural Transformation. *physica status solidi (b)*, vol. 184, n° 1, 1994, p. 121–127.

[ZHA 03a] Zhang Z. F., Eckert J., Schultz L.
Difference in Compressive and Tensile Fracture Mechanisms of Zr59Cu20Al10Ni8Ti3 Bulk Metallic Glass. *Acta Materialia*, vol. 51, n° 4, 2003, p. 1167–1179.

[ZHA 03b] Zhang Z. F., He G., Eckert J., Schultz L.
Fracture Mechanisms in Bulk Metallic Glassy Materials. *Physical Review Letters*, vol. 91, n° 4, 2003, Page 045505.

[ZHO 20] Zhou J., Wu H., Wu Y., Song W., Chen R., Tan C., Xie G., Cao D., Wang H., Liu X., Jiang S., Wang X., Lu Z.
Enhancing Dynamic Mechanical Properties of Bulk Metallic Glass Composites via Deformation-Induced Martensitic Transformation. *Scripta Materialia*, vol. 186, 2020, p. 346–351.

[ZHU 07a] Zhu S. L., Wang X. M., Qin F. X., Inoue A.
A New Ti-based Bulk Glassy Alloy with Potential for Biomedical Application. *Materials Science and Engineering A*, vol. 459, n° 1-2, 2007, p. 233–237.

[ZHU 07b] Zhu S. L., Wang X. M., Qin F. X., Yoshimura M., Inoue A.
New TiZrCuPd Quaternary Bulk Glassy Alloys with Potential of Biomedical Applications. *MATERIALS TRANSACTIONS*, vol. 48, n° 9, 2007, p. 2445–2448.

[ZHU 07c] Zhu S., Wang X., Qin F., Inoue A.
Glass-Forming Ability and Thermal Stability of Ti–Zr–Cu–Pd–Si Bulk Glassy Alloys for Biomedical Applications. *MATERIALS TRANSACTIONS*, vol. 48, n° 2, 2007, p. 163–166.

[ZHU 08a] Zhu S. L., Wang X. M., Inoue A.
Glass-Forming Ability and Mechanical Properties of Ti-based Bulk Glassy Alloys with Large Diameters of up to 1cm. *Intermetallics*, vol. 16, n° 8, 2008, p. 1031–1035.

[ZHU 08b] Zhu S. L., Wang X. M., Qin F. X., Yoshimura M., Inoue A.
Effects of Si Addition on the Glass-Forming Ability, Glass Transition and Crystallization Behaviors of Ti40Zr10Cu36Pd14 Bulk Glassy Alloy. *Intermetallics*, vol. 16, n° 5, 2008, p. 609–614.

[ZHU 12] Zhu S., Xie G., Qin F., Wang X., Inoue A.
Effect of Minor Sn Additions on the Formation and Properties of TiCuZrPd Bulk Glassy Alloy. *MATERIALS TRANSACTIONS*, vol. 53, n° 3, 2012, p. 500–503.

[ZHU 14] Zhu Z.-D., Ma E., Xu J.
Elevating the Fracture Toughness of Cu49Hf42Al9 Bulk Metallic Glass: Effects of Cooling Rate and Frozen-in Excess Volume. *Intermetallics*, vol. 46, 2014, p. 164–172.

[ZYS 99] Zysset P. K., Edward Guo X., Edward Hoffler C., Moore K. E., Goldstein S. A.
Elastic Modulus and Hardness of Cortical and Trabecular Bone Lamellae Measured by Nanoindentation in the Human Femur. *Journal of Biomechanics*, vol. 32, n° 10, 1999, p. 1005–1012.

FOLIO ADMINISTRATIF

THESE DE L'UNIVERSITE DE LYON OPEREE AU SEIN DE L'INSA LYON

NOM : GAUTIER

DATE de SOUTENANCE : le 28 juin 2022

Prénoms : Laurabelle

TITRE : Critical aspects of Titanium-based Bulk Metallic Glasses for biomedical applications: an investigation on casting defects and corrosion sensitivity

NATURE : Doctorat

Numéro d'ordre : 2022LYSEI051

École doctorale : ED 34 Matériaux de Lyon

Spécialité : Matériaux

RÉSUMÉ :

A large majority of dental implants are currently made of Titanium and it alloys. Those dental implants exhibit very good properties and show excellent clinical outputs, although they have now reached a plateau in terms of mechanical and corrosion resistance properties. There is a trend today to decrease the size of implants to preserve the bone stock, but also to get rid of the potential harmful elements and accelerate the bone reconstruction around the implant.

Titanium based amorphous alloys have been describes in literature as very promising biomaterials, with potentially very high mechanical strength and corrosion properties. However, there are still no metallic glass medical devices on the market…

Within this PhD work, the case of $Ti_{40}Cu_{36}Zr_{10}Pd_{14}$ BMG has been investigated as one of the most promising material to manufacture minimally invasive dental implants. Here we focus on two major drawbacks, hardly mentioned in the literature. First, its resistance to corrosion is limited. Second, during its manufacture (by copper mold suction casting) spherical crystalline defects (often referred as spherulites) appear and may severely compromise its tensile strength. The first part of the manuscript focuses on the impact of those spherulites on mechanical properties and corrosion resistance. The second part deals with the identification of the nucleation/growth mechanism of these spherulites. The third part deals with the influence of casting parameters on the appearance of these spherulites and the lack of manufacturing process reliability. Finally, a last more explorative part focuses on the master alloy of $Ti_{40}Cu_{36}Zr_{10}Pd_{14}$ grade and the interest of modifying the atomic distribution to overcome the two major drawbacks mentioned above

MOTS-CLÉS : Metallic glass, biomaterials, dental implant, casting defect, mechanical properties, spherulite, corrosion, suction casting, arc melter

Laboratoire (s) de recherche : MATEIS – UMR CNRS 5510

Directeur de thèse : Jérôme CHEVALIER (Professeur), INSA de Lyon
Damien FABREGUE (Professeur), INSA de Lyon
Claire GAILLARD (Maitre de conférences), UCBL

Composition du jury :

Anne TANGUY	(Professeur), ONERA	Présidente du jury
Jean-Jacques BLANDIN	(Professeur), Univ Grenoble	Rapporteur
Jean-Christophe SANGLEBOEUF	(Professeur), Univ Rennes	Rapporteur
Nathalie BOZZOLO	(Professeur), MINES Paris Tech	Examinatrice
Florian SPIECKERMANN	(Maitre de conférences) Univ Leoben	Examinateur
Benoît TER-OVANESSIAN	(Maitre de conférences), INSA de Lyon	Invité